From the Priority Area Infections
of the Research Center Borstel / Leibniz Lung Center
Director: Prof. Dr. Ulrich Schaible

Mycobacterium tuberculosis infection of human macrophages: effects on cellular metabolism and lipid droplet composition

Dissertation
for Fulfillment of
Requirements
for the Doctoral Degree
of the University of Lübeck

from the Department of Natural Sciences

Submitted by

Simone Christa Tazoll
from Klagenfurt

Lübeck, 2022

First referee: PD Dr. Norbert Reiling

Second referee: Prof. Dr. Tamas Laskay

Date of oral examination: 06.04.2022

Approved for printing. Lübeck, 07.04.2022

Declaration

Hereby I declare that I have written this dissertation completely on my own. Furthermore, I confirm that no other sources have been used than those specified in the dissertation itself.

This dissertation, in the same or similar form, has not been submitted to any other doctoral degree committee yet.

Simone Christa Tazoll

18.01.2022, Hamburg

Table of contents

1. Introduction

1.1 Tuberculosis

1.1.1 Tuberculosis: an overview

Tuberculosis (TB) is an infectious disease and a major cause of death still ranking among the leading causes of death worldwide[1]. The causative agent of TB, *Mycobacterium tuberculosis* (Mtb), is still considered one of the biggest infectious killers globally having caused approximately 1.5 million deaths in 2020 and ranking second after the severe acute respiratory syndrome – coronavirus 2 (SARS-CoV-2). Furthermore, it is estimated that Mtb has latently infected about a quarter of the world's population, thereby presenting a major global health challenge[1,2]. The most common site of TB infection is the lung, but also extrapulmonary dissemination to other organs such as the central nervous system, abdomen, heart or skeletal system can occur[3]. While only a low percentage of infected individuals develop a symptomatic, primary pulmonary TB shortly after being infected with Mtb, the more common manifestation of TB is a post-primary pulmonary TB, which follows after a variably long period of clinically asymptomatic, latent TB infection (LTBI)[4]. Importantly, reactivation to an active form of disease only occurs in 5-10% of infected, immunocompetent individuals[5]. Clinically, TB manifests gradually over weeks and months in immunocompetent individuals, but in immunocompromised people or children, a more acute onset is possible[6]. Typical symptoms are productive cough, hemoptysis, breathlessness, weight loss, fever with night sweats and general malaise, which are also common symptoms of other diseases thereby often hampering rapid diagnosis of the TB[7]. The standard antibiotic treatment regimen against susceptible TB consists of a combination of the four first-line drugs isoniazid (INH), rifampicin (RIF), pyrazinamide and ethambutol over a period of 6 months[8]. The rising number of patients infected with drug-resistant TB represents a major challenge in the fight against TB. However, in 2020 approx. 132 thousand new cases were diagnosed RIF-resistant (RR), or resistant to INH and RIF and classified as multidrug-resistant TB (MDR-TB)[1]. Importantly, treatment of drug-resistant TB is of long duration and accompanied by severe side effects and toxicity, which results in sub-optimal outcomes and high mortality[9].

Taken together, to fight the global TB epidemic better diagnostic tools and improved therapies are needed to shorten treatment, reduce side effects and increase positive treatment outcomes. Moreover, a detailed understanding of TB pathogenesis is the key to improving TB treatment and will help develop innovative host-directed therapeutic approaches as an adjunctive treatment in combination with antibiotics.

1.1.2 Tuberculosis pathogenesis

TB is an airborne disease transmitted by infectious aerosols ranging from 1-5µM in size. These aerosols are generated by individuals with active pulmonary TB through several aerosol-producing respiratory activities such as coughing, sneezing, singing and talking[10]. Upon inhalation of infected aerosols, approximately 10% of the bacilli enter the bronchiole and alveoli of the respiratory tract, where they first encounter the alveolar macrophage (AM) (Fig. 1). Subsequent uptake but failure to kill Mtb by the AM induces a localized inflammatory response, including the production of tumor necrosis factor (TNF), interleukin (IL)- 12, IL-6 and IL-1, which leads to the recruitment of mononuclear cells to the site of infection forming innate immune cell aggregates (Fig. 1)[11,12]. Other types of innate immune cells infiltrating the site of infection are polymorphonuclear neutrophils (PMNs), which are described to increase the inflammatory nature of these granulomatous structures[13]. Apart from macrophages and PMNs and bridging the response of innate and acquired immunity, dendritic cells take up bacteria, dying cells and parts thereof, and subsequently migrate to regional draining lymph nodes, where they prime cells of the adaptive immune system such as B and T cells[14]. Upon activation and differentiation, T cells, most importantly T helper (Th) 1 and Th17 cells[15], migrate to the infection site where they form a lymphocytic cuff at the periphery of the Mtb-harboring macrophage center forming a fully organized granuloma. Importantly, the arrival of primed, Mtb-specific T cells is critical for the growth restriction of Mtb, which is not achieved by the early innate immune response alone[14]. This is due to interferon (IFN)-γ produced by Th1 cells, which leads to activation and enhancement of host defense mechanisms that can control bacterial growth[16–18]. Apart from T cells, B cells are also found in the lymphocyte cuff of the human TB granuloma and described to execute immunomodulatory and regulatory functions (Fig. 1)[19]. While the mature granuloma, with its macrophage center surrounded by a rim of lymphocytes and enclosed by a fibrous cuff, is capable of containing Mtb infection, this process also involves constant cell death of infected cells and recruitment of uninfected macrophages, which take up the debris and bacterial contents of infected macrophages[11,20] (Fig. 1). The recruitment of new immune cells is ensured by a high degree of vascularization mediated by e.g. the vascular endothelial growth factor[21].

At this stage, the infection reaches a latent state in most infected individuals, where the bacilli persist and replicate at a very low rate, but the infection remains contained to the granuloma and can even be resolved[11,22]. However, in 5-10% of immunocompetent individuals, the infection cannot be controlled resulting in the progression to an active form of disease[23]. This coincides with a reduction in vascularization, the disintegration of the highly organized wall

structure of the granuloma, and an increase in caseous debris deriving from the breakdown of infected macrophages in the center of the granuloma[20,24]. Furthermore, Mtb-induced dysregulation of macrophage lipid metabolism results in an increased formation of lipid-laden, foamy macrophages, which further contribute to the accumulation of caseum and provide host cell lipid substrates for Mtb growth[11,22]. An influx of neutrophils, which rapidly die of necrotic cell death and are unable to kill Mtb, are considered to enhance immunopathology and tissue damage[11,20,25,26]. This leads to the collapse of the granulomatous structure, release of virulent bacilli into the airways and extrapulmonary dissemination of the infection (Fig. 1)[22,27].

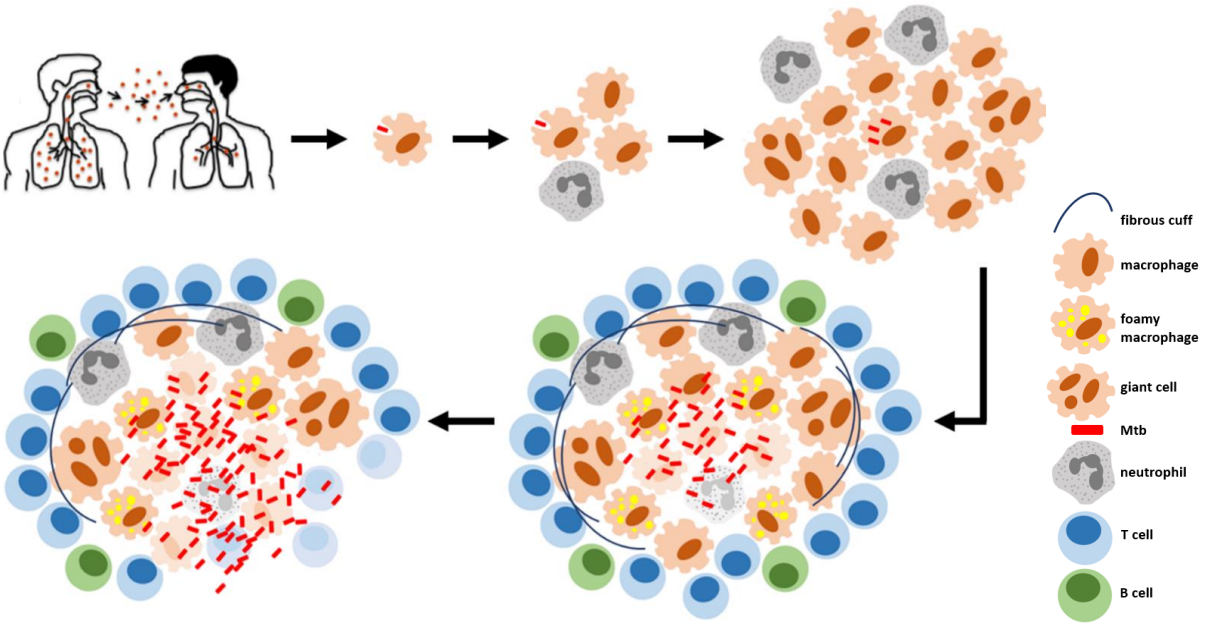

Figure 1: Schematic illustration of TB pathogenesis

Mtb containing aerosols released from infectious individuals are inhaled and enter the lung, where they are taken up by alveolar macrophages. Upon the induction of a local inflammatory response, other macrophages and neutrophils are recruited to the site of infection generating an innate immune cell aggregate. The mature granuloma is fully developed upon activation of acquired immunity. B and T cells are recruited and form a rim of lymphocytes around a center, which contains several macrophage subtypes such as the foamy macrophage and giant cells, surrounded by a fibrous cuff. Disease reactivation leads to bacterial replication, followed by the collapse of the granulomatous structure and dissemination of bacilli[11,14,22].

While the reasons for the progression to an active TB are not fully understood, several mechanisms have been identified which promote reactivation of the disease. TNF is described to be critical for the initial and long-term control of TB, as it is required for granuloma formation and maintenance and together with IFN-γ leads to activation of macrophages[12]. This also becomes evident in patients with LTBI, who were subjected to treatment with TNF neutralizing antibodies and subsequently developed active TB[28]. Aside from that, IFN-γ has also been

described as pivotal for Mtb growth control, as humans deficient in either IFN-γ or IFN-γ receptor are more susceptible to Mtb infection[29]. This is further highlighted in HIV-positive individuals, where the lack of cluster of differentiation (CD) 4^+ T cells drastically increases the likelihood of developing active disease[30]. Linked to IFN-γ production and TB reactivation is also the cytokine transforming growth factor (TGF) -β, which is expressed at high levels in the lung tissue of TB patients and suppresses T cell response and macrophage activation[31]. In summary, this supports the critical role of macrophage activation and function in the control of Mtb infection.

1.1.3 Macrophages in tuberculosis

Macrophages are key players in the control of Mtb infection. Upon interaction with and uptake of Mtb by macrophages, several cellular processes are known to be essential for a successful immune response, such as cytokine signaling, inflammasome activation, antigen, processing/presentation, phagosome maturation and cell death, are activated. However, although macrophages are generally equipped with a good arsenal for killing Mtb, the bacteria have developed several strategies to modulate macrophage response in order to survive and replicate in these cells[32,33].

For example, several structures on the mycobacterial envelope are preferentially recognized through phagocytic receptors such as the mannose receptor, Fc receptor and complement receptor, which are not coupled to strong activation of macrophage antimicrobial mechanisms. This may lead to impaired phagosome maturation and promote intracellular survival[34–36]. Furthermore, one critical response of macrophages induced by Mtb and promotes Mtb infection is the secretion of type-1-IFNs. Cytosolic recognition of mycobacterial structures or recognition through surface receptors induces type-1-IFN production and the overexpression of IFN response genes such as *STAT*s, *IRF*s and *IFIT*s has been observed[37]. Type-1-IFNs then induce cell death and dissemination of bacteria and thereby exacerbate TB pathology *in vitro* and *in vivo*[38]. Furthermore, high levels of type-1-IFNs impair the protective effect of IFN-γ signaling, which is required for macrophage activation of antibacterial defenses by increasing phagocytosis, phagolysosomal fusion, pro-inflammatory cytokines and oxidative burst and thereby restricting Mtb growth[17,39,40]. Another way of evading excessive T-cell mediated immunity and IFN-γ production by Mtb is the interference with macrophage antigen processing and presentation. Upon Mtb infection macrophages present Mtb antigens to $CD4^+$ T-cells through the major histocompatibility complex (MHC) class II. However, Mtb-induced

interference with antigen processing and presenting as well as downregulation of MHC class II expression inhibits T-cell immunity against Mtb[41]. Taken together, Mtb-induced modulation of macrophage function allows mycobacterial persistence and growth. One critical aspect of macrophage function, which also directs the immune response to several stimuli including Mtb, is the macrophage energy metabolism[2,42,43]. It is now well appreciated that the metabolic state of macrophages influences their inflammatory phenotype. Pro-inflammatory, so-called M1 macrophages are characterized by increased glycolytic metabolism and a broken tricarboxylic acid cycle (TCA). In contrast, anti-inflammatory, M2 macrophages rely on the metabolization of fatty acids and oxidative phosphorylation (OXPHOS) for energy production[44]. During TB, macrophages undergo metabolic alterations, which cause increased accumulation of lipids and differentiation into foamy macrophages. These macrophages are less microbicidal, show impaired anti-mycobacterial properties and fail to control the Mtb-infection[45]. Furthermore, intracellular Mtb utilizes host-derived lipids for persistence and subsequent necrosis of foamy macrophages contributes to the caseum formation at the center of the TB granuloma, which promotes extracellular growth of bacteria[46].

Collectively, Mtb-induced manipulation of macrophage function, including disruptions in bioenergetic metabolism, promotes bacterial persistence and growth in macrophages. The investigation of macrophage metabolism could provide a better understanding of the human TB pathology, therefore, bearing the chance to develop future treatment approaches for the disease[47].

1.2 Metabolism

1.2.1 Cellular energy metabolism

Cellular energy is produced through the oxidation of the three major fuels, namely carbohydrates, lipids and proteins. The free energy produced in these oxidation processes is ultimately stored in energy bonds within nucleoside phosphates such as adenosine 5′ diphosphate (ADP) and most importantly, adenosine 5′ trisphosphate (ATP)[48]. However, cellular metabolism also has functions beyond the mere production of energy, as evident by the synthesis of crucial metabolic intermediates, which contribute to cellular growth, differentiation, cell signaling pathways and immune cell function and response[49–51]. Metabolic pathways such as glycolysis and OXPHOS are two major processes producing energy and critical metabolic intermediates and thus define the metabolic signature of the macrophage response to various stimuli[44].

1.2.1.1 Glycolysis

Glycolysis has been described as one of the simplest ways for cells to produce energy[44,52]. Aside from its role in energy production, glycolytic intermediates are also involved in the biosynthesis of ribose, amino acids and lipids. For example, glycolysis also supplies the pentose phosphate pathway (PPP), which is critical for the biosynthesis of nucleotides and the production of nicotinamide adenine dinucleotide phosphate (NADPH)[53]. This is a molecule used by the NADPH oxidase for pathogen clearance and is required for the generation of the glutathione (GSH), which protects the cell from oxidative stress[44,54,55].

Taking place in the cytosol, glycolysis involves a series of 10 enzymatic reactions resulting in the conversion of one molecule of glucose into two molecules of pyruvate and two molecules of ATP and nicotinamide adenine dinucleotide (NADH)[48]. Following the uptake of glucose through several glucose transporters (GLUTs), which belong to the solute carrier family (SLC) and comprise 14 isoforms (SCLA1-14), followed by rapid phosphorylation to glucose-6-phosphate (G-6-P) by hexokinases (HK) (Fig. 2)[56,57]. When not entering the PPP, isomerization of G-6-P and a second phosphorylation by phosphofructokinase (PFK) to form fructose-1,6-biphosphate (F-1,6-BP) occur. Subsequently, the six-carbon sugar is ultimately cleaved into two molecules of the three-carbon glyceraldehyde-3-phosphate (GAP), which is phosphorylated by the glyceraldehyde-3-phosphate dehydrogenase (GAPDH) in a process that produces NADH[44,58]. Further metabolization leads to the formation of 3-phosphoglycerate (3-PG) by the phosphoglycerate kinase (PGK) and ultimately the formation of pyruvate by the pyruvate kinase (PK), both being ATP-producing steps (Fig. 2)[48,58].

The cellular microenvironment determines further metabolization of pyruvate. For example, under anaerobic conditions or low NAD^+ concentrations, pyruvate is reduced to lactate by lactate dehydrogenase (LDH) in a process called lactate fermentation and requires the oxidation of NADH to NAD^+[59,60]. Importantly, lactate fermentation can also happen under aerobic conditions, which is known as the "Warburg effect" and was first discovered in rapidly growing cancer cells but is now also described in activated immune cells[42,58,61]. Alternatively, under normal physiological conditions, pyruvate is converted to acetyl-Coenzyme A (CoA), which is further metabolized through the TCA or OXPHOS in mitochondria resulting in the production of a total of 36 molecules of ATP per molecule glucose (Fig. 2)[60,62].

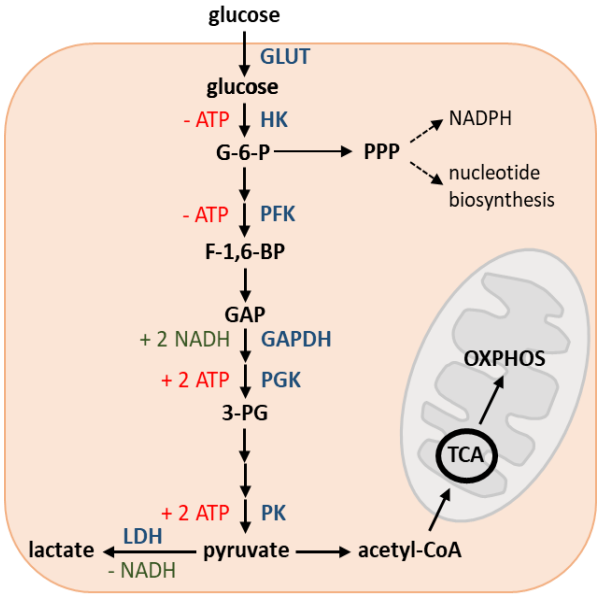

Figure 2: Schematic illustration of glycolysis

After uptake, glucose is metabolized through glycolysis in a series of enzymatic reactions resulting in the formation of pyruvate, ATP and NADH. Pyruvate can be converted to lactate or acetyl-CoA, the latter of which fuels the TCA and subsequently OXPHOS. Aside from that, glucose also feeds into the PPP required for NADPH formation and nucleotide biosynthesis[53,58].

1.2.1.2 Oxidative phosphorylation

For a long time, mitochondria have been labeled the powerhouse of cells as they are the primary source of energy produced through OXPHOS. Prior to OXPHOS, several substrates derived from the breakdown of glucose, fatty acids and glutamine are metabolized through the TCA in a series of enzymatic reactions, which leads to the production of the NADH and flavin adenine dinucleotide ($FADH_2$)[63,64]. NADH and $FADH_2$ then transfer electrons to the electron transport chain (ETC), which are transported through several multimeric complexes along the ETC, generating a proton gradient that is used for the synthesis of ATP[65]. OXPHOS can only occur in aerobic conditions, as the last step of OXPHOS requires the reduction of oxygen (O_2) to H_2O[66].

In the first step, NADH and $FADH_2$ transfer electrons to complex I (NADH: ubiquinone oxidoreductase) and complex II (succinate dehydrogenase) of the ETC, respectively (Fig. 3). These electrons are next supplied to the Q cycle, where the ubiquinone is reduced to ubiquinol[67]. Subsequently, in complex III (ubiquinol- cytochrome c oxidoreductase) electrons from ubiquinol are transferred to cytochrome c (C) in a process that is again linked to the transfer of protons into the IMS[68]. Ultimately, electrons are passed on from cytochrome C to the complex IV (cytochrome c oxidase), where they are used to reduce the final electron acceptor oxygen to water[48]. Importantly, this transport of electrons along the ETC is coupled to the translocation

of protons from the mitochondrial matrix into the inner membrane space (IMS), in complex I and III and complex IV[65–67]. This results in the formation of an electrical potential and a proton gradient (ΔpH) over the inner mitochondrial membrane generating the mitochondrial membrane potential ($\Delta\boldsymbol{\Psi}$). Complex V, which is an ATP synthase, uses this $\Delta\boldsymbol{\Psi}$ to produce energy[69]. Protons, driven by the $\Delta\boldsymbol{\Psi}$, re-enter the mitochondrial matrix through complex V, which is an ATP synthase, causing conformational rearrangements that allow the synthesis of one molecule ATP from 4 protons, that translocate along the $\Delta\boldsymbol{\Psi}$ (Fig. 3)[48,69].

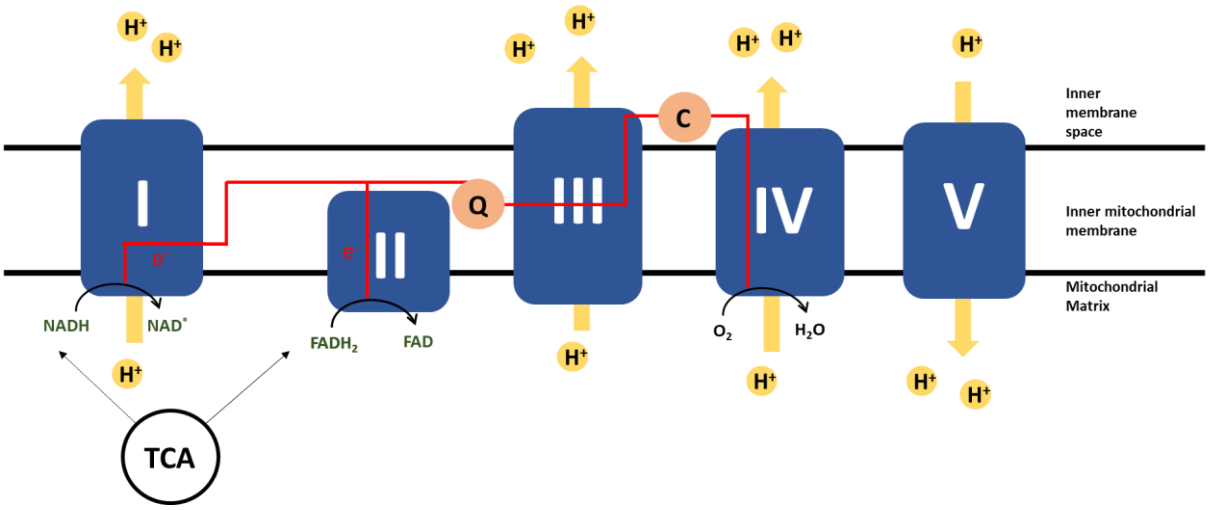

Figure 3: Schematic illustration of the electron transport chain

NADH and $FADH_2$ produced in the TCA transfer electrons to complex I and complex II of the ETC, respectively. After entering the Q cycle electrons are further transferred from complex III to cytochrome C and are ultimately passed on to complex IV, where the final electron acceptor O_2 is reduced to H_2O. This electron transferring process is coupled to the translocation of H+ from the mitochondrial matrix to the IMS in complexes I, III and IV. H+ translocate back to the mitochondrial matrix coupled to the production of ATP in complex V[48,69].

OXPHOS, while being approximately 100 times slower than glycolysis, can result in the production of approximately 36 molecules of ATP from one molecule of glucose[70]. This stoichiometry changes even more when other substrates, such as fatty acids fuel OXPHOS, highlighting the efficiency of OXPHOS[70]. Importantly, not all the potential energy deriving from the electron transport across the ETC is fully converted into ATP. Processes such as proton leak or electron slipping can lead to uncoupling of the substrate oxidation from ATP synthesis[71,72]. Furthermore, leak of electrons from the ETC can result in the production of reactive oxygen species (ROS), such as superoxide anion $O2^-$, which is an important signaling molecule, but can also be harmful when produced excessively[67,71]. While mitochondria are highly dynamic organelles and constantly undergo structural changes to adapt to bioenergetic

demands, mitochondrial damages can also lead to cell death. Processes like mitochondrial fusion and fission to remove damaged mitochondria or propagate mitochondria under conditions of high energy demand aim to maintain and regulate mitochondrial function and cell fate[73]. Collectively, mitochondrial homeostasis is critical for cellular health and function and dysregulations in mitochondrial metabolism can have detrimental effects on immune cells.

1.2.2 Lipid metabolism

Fatty acids are one major substrate fueling energy metabolism in macrophages. Lipid homeostasis is critical for macrophage function, as dysregulations of fatty acid metabolism are found in many inflammatory diseases and can lead, for example, to increase the accumulation of fatty acids and formation of lipid-laden, foamy macrophages[74]. Structurally, fatty acids consist of an aliphatic chain of methylene groups of diverse length (usually 2-36 carbon atoms) with a carboxyl group on one end of the chain. Depending on their length, they can be categorized into short or long-chain fatty acids and determined by the number of double bonds be classified into unsaturated, monosaturated and polyunsaturated fatty acids[75]. Functionally, apart from providing energy for cells, fatty acids are also crucial in the synthesis of lipid mediators, they are the building blocks of membrane lipids, act as metabolic regulators and can modulate gene expression and survival pathways[76,77]. In general, fatty acid metabolism can be separated into the synthesis of fatty acids and the degradation thereof.

1.2.2.1 Fatty acid synthesis

Fatty acids can be either synthesized *de novo* or can be taken up from the environment. *De novo* synthesis of fatty acids involves the enzyme acetyl-CoA carboxylase (ACC) 1, which converts acetyl-CoA to malonyl-CoA, and the fatty acid synthase (FASN), which catalyzes the formation of long-chain fatty acids from acetyl-CoA and malonyl-CoA through several rounds of elongation (Fig. 4)[78]. Interestingly, however, some studies also suggest that de novo synthesis of fatty acids is a common feature of highly proliferating cells, such as cancer cells, or in macrophages during atherosclerosis or under hypoxic conditions[79–81]. Alternatively, exogenous fatty acids can be taken up in a process that is facilitated by several integral or membrane-associated proteins, such as the fatty acid transport proteins (FATP) 1-6 and the scavenger receptor CD36 (Fig. 4)[82]. Aside from that, transmembrane diffusion was also described as a way to take up dietary fatty acids. In this process, fatty acid of the polar head reorient from the aqueous interface to the opposite interface ("flip-flop")[83]. Upon entry or *de novo* synthesis, non-esterified, free fatty acids (FFA), are rapidly esterified with CoA to form acyl-CoAs mediated

by the long-chain acyl-CoA synthetase ligases (ACSLs) before they can undergo any further metabolic processing[84]. Once esterified, fatty acids can be further elongated in an enzymatic reaction that is catalyzed by the elongation of very-long-chain fatty acids protein (ELOVL)[85,86]. The activity of fatty acid desaturase (FADS) can further alter the structure of fatty acids by introducing carbon double bonds and thereby leading to the formation of mono- and polyunsaturated fatty acids[87]. The traffic of fatty acids within the cell is mediated by fatty acid-binding proteins (FABPs), which facilitate the transport of fatty acids to specific organelles such as lipid droplets, the ER and mitochondria[77].

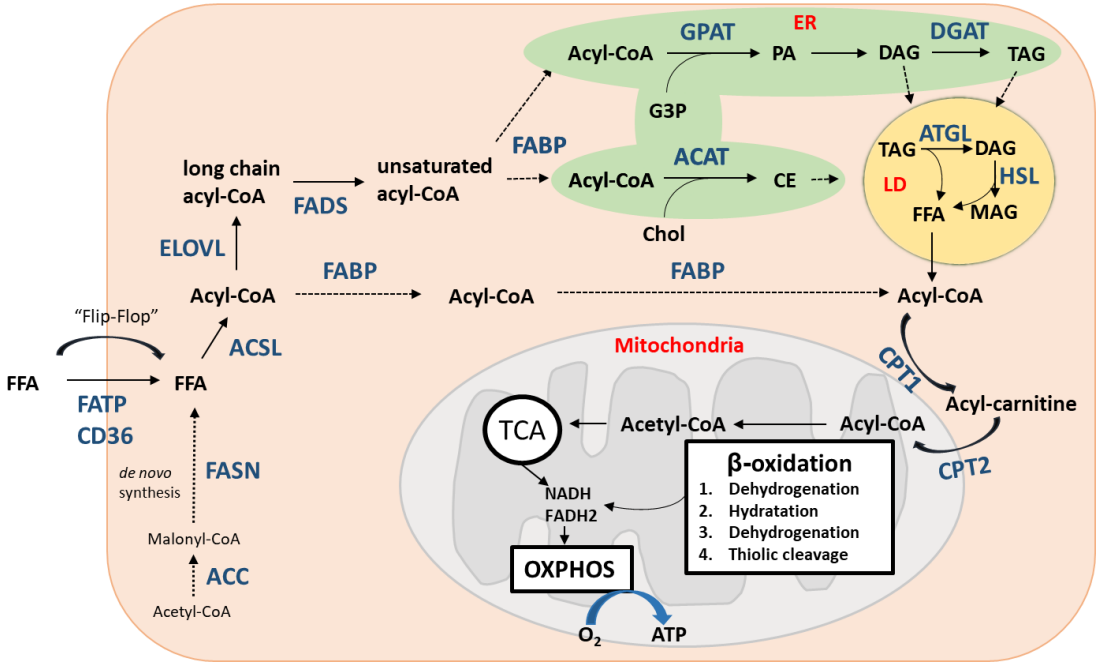

Figure 4: Schematic illustration of the cellular fatty acid metabolism

FFA are either taken up or synthesized *de novo*, esterified to acyl-CoA by ACSL and subsequently elongated and/or desaturated by ELOVL and FADS, respectively. Fatty acyl-CoA are transported to other organelles mediated by FABP and can be incorporated into complex neutral lipids such as DAGs, TAGs and CEs, which are stored in LDs. Acyl-CoAs can be released from neutral lipids by lipases and transported into mitochondria mediated by the carnitine shuttle. Degradation of fatty acids through β-oxidation occurs in 4 enzymatic steps generating acetyl-CoA, which enters the TCA and thereby fuels OXPHOS and mitochondrial ATP production.

After synthesis and esterification, fatty acids can be incorporated into complex lipids such as membrane lipids or neutral lipids, which are synthesized at the endoplasmic reticulum (ER), but also in mitochondria[88,89]. The first step in *de novo* lipid synthesis involves the transfer of fatty acyl chains to glycerol-3-phosphate (G-3-P) catalyzed by the family of glycerol-3-phosphate acyltransferases (GPATs), localized to the ER- and mitochondrial membrane to form phosphatidic acid (PA)[90]. PA is further metabolized to diacylglycerol (DAG), which is a major

precursor for phospholipids and triacylglycerol (TAG) synthesis[90,91]. TAGs are formed through further esterification of a third acyl-CoA chain to DAG by the diacylglycerol-*O*-acyltransferases 1 and 2 (DGAT1 and 2), which is localized in the ER [91]. Also, localized in the ER is the synthesis of cholesterol esters (CEs), which involves the esterification of one fatty-acyl-CoA to cholesterol by the acyl-CoA: cholesterol acyltransferase (ACAT)[92]. The newly synthesized TAGs, DAGs and CEs are then stored in lipid droplets (LDs), the intracellular storage organelles for fatty acids, and can be used at later times for energy production through fatty acid oxidation (FAO) or for other cellular functions (Fig. 4)[93].

1.2.2.2 Fatty acid degradation

As described before, fatty acids are also an important source of energy, as degradation of fatty acids through FAO. This results in the production of NADH and $FADH_2$ and acetyl-CoA, which is supplied to the TCA[94]. Fatty acids as energy substrates can be provided by the hydrolysis of fatty acids from neutral lipids in a process called lipolysis. This process is catalyzed by lipases such as the adipose triglyceride lipase (ATGL) and the hormone-sensitive lipase (HSL), which each hydrolyze one fatty acid chain from TAG and DAG, respectively (Fig. 4)[95]. These fatty acids are again esterified by ACSL transported across the mitochondrial membrane using the carnitine shuttle system. This transport process requires the conjugation of long-chain acyl-CoAs to carnitine mediated by the carnitine-palmitoyl transferase 1 (CPT1) located in the outer mitochondrial membrane. Acyl-carnitines then cross the inner mitochondrial membrane through a translocase and free acyl-CoAs are released into the mitochondrial matrix mediated by CPT2 located at the inner mitochondrial membrane, while free carnitine is transported back into the cytoplasm. Once in the mitochondria, fatty acids are oxidized in a sequence of 4 enzymatic steps: the dehydrogenation by the acyl-CoA dehydrogenase (ACAD) resulting in the formation of $FADH_2$, hydration by the enoyl-CoA hydratase, another dehydrogenation by the hydroxy acyl-CoA dehydrogenase (HADH) producing NADH and ultimately the thiolic cleavage into a two-carbon chain-shortened acyl-CoA and acetyl CoA. The resulting shortened acyl-CoA can then enter this process again until the fatty acid is fully degraded[94,96]. Aside from mitochondria, peroxisomes also partake in the degradation of fatty acids. However, the first step in peroxisomal fatty acid degradation is mediated by acyl-CoA oxidases (ACOXs), which directly donate the produced electrons to O_2 without producing $FADH_2$. Furthermore, peroxisomal beta-oxidation can either shorten fatty acids or fully degrade them to acetyl-CoA., which are then transferred to mitochondria for full degradation through the TCA and OXPHOS (Fig. 4)[96]. In summary, acetyl-CoA produced by both, mitochondrial and peroxisomal FAO,

ultimately fuels the TCA, which provides further reducing equivalents for the ETC[94,96]. Apart from producing energy, FAO has also been described to be critical for regulating NADPH levels, thereby contributing to maintaining cellular redox homeostasis, and FAO-derived carbon also contributes to replenishing the TCA to fuel *de novo* nucleotide synthesis[97,98]. Therefore, in healthy cells, an equilibrium of the synthesis and degradation of fatty acids is required to maintain energy levels and cellular function. Disruptions in FAO can result in increased accumulation of fatty acids, increased LD formation and lipid overload, which can cause cellular dysfunction and cell death[99,100]. Particularly in macrophages disruptions in lipid homeostasis have been described to promote differentiation into foamy macrophages, which are characterized by increased accumulation of LDs. Furthermore, these foam cells are associated with chronic inflammation and increased pathology in cancer, as well as metabolic, infectious and autoimmune disorders[74].

1.2.3 Lipid droplets

For a long time, LDs have been simply considered as cytoplasmic inclusions of fat, however, in recent years the knowledge about the function and role of LD has expanded[93]. They are not only involved in the storage of fatty acids and hubs for fatty acid trafficking but are also storage organelles for antimicrobials and proteins. In addition to that, they act as organizing platforms for immune cell signaling, manage stress responses, act as redox and energy buffers and function in RNA biology[93,101–104].

Structurally, LDs consist of a central, hydrophobic core of TAGs, DAGs, CEs and FFA, which is surrounded by a monolayer of amphipathic phospholipids (PLs) and proteins[105]. The formation of LDs starts at the ER, where also the neutral lipid synthesizing enzymes DGAT1 and 2 and ACAT enzymes are localized[106] (Fig. 5). Accumulation of neutral lipids between the two leaflets of the ER lipid bilayer leads to the formation of a lens of neutral lipids, named pre-LDs, which grow with the arrival of more neutral lipids. The decreased bilayer tension at the cytoplasmic monolayer caused by ER proteins and lipids, such as lyso-PLs, as well as increased bilayer tension at the lumenal layer then lead to the unidirectional growth of LD into the cytoplasm. In consequence, a spherical structure containing neutral lipids surrounded by the outer layer of the ER is formed representing the budding LD. Subsequently, surface tension and lipid composition at the LD budding side are considered to drive the LD growth and scission process, as in higher eukaryotes no protein responsible for the separation of the nascent LD has been identified yet[106,107].

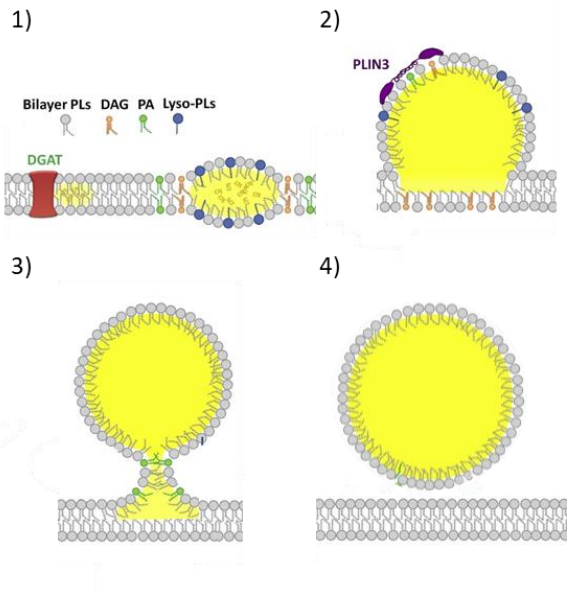

Figure 5: Schematic illustration of the LD formation

1) Localized neutral lipid synthesis between the leaflets of the ER membrane leads to the accumulation of lipids and lens formation. 2) Decreased tension of the cytoplasmic layer of the membrane, mediated by lyso-PLs leads to unidirectional growth of the LD. 3) and 4) A neck is formed where the spherical LD starts budding off and ultimately completely separates from the ER[106,107].

Once matured and fully separated from the ER, further LD growth can occur through protein-mediated interaction and fusion of two LDs or local lipid synthesis on LDs using lipid metabolic enzymes localized to the LDs. Similarly, they can also decrease in size by the activity of the LD-localized lipases ATGL and HSL or are completely degraded through lipophagy[93,108]. Importantly, LDs can vary greatly in size generally ranging from 20nm to up to 5µm in non-adipocytes, but they also vary in their number and spatial organization[109]. These parameters also determine the function of the LDs, as for example in adipocytes, few and very large LDs function primarily for long-term lipid storage[110]. Aside from size and number, LDs can differ strongly in their lipid and protein composition, which significantly affects LD functionality. The majority of PLs are phosphatidylcholines found in the membrane monolayer of LDs, also phosphatidylethanolamine (PE), phosphatidylinositol (PI), phosphatidylserine (PS) and sphingomyelin (SM). Of note, changes in the PL ratios affect LD synthesis, size and degradation[111]. In line with that, the neutral lipid composition is linked to the recruitment of the perilipins (PLINs) 1-5, which are major LD-associated proteins, which exert numerous functions such as stabilizing LD structure, lipolysis, lipid mediator production and also mediate direct interaction with mitochondria[93,112]. The movement of LDs required for interaction with other organelles can occur randomly over short distances. However, they can also be transported bi-directionally over longer distances, a process mediated by the cytoskeleton and motor proteins such as dynein and kinesin, which associate with LDs. Due to the movement of LDs, the spatial organization of LDs within the cell is directed, which can vary strongly depending on the cell type and function of the cell[109]. In summary, LDs show a high degree of diversity, which is linked to the diverse functions of LDs within different cell types and tissues.

1.3 The role of metabolism during Mtb infection

In TB, energy metabolism, particularly fatty acid metabolism, plays a critical role, as dysregulation in fatty acid metabolism leads to the formation of foamy macrophages[11,22,22]. Although foamy macrophages, which are characterized by the accumulation of fatty acids and LDs, are a cellular hallmark of the human TB granuloma, little is known about the metabolic alterations in macrophages during Mtb infection[22].

Transcriptional profiling of murine lung tissue identified an upregulation of glycolytic genes upon Mtb infection, suggesting an Mtb-induced shift towards aerobic glycolysis, which was also corroborated *in vitro* in human and murine macrophages[42,113,114]. In contrast to that, another recent study using extracellular flux analysis in primary human macrophages showed that virulent Mtb induces a decrease in bioenergetic metabolism including glycolysis, an effect not observed when using avirulent Mtb strains[115]. Looking at macrophage lipid metabolism, characterization of macrophages isolated from Mtb-infected mouse lungs showed that alveolar macrophages committed to FAO demonstrate an increased bacterial burden and reduced effector functions[114]. This was corroborated *in vitro* in murine macrophages, where inhibition of FAO results in decreased bacterial growth[116]. In contrast to that, a recent *in vitro* study in murine macrophages showed that Mtb-induced expression of the Wnt family member 6 (WNT6) leads to downregulations of factors involved in FAO thereby promoting lipid accumulation and Mtb growth[117]. This is in line with the observation in human macrophages showing that Mtb infection interferes with FAO in a hypoxia-inducible factor (HIF)-1-dependent manner in alternatively activated macrophages, thereby promoting the foamy phenotype of human macrophages[45].

These partly contradicting results in both, the human and murine system, highlight the need for further detailed characterization of macrophage metabolism, particularly fatty acid metabolism during Mtb infection. Furthermore, there is only little information regarding the exact role and composition of LDs during Mtb infection. The observation that the accumulation of LDs in macrophages promotes Mtb infection has been substantiated by studies showing that Mtb uses host-derived fatty acids as a nutrient source and that Mtb-containing phagosomes localize to LDs[117–119]. However, recent findings of nonconventional roles of LDs suggest that they might also exert other functions beyond the storage of lipids, such as immunomodulatory functions, as has been proposed before[101]. However, a more detailed characterization of LDs is required to better understand their function and structural composition during Mtb infection.

2. Objectives

As described above, macrophages undergo significant metabolic reprogramming when infected with Mtb. Dysregulation of lipid metabolism is linked to the accumulation of LDs and differentiation of macrophages into foam cells, which are a hallmark of the human TB granuloma. Although of critical importance, the metabolic alterations caused by an Mtb infection, particularly in human macrophages, are not well studied. Furthermore, the structure and composition of LDs, the intracellular storage organelles of lipids, have not been characterized well during Mtb infection.

In this doctoral study, human monocyte-derived macrophages (hMDMs) were used to study the effect of an infection with live, virulent Mtb on macrophage metabolism. To this end, hMDMs were infected with Mtb H37Rv and analyzed using several approaches including mass spectrometry-based approaches, flow cytometry as well as real-time extracellular flux analysis to analyze the following aspects:

- How is glycolytic and respiratory metabolism affected by an infection of hMDMs with Mtb?
- How does Mtb infection influence intracellular fatty acid and lipid metabolism in hMDMs?

In addition to that, this project also aimed to isolate and characterize LDs from hMDMs in order to address the following points:

- How can LDs be successfully isolated from primary human macrophages?
- How does Mtb infection influence the neutral lipid and protein composition of isolated LDs?

3. Materials and Methods

3.1 Materials

Table 1:List of reagents and disposals	
Material	**Manufacturer**
1.5ml protein low bind tubes	Eppendorf, Hamburg, Germany
16G needle	Becton Dickinson, Heidelberg, Germany
2-Deoxyglucose	Thermo Scientific, Waltham, USA
2-Mercaptoethanol	Sigma-Aldrich, St. Louis, USA
50ml Luer Lock Spritzen	Becton Dickinson, Heidelberg, Germany
96-well-plates; flat bottom	Corning, New York, USA
96-well-plates; round bottom	Corning, New York, USA
Absolut ethanol for molecular biology	APPLICHEM, Darmstadt, Germany
Acrylamid/Bis solution 37,5:1	Serva Electrophoresis GmbH, Heidelberg, Germany
Albumin (BSA) Fraction V (pH7,0)	APPLICHEM, Darmstadt, Germany
Antimycin A from Streptomyces sp.	Sigma-Aldrich, St. Louis, USA
APS	Sigma-Aldrich, St. Louis, USA
Aqua Ecotainer®	Braun, Melsungen, Germany
BCA Protein Assay Kit	Thermo Scientific, Waltham, USA
BHT (2,6-Di-tert-butyl-4-methylphenol)	Sigma-Aldrich, St. Louis, USA
Blunt needle 27G, Endospülkanüle	M+W Dental, Illnau, Swizzerland;
BODIPY™ 493/503	Thermo Scientific, Waltham, USA
Boric acid	Carl-Roth, Karlsruhe, Germany
Bovine serum albumin (LE)	Sigma-Aldrich, St. Louis, USA
Bromphenol blue sodium salt	Carl-Roth, Karlsruhe, Germany
Calf Serum	Serana Europe GmbH, Pessin, Germany
Casy Kapillar-und Systemreiniger	Roche, Basel, Switzerland
Cell scraper	VWR,Radnor, USA
Corning costar Stripette (5ml, 10ml, 25ml)	Corning, New York, USA
Corning® 96 well microplates	Sigma-Aldrich, St. Louis, USA
Costar Stripette™, 10ml	Corning, New York, USA
Costar Stripette™, 25ml	Corning, New York, USA
Costar Stripette™, 5ml	Corning, New York, USA
Deckel für Küvetten	Th.Geyer GmbH, Renningen, Germany
D-glucose, cell culture grade	APPLICHEM, Darmstadt, Germany
Difco™ Middlebrook 7H10 Agar	Becton Dickinson, Heidelberg, Germany
Difco™ Middlebrook 7H9 Broth	Becton Dickinson, Heidelberg, Germany
Dilution solution Casy Cellpack	Sysmex Corporation, Kobe, Japan
Dimethylsulfoxide for cell culture	APPLICHEM, Darmstadt, Germany
Direct-zol™ RNA MiniPrep	Zymo Research, Irvine, Canada;
DL-Dithiothreitol	Sigma-Aldrich, St. Louis, USA

Dodecysulfate-Na-salt in pellets	Serva Electrophoresis GmbH, Heidelberg, Germany
DRAQ7™	Abcam, Cambridge, UK
Dulbecco's PBS (10x)	Biochrom, Berlin, Germany
ECL Kit	GE Healthcare, Illinois, USA
Eppendorf® Safe-Lock microcentrifuge tubes (1.5ml, 2ml)	Sigma-Aldrich, St. Louis, USA
Eppendorf®Combitips advanced 0.25ml	VWR,Radnor, USA
Eppendorf®Combitips advanced 0.5ml	Eppendorf, Hamburg, Germany
Ethanol non-denatured	Walther CMP GmbH, Kiel, Germany
Ethylenediamine tetraacetic acid disodium (Na_2-EDTA)	Carl-Roth, Karlsruhe, Germany
Falcon® 5ml polystrene round-bottom	Corning, New York, USA
FCCP	Cayman Chemical , Ann Arbor, USA
FCS Standard South America sterile filtered	Pan-Biotek, Aidenbach, Germany
Filter Tip 10-1000µl	Nerbe plus, Winsen, Germany
Filtropur S 0.2 syringe filter	Sarstedt, Nümbrecht, Germany
Glaspasteurpipetten	Brand, Wertheim, Germany
Gloves, powder free nitrile	VWR,Radnor, USA
Glycerol	Carl-Roth, Karlsruhe, Germany
Glycine, analytical grade	Serva Electrophoresis GmbH, Heidelberg, Germany
HBSS	Pan-Biotek, Aidenbach, Germany
Hydrochloric Acid 1mol/l	APPLICHEM, Darmstadt, Germany
InnuPREP DNA mini kit	Analytik Jena, Jena, Germany
Inoculation loop with needle	Brand, Wertheim, Germany
Küvetten	Sarstedt, Nümbrecht, Germany
L-Glutamine	Pan-Biotek, Aidenbach, Germany
LiChrosolv® Methanol	MERCK MILLIPORE, Darmstadt, Germany
LightCycler®480 multiwell plate 96, white	Roche, Basel, Switzerland
LightCycler®480 sealing foil	Roche, Basel, Switzerland
LightCycler®480 SYBR Green I Master	Roche, Basel, Switzerland
Lipid droplet isolation kit	Cell Biolabs Inc., San Diego, USA
Methanol	MERCK MILLIPORE, Darmstadt, Germany
Microtube 1.5ml	Sarstedt, Nümbrecht, Germany
Mini Cell scrapers	Biotium, Freemont, USA
MitoTracker™ Deep Red FM	Thermo Scientific, Waltham, USA
Multiply®PCR strips, 0.2ml chain	Sarstedt, Nümbrecht, Germany
Multiply®-Pro tube 0.5ml	Sarstedt, Nümbrecht, Germany
Nalgene™ square bottles	Thermo Scientific, Waltham, USA
NaOH 1N	Carl-Roth, Karlsruhe, Germany
Neubauer Zählkammer	NeoLab Migge GmbH, Heidelberg, Germany

Nunc® Cyro Tubes®	Sigma-Aldrich, St. Louis, USA
Nunclon™ Delta surface petridish	Thermo Scientific, Waltham, USA
Nunclon™ Delta surface, 24-well	Thermo Scientific, Waltham, USA
Nunclon™ Delta surface, 6-well	Thermo Scientific, Waltham, USA
Nunc™ 48 and 96 well multidishes	Thermo Scientific, Waltham, USA
Nunc™ cell culture Petri dish	Thermo Scientific, Waltham, USA
OADC (oleic acid, albumin, dextrose, catalase)	Becton Dickinson, Heidelberg, Germany
Oleic acid	APPLICHEM, Darmstadt, Germany
Oligomycin	Cayman Chemical, Ann Arbor, USA
PageRuler™ Plus prestained Protein Ladder	Thermo Scientific, Waltham, USA
Palmitic acid	Sigma-Aldrich, St. Louis, USA
Pancoll	Pan-Biotek, Aidenbach, Germany
Paraformaldehyde, methanol free	Alfa Aesar, Massachusetts, USA
Penicillin-Streptomycin	Pan-Biotek, Aidenbach, Germany
peqGOLD TriFast	VWR, Radnor, USA
Petridish 92x16mm	Sarstedt, Nümbrecht, Germany
Pipet reservoir	NeoLab Migge GmbH, Heidelberg, Germany
Pipette tip, 1000µl	Sarstedt, Nümbrecht, Germany
Pipette tip, 20µl	Sarstedt, Nümbrecht, Germany
Pipette tip, 200µl	Sarstedt, Nümbrecht, Germany
Pipette tips, no filter; 10 - 1000 µl	Sarstedt, Nümbrecht, Germany
Ponceau S solution	Sigma-Aldrich, St. Louis, USA
Protease Inhibitor Cocktail Tabletten	Roche, Basel, Switzerland
PVDF-Membran Immobilo P	MERCK MILLIPORE, Darmstadt, Germany
Recombinantes humanes MCSF	R&D Systems, Minneapolis, USA
Rhodamine 123	Thermo Scientific, Waltham, USA
Rollerbottles	Corning, New York, USA
Rotenone	Abcam, Cambridge, UK
RPMI 1640 VLE	Pan-Biotek, Aidenbach, Germany
SafeSeal microtube 2ml	Sarstedt, Nümbrecht, Germany
Screw Cap tube, 15ml	Sarstedt, Nümbrecht, Germany
Screw Cap tube, 50ml	Sarstedt, Nümbrecht, Germany
Seahorse XF DMEM medium, pH7.4	Agilent Technologies, Santa Clara, USA
Seahorse XFe96 FluxPak	Agilent Technologies, Santa Clara, USA
Sealing foil	Kisker Biotech GmbH, Steinfurt, Germany
Sodium chlorid 99,9%	APPLICHEM, Darmstadt, Germany
Sodium hydrogen carbonate	MERCK MILLIPORE, Darmstadt, Germany
Solution 555 rotor cleaning concentrate	Beckman Coulter, Brea, USA
SuperBlock™ Blocking Buffer (TBS)	Thermo Scientific, Waltham, USA
Syringe, 1ml	Becton Dickinson, Heidelberg, Germany

TEMED	APPLICHEM, Darmstadt, Germany
Tissue culture flask T25, stand. vent. cap	Sarstedt, Nümbrecht, Germany
Tissue culture flask T75, stand. vent. cap	Sarstedt, Nümbrecht, Germany
Tissue culture plate 96well Standard F	Sarstedt, Nümbrecht, Germany
Tissue culture plate 96well Standard R	Sarstedt, Nümbrecht, Germany
Transferpipetten 3,5ml	Sarstedt, Nümbrecht, Germany
TRIS PUFFERAN®	Carl-Roth, Karlsruhe, Germany
Triton™ X-100	Sigma-Aldrich, St. Louis, USA
Trypanblau, 0,5%	Biochrom, Berlin, Germany
Tween® 20 molecular biology grade	ChemSolute®; Renningen, Germany
TWEEN®80	Sigma-Aldrich, St. Louis, USA
UltraPure™ agarose	Carl-Roth, Karlsruhe, Germany
Vue life cell culture bags	Cellgenix, Freiburg, Germany

Table 2: List of buffers and solutions

Name	**Ingredients**
5x TBE	108 g TRIS PUFFERAN® 55 g Boric acid 5.8 g Na_2-EDTA Ad 2 litres ddH_2O Adjust to pH8
7H10 agar plates	19 g Difco Middlebrook 7H10 Agar 900 ml ddH_2O 5 ml glycerol 100 ml bovine serum
Cell culture medium	VLE-RPMI (1640) +10% FCS +1% L-Glutamine
10xElectrode Buffer	30g Tris base 144g Glycin auf 1L ddH_2O
Blotting Buffer	100ml 1xElectrode buffer 100ml MeOH 800 ml ddH_2O
Running Buffer	100ml 1xElectrode buffer 10ml SDS (10%) 890 ml ddH_2O
4x Lämmli Buffer	3 ml ddH_2O 1ml TRIS base (pH 6.8) 1.6ml glycerol 1.64ml SDS (10%) 0.4ml β-mercaptoethanol Small crumb of bromophenolblue

10xTBS	24.2g TRIS base 80.0g NaCl in 1l ddH_2O pH adjusted to 7.6 using 1M HCl
1xTBS-T	100ml TBS (10x) 900ml ddH_2O 0.1% Tween-20
8x SDS Lysis Buffer	16%SDS, 1M Tris 160mM DTT (added freshly) in ddH_2O pH adjusted to 7.8 using 1M HCl
SDS-PAGE Gel (1.5mm Thickness)	Stacking gel (5%): 3.075 ml ddH_2O 1.25ml Tris/HCl (0.5M) 0.625ml Acrylamid 0.050ml SDS (10%) 0.015ml TEMED 0.025ml APS (10%) Resolving gel (12%): 3.75 ml ddH_2O 2.125ml Tris/HCl (1.5M) 2.55ml Acrylamid 0.085ml SDS (10%) 0.015ml TEMED 0.025ml APS (10%)

Table 3: List of instruments and devices

Instrument	**Manufacturer**
Autoclave Systec DX-150	Systec GmbH, Münster, Germany
Avanti J 26S XP	Beckman Coulter, Brea, USA
Balance	Sartorius AG, Göttingen, Germany
Binder CO_2 Incubator	Binder GmbH, Tuttlingen, Germany
Biometra TAdvanced	Analytik Jena, Jena, Germany
Block Thermostat QBD1	Grant Instruments, Shepreth, UK
Casy2 Modell TT	Schärfe System GmbH, Reutlingen, Germany
Centrifuge 5430R	Eppendorf, Hamburg, Germany
ChemiDoc™ Touch Imaging System	BIO-RAD, Hercules, USA
Cytation 1Cell Imaging Reader	BIOTEK, Winooski, USA
DeNovix DS-11+ Spectrophotometer	DeNovix Inc., Wilmington, USA

Eppendorf Multipette®Xtream	Eppendorf, Hamburg, Germany
Eppendorf Research Pro multichannel pipette	Eppendorf, Hamburg, Germany
FACS Canto ll	Becton Dickinson, Heidelberg, Germany
Hera Freeze HFU T Series -80°C freezer	Thermo Scientific, Waltham, USA
HeraCell 240 Incubator	Thermo Scientific, Waltham, USA
HeraeusFresco™ 21 benchtop centrifuge	Thermo Scientific, Waltham, USA
Herasafe safety cabinet	Heraeus Instruments, Hanau, Germany
Hettich® Rotanta 460R	Hettich, Tuttlingen, Germany
Hund Wetzlar mikroscope h500	Helmut Hund GmbH, Wetzlar, Germany
Julbalo TW12 waterbath	Julabo, Seelbach, Germany
LightCycler 480	Roche, Basel, Switzerland
Magnetrührer	IKA-Werke GmbH, Staufen, Germany
MasterflexL/S easy-load II Model 77200-60	Masterflex, Gelsenkirchen, Germany
MiniSpin® centrifuge	Eppendorf, Hamburg, Germany
NanoDrop™ 1000	Thermo Scientific, Waltham, USA
Nikon Eclipse TS100 microscope	Nikon, Minato, Japan
Odyssey CLx® imaging system	LI-COR, Hercules, USA
pH-Meter	Mettler-Toledo, Columbus, USA
Pipetboy acu	Integra Bioscience, Zizers, Switzerland
Pipettes (10, 100, 200, 1000µl)	Eppendorf, Hamburg, Germany
PowerPac	Bio-Rad Laboratories, Hercules, USA
S1 Pipet Filler Pipetboy	Thermo Scientific, Waltham, USA
ScanLaf Mars Safety Class 2, biosafety cabinet	Labogene, Lynge, Denmark
Scotsman™ AF-10 Ice Flake Maker	Thermo Scientific, Waltham, USA
SDS Gelapparatur/WB	Bio-Rad Laboratories, Hercules, USA
Seahorse XFe96	Agilent Technologies, Santa Clara, USA
Spektrophotometer Ultrospec10	Biochrom, Berlin, Germany
Stepper	Brand, Wertheim, Germany
Synergy™ 2 plate reader	BIOTEK, Winooski, USA
Transferpette®-8	Brand, Wertheim, Germany
Ultrasonic bath	EMAG, Salach, Germany
Vortex	VWR, Radnor, USA
Workbench elutriator	Camfil, Reinfeld, Germany
ZetaSizer Nano ZS	Malvern Pananalytical, Malvern, UK

3.2 Methods

3.2.1 Isolation of human peripheral blood monocytes and subsequent differentiation macrophages

Isolation of monocytes from either human heparinized peripheral blood from healthy donors of the clinic in Borstel (approved by the Ministry of Agriculture, Environment and Rural Areas in Kiel, Germany) or buffy coats purchased at the UKSH Lübeck (Ethics application: file reference 19-367) was performed using density gradient centrifugation and subsequent counterflow centrifugation as described in Brandenburg *et al* [117]. In brief, blood or buffy coats were diluted 1:2 or 1:6, respectively, in pre-warmed phosphate-buffered saline (PBS) (37°C) and subsequently 40 ml thereof were layered carefully onto a 10 ml polysucrose solution (Pancoll) of a density of 1.077 g/ml. Next, tubes were centrifuged for 45min at 160 relative centrifugal force (rcf) at 21°C with the centrifuge set at a low braking rate. The upper layer was discarded, while the peripheral blood mononuclear cell (PMBC) layer, which is found in the interphase, was carefully transferred into a new 50ml tube. PBMCs were washed twice with 50 ml PBS with centrifugation steps at 200 rcf for 15 minutes in between, re-suspended in 100ml Hank's buffered salt solution (HBSS) containing 0.1% bovine serum albumin (BSA) and mounted onto the elutriation chamber. PBMCs, which include lymphocytes, monocytes and thrombocytes were then separated using counterflow centrifugal elutriation (CCE), which is a commonly used method to separate mixed cell populations based on their different sizes and densities[120]. Prior to CCE, the tubing system and elutriation chamber were disinfected with 200ml 70% ethanol, 300ml dH_2O and 200ml HBSS. Next, the PBMC suspension was pumped through a tubing system into the elutriation chamber using a peristaltic pump while centrifuging at 3500 rpm. (Avanti J 26S XP). In the elutriation chamber, a cell gradient of increasing size is generated by the centrifugal outward force and the inward counterflow, by a stepwise increase of the flow rate (from 27 up to 39 ml/min (Table 4). At a flow rate of 39 ml/min, the centrifuge was stopped and the monocyte fraction was eluted and collected in a 50ml tube. The purity and cell count of the monocyte fraction was determined using the Casy29 cell counter. Next, the monocyte fraction with a purity of at least 93% was centrifuged at 150 rcf for 10 minutes and the pellet was re-suspended in RPMI 1640 containing 2% human serum, 10ng/ml recombinant human macrophage colony-stimulating factor (M-CSF), 100µg/ml Streptomycin and 100U/ml Penicillin (P/S) and 4mM L-glutamine at a cell density of 5×10^5 cells/ml. The cell suspension was then transferred into Teflon-coated cell culture bags and incubated for 7 days at 37°C and 5% CO_2 to differentiate monocytes to macrophages.

Table 4: Protocol including flow rates and volumes used for counterflow centrifugal elutriation	
Setting	**Flow rate (ml/min)**
1,8	**27**
2,0	**30**
2,2	**33**
2,3	**34**
2,4	**35**
2,5	**36**
2,6	**37**
2,7	**38**
2,8	**39**

After differentiation, human monocyte-derived macrophages (hMDMs) were removed from the Teflon bags by incubating cells on ice for 1 h and subsequently detaching cells by gently pulling the Teflon bag over the edge of the bench. The cell suspension was transferred into a 50 ml tube, centrifuged for 10 min at 160 rcf at 4°C, and re-suspended in RPMI 16040 containing 10% FCS and 4mM L-glutamine, herein referred to as cell culture medium. Trypan blue staining was used to determine the count of viable cells using a Neubauer counting chamber and cell count per ml was determined using the following formula:

$$\text{cell count} = \text{number of cells in 4 quadrants} * \text{dilution factor} * 10{,}000$$

Cells were seeded in 48-Well plates, unless indicated otherwise, and were allowed to attach for 2 h at 37°C and 5% CO_2 before further processing.

3.2.2 Bacteria and stimuli

3.2.2.1 Preparation of Mtb H37Rv

Mtb H37Rv (derived from *Mtb* strain H37Rv American Type Culture Collection (ATCC) 27294; ATCC, Manassas, USA) frozen aliquots were prepared according to Brandenburg *et al.* [117]. In brief, bacteria were grown to mid-log phase (optical density $(OD)_{600}$= 0.4) in Middlebrook 7H9 medium supplemented with 10% OADC, 0.5% Glycerol and 0.05% Tween 80. The bacteria were harvested, the bacterial number was determined and frozen at -80°C. On the day of infection, aliquots were thawed and centrifuged at 4500 rcf for 10 minutes. The pellet was next re-suspended and to homogenize the bacterial suspension and dissolve clumps a 1ml syringe with a 27-gauge needle was used.

3.2.2.2 Preparation of fatty acid – BSA conjugates

Oleic acid and palmitic acid are insoluble in the cell culture medium and were therefore conjugated to BSA before supplementation to the cells. To do so, fatty acids were diluted in 0.1 M sodium hydroxide (NaOH) (in double-distilled hydrogen dioxide (ddH_2O)) to a working concentration of 20 mM and incubated at 80 °C for 30 minutes. Next, 50 µl of 0.1 M NaOH was added repeatedly during incubation at 80°C until the fatty acid was completely solubilized. The fatty acid solution was added dropwise to pre-warmed (37°C) 5% BSA solution forming a 1:4.33 dilution, which allowed the conjugation of the fatty to BSA. The fatty acid-BSA conjugate was then diluted in a pre-warmed cell culture medium and added to the cells to achieve the desired final concentration.

3.2.2.3 Infection with Mtb

HMDMs were seeded and incubated for 2 hours (h) at 37°C, 5% CO_2 prior to infection with frozen stocks of Mtb H37Rv. After thawing and centrifugation of Mtb H37Rv like described before, the following formula was used to calculate the resuspension volume to achieve the desired multiplicity of infection (MOI):

$$\text{resuspension volume} = \frac{\text{number of bacteria per aliquot} * 10\ \mu l}{\text{number of bacteria to obtain desired MOI}}$$

After homogenization, the bacterial suspension was added to the cells and cells were incubated for 4 hours at 37°C, 5% CO_2. The supernatant was removed, cells were washed three times with PBS and cell culture medium with or without additional stimuli was added to the cells. Cells were incubated at 37°C, 5% CO_2 for 24 hours or 7 days, with fresh medium being added at day 3, before further processing.

3.2.2.4 Determination of Mtb growth

To determine Mtb growth in hMDMs, the colony forming units (CFU) analysis was performed. To do so, the supernatant was removed, 500 µl ddH_2O was added to the wells followed by incubation at room temperature for 15 minutes. After microscopic confirmation that cells are fully lysed, one part of the cell suspension was used to determine the protein concentration in the sample as described below, and 100µl of the remaining suspension was serially diluted 1:10 in H_2O containing 0.1% Tween-80.

100µl of the 10^{-1}-10^{-4} dilutions were plated on 7H10 agar plates containing 5% bovine serum, incubated for approximately three weeks at 37 °C before the colonies were counted and the CFU per well was determined according to the following formula:

$$\frac{\text{CFU}}{\text{well}} = \text{number of colonies} * \frac{1}{dilution} * 5$$

3.2.3 Flow cytometry

3.2.3.1 Determination of neutral lipid content, mitochondrial activity and mass

Flow cytometry was used to determine the neutral lipid content in hMDMs using the neutral lipid dye BODIPY™ 493/503. For this purpose, hMDMs were infected and incubated with or without supplementation of exogenous fatty acids for 7 days at 37°C and 5% CO_2. Cells were washed twice with PBS and stained with 5ug/ml BODIPY™ 493/503 in PBS for 20 minutes at room temperature. Further, cells were washed twice with PBS, fixed with 4% paraformaldehyde (PFA) (in PBS) for 2 hours, resuspended in PBS and analyzed on a FACSCanto II in the fluorescein isothiocyanate (FITC) (530/30nm filter) using an excitation laser at 488nm.

To determine mitochondrial mass and activity the mitochondrial membrane potential ($\Delta\boldsymbol{\Psi}$)-independent dye MitoTracker™ Deep Red FM and the ($\Delta\boldsymbol{\Psi}$)- dependent dye Rhodamine 123 (Rho123) were analyzed using flow cytometry. To do so, $2*10^5$ hMDMs were seeded in tubes for flow cytometry and infected as described before. On day 7, the supernatant was removed, cells washed with PBS and stained with 300nM MitoTracker™ Deep Red FM and 0.5ug/ml Rhodamine 123 (both in cell culture medium) for 25 min at 37°C and 5% CO_2 in the dark. Cells were washed with pre-warmed PBS and analyzed immediately on a FACS Canto II using an excitation laser at 488 and 633 nm, respectively, for the FITC (530/30nm filter) and Cy5 channel (660/20 filter).

For the measurement BD Diva Software version 6.1.2. was used. The data were analyzed with FCS Express v7 or newer software. As a gating strategy, the macrophage population (cells) was first identified by plotting the area of the forward scatter (FSC) against the area of side scatter (SSC), followed by doublet exclusion by plotting the height against the area of the FSC as depicted in figure 6.

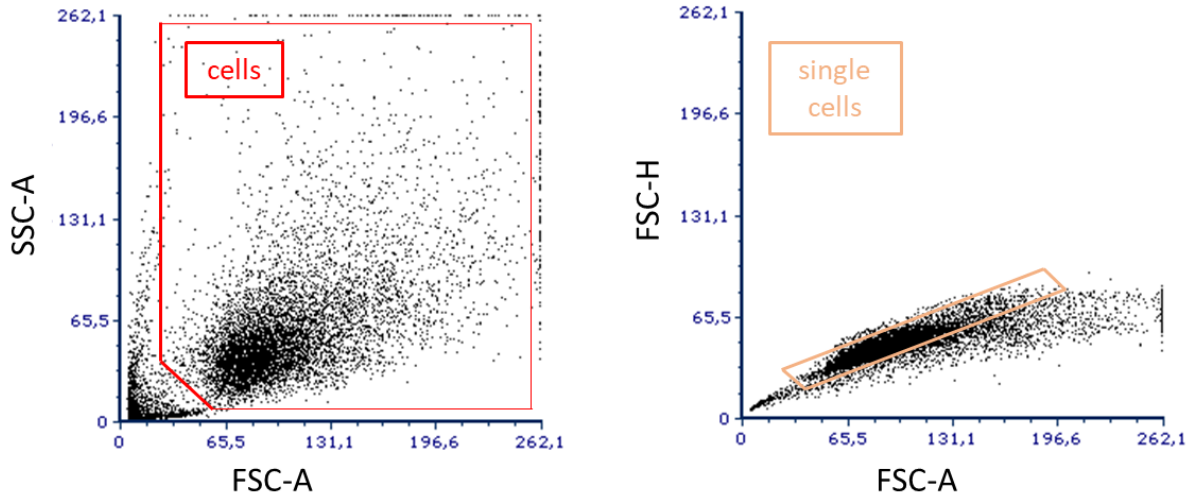

Figure 6: Gating strategy for flow cytometric analysis of primary human macrophages

Using the FCS Express software, the cell population (gate labeled "cells") was first identified by plotting the FSC-A and SSC-A. Subsequently, doublets were excluded using the FSC-A and FSC-H and further analysis was performed with the single-cell population (gate labeled "single cells").

3.2.4 Quantification of mitochondrial and nuclear DNA

To quantify mitochondrial and nuclear deoxyribonucleic acid (DNA), cells were infected and incubated as described before. After 7 days, cell culture supernatants were removed, cells were lysed in 250µl trizol (peqGOLD TriFast™; VWR International, Radnor, USA) and DNA was isolated using the InnuPREP DNA Mini Kit (Analytik Jena) according to the manufacturer's instruction. In brief, 250µl of 100% ethanol was added to the trizol, the suspension was mixed vigorously by pipetting up and down, loaded onto the column placed on a collection tube and centrifuged at 11,000 rcf for 2 minutes. The flow-through was replaced with a new one and 500µl Washing Solution HS followed by another centrifugation step at 11,000 rcf for 1 min. The flow-through was removed from the collection, 750µl Washing Solution MS was added to the column and the centrifugation step was repeated. Next, the column was placed on a new collection tube and dry centrifuged at 11,000 rcf for 3 minutes. Lastly, the 50µl of elution buffer was added to the column and the DNA was eluted into a fresh 1.5 ml Eppendorf tube (low bind) by centrifugation at 11,000 rcf for 1.5 minutes. The DNA content and purity were measured on a Nanodrop spectrophotometer and the DNA concentration was adjusted to 5ng/µl in DNAse-free ddH_2O.

Quantification of mitochondrial and nuclear DNA was performed using quantitative *real-time* polymerase chain reaction (RT-PCR). The gene-specific primer pairs for the beta-2 microglobulin (*B2M*) and $tRNA^{Leu(UUR)}$ (Table 6) were used to amplify nuclear and mitochondrial DNA [121], respectively, utilizing the LightCycler® 480 SYBR Green I Master and

the LightCycler 480 II system (Roche Applied Science). The master mix consisted of 2,4µl of ddH_2O, 5µl of LightCycler 480 SYBR Green I Master, 0.6µl of sense and antisense primer mix (10µM) and 2µl of DNA (5ng/µl). The PCR was performed according to the protocol listed in table 5. Gene expression was quantified using the ΔΔCt method and relative expression of *B2M* to $tRNA^{Leu(UUR)}$ was calculated to display the mitochondrial/nuclear DNA ratio.

Table 5: Protocol for quantitative RT-PCR

Step	**Temperature (°C)**	**Duration (min:sec)**	**# of cycles**
Pre-Incubation	50 95	02:00 10:00	1
Amplification	95 62 62	00:15 01:00 00:01	40
Melting Curve	95 65 Increase up to 97	00:10 00:10	1
Cooling	37	00:10	1

Table 6: Primers used for quantitative RT-PCR

Target	**Orientation**	**Sequence (5' – 3')**
B2M	FWD REV	TGC TGT CTC CAT GTT TGA TGT ATC T TCT CTG CTC CCC ACC TCT AAG T
$tRNA^{Leu(UUR)}$	FWD REV	CAC CCA AGA ACA GGG TTT GT TGG CCA TGG GTA TGT TGT TA

3.2.5 Analysis of cell death using DRAQ7 staining

$5*10^4$ hMDMs were seeded in 96-well Corning plates and incubated in cell culture medium infected with Mtb as described before, or left uninfected and supplemented with exogenous FA and incubated at 37°C and 5% CO_2 in presence of 3µM of the DRAQ7 dye, which was added to the cell culture medium. As a positive control, 1% Triton-X100 was added to the cell culture medium approximately 15 minutes before the start of the measurement. At 24 hours post infection, the DRAQ7 fluorescence counts and the number of cells were determined on a Cytation 1 Cell Imaging Reader (BioTek) using the automatic focus. To this end, a brightfield, as well as a fluorescence (Cy5 628/685 filter cube) image, was captured at the same position in

each well at a 4x magnification. The images were then analyzed using the Gen5 software (version 1.11.5) to determine the DRAQ7 count and the cell number.

3.2.6 Extracellular flux analysis

Four assays were performed on an XFe96 Seahorse Analyzer (Agilent Technologies): the XF Mito Stress Test to analyze respiratory parameters by measuring the oxygen consumption rate (OCR), the XF Glycolysis Stress Test to measure glycolytic parameters measuring the extracellular acidification rate, the XF Real-Time ATP Rate Assay to analyze ATP production and the XF MitoFuel Dependency Assay to analyze mitochondrial substrate dependency on glucose, fatty acids and glutamine. Results were recorded using the Wave Desktop 2.6 Software from Agilent, which allowed normalization to cell viability and export of data into the XF Report generators to calculate respiratory and glycolytic parameters, as well as mitochondrial dependency and ATP production rates.

For the analysis, $3*10^4$ hMDMs per well were seeded on an XFe96 cell culture plate forming a cell monolayer. Cells were subsequently infected and incubated as described before. The sensor cartridges were prepared according to the manufacturer's instructions. In brief, the sensor cartridge was placed in the utility plate filled with 200µl ddH_2O/well overnight at 37°C. One hour prior to the measurement, the sensor cartridge was placed in the utility plate containing 200µl Calibrant solution per well, which was incubated overnight at 37°C.

Before starting the measurement, the cell culture medium was removed, cells were washed three times and incubated for 45 min at 37°C with an assay medium consisting of XF DMEM medium (pH 7.4) containing 5.5mM glucose, 1% FCS and 1mM L-glutamine. Importantly, for the Glycolysis Stress test, the assay medium consisted of XF DMEM medium (pH 7.4) containing 1% FCS and 1mM L-glutamine and without glucose.

In the Mito Stress Test, the OCR was measured first under basal conditions and subsequently upon serial injection of oligomycin (1µM), FCCP (1µM) and antimycin A/rotenone (each 0.5µM). Under each condition 3 cycles consisting of 3 minutes of mixing, 2 minutes of waiting and 3 minutes of measurement were performed. Wave data were exported using the Seahorse XF Mito Stress Report Generator, which automatically calculates the basal respiration, ATP-linked respiration, proton leak, maximal respiration, non-mitochondrial respiration and the spare respiratory capacity. OCR curves were generated by exporting Wave data into a Graphpad Prism (Version 8 or newer).

For the Glycolysis Stress Test, the ECAR was first measured under basal conditions and subsequently under serial injection of D-glucose (10mM), oligomycin (1µM) and 2-deoxyglucose (2-DG) (50mM). Under each condition 3 cycles consisting of 3 minutes of mixing, 2 minutes of waiting and 3 minutes of measurement were performed. Using the Seahorse XF Glycolysis Stress Report Generator the non-glycolytic acidification, glycolysis, glycolytic capacity and the glycolytic reserve were automatically calculated. ECAR curves were generated by exporting Wave data into a Graphpad Prism (Version 8 or newer).

In the Real-Time ATP Rate Assay the ECAR and OCR were measured first under basal conditions and subsequently upon serial injection of oligomycin (1µM) and antimycin A/rotenone (each 0.5µM). Under each condition, 3-5 cycles consisting of 3 minutes of mixing, 2 minutes of waiting and 3 minutes of measurement were performed. Wave data were exported using the Seahorse XF Real-time ATP Rate Assay Report Generator, which automatically calculates the mitochondrial, glycolytic and total ATP production rates, the ATP rate index and the % contribution of glycolysis and OXPHOS to the total ATP production.

Lastly, for the MitoFuel Dependency test, the OCR was first measured under basal conditions and subsequently under serial injection of i) BPTES (3µM) followed by a combination of etomoxir (16µM) and UK5099 (2µM) to determine glutamine dependency, ii) etomoxir (16µM) followed by a combination of BPTES (3µM) and UK5099 (2µM) to determine fatty acid dependency and iii) UK5099 (2µM) followed by the combination of BPTES (3µM) and etomoxir (16µM) to determine glucose dependency. Under each condition, 3-6 cycles consisting of 3 minutes of mixing, 2 minutes of waiting and 3 minutes of measurement were performed. Using the Seahorse XF MitoFuel Flex Test Report Generator, the % dependency on glutamine, fatty acids and glucose were automatically calculated.

After the measurement, the assay medium was removed and for normalization, a crystal violet staining was performed to determine cell viability.

3.2.7 Crystal violet staining

Crystal violet staining is a method, which was previously described to determine cell viability [122] and which was used to normalize Seahorse data before[2]. In brief, cells were washed twice gently with ddH_2O and air-dried for one hour. Cells, and several wells without cells (blank), were incubated in a 0.5% crystal violet solution (containing 20% MeOH in ddH_2O) for 30 minutes at room temperature. The crystal violet solution was removed and cells were gently washed with ddH_2O 4 - 5 times until the water remained clear. The plates were dried overnight

and cells were then lysed in 100µl 100% MeOH for 10 minutes. The lysate was transferred into a new 96 –well plate and the OD_{590nm} was measured on a microplate reader (Synergy 2). Data were analyzed using the Gen5 software (Version 1.11.4 or newer) and subsequently used to normalize Seahorse data using the Wave Desktop 2.6 Software.

3.2.8 Fractionation of lipid droplets, mitochondria and ER

To isolate and characterize LDs from uninfected and Mtb-infected cells, 2.2 $*10^7$ hMDMs were seeded in a T175 cell culture flask, infected with Mtb or left uninfected and incubated for 7 days at 37°C and 5% CO_2. Cells were then washed twice with 1xPBS, detached from the culture flask using a cell scraper, the cell suspension was transferred into a 50ml tube and topped up to 50ml with 1xPBS. After centrifugation for 10 minutes at 300 rcf, the pellet was resuspended in 1ml PBS, transferred into a 1.5ml tube and centrifuged again for 10 minutes at 300 rcf. After the supernatant was removed, 200µl of Reagent A from the Lipid Droplet Isolation Kit (Cell Biolabs) was added to the pellet, the suspension was vortex for 30 seconds and incubated at 4°C for 10 minutes. Then, 800µl of 1x Reagent B was added and the suspension was vortexed vigorously. The tube was then placed in a Sonifier 450 (Branson Ultrasonics) and the sample was continuously sonicated for 2 minutes at an amplitude of 2 and 4 minutes at an amplitude of 3. Next, the sample was centrifuged for 10 minutes at 600 rcf (4°C) to remove all intact cells and cell debris from the sample to obtain the whole cell lysate (WCL) (Fig. 7). To obtain the mitochondrial fraction (MF), the WCL was centrifuged for 20 minutes at 10,200 rcf (4°C) and the pellet containing the MF was resuspended in 100µl PBS. The supernatant, which contained LDs and the ER, was transferred into a fresh tube, overlayed with 600µl of 1x Reagent B and centrifuged for 3 hours at 25,000 rcf (4°C). After the centrifugation, the LDs were floating on the top of the sample in a visual fat layer, while the ER was pelleted. Therefore, the top ~1ml of the supernatant was carefully removed using a blunt 16-gauge syringe and transferred into a fresh 1.5ml tube. The rest of the supernatant was removed and the pellet containing the ER fraction (ERF) was resuspended in 100µl PBS.

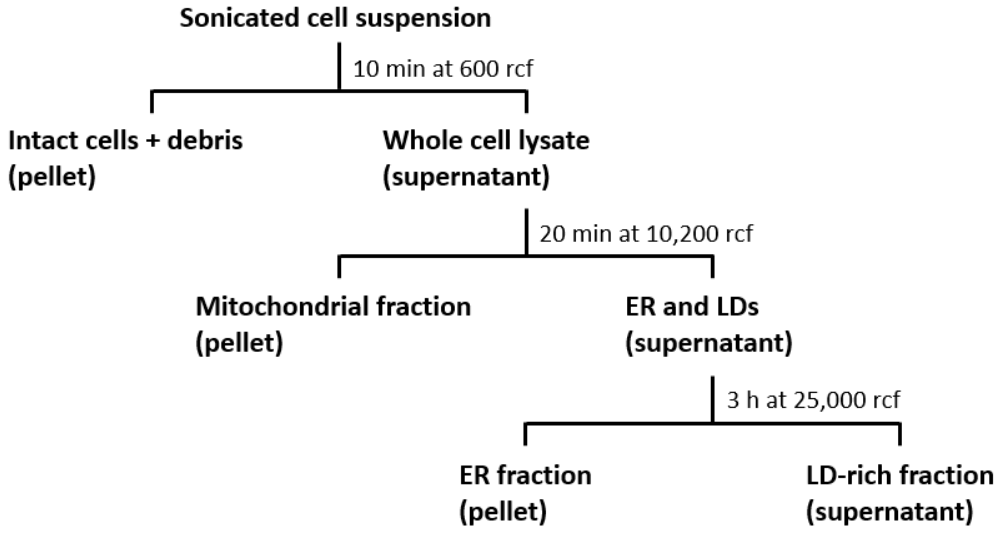

Figure 7: Schematic illustration of the isolation of lipid droplets

The sonicated cell suspension was subjected to several centrifugation steps to separate the mitochondrial fraction, ER fraction and LD-enriched fraction from the whole cell lysate.

The supernatant containing the LDs was again centrifuged for 10 minutes at 25,000 rcf in order to separate the LDs, which are floating in a fat layer, from the rest of the sample. The volume of the sample was then carefully reduced by slowly drawing up the sample from the bottom of the tube using a 16-gauge syringe without taking up the visual fat layer containing the LDs (Fig. 7). The last centrifugation step was repeated until the volume of the LD-enriched fraction (LDF) could be reduced to ~100µl.

For lipidomics analysis, 10µl of WCL, MF, ERF and LDF suspension was used to determine the protein concentration of each sample. The samples containing the WCL, MF, ERF and LDF were transferred into 1.5ml Safe-Lock Eppendorf tubes and 800µl MeOH (containing 0.184% BHT) was added. Then, the samples were shaken for 2 hours at room temperature to inactivate Mtb and stored at -80°C before further processing.

For proteomics and Western Blot analysis, the WCL, MF, ERF and LDF were diluted 4:1 in 8x SDS Lysis buffer, the samples were incubated at 95°C for 20 minutes to heat inactivate Mtb and stored at -80°C before further processing. For proteomics analysis, samples were further diluted 1:2 in ddH_2O.

For analysis of LD size, 5 µl of LDF were diluted 1:10 in PBS and inactivated in 4% PFA for 24h. Samples were analyzed on a ZetaSizer in biosafety laboratory 2 conditions as described below.

3.2.8.1 Protein quantification

For the determination of the protein concentration in cell lysates, the Pierce™ BCA Protein Assay Kit was used according to the manufacturer's instructions. The principle of this assay is based on the reduction of Cu^{2+} to Cu^{1+} by the protein under alkaline conditions, followed by the complex formation of bicinchoninic acid (BCA) with Cu^{1+} resulting in a colorimetric reaction [123]. In brief, samples were diluted in ddH_2O if necessary and up to 50µl of the sample as well as a standard (ranging from 32.5 - 2000µg/ml) was pipetted in duplicates or triplicates into a transparent 96-well plate. 50 parts of Reagent A were mixed with 1 part of Reagent B and 200µl of the mixture was added to the sample and standard. The plate was incubated in the dark for 20 minutes at 37°C and the OD_{562nm} was measured on a microplate reader (Synergy 2). Data was analyzed using the Gen5 software (Version 1.11.4 or newer) and the protein concentration in each sample was calculated using the standard curve.

3.2.8.2 SDS-PAGE

Sodium dodecyl-sulfate polyacrylamide gel electrophoresis (SDS-PAGE) is a commonly used method to separate denature proteins in a protein mixture depending on their molecular mass using electrophoresis through a porous acrylamide gel [124]. To separate the proteins in the lysate of the WCL, the MF, the ERF and the LDF, the samples were first thawed and the protein concentration was determined as described above. The samples were diluted 1:4 in 4xLämmli buffer and incubated for 10 minutes at 95°C, which allowed complete denaturation of proteins. 20µg of WCL and 7.5µg of the MF, the ERF and LDF, as well as 4µl of the protein marker were then loaded into the wells of the gel, which was fixed in the gel cassette and placed in the running module. The inner chamber of the cassette was completely submerged in 1x Running buffer and the module was filled with buffer according to the manufacturer's instructions. The electrophoresis was started at 75V and when the protein band reached the end of the resolving gel voltage was then increased to 150V at a constant current. The electrophoresis was stopped when the dye front reached the end of the gel and the gel cassette was disassembled and the stacking gel was removed. The gel was used immediately for further Western Blot analysis.

3.2.8.3 Western Blot Analysis

Western Blot (WB) analysis is a method to detect or identify specific proteins in a protein mixture by using specific mono- or polyclonal antibodies (ABs) directed against the target protein [125]. In this doctoral study, WB analysis was used to detect and measure the expression levels of organelle-specific proteins in the WCL, the MF, the ERF and the LDF using a chemiluminescence detection approach. To achieve that, the samples previously separated during SDS-PAGE were blotted on a polyvinylidene fluoride (PVDF) membrane, which was preactivated by incubating the membrane briefly in 100% methanol. Next, the SDS-PAGE gel was assembled by placing Whatman filter paper on a sponge followed by the membrane, the gel, another Whatman filter and sponge, and fixing it within the cassette (Fig. 8). The cassette was then placed in the electrode assembly and moved into the tank, which was filled with blotting buffer and the cooling unit. The proteins were blotted from the gel onto the membrane for 90 minutes at 75V.

The membrane was removed from the cassette, washed once with 1x tris-buffered saline (TBS) and blocked for 1 hour at room temperature in Superblock shaking to block remaining binding surfaces and reduce unspecific binding. Next, the membrane was cut into three pieces at the 100 kDa and 35 kDa mark of the protein ladder, and the membrane pieces were incubated overnight shaking at 4°C with the primary antibodies, which were directed against the target protein and were diluted as indicated in table 7. Next, the primary antibody solution was removed, the membrane was washed 5x for 5 minutes in 1xTBS-T (0.05% Tween-80 in 1x TBS) and was incubated for one hour at room temperature with the respective secondary antibody directed against the primary antibody (Table 8). Again, the antibody solution was removed and the membrane was washed 5x for 5 minutes in 1xTBS-T. A chemiluminescence detection approach was used to detect antibodies bound to the membrane using the horseradish peroxidase (HRP) conjugated to the secondary antibody. To do so, 500µl of solution A and solution B from the ECL prime detection kit were mixed and diluted 1:2 in ddH_2O and incubated with the membrane for up to 3 minutes. The oxidation of luminol in the ECL prime mix by the HRP leads to the emission of light, which was detected on a Chemidoc Imaging System and analyzed using the ImageLab software (Version 6.1). After visualization of the protein bands on the membrane and the antibodies were stripped from the membrane by incubating the membrane for 30 minutes at room temperature in stripping buffer shaking. The membrane was then again blocked and incubated with the second set of antibodies as described before.

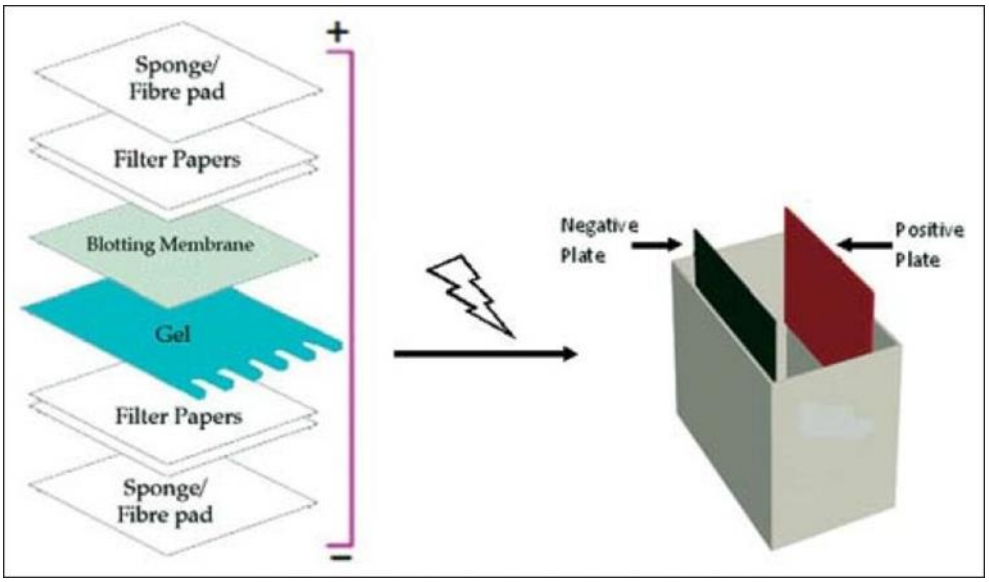

Figure 8: Schematic illustration of the assembly of the blotting cassette

The SDS-PAGE gel was positioned on a PVDF membrane and fixed between Whatman filters and sponges in the blotting cassette. The cassette was subsequently placed in an electrode assembly and moved into a tank filled with blotting buffer. Adapted after Mahmood and Yang (2012)[126].

Table 7: Primary Antibodies used for WB Analysis

Target	Species	Clone	Dilution	Supplier
Calreticulin	Rabbit	polyclonal	1:1000 in Superblock	EnzoLifeScience (ADI-SPA-600)
α-Tubulin	Mouse	monoclonal	1:2000 in Superblock	Santa Cruz (SC-32293)
Manganese Superoxide Dismutase	Rabbit	polyclonal	1:2500 in Superblock	EnzoLifeScience (ADI-SOD-111-F)
Perilipin-3	Rabbit	polyclonal	1:1000 in Superblock	Abcam (ab47639)

Table 8: Secondary Antibodies used for WB Analysis				
Antibody	**Species**	**Clonality**	**Dilution**	**Supplier**
HRP conjugated anti-rabbit IgG(H+L)	goat	polyclonal	1:4000 in 1xTBS-T	Dianova (#GtxRb-003-FHRPX)
HRP conjugated anti-mouse IgG(H+L)	goat	polyclonal	1:4000 in 1xTBS-T	Jackson ImmunoResearch (#115-035-146)

3.2.8.4 Analysis of lipid droplet size using ZetaSizer analysis

ZetaSizer analysis was used to determine the mean lipid droplet size in the LDF. This analysis allows to investigate the size of particles in a sample by measuring the scattered light when they move through a light beam. To do so, samples were fixed and prepared as described above and 50µl of the sample were transferred into a Sarstedt measuring cuvette. Before every measurement on the ZetaSizer (Malvern Pananalytical), an equilibration step was performed. The diameter of particles in nm was measured at 25 °C at an angle of 90°C using automatic measure run times allowing to measure between 400 and 3000 counts per picosecond. Samples were recorded three times per run and in total three runs were performed of each sample. Overall, two peaks were detected with a size of ~500nm and <100nm contributing to >90% and <10% of the signal. The smaller peak, which was likely caused by contamination of the sample with small particles was excluded. For the bigger peak, the average peak size of all runs for each donor and condition was calculated and depicted as mean peak diameter in nm (d: nm).

3.2.9 Quantification of free fatty acid levels using gas-liquid chromatography-mass spectrometry

To prepare samples for the analysis of FFA levels, $8*10^6$ hMDMs were seeded in a petri dish (92mm diameter) and infected with Mtb as described before. After 7 days of infection, cells were washed twice with PBS, removed from the dish using a cell scraper and transferred into a 50ml tube. Cells were centrifuged at 200 rcf for 10 minutes and resuspended in 210µl PBS. 10µl of the cell suspension was further processed to determine the protein concentration and the remaining 200µl were transferred into glass tubes. Next, 800µl MeOH (containing 0.184% BHT) was added to the glass tubes, which were shaken for 2 h at room temperature to inactivate Mtb. Samples were then handed over to Dr. Nicolas Gisch from Research Group Bioanalytical Chemistry at the Research Center Borstel for further processing.

Importantly, all processes starting from adding the MeOH to the sample is performed with glassware that has been washed 3x with H_2O for chromatography, 3x with MeOH and 3x with chloroform ($CHCl_3$) and was subsequently dried using nitrogen gas (N_2).

FFA levels in the samples were analyzed using gas-liquid chromatography-mass spectrometry (GLC-MS). To facilitate the separation of FFA using gas-liquid chromatography, samples were depolarized through methylation using diazomethane (CH_2N_2) to form fatty acid methyl esters[127]. To do so, the methanol in the samples was evaporated using N_2, the internal standard (pentadecylic acid C15:0) and 500µl deionized Millipore water were added and the sample was adjusted to pH between 1-2 by adding ~50µl of an 8M HCl solution. Then, 500 µL $CHCl_3$ was added, the sample vortexed vigorously, and the lower $CHCl_3$ phase was transferred in a new 1.5ml glass vial. This step was repeated twice. The $CHCl_3$ was next evaporated using N_2, 100µL $CHCl_3$/MeOH (at a ratio of 95:5) and 1-2 drops of CH_2N_2 were added. The mixture was evaporated using N_2 until the extract was completely dried. Again 1-2 drops of CH_2N_2 were added, vortexed, incubated at RT for 5 min and dried using N_2. The dried extract was resuspended in up to 100µL $CHCl_3$ and injected into a glass vial using a Hamilton™ syringe. Subsequently, samples were loaded and GLC-MS analysis was performed on an Agilent Technologies 6890N gas chromatograph coupled to a 5975 inert XL Mass Selective Detector (Agilent Technologies) applying a temperature gradient kept at 70°C for 1.5 minutes, then raised to 60 °C/min to 150 °C followed by an increase at 1.5 °C/min to 220 °C. A 30-m Agilent J&W DB-WAX Ultra Inert column (0.25 mm inner diameter, 0.25 µm film thickness) was. All analyses were done using MSD ChemStation (Agilent Technologies) as software.

3.2.10 Shotgun-lipidomics

Shotgun lipidomics is a high-throughput approach to identify and quantitate lipid species directly from biological samples based on their ionization propensities, which does not require liquid chromatographic separation prior to the MS. This method involves the ionization of molecules transferring them into a gas phase and subsequent acceleration of the ions in an electrical field to separate them based on their mass–to–charge ratio (m/z ratio) in the MS. To perform shotgun lipidomics, samples from the fractionation, i.e. WCL, MF, ERF and LDF, as well es cell lysates from uninfected and infected hMDMs were inactivated in 800µl MeOH (containing 0.184% BHT) as described above and analyzed by the Research Group Bioanalytical Chemistry from PD Dominik Schwudke at the Research Center Borstel.

For the extraction of lipids, the methyl- tret- butyl ether (MTBE) extraction procedure was used. Similar to the extraction of FFA, all glassware used was washed 3x with H_2O for chromatography, 3x with MeOH and 3x with MTBE and was then dried using nitrogen gas (N_2). In brief, all samples were first dried at RT for 5h in a Speedvac at 37°C and resuspended in up to 1.5ml storage solution ($CHCl_3$: MeOH: H_2O, 60:35:4.5) depending on the protein concentration of the sample. The samples were then vortexed for 2 min, sonicated for 30 min in an ultrasound bath and incubated for 17h at 20°C shaking at 1400 rpm to solubilize the sample in the storage solution. Samples were again sonicated for 30 minutes and centrifuged at 15000 rcf at 20°C. The amount of sample required to obtain 20µg protein was then transferred into a fresh tube, dried in a Speedvac as before and resuspended in 270µl MeOH containing 3% acetic acid. 20µl of internal standard (table 9) and 1 ml MTBE was added, vortexed and incubated for 1 h at 20°C shaking (1400 rpm, Eppendorf, MixMate). 250µl of H_2O suitable for chromatography was added, vortexed and incubated for 5 min shaking as described before. Subsequently, the mixture was centrifuged for 2 min at 15000 rcf at 20°C. The organic phase was transferred into a new Eppendorf tube, dried in a Speedvac as described before and resuspended in 100µl storage solution. Prior to MS, the samples were diluted 1:20 in MS-Mix.

Shotgun lipidomics measurements were performed using a Q Exactive (Thermo Fisher Scientific) or an Apex Qe Fourier Transform Ion Cyclotron Resonance mass spectrometer (Bruker Daltonik), both equipped with a TriVersa NanoMate (Advion BioSciences) as autosampler and ion source. Lipid identification was performed using LipidXplorer as described before[128] and quantitation was achieved referenced to a mix of internal standards, which were added prior to extraction (SPLASH® Lipidomix® Mass Spec Standard).

Table 9: Composition and characteristics of the IS39794 internal standard.

Mixture Components	Conc. (µg/ml)	Molecular Weight	µM - pmol/µl	Chemical Formula	m/z (positive)	m/z (negative)
15:0-18:1(d7) PC	5.904	753.11	7.839	$C_{41}H_{73}D_7NO_8P$	753.6134 $[M+H]^+$	811.6199 $[M+CH_3COO]^-$
15:0-18:1(d7) PE	0.208	711.03	0.292	$C_{38}H_{67}D_7NO_8P$	711.5664 $[M+H]^+$	709.5519 $[M-H]^-$
15:0-18:1(d7) PS (Na-Salt)	0.153	777.02	0.197	$C_{39}H_{66}D_7NNaO_{10}P$	-	753.5417 $[M-H]^-$
15:0-18:1(d7) PG(Na-Salt)	1.047	764.02	1.370	$C_{39}H_{67}D_7NaO_{10}P$	-	740.5464 $[M-H]^-$
15:0-18:1(d7) PI(NH_4-Salt)	0.333	847.13	0.393	$C_{42}H_{75}D_7NO_{13}P$	-	828.5625 $[M-H]^-$
15:0-18:1(d7) PA(Na-Salt)	0.270	689.94	0.392	$C_{36}H_{61}D_7NaO_8P$	-	666.5097 $[M-H]^-$
18:1(d7) LPC	0.933	528.72	1.765	$C_{26}H_{45}D_7NO_7P$	529.3994 $[M+H]^+$	587.4059 $[M+CH_3COO]^-$
18:1(d7) LPE	0.192	486.64	0.395	$C_{23}H_{39}D_7NO_7P$	487.3524 $[M+H]^+$	485.3378 $[M-H]^-$
18:1(d7) Chol Ester	12.901	658.16	19.601	$C_{45}H_{71}D_7O_2$	675.6779 $[M+NH_4]^+$	-
18:1(d7) MG	0.071	363.59	0.194	$C_{21}H_{33}D_7O_4$	381.3704 $[M+NH_4]^+$	-
15:0-18:1(d7) DG	0.345	587.98	0.587	$C_{36}H_{61}D_7O_5$	605.5844 $[M+NH_4]^+$	-
15:0-18:1(d7)-18:1 TG	2.070	812.37	2.548	$C_{51}H_{89}D_7O_6$	829.7985 $[M+NH_4]^+$	-
18:1(d9) SM	1.160	738.12	1.572	$C_{41}H_{72}D_9N_2O_6P$	738.6470 $[M+H]^+$	796.6529 $[M+CH_3COO]^-$
Cholesterol(d7)	3.857	393.71	9.797	$C_{27}H_{39}D_7O$	411.4326 $[M+NH_4]^+$	-
Ceramide C17	2.080	551.93	3.769	$C_{35}H_{69}NO_3$	552.5350 $[M+H]^+$	610.5415 $[M+CH_3COO]^-$

3.2.11 Label-free proteomics

For proteomics and Western Blot analysis, the WCL, MF, ERF and LDF were diluted 4:1 in 8x SDS Lysis buffer, the samples were incubated at 95°C for 20 minutes to heat inactivate Mtb and stored at -80°C before further processing. For proteomics analysis, samples were further diluted 1:2 in ddH_2O. Samples were then shipped on dry ice to the Research group of Dr. Stefan Tenzer from Mainz University, and proteomics analysis was performed as follows.

Total protein of the SDS-buffer lysates was quantified using the Pierce 660 Protein Assay in 96-well plates on a Tevan GENios Microplate Reader according to the manufacturer's instructions. Subsequently, 10 µg of protein from each sample was digested in trypsin using a modified single-pot solid phase-enhanced sample preparation (SP3) as described before [129]. In brief, samples were reduced and alkylated using dithiothreitol (DTT) and iodoacetamide (IAA), and 2µl of a carboxylate-modified paramagnetic bead mix (1:1 of Sera-Mag SpeedBeads (Hydrophilic): Sera-Mag SpeedBeads (Hydrophobic)). Next, acetonitrile (ACN) was added (final concentration of 70% in the sample), samples incubated at RT for 18 min and subsequently, magnetic beads pelleted on a magnetic rack for 2 min. The pellet was washed with 70% EtOH and 100% ACN and next resuspended in 5µl of 50mM ammoniumhydrocarbonate/trypsin at a ratio of 1:25 for overnight digestion at 37°C. After that, ACN was added to a final concentration of 95%, mixed and incubated as before and the beads pellet washed with 100% ACN. Lastly, 2% dimethyl sulfoxide (DMSO) was used to elute the purified peptides from the beads. The peptide solution was then acidified using 1% formic acid and normalized amounts of digested samples were loaded into single-use Evotips and loaded into an EvoSep-One LC coupled to a TIMS-TOF-Pro MS in technical replicates. In brief, peptides were separated in a reversed-phase analytical column (Pepsep 150mm x 150umID, .1.9umC18, 40C) using the standard 30 samples per day method by EvoSep Biosystems (approx. 48 min gradient), which is characterized by a high proteome coverage and effective gradient elution thereby allowing the identification of up to 24,000 peptides. Data were acquired in the MS in standard 1.1 cycles per second DDA-PASEF mode as described by Meier *et al* [130]. Protein identification and label-free quantification were performed using MaxQuant version 2.0.0.0 [131] and protein intensities were normalized employing the built-in MaxLFQ algorithm [132]. After protein identification, reversely marked proteins, possible contaminants such as BSA and keratins and below the threshold proteins were removed as negative identifications. Proteins with at least two identified peptides and which were found in more than 50% of the biological replicates and enough technical replicates were labeled as quantifiable. Performing this analysis, ~2800 and ~2400 proteins were marked as quantifiable in the WCL and LDF, respectively, which were subsequently used for statistical analysis as described below.

3.2.12 Statistical Analysis

The GraphPad Prism 8 or newer software was used for the statistical analysis and graphic representation of data sets. Prior to performing statistical testing, data were log(Y)-transformed to assume a parametric distribution as described by Willems *et al.* [133] unless indicated otherwise. A one-way or two-way analysis of variance (ANOVA) followed by a Holm-Šídák's test for multiple comparison test was performed for hypothesis testing with more than two groups. For hypothesis testing with two groups, a two-sided, paired students t-test was used. Importantly, the statistical analysis was always performed with not-normalized data, even when presented as fold-change or %-change compared to the baseline control. For lipidomic analysis of TAG, DAG and CE species a paired multiple t-test followed by a multiple testing correction using the false discovery rate was performed. Statistical analysis for proteomics data was performed by Dr. David Gomez-Zepeda from the Proteomics Group at the University of Mainz, who determined the differences on the LFQ intensity across uninfected and Mtb-infected samples using a paired t-test followed by a Benjamini-Hochberg correction. Based on this analysis, differentially regulated proteins with a $p \leq 0.05$ or $p \leq 0.1$ (as indicated) were compared to the reactome, KEGG, or gene ontology database using the online tool g: profiler (https://biit.cs.ut.ee/gprofiler/gost)[134]. Results from the reactome-based analysis were additionally validated using the ReactomePA package[135]. Data are presented as image, table, bar graphs and line graphs showing the mean + standard error unless indicated otherwise.

4. Results

4.1 Mtb growth kinetic in human monocyte-derived macrophages over 7 days

Mtb infection induces alterations in several cellular processes. However, little is known about the cellular response to Mtb infection *in vitro* in human macrophages, particularly at later stages of infection.

Mtb growth kinetics in murine macrophages showed, that there is little to no Mtb growth in the first 24 hours of infection and Mtb replication becomes more prominent at later stages of post infection [117]. To investigate the Mtb growth kinetic in human macrophages, hMDMs were infected and CFU development in hMDMs over 7 days was determined. As depicted in Fig. 9, a decrease of CFU was observed between uptake (4h) and 24 hours post infection, which almost reached statistical significance at an MOI of 0.1 (p=0.08). At 3 days post infection, CFU remained constant compared to the uptake and 24 hours post infection. However, after 7 days of infection, a significant increase in CFU of approximately 4-fold was observed compared to the uptake indicating that Mtb growth is most prominent between day 3 and day 7 post infection. Therefore, for further analyses of the cellular response to Mtb infection, the 7 days post infection time point was chosen, when the Mtb is replicating prominently.

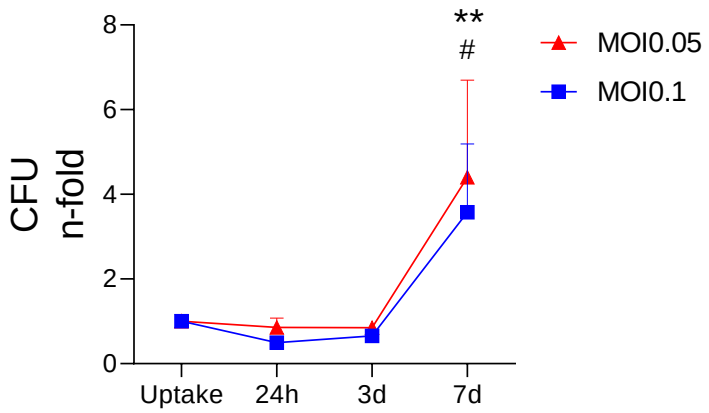

Figure 9: Mtb growth kinetic over 7 days.

Human monocyte-derived macrophages infected with Mtb H37Rv at an MOI of 0.05 or 0.1 and incubated for up to 7 days. At 4h (uptake), 24h, 3d and 7d cells were lysed, dilutions of lysates were plated on 7H10 agar plates and the colony forming units (CFU) were determined. Statistical analysis was performed with not-normalized data using two-way ANOVA followed by a Holm-Šídák's test for multiple comparison. Depicted is the mean fold-change normalized to the uptake + the standard error (n=4). ** = $p \leq 0.01$ for MOI of 0.05; # = $p \leq 0.05$ for an MOI of 0.1. d=days

4.2 Infection of human monocyte-derived macrophages with Mtb results in alterations in cellular metabolism

To analyze the cellular response to Mtb infection at later stages of infection, the proteome of uninfected and Mtb-infected human monocyte-derived macrophages after 7 days of infection was characterized. Label-free proteomics of cell lysates from uninfected and Mtb-infected hMDMs was performed to determine the relative amounts of proteins. Subsequently, differentially regulated proteins between uninfected and Mtb-infected cells were identified and a pathway enrichment analysis was conducted by comparing the identified proteins with the reactome pathway database [136].

This analysis revealed that only 130 proteins were differentially regulated between uninfected and Mtb-infected hMDMs (Suppl. Fig. 1). These differentially regulated proteins were significantly enriched in signaling pathways such as “Interferon signaling”, “PD-1 signaling”, “Translocation of ZAP-70 to immunological synapse” and “Phosphorylation of CD3 and TCR zeta chains” (Fig. 10).

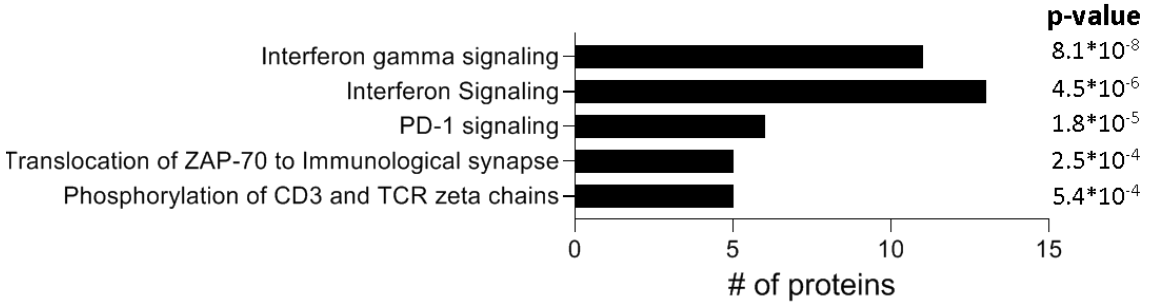

Figure 10: Top 5 pathways significantly enriched in Mtb-infected primary human macrophages.

Human monocyte-derived macrophages were infected with Mtb at an MOI of 0.1 or left untreated for 7 days. Subsequently, cells were lysed, digested and a liquid chromatography-based approach was performed to determine relative protein levels using label-free proteomics. A paired t-test followed by a Benjamini-Hochberg correction was used to determine differentially regulated proteins between Mtb-infected hMDMs compared to uninfected hMDMs ($p<0.05$). Pathway enrichment analysis was performed and differentially regulated proteins were compared to the reactome database using the online tool g: profiler. Depicted are the top 5 enriched pathways and the respective p-values (n=5).

Due to the high donor variability, which is also observed in the 4 donors used in figure 9, and the low number of independent experiments (n=5), pathway enrichment analysis (PWE) was repeated with all differentially regulated proteins with a p-value of 0.1 or smaller. Performing this analysis revealed a total of 490 differentially regulated proteins, which were then used to determine enriched pathways.

The top 10 enriched pathways in Mtb-infected hMDMs compared to uninfected cells are illustrated in figure 11. The number 1 significantly enriched pathway was "Antigen presentation" (p=2.8*10-9). Additional to the enriched pathways previously detected (Fig. 10), "Neutrophil degranulation" (p=1.2*10-6), "Immune System" (p=1.4*10-5), and "Interferon alpha/beta signaling" (p=1.5*10-4) were among the enriched pathways with 30, 78, and 13 upregulated proteins, respectively, and 10, 31 and 0 downregulated proteins, respectively. Furthermore, pathways such as "Endosomal/vacuolar pathway" (p=2.6*10-4), "ER phagosome pathway" (p=2.7*10-4), and "Antigen processing" (p=4.5*10-4) were also found among the top 10 significantly enriched pathways comprising 6 and 13 upregulated proteins and 0, 1 and 2 downregulated proteins, respectively. "Interferon signaling" ($p=5.9*10^{-5}$) and "Interferon gamma signaling" ($p=1.2*10^{-5}$), which were also detected in the previous analysis, comprised 23 and 17 upregulated proteins, respectively, in Mtb-infected hMDMs compared to uninfected cells. Most interestingly, "Metabolism" was found number 5 under the top 10 enriched pathways comprising the highest number of differentially regulated proteins, 78 of which were upregulated and 38 downregulated. Collectively, Mtb-infection induces alterations in several cellular processes related to immune response, subcellular compartments and cellular metabolism (Fig. 11).

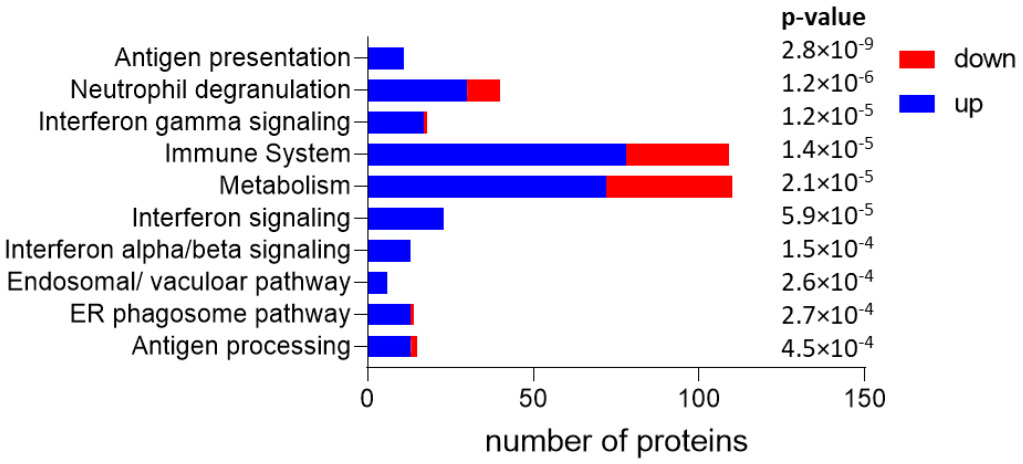

Figure 11: Proteome analysis of human macrophages revealed several enriched pathways upon Mtb infection.

Human monocyte-derived macrophages were infected with Mtb at an MOI of 0.1 or left untreated for 7 days. Subsequently, cells were lysed, digested and a liquid chromatography-based approach was performed to determine relative protein levels using label-free proteomics. A paired t-test followed by a Benjamini-Hochberg correction was used to determine differentially regulated proteins between Mtb-infected hMDMs compared to uninfected hMDMs with a p-value less than or equal to 0.1. Pathway enrichment analysis was performed and differentially regulated proteins were compared to the reactome database using the online tool g: profiler. Depicted are the top 10 significantly enriched pathways, the number of up-and downregulated proteins found in this pathway and the respective p-values (n=5).

4.2.1 The effect of Mtb infection on glycolytic metabolism in primary human macrophages

4.2.1.1 Mtb infection increases glycolytic parameters in human macrophages at day 7 post infection

As described above, results from proteomics analysis revealed "Metabolism" to be one of the significantly enriched pathways upon Mtb infection, suggesting that Mtb infection induces alterations in macrophage bioenergetic metabolism. To examine the effect of Mtb infection on macrophage energy metabolism in more detail, hMDMs were left uninfected or infected with Mtb at an MOI of 0.05 and 0.1 for 7 days and subsequently, extracellular flux analysis was performed to study glycolytic metabolism. Glycolytic metabolism was analyzed by measuring the ECAR (mpH/min) of cell culture supernatants in real-time under basal conditions and upon serial injection of compounds interfering with glycolytic metabolism allowing the determination of several glycolytic parameters.

Injection of glucose to the cells induces glycolysis and is reflected in an increase in ECAR levels (Fig. 12). As depicted in figure 13, Mtb infection resulted in increased ECAR levels after glucose injection by ~45% at an MOI of 0.1, respectively, when compared to uninfected cells.

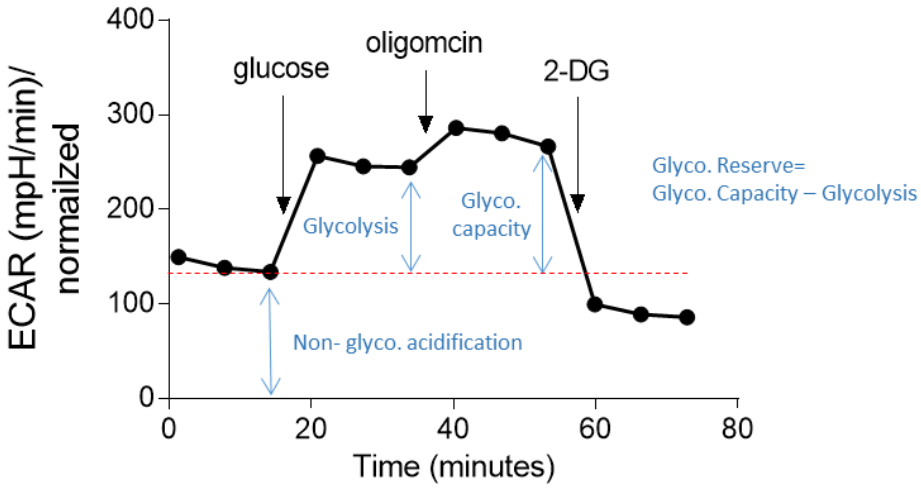

Figure 12: Graphic representation of the ECAR measurement of uninfected monocyte-derived macrophages during the XF Glyco Stress Test.

Human monocyte-derived macrophages were seeded in XFe96 well plates, incubated for 7 days followed by extracellular flux analysis using the Glyco Stress Test according to the manufacturer's instructions. ECAR (mpH/min) was first determined under basal conditions in absence of glucose, followed by ECAR measurement upon serial injection of glucose (10mM), oligomycin (1.5µM) and 2-DG (50mM). After the measurement, cell viability was determined using crystal violet staining and normalized data was analyzed using the Wave Desktop Software 2.6 (Agilent Technologies).

Following glucose injection, oligomycin was added to the cells, which blocks mitochondrial ATP production and increases the ECAR to its maximum thereby allowing to determine glycolytic capacity (Fig. 12). Mtb-infected cells show an increase in glycolytic capacity as determined by an increase in ECAR of ~21% and 50% at an MOI of 0.05 and 0.1, respectively, when compared to the uninfected control. The increase in both glycolysis and glycolytic capacity in Mtb-infected cells reaches statistical significance at an MOI of 0.1 compared to uninfected cells (Fig. 13).

The glycolytic reserve is determined by the difference between the ECAR after glucose injection and the ECAR after oligomycin injection (Fig. 12) and allows to determine how close cells work to their glycolytic maximum. Figure 13 shows that glycolytic reserve is dose-dependently and significantly upregulated in Mtb-infected compared to uninfected hMDMs with an increase of up ~73% at an MOI of 0.1.

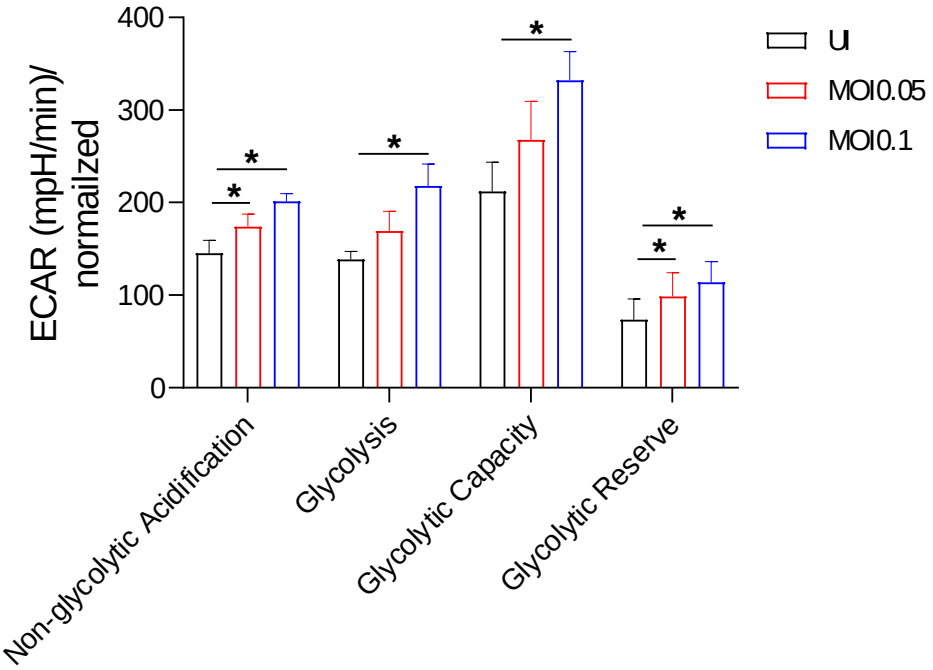

Figure 13: Mtb-infection of hMDMs induces an increase in glycolytic parameters.

Human monocyte-derived macrophages were infected with Mtb at an MOI of 0.05 and 0.1 or left untreated (UI) for 7 days and analyzed by extracellular flux analysis using the XF Glyco Stress Test. ECAR (mpH/min) was first determined under basal conditions in absence of glucose, followed by ECAR measurement upon serial injection of glucose (10 mM), oligomycin (1.5 µM) and 2-DG (50 mM). After the measurement, cell viability was determined using crystal violet staining for the normalization of data. Glycolytic parameters were then calculated using the XF Glycolysis Stress Test report generator (Wave Desktop Software 2.6; Agilent Technologies). Statistical analysis was performed using a one-way ANOVA followed by a Holm-Šídák's test for multiple comparison (n=3). Depicted is the mean + the standard error. * = $p \leq 0.05$.

Importantly, the ECAR measured before injection of glucose is due to non-glycolytic acidification caused by mitochondrial metabolism (Fig. 12). As shown in figure 13, Mtb infection resulted in the dose-dependent and significant increase ECAR values of the non-glycolytic acidification amounting to approximately 28% and 16% increase at an MOI of 0.1 and 0.05, respectively, compared to uninfected hMDMs. Albeit small, this increase in non-glycolytic acidification might indicate induction of mitochondrial metabolism upon Mtb infection. Lastly, injection of the competitive inhibitor 2-DG results in the complete block of glycolysis (Fig. 12).

In summary, these results indicate that Mtb infection results in a dose-dependent increase in glycolysis in hMDMs at day 7 post infection as evident by increased ECAR levels for the glycolytic parameters glycolysis, glycolytic capacity and glycolytic reserve.

4.2.1.2 Mtb infection results in the upregulation of glycolytic proteins

Extracellular flux analysis revealed that Mtb infection induces glycolytic metabolism in hMDMs. To further substantiate this, the protein expression of several proteins known to be involved in glucose metabolism was analyzed using label-free proteomics.

The proteins SLC2A3 and SLC2A6, also referred to as GLUT3 and GLUT6, are involved in the uptake of glucose into macrophages[56,57]. As depicted in figure 14, a significant increase of ~1.9 and ~2.1 fold was observed in SLC2A3 and SLC2A6 expression, respectively, in Mtb-infected hMDMs compared to the control. In line with that, also an upregulation of two major kinases involved in the early steps of glycolysis[137], namely ADP-dependent glucokinase (ADPGK) and HK2 was detected in Mtb-infected hMDMs compared to the control. However, due to donor variability, as reflected by the high standard errors, the Mtb-induced increase for these two proteins did not reach statistical significance yet (p-value of 0.1 and 0.09 for ADPGK and HK2, respectively). Interestingly, a substantial Mtb-induced decrease of approximately 25% was observed for GAPDH protein expression compared to uninfected cells. Similarly, also a the aldo-keto reductase family 1 member A1 (AKR1A1), which is a regulator of glycolysis, was downregulated upon Mtb infection (p=0.1). This may indicate that the expression of several glycolytic proteins is differentially affected by Mtb infection.

The pyruvate dehydrogenase (PDH) is known to couple glycolysis to OXPHOS in mitochondria by converting pyruvate to acetyl-CoA[138]. Interestingly, the protein expression of the regulatory subunit of the pyruvate dehydrogenase phosphatase, PDPR, was increased by ~31% during Mtb

infection of hMDMs compared to uninfected cells (p=0.052) (Fig. 14). This may indicate that there is an enhanced shift towards OXPHOS from the glycolytic pathway.

Collectively, these results support the notion that Mtb infection induces glycolysis in hMDMs at day 7 post infection as demonstrated by the upregulation of several critical proteins involved in glucose metabolism.

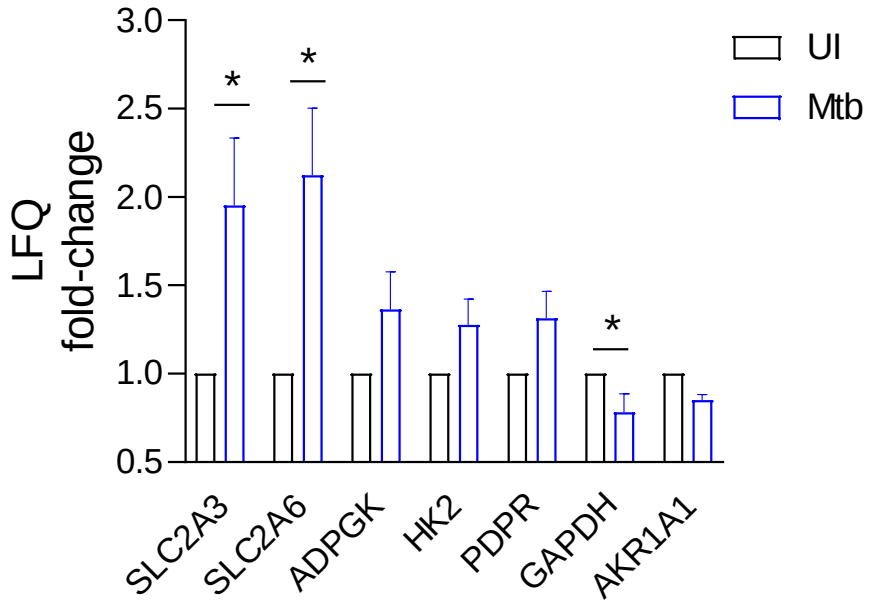

Figure 14: Mtb-infection results in the regulation of proteins involved in glycolysis.

Human monocyte-derived macrophages were infected with Mtb at an MOI of 0.1 or left untreated for 7 days. Subsequently, cells were lysed, digested and a liquid chromatography-based approach was performed to determine relative protein levels using label-free proteomics. Depicted is the label-free quantitation (LFQ) intensity of selected glycolytic proteins (all $p \leq 0.1$), which were normalized to the respective uninfected control. Statistical analysis of proteomics data was performed with not-normalized data using a paired t-test followed by a Benjamini-Hochberg correction with not-normalized data (n=5). Depicted is the mean + standard error. * = $p < 0.05$

4.2.2 Mtb-infected primary human macrophages have higher ATP demands

The above described Mtb-induced upregulation of glycolytic parameters and increased expression of glycolytic proteins suggests that upon Mtb infection ATP might be produced through increased glycolysis. Therefore, extracellular flux analysis was performed to determine glycolytic ATP production rates (pmol ATP/min) (glycoATP) in uninfected and Mtb-infected hMDMs at day 7 post infection by measuring the ECAR and the proton efflux rate (pmol H^+/min). Aside from the glycolytic ATP production, also the mitochondrial production of ATP

(mitoATP) through OXPHOS was determined by measuring the OCR (pmol O_2/min). Serial injection of the mitochondrial inhibitors oligomycin and antimycin A/rotenone, respectively, enables the calculation of total ATP production rates, aside from the determination of mitochondrial and glycolytic contribution to the total ATP production.

As depicted in figure 15, a substantial increase of ~45% in glycoATP was observed upon Mtb infection at an MOI of 0.1 compared to uninfected cells. However, the increase did not reach statistical significance in the three donors tested.

MitoATP production was significantly increased in Mtb-infected hMDMs compared to the uninfected control leading to an increase of ~100% at an MOI of 0.1. In consequence of increased glycolytic and mitochondrial ATP production, total ATP production was also significantly increased by ~84% in hMDMs infected with Mtb at an MOI of 0.1, when compared to uninfected cells (Fig. 15).

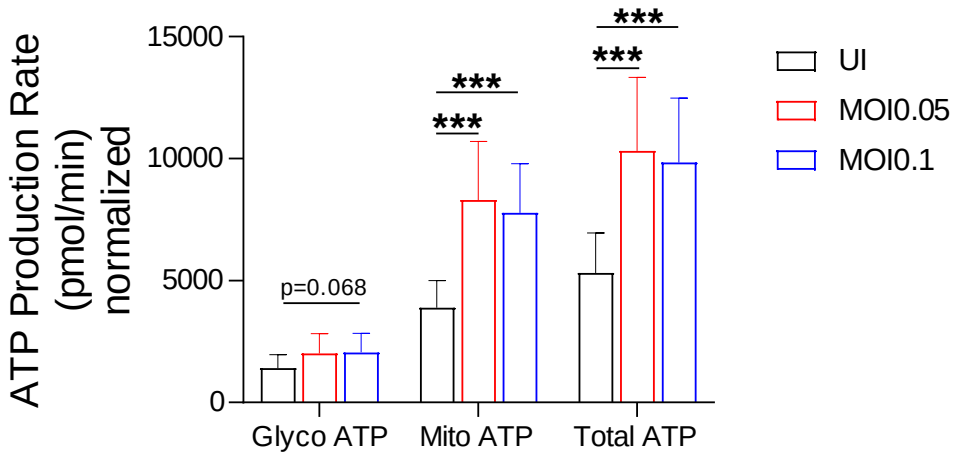

Figure 15: Mtb-infection induces an increase in ATP production in human macrophages.

Human monocyte-derived macrophages were infected with Mtb at an MOI of 0.05 and 0.1 or left untreated (UI) for 7 days. Subsequently, extracellular flux analysis was performed using the XF Real-time ATP Rate Assay. ECAR (mpH/min) and OCR (pmol/min) were first determined under basal conditions, followed by serial injection oligomycin (1.5 µM) and antimycin A/ rotenone (0.5 µM). After the measurement, cell viability was determined using crystal violet staining for the normalization of data. ATP production rates were then calculated using the report generator (Wave Desktop Software 2.6; Agilent Technologies). Statistical analysis was performed using one-way ANOVA followed by a Holm-Šídák's test for multiple comparison. Depicted is the mean + the standard error (n=3). ***= $p \leq 0.001$.

Interestingly, glycolytic ATP production in uninfected hMDMs accounts for approximately ~27% of the total ATP production. In contrast, the contribution of mitoATP production in uninfected hMDMs is substantially higher compared to glycoATP and amounts to 73% of the total contribution, indicating that the bulk of energy in human macrophages is produced in mitochondria (Fig. 15).

Taken together, the results indicate that Mtb infection in hMDMs induces glycolytic and mitochondrial ATP production leading to an increase in total ATP production. Furthermore, the data suggest that human macrophages produce most of the energy through mitochondrial respiration.

4.2.3 The effect of Mtb infection on mitochondrial metabolism in primary human macrophages

4.2.3.1 Respiratory metabolism in human macrophages is significantly increased upon Mtb infection

As determined before (Fig. 15), the bulk of ATP in macrophages is produced in mitochondria compared to glycolysis. To further investigate this, extracellular flux analysis was used to study respiratory metabolism in hMDMs upon Mtb infection by measuring the OCR in cell culture supernatants in real-time under basal conditions and upon serial injection of compounds interfering with the ETC. This allowed the determination of several respiratory parameters.

OCR was first measured under basal conditions to determine basal respiration (Fig. 16). Mtb infection resulted in an increase in OCR levels for basal respiration, which amounted to ~69% and ~30% at an MOI of 0.1 and 0.05, respectively, compared to uninfected cells. This effect reached statistical significance at an MOI of 0.1 (Fig. 17).

After injection of oligomycin, OCR levels decreased due to the inhibition of the mitochondrial ATP synthase, allowing to determine the ATP-linked respiration as well as the proton leak (Fig. 16). As depicted in figure 17, Mtb infection induced a significant increase of up to 76% in the OCR levels for the ATP-linked respiration at an MOI of 0.1 compared to uninfected cells. This observation further supports previous results indicating that mitochondrial ATP production is increased upon Mtb infection. While there is also a substantial, dose-dependent increase of up to 46% in the proton leak upon Mtb-infected compared to uninfected hMDMs, this effect did not reach statistical significance (Fig. 17).

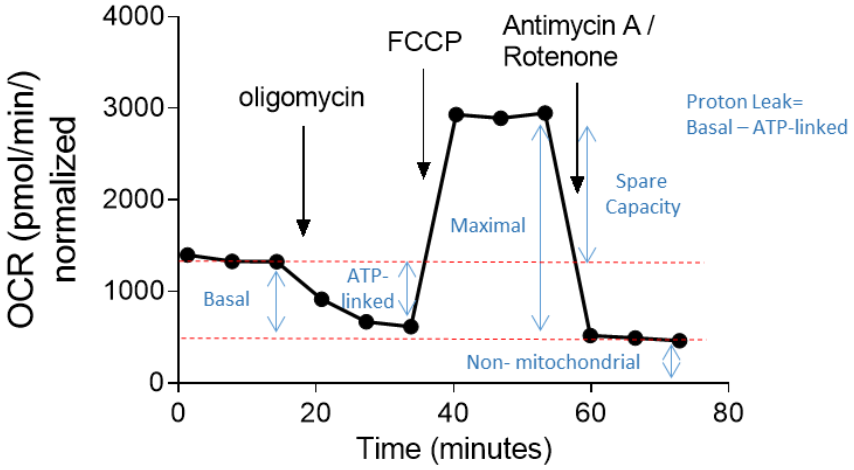

Figure 16: Graphic representation of the OCR measurement of uninfected human macrophages during the XF Mito Stress Test.

Human monocyte-derived macrophages were seeded in XFe96 well plates, incubated for 7 days, and subsequently, extracellular flux analysis was performed using the XF Mito Stress Test according to the manufacturer's instructions. OCR (pmol/min) was first determined under basal conditions, followed by serial injection oligomycin (1.5 µM), FCCP (1 µM) and antimycin A/ rotenone (0.5 µM). After the measurement, cell viability was determined using crystal violet staining and normalized data were analyzed using the Wave Desktop Software 2.6 (Agilent Technologies).

The subsequent injection of FCCP results in the depolarization of the inner mitochondrial membrane, which induces the free flow of protons across the mitochondrial membrane thereby inducing maximal respiration and an increase in OCR levels (Fig. 16). Figure 17 shows that the OCR levels for the maximal respiration were dose-dependently and significantly increased upon Mtb infection compared to uninfected hMDMs. This increase amounted to ~58% and 49% at an MOI of 0.1 and 0.05, respectively. Another respiratory parameter that can be calculated after injection of FCCP is the spare respiratory capacity, which is an indicator of how close cells work to their theoretical respiratory maximum (Fig. 16). As evident by increase OCR values, the spare respiratory capacity is substantially increased upon infection of hMDMs with Mtb compared to uninfected cells, indicating that Mtb infected cells have higher respiratory capacities (Fig. 17).

Lastly, complete blockage of OXPHOS by injection of the complex I and II inhibitors antimycin A and rotenone, respectively, results in the decrease in OCR levels enabling the determination of non-mitochondrial respiration (Fig. 16). Similar to other respiratory parameters, non-mitochondrial respiration is significantly upregulated upon Mtb infection, as suggested by a significant increase in OCR of up to ~70% at an MOI of 0.1 compared to the uninfected cells

(Fig. 17). This indicates, that other oxidative processes, which are not occurring in mitochondria, might be upregulated during infection with Mtb.

Collectively this suggests that Mtb infection results in dose-dependently increased respiration in hMDMs at day 7 post infection, which was demonstrated by increased OCR levels for basal respiration, ATP-linked respiration and maximal respiration. Furthermore, an increase in non-mitochondrial respiration might indicate that oxygen-consuming processes for example during detoxification processes or processes involving oxidases and oxygenase activity are upregulated during Mtb infection.

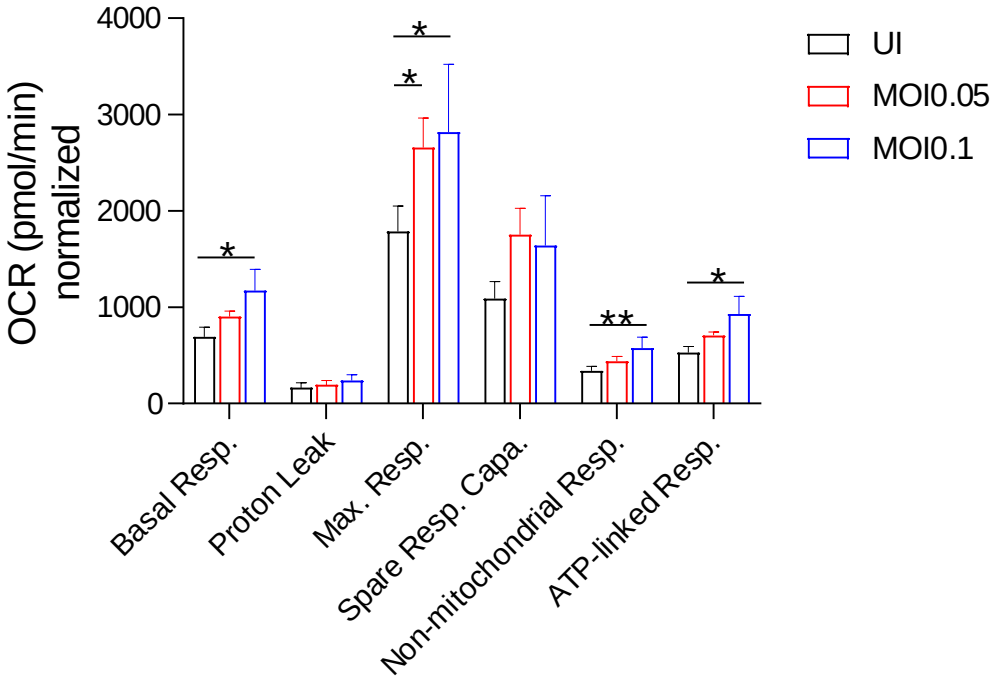

Figure 17: Mtb-infection induces an increase in respiratory parameters.

Human monocyte-derived macrophages were infected with Mtb at an MOI of 0.05 and 0.1 or left untreated (UI) for 7 days, and subsequently, extracellular flux analysis was performed using the XF Mito Stress Test. OCR (pmol/min) was first determined under basal conditions, followed by serial injection oligomycin (1.5 µM), FCCP (1 µM) and antimycin A/ rotenone (0.5 µM). Measurements were normalized using crystal violet staining. Respiratory parameters were then calculated using the XF Mito Stress Test report generator (Wave Desktop Software 2.6; Agilent Technologies). Statistical analysis was performed using one-way ANOVA followed by a Holm-Šídák's test for multiple comparison. Depicted is the mean + the standard error (n=5). * = $p \leq 0.05$; ** = $p \leq 0.01$.

4.2.3.2 Mtb infection induces an increase in mitochondrial membrane potential

As described above, extracellular flux analysis of hMDMs showed that Mtb infection induces an increase in cellular respiration and mitochondrial ATP production at day 7 post infection. This suggests, that mitochondria undergo substantial metabolic changes in response to Mtb infection. To further investigate this finding, mitochondrial activity was analyzed using flow cytometry.

The mitochondrial dye Rho123 is often used to measure mitochondrial activity, as it accumulates in mitochondria depending on the $\Delta\Psi$. In contrast, MitoTracker™ is a $\Delta\Psi$-independent dye used to determine mitochondrial mass[117]. Here, flow cytometry was used to determine Rho123 and MitoTracker Deep Red fluorescence intensity to determine mitochondrial activity relative to the mass. Infection of hMDMs with Mtb leads to a significant increase in the Rho123/MitoTracker mean fluorescence intensity (MFI) of approx. ~30% compared to uninfected cells (Fig. 18). This suggests that Mtb infection induces the activity of mitochondria in hMDMs, which is in line with the Mtb-induced increase in respiratory parameters observed by extracellular flux analysis.

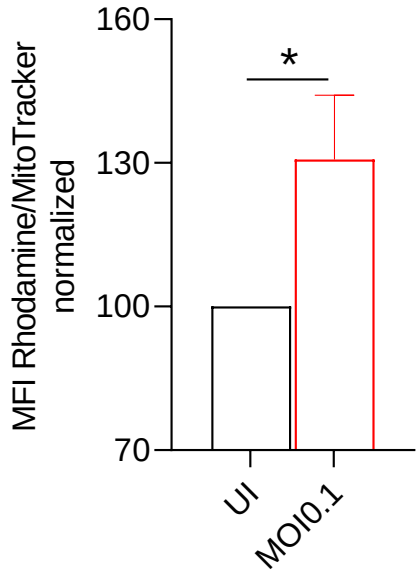

Figure 18: Mtb-infection induces alterations in mitochondrial activity.

Human monocyte-derived macrophages infected with Mtb at an MOI of 0.1 or left untreated (UI) for 7 days, washed and stained with Rho123 (0.5 µg/ml) and MitoTracker (300nM) and subsequently analyzed using flow cytometry. The ratio of Rho123/MitoTracker MFI was determined and normalized to the uninfected sample (n=4). Statistical analysis was performed with not-normalized data using a paired t-test. Depicted is the mean + the standard error. * = $p \leq 0.05$

4.2.3.3 Mtb infection results in alterations to the mitochondrial organization

Mitochondrial morphology is directly and indirectly linked to cellular energetic metabolism[73]. As prior observations (section 4.2.3.1 and 4.2.3.2) suggest alterations in mitochondrial energy production upon infection, structural changes in mitochondria of Mtb-infected hMDMs were analyzed by determining the expression of mitochondrial proteins.

Analysis of the proteome of hMDMs using the gene ontology database allowed to determine in which cellular component differentially regulated proteins are significantly over-or underrepresented in Mtb-infected cells. This analysis revealed that the cellular components "Mitochondrion", "Mitochondrial matrix" and "Mitochondrial envelope" are among the significantly enriched cellular components upon Mtb infection (Suppl. fig. 2). This suggests that in Mtb-infected hMDMs the expression of proteins, which are either localized in mitochondria or the function of which is associated with mitochondrial function, is significantly altered upon Mtb-infection.

Among the significantly upregulated mitochondria-associated proteins, the superoxide dismutase 2 (SOD2), which is involved in detoxification of mitochondrial ROS[139], the surfeit locus protein 1 (SURF1), a regulator of cytochrome C oxidase[140], and paraplegin (SPG7), which is a regulator of the mitochondrial permeability transition pore[141], showed the strongest fold increase upon Mtb-infection compared to uninfected cells (Fig. 19).

Moreover, the mitochondrial fission process protein 1 (MTFP1), the mitochondrial polyribonucleotide nucleotidyltransferase 1 (PNPT1), which are both involved in regulating mitochondrial translation are also significantly upregulated[142,143]. Further significantly upregulated proteins include the thymidine phosphorylase TYMP, which is required for mitochondrial DNA replication, the urokinase plasminogen activator surface receptor (PLAUR), which regulates cytochrome c release, and the protein arginine methyltransferase NDUFAF7, which is required for complex I stability[144]. Interestingly, also the signal transducer and activator of transcription family 3 (STAT3), which has a regulatory role in the ETC, as well as ATP and ROS production[145], was also among the significantly upregulated proteins in Mtb-infected hMDMs compared to uninfected cells (Fig. 19).

Collectively, analysis of the expression of mitochondrial proteins suggests that mitochondria undergo significant organizational alterations upon infection Mtb, which might affect the function, activity and morphology of mitochondria.

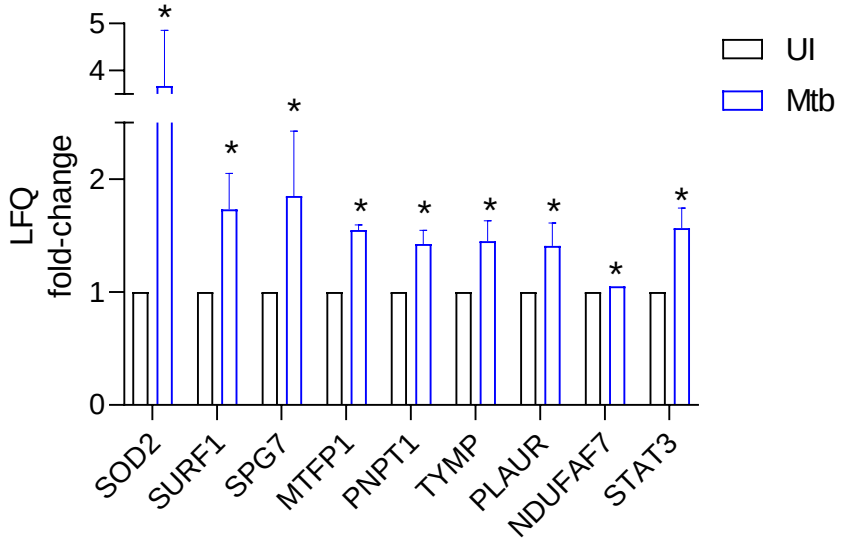

Figure 19: Mtb-infection results in the significant upregulation of mitochondrial proteins.

Human monocyte-derived macrophages were infected with Mtb at an MOI of 0.1 or left untreated for 7 days. Subsequently, cells were lysed, digested and a liquid chromatography-based approach was performed to determine relative protein levels using label-free proteomics. Depicted is the fold-change of selected upregulated proteins ($p < 0.05$), which are related to mitochondria, in Mtb-infected hMDMs compared to uninfected cells. Statistical analysis was performed with not-normalized data using a paired t-test followed by a Benjamini-Hochberg correction with not-normalized data (n=5). Depicted is the mean + the standard error. * = $p \leq 0.05$

4.2.3.4 Mtb infection causes a decreased mitochondrial DNA content

To further substantiate Mtb-induced changes in mitochondria, the mitochondrial DNA content was measured using quantitative RT-PCR. As depicted in figure 20, Mtb-infection results in a dose-dependent, significant decrease in the mitochondrial/nuclear DNA ratio compared to uninfected hMDMs amounting to a ~32% decrease at an MOI of 0.1 compared to the uninfected control. This suggests that Mtb infection induces a significant decrease in mitochondrial DNA, which might affect the morphology and function of mitochondria[146].

Collectively, the results obtained when analyzing mitochondrial metabolism indicate that mitochondria might undergo substantial structural and bioenergetic alterations as evident by increased respiratory rates and mitochondrial membrane potential, altered mitochondrial organization and mitochondrial protein expression as well as a decrease in mitochondrial DNA.

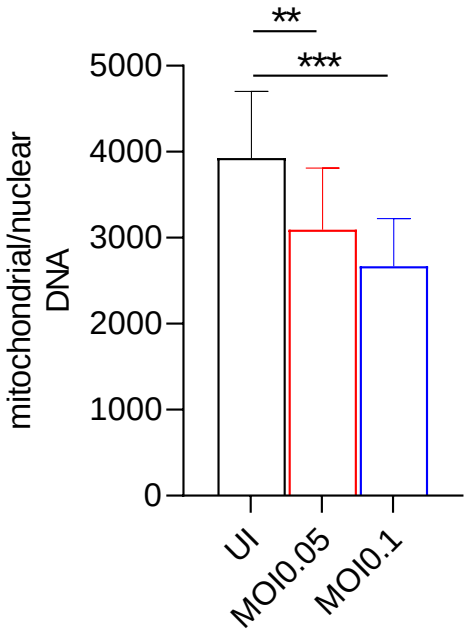

Figure 20: Mtb-infection reduces mitochondrial DNA levels.

Human monocyte-derived macrophages were infected with Mtb at an MOI of 0.1 or left untreated (UI) for 7 days and lysed in trizol. After DNA extraction quantitative RT-PCR was performed determining expression levels of microglobulin (*B2M*) and $tRNA^{Leu(UUR)}$, which are encoded on the nuclear and mitochondrial DNA, respectively. The $tRNA^{Leu(UUR)}$ expression relative to the *B2M* expression was calculated, thereby determining the ratio of mitochondrial/nuclear DNA. Statistical analysis was performed using one-way ANOVA followed by a Holm-Šídák's test for multiple comparison (n=4). Depicted is the mean + the standard error. ** = $p \leq 0.01$; ***= $p \leq 0.001$.

4.2.3.5 Fatty acids are the major substrate fueling respiration in Mtb-infected human macrophages

As described above, Mtb infection results in increased mitochondrial activity and respiration in hMDMs. Respiration is fueled by the metabolization of three major substrates, glucose, glutamine, or fatty acids. To determine which substrate fuels OXPHOS during Mtb infection, extracellular flux analysis was performed and OCR was measured. By injection of the compounds UK5099, BPTES and etomoxir the supply of glucose, glutamine and fatty acids, respectively, was pharmacologically blocked, which allows calculating the dependency of hMDMs respiration on each of these substrates as has been described before[115].

As illustrated in figure 21, uninfected cells show the highest dependency of ~40% on glucose, followed by ~31% dependency on fatty acids and ~22% glutamine dependency. However, when hMDMs are infected with Mtb, a shift in the substrate dependency is observed. This becomes evident by a substantial decrease of ~23% in the dependency on glucose upon Mtb infection compared to uninfected cells. In contrast, the dependency on fatty acids significantly increases from ~31% in uninfected cells to ~40% in Mtb-infected cells. No significant difference was observed in the dependency on glutamine upon Mtb infection in hMDMs.

These results suggest that upon Mtb infection, hMDMs increasingly depend on fatty acids to fuel OXPHOS, as demonstrated by increased fatty acid dependency in cells infected with Mtb compared to the control. This might suggest, that infection of hMDMs with Mtb, induces an increase in FAO at 7 days post infection.

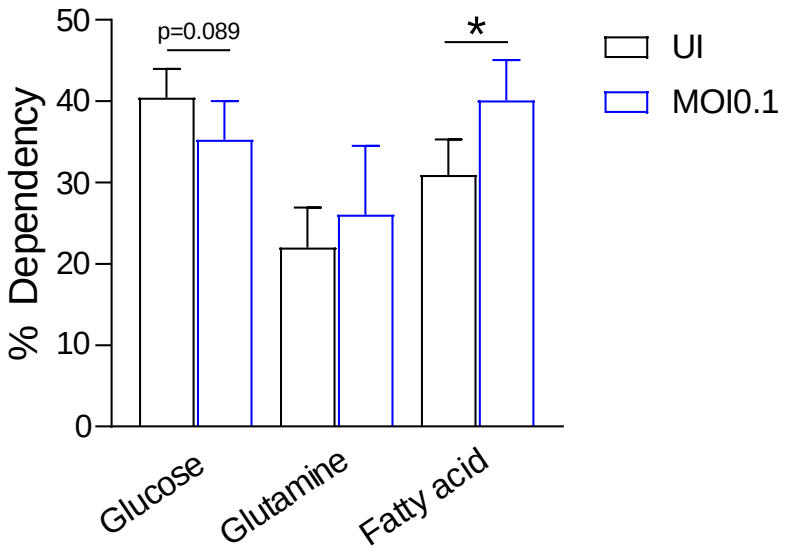

Figure 21: Mtb-infection induces an increase in the dependency on fatty acids in human macrophages.

Human monocyte-derived macrophages infected with Mtb at an MOI of 0.1 or left untreated (UI) for 7 days, and subsequently extracellular flux analysis performed using the XF MitoFuel Dependency Assay. OCR (pmol/min) was determined under basal conditions and following the injection of either BPTES (3µM), UK5099 (2µM) and etomoxir (16µM) or a combination thereof (section 3.2.6). % Dependency to each substrate was calculated using the report generator (Wave Desktop Software 2.6; Agilent Technologies). Statistical analysis was performed using a paired t-test (n=4). Depicted is the mean + the standard error. * = $p \leq 0.05$.

4.2.4 Mtb infection alters fatty acid metabolism in primary human macrophages

4.2.4.1 Infection of human monocyte-derived macrophages with Mtb induces alterations in pathways related to the degradation of fatty acids

Extracellular flux analysis indicated that Mtb infection induces respiratory metabolism through the increased metabolization of fatty acids. To investigate this further, the relative protein expression of proteins related to fatty acid oxidation in uninfected and Mtb-infected hMDMs was analyzed.

Comparing differentially regulated proteins between uninfected and Mtb-infected cells to the KEGG database to perform a functional enrichment analysis revealed that "Fatty acid degradation" is among the significantly enriched pathways (Suppl. Fig. 3).

To analyze this further, relative protein expression of selected proteins involved in peroxisomal and mitochondrial fatty acid degradation were evaluated. As depicted in figure 22, infection of hMDMs with Mtb at an MOI of 0.1 resulted in the increase of relative protein expression of several proteins as evident by increased LFQ intensity values.

Peroxisomal acyl-coenzyme A oxidase (ACOX) 1 and 3 are two proteins that are critically involved in the first step of FAO in peroxisomes[147]. Upon Mtb infection relative protein expression is significantly upregulated by 1.9 and 2.2-fold compared to the uninfected control for both ACOX1 and ACOX3, respectively. In line with that, the peroxisomal protein acyl-CoA thioesterase (ACOT) 8, which is described to be involved in peroxisome proliferation and lipolysis[148], was substantially increased by ~40% in Mtb-infected cells compared to the control (Fig. 22). This might indicate that peroxisomal metabolism and fatty acid degradation are increased upon Mtb infection in primary human macrophages.

The aldehyde dehydrogenase (ALDH2) is a mitochondrial enzyme important for the breakdown of byproducts from the oxidative degradation of lipids[149]. As depicted in figure 22, Mtb infection causes a significant increase of ~80% in ALDH2 LFQ intensity compared to the control, which might indicate that upon Mtb infection increased removal of byproducts of FAO is required in hMDMs.

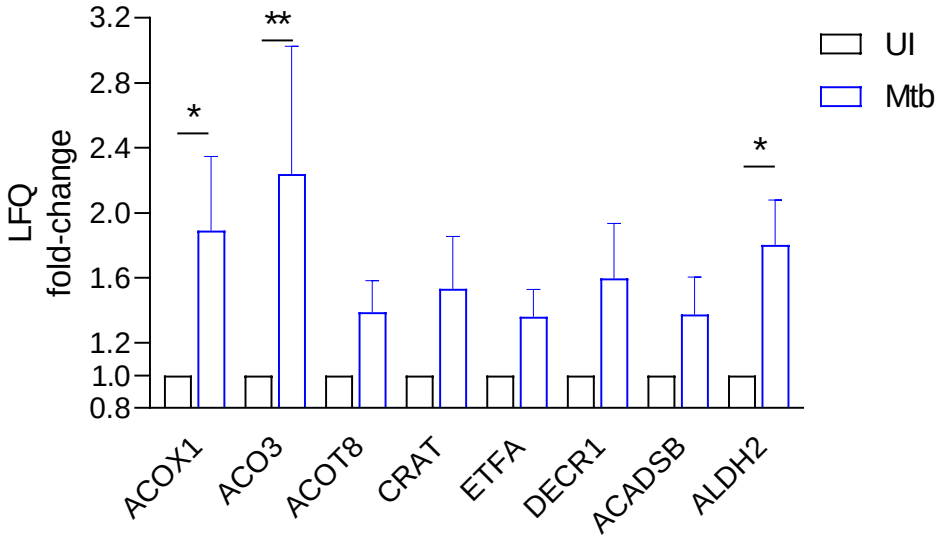

Figure 22: Proteins related to fatty acid degradation and peroxisome are upregulated in Mtb-infected human macrophages.

Human monocyte-derived macrophages were infected with Mtb at an MOI of 0.1 or left untreated for 7 days. Subsequently, cells were lysed, digested and a liquid chromatography-based approach was used to determine relative protein expression using label-free proteomics. Depicted is the fold-change of selected upregulated proteins involved in FAO in Mtb-infected hMDMs compared to uninfected cells. Statistical analysis was performed with not-normalized data using a paired t-test followed by a Benjamini-Hochberg correction with not-normalized data (n=5). Depicted is the mean + the standard error. * = $p \leq 0.05$; ** = $p \leq 0.01$

Another protein involved in the transport of FA for FAO is the carnitine acetyltransferase (CRAT), which transfers the acyl-group from acyl-CoA to carnitine[150]. In figure 22 it is shown that the relative CRAT expression was substantially increased by ~1.5-fold in hMDMs infected with Mtb compared to the uninfected control. Similarly, in Mtb-infected hMDMs, the ACASDB expression was substantially upregulated by ~37% compared to uninfected cells. The acyl-CoA dehydrogenase ACADSB is a mitochondrial protein required for the dehydrogenation of short/branched fatty acids during FAO[151]. Another protein required for the transfer of electrons produced by ACAD during FAO is the electron transfer flavoprotein subunit alpha (ETFA)[152]. Similar to other enzymes involved in FAO, ETFA expression was upregulated by ~36% upon Mtb infection. In addition to that, the relative protein expression of the 2,4-dienoyl-CoA reductase 1 (DECR1), which is an auxiliary enzyme for the FAO of unsaturated fatty acids[153], is substantially increased in response to an Mtb in hMDMs.

Collectively, analysis of the expression of proteins involved in peroxisomal and mitochondrial fatty acid metabolism supports the notion that Mtb infection induces FAO in primary human macrophages at day 7 post infection.

4.2.4.2 Mtb infection induces the expression of several ACSL isoforms in human macrophages

ACSL proteins are a family of enzymes catalyzing the thioesterification of FFA forming acyl-CoAs. As this is a critical step for the degradation of fatty acids in mitochondria, the protein expression of several ACSL isoforms was analyzed in hMDMs during Mtb infection.

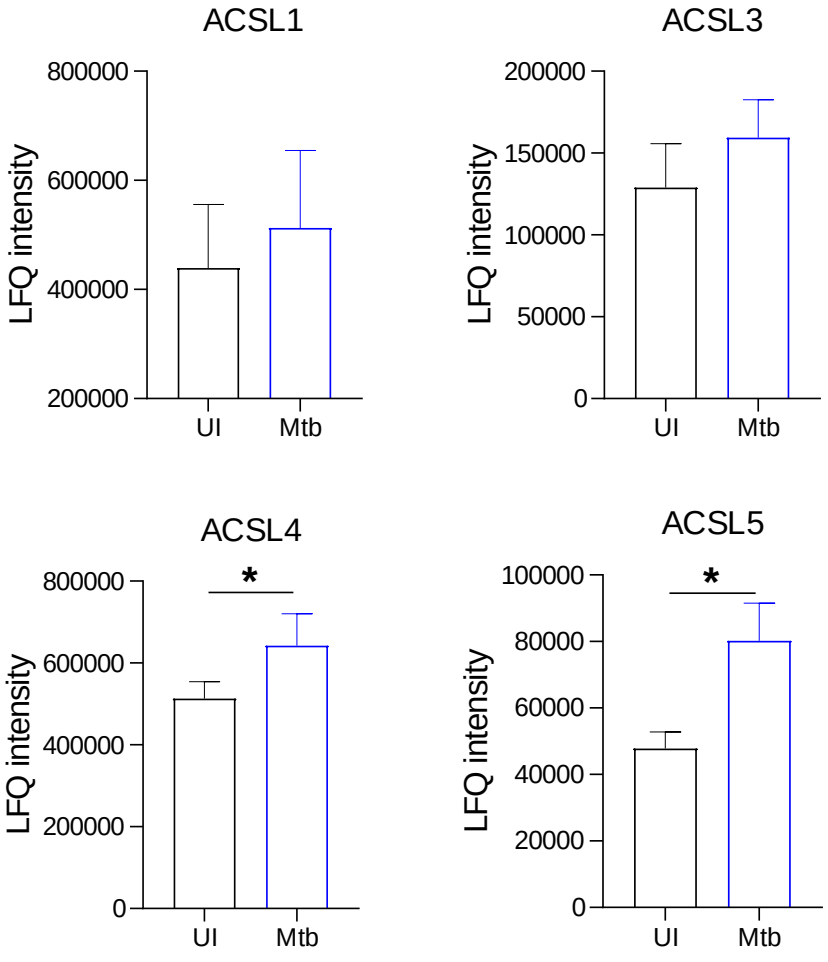

Figure 23: ACSL protein expression is upregulated in Mtb-infected human macrophages.

Human monocyte-derived macrophages were infected with Mtb at an MOI of 0.1 or left untreated (UI) for 7 days. Subsequently, cells were lysed, digested and a liquid chromatography-based approach was used to determine relative protein expression levels (LFQ intensity) of ACSL1, 3, 4, and 5 using label-free proteomics. Statistical analysis was performed using a paired t-test followed by a Benjamini-Hochberg correction (n=5). Depicted is the mean + the standard error. * = $p \leq 0.05$.

As shown in figure 23, the protein expression of ACSL4 and ACSL5 is significantly upregulated by ~37% and ~81%, respectively, in Mtb-infected cells compared to the uninfected control. In line with that, also the relative expression of ACSL1 and ACSL3 is increased by 22% (p=0.07) and 31% (p=0.06) in Mtb-infected hMDMs. However, the difference observed for ACLS1 and ACLS3 does not reach statistical significance due to high donor variability.

In summary, these data show that ACSL protein expression is substantially upregulated in Mtb-infected hMDMs, which supports the observation of increased FAO during Mtb infection. Furthermore, these data also imply increased thioesterification of FFAs to acyl-CoAs due to increased ACSL expression, which might result in reduced levels of FFAs.

4.2.4.3 Infection of human macrophages with Mtb results in decreased FFA levels

Since a significant increase in the expression of FFA metabolizing ACSL proteins, which convert FFA to acyl-CoA, was observed, the FFA levels in uninfected and Mtb-infected human macrophages were next analyzed. To do so gas chromatography followed by mass spectrometry was used to determine total FFA levels and the levels of specific FFA species (ng FFA/µg protein).

As depicted in figure 24, Mtb infection resulted in a dose-dependent reduction of total FFA levels in hMDMs compared to uninfected cells. This reduction reached up to ~41% at an MOI of 0.5, but due to the variability of the four donors tested, this effect did not reach statistical significance yet.

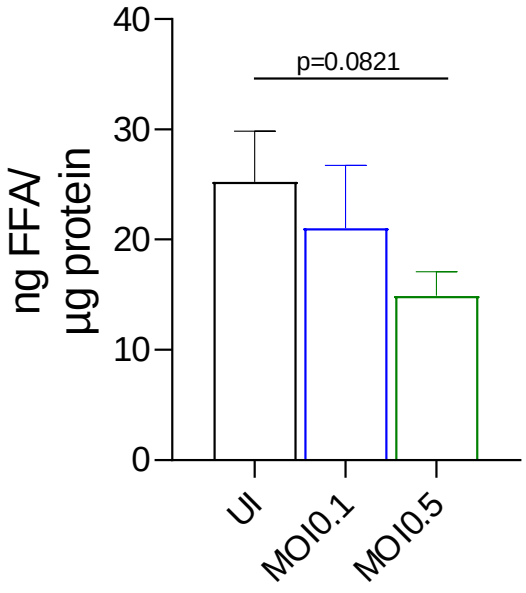

Figure 24: Dose-dependent decrease in total FFA levels upon Mtb infection of hMDMs.

Human monocyte-derived macrophages were infected with Mtb at an MOI of 0.1 and 0.5 or left untreated (UI) for 7 days, subsequently lysed in methanol containing 0.147% BHT and FFA as described before. Subsequently, gas chromatography followed by mass spectrometry was used to quantify the total abundance (ng FFA/µg protein) of FFA. Statistical analysis was performed using one-way ANOVA followed by a Holm-Šídák's test for multiple comparison.

When analyzing the levels of individual FFA species (Fig. 25), a dose-dependent decrease for lauric acid (C12:0), palmitoleic acid (C16:1) and stearic acid (C18:0) upon Mtb infection compared to uninfected cells was observed. Myristic acid (C14:0) levels and palmitic acid (C16:0) levels were significantly reduced upon Mtb infection amounting to a ~70% and a ~51% decrease, respectively, at an MOI of 0.5. Oleic acid (C18:1) is the most prominent FFFA and was substantially reduced in Mtb infected hMDMs compared to the control. However, this effect did not reach statistical significance in the 4 donors tested. No clear effect in response to Mtb infection was observed for linoleic acid (C18:2), eicosenoic acid (C20:1) and arachidonic acid (C20:4) in the four donors tested, indicating no substantial differences in these FFA species (Fig. 25).

In summary, these results indicate that Mtb infection results in a reduction of FFA levels, particularly free myristic acid, palmitic acid and oleic acid levels. This effect could be related to the increased expression of ACSL proteins during Mtb infection.

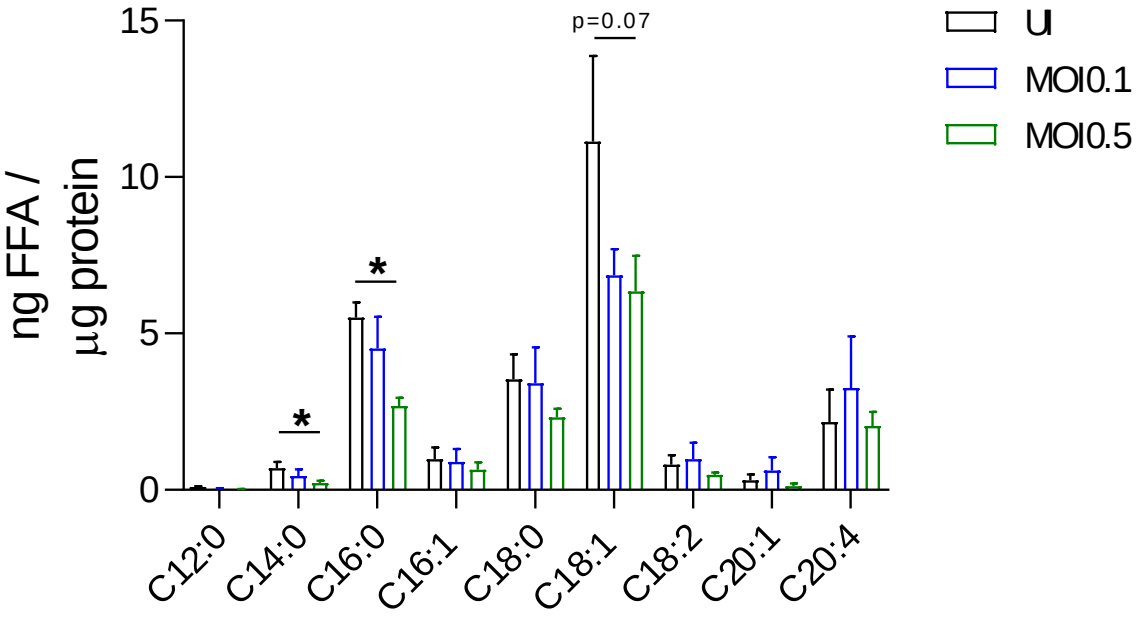

Figure 25: Dose-dependent decrease of several FFA species upon Mtb infection of hMDMs.

Human monocyte-derived macrophages were infected with Mtb at an MOI of 0.1 and 0.5 or left untreated (UI) for 7 days, subsequently lysed in methanol containing 0.147% BHT and FFA as described before. Subsequently, gas chromatography followed by mass spectrometry was used to quantify the total abundance (ng FFA/µg protein) of several FFA species. Statistical analysis was performed using a one-way ANOVA followed by a Holm-Šídák's test for multiple comparison. * = $p \leq 0.05$.

4.2.4.4 Infection of human macrophages with Mtb does not affect cellular neutral lipid levels

Free fatty acids, upon esterification by ACSL, can be degraded in mitochondria or incorporated into neutral lipids such as TAGs. As an Mtb infection-induced decrease in FFA levels and increased ACSL expression was detected, it was next determined if these FFA are incorporated into neutral lipids. To do so mass spectrometry was used to determine the levels of neutral lipids such as TAGs, DAGs and CEs in Mtb-infected and uninfected hMDMs.

Mass spectrometric analyses revealed that Mtb infection of hMDMs for 7 days has no significant effect on total TAG levels (pmol/µg protein) at both MOIs tested compared to uninfected cells (Fig. 26A). In agreement with that, mass spectrometric analysis of 6 additional donors revealed that also total neutral lipid levels, i.e. the sum of DAGs, TAGs and CEs, of uninfected hMDMs were indistinguishable between uninfected and Mtb-infected hMDMs (Suppl. Fig. 4).

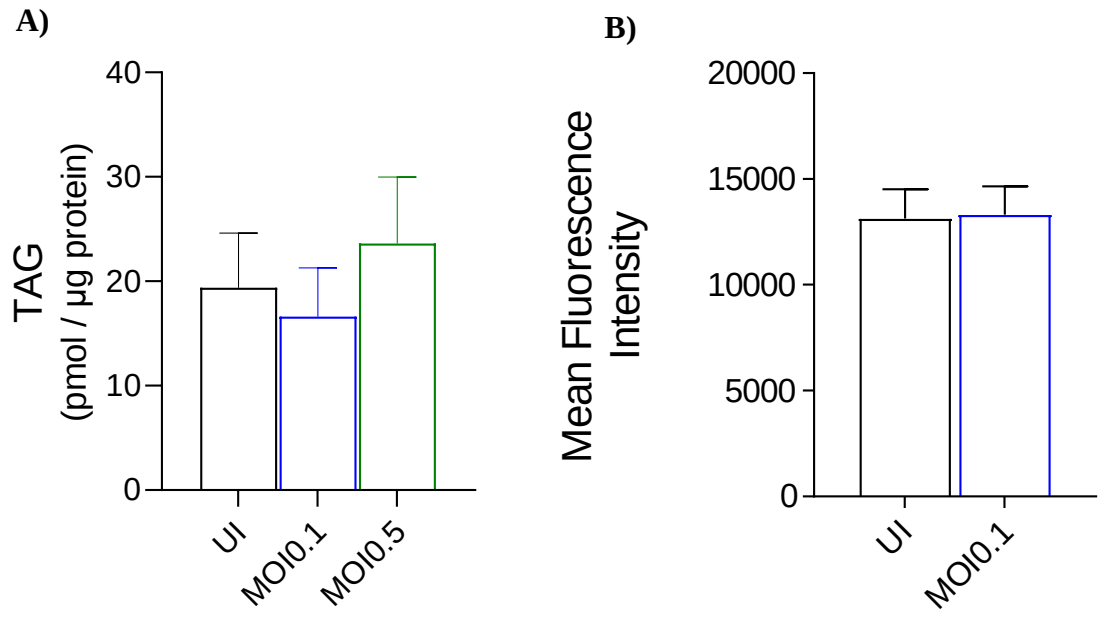

Figure 26: TAG levels and neutral lipid levels in human macrophages upon Mtb infection.

Human monocyte-derived macrophages infected with Mtb at an MOI of 0.1 and 0.5 or left untreated (UI) for 7 days, and **A)** subsequently lysed in methanol containing 0.147% BHT and total lipids were extracted according to the MTBE-method. Subsequently, mass spectrometry was used to quantify the total abundance (pmol/µg protein) of TAG (n=4). **B)** Cells were fixed with 1% PFA for 24 hours and then stained with 1µg/ml BODIPY™493/503 for 15 minutes. Subsequently, the mean fluorescence intensity of cells was measured using flow cytometry Statistical analysis was performed using one-way ANOVA followed by a Holm-Šídák's test for multiple comparison.

To corroborate these mass spectrometric results, uninfected and Mtb-infected hMDMs were stained with the neutral lipid dye BODIPY™493/503 and analyzed by flow cytometry. This revealed that Mtb infection did not affect neutral lipid levels compared to uninfected cells, as shown by similar BODIPY™493/503 mean fluorescence intensity in uninfected and infected cells (Fig. 26B).

Collectively, these data suggest that, while total FFA levels are reduced, neutral lipid levels remain unchanged in Mtb-infected hMDMs compared to the control. Taken together with previous observations this could be explained by increased esterification of FFAs to acyl-CoAs by ACSL and subsequent degradation through FAO.

4.2.4.5 Supplementation of Mtb-infected macrophages with exogenous fatty acid enhances intracellular neutral lipid levels

As described before, Mtb-infection did not result in increased total neutral lipid levels in hMDMs on a whole-cell level. However, the occurrence of lipid-laden, foamy macrophages has been described to promote TB by contributing to a high lipid environment that promotes Mtb growth[22]. As Mtb infection itself did not induce accumulation of neutral lipids in human macrophages (Fig. 26), Mtb-infected hMDMs were supplemented with exogenous fatty acids, such as the saturated palmitic acid and the unsaturated oleic acid and subsequently the effect on neutral lipid levels was analyzed using flow cytometry.

Mtb-infected hMDMs were incubated with increasing concentrations (i.e. 40µM and 200µM) of palmitic acid and oleic acid for 7 days and stained with BODIPY493/503 as described above. As depicted in figure 27, supplementation with palmitic and oleic acid leads to a dose-dependent increase in the BODIPY signal. This increase amounted to approximately 26% and 44% with 40µM and 200µM of palmitic acid, respectively. Interestingly, however, the supplementation of 40µM and 200µM of oleic acid, resulted in a statistically significant increase of approximately 90% and 180%, respectively.

This indicates that Mtb-infected macrophages accumulate neutral lipids when supplemented with exogenous fatty acids and that unsaturated oleic acid is more prominently incorporated into neutral lipids than saturated palmitic acid.

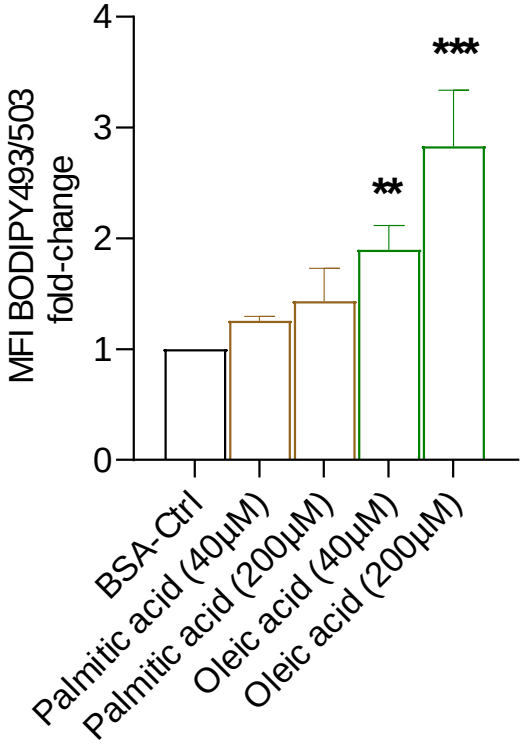

Figure 27: **Supplementation with exogenous fatty acids leads to enhance BODIPY fluorescence in hMDMs.**

Human monocyte-derived macrophages infected with Mtb at an MOI of 0.1 and incubated with either BSA or exogenous palmitic acid and oleic acid at the indicated concentration for 7 days. Cells were fixed with and then stained with BODIPY™493/503. The mean fluorescence intensity was measured using flow cytometry (n=3). Statistical analysis was performed with non-normalized data using one-way ANOVA followed by a Holm-Šídák's test for multiple comparison. Depicted is the fold-change compared to the BSA-Ctrl as mean + the standard error. ** = $p \leq 0.01$; ***= $p \leq 0.001$.

4.2.4.6 Supplementation of Mtb infected cells with exogenous palmitic and oleic acid induces macrophage death

Lipid overload was described to cause cell dysfunction and cell death[99,154]. As the above-described data show that incubation of Mtb-infected hMDMs with exogenous palmitic and oleic acid results in a strong accumulation of intracellular neutral lipid, the effect of exogenous fatty acid supplementation on cell death was analyzed.

To this end, hMDMs were treated with palmitic and oleic acid as described before and cell death was analyzed in uninfected and Mtb-infected cells after 24 hours of infection by measuring the DRAQ7 fluorescence signal[155]. In figure 28 it is shown that in uninfected cells palmitic acid at a concentration of 400µM resulted in a significant increase of DRAQ7 fluorescence counts of approx. 7.7-fold compared to the BSA control. In contrast, oleic acid treatment did not affect DRAQ7 fluorescence in uninfected cells, even at the highest concentration. This suggests, that in uninfected cells only palmitic acid, but not oleic acid, results in increased cell death.

Interestingly, however, in Mtb-infected hMDMs palmitic and oleic acid had similar effects. Given the earlier time point of measurement (24h), a higher infectious dose, e.g. an MOI of 1,

was chosen for this set of experiments. This analysis revealed that palmitic acid induces a statistically significant increase of 5.9-fold in DRAQ7 fluorescence at a concentration of 400µM compared to BSA control in Mtb-infected hMDMs. Similar to palmitic acid, also oleic acid resulted in increased DRAQ7 fluorescence counts in Mtb-infected hMDMs. This oleic acid-induced increase reached up to 8.3-fold at a concentration of 400µM compared to the BSA control (Fig. 28). This suggests, that both, palmitic and oleic acid treatment, induces cells death in Mtb-infected hMDMs already after 24h of treatment. Importantly, Mtb infection alone resulted in a 2.1-fold increase compared to uninfected cells upon in BSA control treatment. However, this increase did not reach statistical significance.

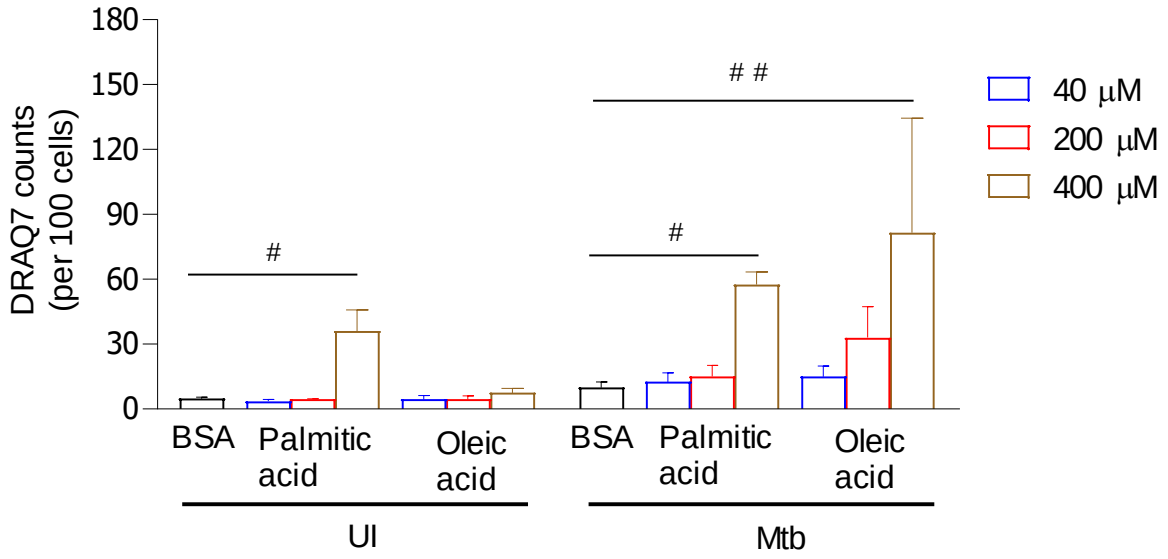

Figure 28: DRAQ7 fluorescence is increased upon supplementation with exogenous fatty acids in Mtb-infected hMDMs.

Human monocyte-derived macrophages infected with Mtb at an MOI of 1 and incubated with either BSA or exogenous palmitic acid and oleic acid at the indicated concentration for 24 hours. Cells were stained with 3µM DRAQ7 and DRAQ7 fluorescence counts and cell count was measured on a Cytation 1 plate reader. Statistical analysis was performed using one-way ANOVA followed by a Holm-Šídák's test for multiple comparison (n=3). Depicted is the mean + the standard error. # = $p \leq 0.05$; ## = $p \leq 0.001$. PA= palmitic acid; OA= oleic acid.

Collectively, these data suggest that Mtb infection in a lipid-rich environment is associated with enhanced levels of cell death. Furthermore, it was observed that treatment with exogenous palmitic acids promotes cell death in Mtb-infected as well as uninfected cells. In contrast, supplementation with exogenous oleic acid requires infection with Mtb to induce cell death in hMDMs at the time points and concentrations tested.

4.2.4.7 Supplementation with exogenous palmitic and oleic acid promotes Mtb growth in primary human macrophages

Mtb infection was described to induce necrotic cell death in macrophages to promote dissemination and growth[156]. As described above, supplementation with exogenous fatty acids leads to an accumulation of neutral lipids and induces cell death in Mtb-infected human macrophages. Therefore, it was next analyzed how exogenous fatty acid supplementation affects Mtb growth in hMDMs *in vitro*. To this end, Mtb-infected hMDMs were incubated with palmitic acid and oleic acid for 7 days and CFU were determined. Incubation with palmitic acid resulted in a significant increase in CFU of 69% at a concentration of 40µM compared to the BSA control. Similarly, also oleic acid supplementation significantly induced Mtb growth as reflected by a 45% increase in CFU compared to the BSA control (Fig. 29). Collectively, these data suggest that fatty acid supplementation of hMDMs leading to increased neutral lipid levels and cell death promotes Mtb growth *in vitro*.

Collectively, these data indicate that supplementation of Mtb-infected hMDMs with exogenous fatty acids resulted in increased accumulation of neutral lipids, which coincides with increased Mtb growth and cell death.

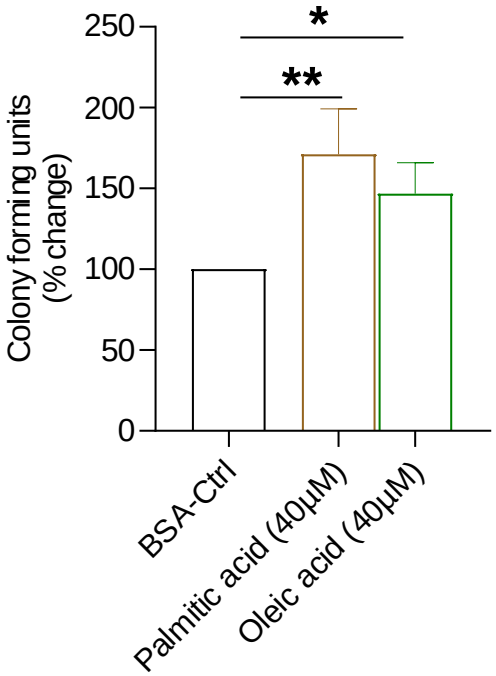

Figure 29: Mtb growth is increased upon supplementation with exogenous fatty acids.

Human monocyte-derived macrophages infected with Mtb at an MOI of 0.1 and incubated with either BSA or exogenous palmitic acid and oleic acid at the indicated concentration for 7 days. Cells were lysed in water, plated in 7H9 agar plates and incubated for 3 weeks. Colonies were counted and colony forming units determined (n=7) and normalized to the protein concentration. Statistical analysis was performed with non-normalized data using one-way ANOVA followed by a Holm-Šídák's test for multiple comparison. Results were normalized to the BSA-Control and depicted as the mean + the standard error. * = $p \leq 0.05$; ** = $p \leq 0.01$.

4.3 Isolation of lipid droplets from primary human macrophages

The above-described results indicate that neutral lipids play a crucial role during Mtb infection as excess lipids lead to increased macrophage cell death and Mtb growth. Since in the present study neutral lipid levels remained unchanged on a whole-cell level, compartmentation of neutral lipids, particularly in LDs, was analyzed next. To do so LDs were isolated from a whole cell lysate (WCL) and separated from other cellular compartments such as mitochondria and the ER as described in section 3.2.8. Western blot analysis was then used to determine the protein expression of several organelle-specific markers proteins in the WCL, the lipid droplet-enriched fraction (LDF), the mitochondrial fraction (MF) and the ER fraction (ERF). Subsequently, lipidomics and proteomics were performed to determine the lipidome and proteome of the LDF in uninfected and Mtb-infected hMDMs.

4.3.1 Characterization of organelle fractions isolated from primary human macrophages

4.3.1.1 The lipid droplet-enriched fraction shows low protein expression levels of calreticulin and manganese-dependent superoxide dismutase

Firstly, the protein expression of distinct marker proteins, which are localized to mitochondria, the ER and LDs, respectively, was analyzed in the WCL, LDF, MF and ERF to address the purity of each fraction. To do so, WB analyses using antibodies against distinct marker proteins were performed and protein expression was quantified using a chemiluminescence detection approach.

The manganese-dependent superoxide dismutase (MnSOD) is a mitochondrial protein localized in the mitochondrial matrix, where it is required for the removal of mitochondrially generated superoxide[139]. Supplementary figure 5 shows that a distinct signal was observed in the WCL and MF when using an antibody-directed against MnSOD (~20 kDa) in contrast to the ERF and LDF, where no band was detected. Quantification of the relative signal intensity per µg protein revealed a mean signal intensity of ~6.4 in the MF, which was significantly higher compared to WCL with a mean signal intensity of ~1.3 (Fig. 30). In contrast, the relative signal intensity in LDF and ERF was below 1, which indicates a low presence of the mitochondrial protein MnSOD in the LDF and ERF compared to the WCL or MF.

Calreticulin (CAL) is a protein localized in the ER involved in Ca^{2+} storage, cell adhesion, phagocytosis and nuclear export[157]. Chemiluminescent detection of a specific antibody directed against CAL (~60 kDa) resulted revealed a prominent signal in the WCL and

ERF, but also a weaker signal in the MF (Suppl. Fig. 5). Quantification of the CAL signal intensity/µg protein showed the highest intensity of ~54 in the ERF, which is significantly higher compared to the WCL and the LDF (Fig. 30). Similarly, also in the MF the relative signal intensity of CAL was substantially lower compared to the ERF, suggesting an enhanced presence of the ER protein CAL in the ERF compared to a lower abundance in the WCL, LDF and MF.

Alpha tubulin (α-TUB) with the other tubulin isoforms assembles into heterodimers thereby forming microtubules[158]. It is often used as a cytoplasmic or cytoskeletal marker[159]. Supplementary figure 5 demonstrates a substantial chemiluminescence signal when using an antibody directed against α-TUB (~50 kDa) in the WCL and LDF, while no or only a signal is observed in the MDF and ERF, respectively. In line with this, the highest α-TUB intensity was observed in the LDF followed by the WCL amounting to 9.4 and 4.0, respectively. While in the WCL the signal was substantially lower compared to the LDF, this difference did not reach statistical significance due to high variation between the experiments (Fig. 30). Compared to the LDF, a significantly lower (~90%) α-TUB signal intensity was detected in the ERF and MF, indicating that the ERF and MF contain low levels of this cytoskeletal protein, while it is highly present in the WCL and LDF.

The protein perilipin 3 (PLIN3) is described to attach to the membrane of LDs and plays a crucial role in LD biogenesis and stabilization, prostaglandin production and intracellular trafficking[160,161]. As depicted in supplementary figure 5, signals were observed in the WCL and LDF when using an antibody directed against PLIN3 (~47 kDa). Quantification of the relative intensities per µg protein revealed a strong PLIN3 signal in the WCL of ~11. In the LDF the PLIN3 signal was substantially higher by ~68%, but due to strong variations between the independent experiments, this increase is not statistically significant (Fig. 30). In the ERF and MF, a significantly reduced PLIN3 intensity was observed compared to the WCL, which collectively indicates that LD-coating protein PLIN3 is enriched in the LDF compared to the other fractions analyzed.

Collectively, these results indicate that the LDF shows a low presence of mitochondrial and ER proteins, as determined by a low intensity of MnSOD and CAL. In line with that, enrichment of the LD protein PLIN3 was observed in the LDF, which indicates a strong accumulation of LDs in the LDF isolated from hMDMs.

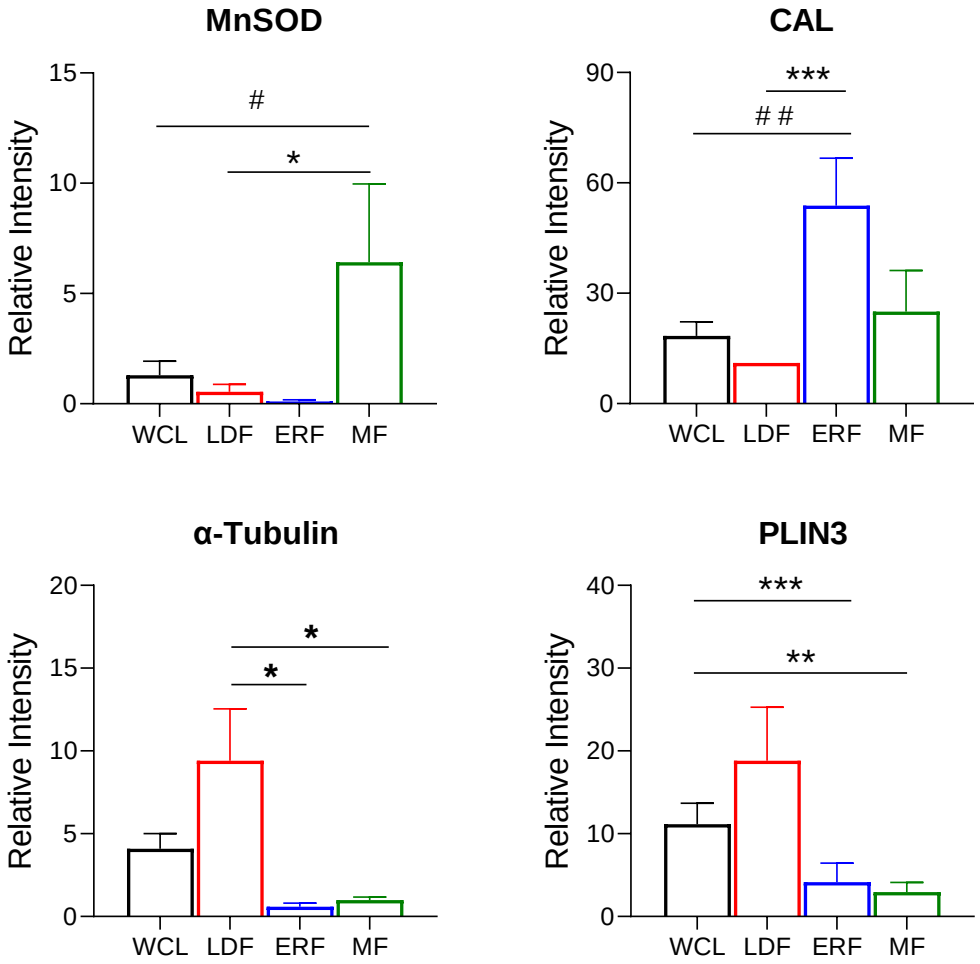

Figure 30: MnSOD, CAL, α-TUB and PLIN3 expression levels in the WCL, LDF, ERF, MF isolated from primary human macrophages.

Human monocyte-derived macrophages were incubated for 7 days, lysed and subsequently, the MF, ERF and LDF were isolated from the WCL as described in section 3.2.8. SDS lysis buffer was added to each fraction and SDS-PAGE followed by a Western Blot analysis was performed. Antibodies against MnSOD, CAL, α-TUB and PLIN3 were used to measure the protein expression using a chemiluminescence detection approach on the Chemidoc Imaging System (Bio-Rad). The relative intensities of protein bands (per µg protein) compared to the background were quantified using the Image Lab Software. Statistical analysis was performed using one-way ANOVA followed by a Holm-Šídák's test for multiple comparison. For comparison with the LDF * = $p \leq 0.05$; ** = $p \leq 0.01$; ***= $p \leq 0.001$; For comparison to the WCL # = $p \leq 0.05$; ## = $p \leq 0.01$;

4.3.1.2 Relative distribution of several lipid classes in the WCL, MF, ERF and LDF isolated from human macrophages

As described before, WB analysis indicated a strong expression of the LD marker PLIN3 in the LDF, while the mitochondrial and ER marker MnSOD and CAL, respectively, were present at a low level. To further characterize the LDF, lipidomic analysis was performed to analyze the lipid composition of each fraction and determine the relative abundance of lipids.

Depicted in figure 31 is the relative abundance (in Mol%) of lipid classes detected in the WCL, LDF, ERF and the MF of uninfected hMDMs. The most abundant lipids accounting for ~98% of total lipids were phosphatidylcholines (PCs), TAGs, cholesterol, sphingomyelins (SMs), phosphatidylethanols (PEs), phosphatidylinositols (PIs), phosphatidylserines (PSs) and DAGs. As shown in this figure, the relative abundances of these lipids strongly vary between the LDF and the WCL, ERF and MF. While the most abundant lipid in the WCL, the ERF and the MF are PCs with ~41%, 42% and 37%, respectively, the most abundant lipid in the LDF are TAGs, which account for ~40% of all lipids. In contrast, TAGs account for a substantially lower amount of only ~8% in the WCL. Similar to PCs, the Mol% of other lipids such as cholesterols, SMs, PEs, PIs, PSs and LPCs is substantially smaller in the LDF compared to the WCL, the ERF and the MF. Contrary to that, the relative abundance of the DAGs is higher in the LDF accounting for 4.5% compared to the other three fractions, where DAGs only accounted for up to 1% of all lipids detected (Fig. 31).

Taken together, the data indicate that there is an increased relative abundance of the neutral lipids TAGs and DAGs and a decreased abundance of membrane lipids in the LDF compared to WCL, the ERF and the MF. In agreement with results from the Western Blot analysis, this indicates that the LDF indeed shows a high enrichment of LDs, as indicated by high levels of neutral lipids versus membrane lipids and enrichment of the LD-associated protein PLIN3.

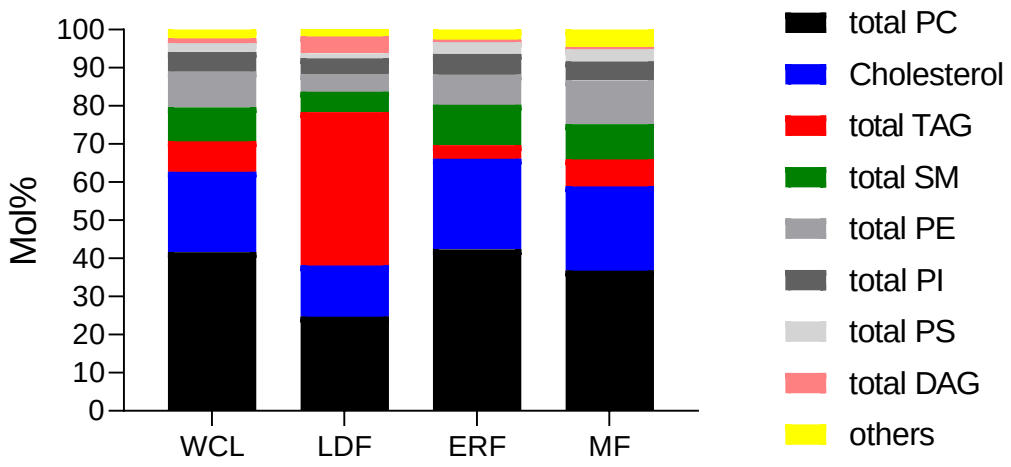

Figure 31: Relative distribution of lipid classes in the WCL, LDF, ERF and MF isolated from primary human macrophages.

Human monocyte-derived macrophages were incubated for 7 days, lysed and subsequently, the MF, ERF and LDF were isolated from the WCL as described in section 3.2.8. The MF was pelleted from the WCL by centrifugation for 20 minutes at 10,200 x g. The supernatant was removed and centrifuged for 3 hours at 25,000 x g to separate the ERF (pellet) and LDF, which are floating on top. Methanol was added to the fractions and total lipids were extracted according to the MTBE-method. Subsequently, mass spectrometry was used to quantify lipid classes in each fraction and the Mol% of each lipid class was calculated. Others= sum of LPC, LPE, CL, CE, Cer, PG, PA

4.3.1.3 Neutral lipid levels are significantly increased while other lipid classes are decreased in the LDF isolated from human macrophages compared to the other fractions

According to figure 31, it was determined, that the lipid composition in the LDF differs from that of the WCL, the ERF and the MF. To further investigate the purity of the LDF compared to other fractions, the absolute lipid concentration (pmol/µg protein) of selected lipids in the LDF was quantified and compared to the other fractions.

As demonstrated in figure 32, the total TAG levels in the LDF were the highest of all fractions (~540 pmol/µg protein), and with that significantly higher in the LDF compared to the WCL, the ERF and the MF. The concentration of total DAGs in the LDF was with 70 pmol/µg protein substantially lower compared to the TAG levels, indicating that the main neutral lipid species in LDs of hMDMs are TAGs. However, also the DAG levels were significantly increased in the LDF compared to the WCL, the ERF and MF, while no substantial difference was detected between the WCL and the ERF and MF (Fig. 32). The third class of neutral lipids detected in the LDF detected, CEs, showed the lowest concentration in the LDF with on average ~6 pmol/µg protein. In line with TAGs and DAGs, also the total CEs levels were significantly

increased in the LDF compared to the WCL and MF. CEs were also substantially lower in the ERF compared to the LDF however, this did not reach statistical significance (p=0.057) (Fig. 32). This indicates, that neutral lipids are significantly enriched in the LDF compared to the other fractions.

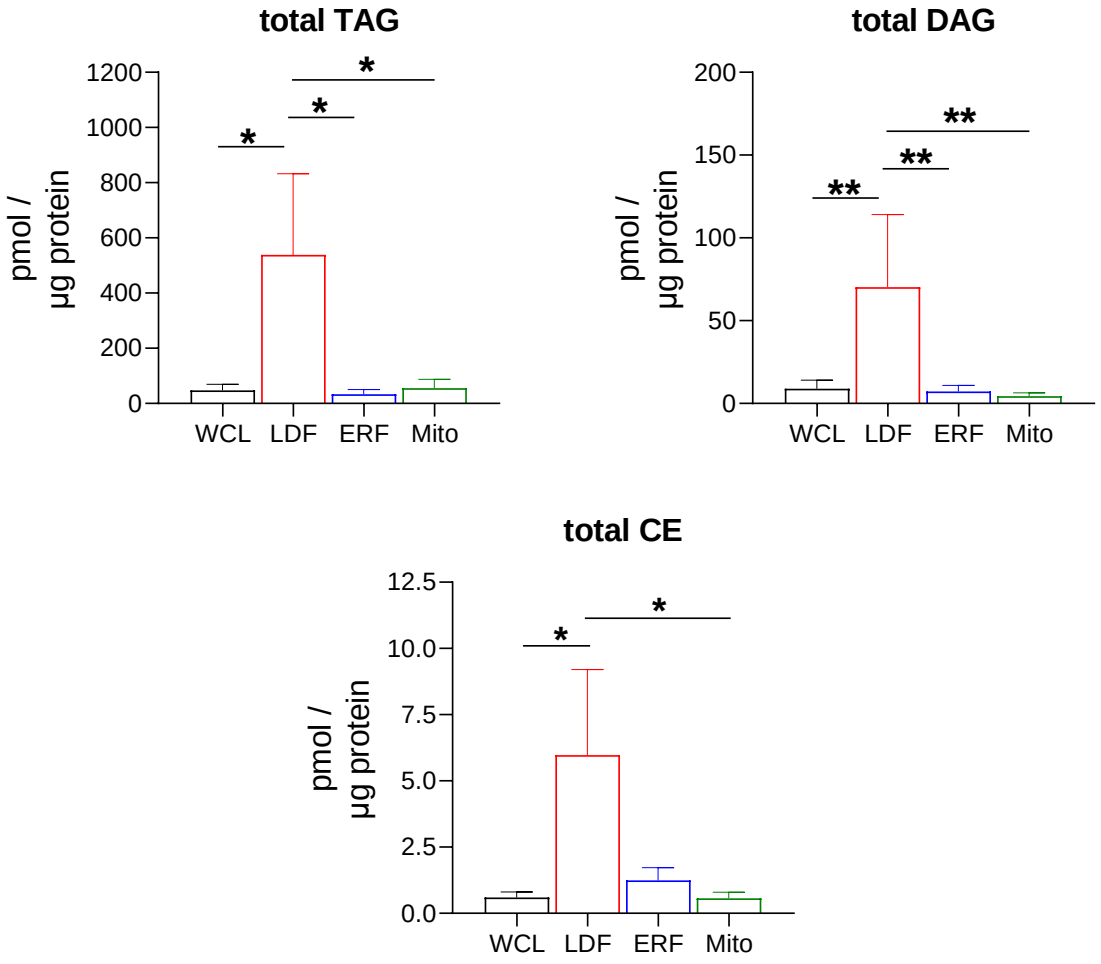

Figure 32: Total abundance of the neutral lipids TAG, DAG and CE in the WCL, LDF, ERF and MF isolated from primary human macrophages.

Human monocyte-derived macrophages were incubated for 7 days, lysed and subsequently, the MF, ERF and LDF were isolated from the WCL as described in section 3.2.8. The MF was pelleted from the WCL by centrifugation for 20 minutes at 10,200 x g. The supernatant was removed and centrifuged for 3 hours at 25,000 x g to separate the ERF (pellet) and LDF, which were floating on top. Methanol was added to the fractions and total lipids were extracted according to the MTBE-method. Subsequently, mass spectrometry was used to quantify the total abundance (pmol/µg protein) of TAG, DAG and CE in the WCL, LDF, ERF and MF and normalized to the protein content as determined using a BCA-test. Statistical analysis was performed using one-way ANOVA followed by a Holm-Šídák's test for multiple comparison. * = $p \leq 0.05$; ** = $p \leq 0.01$.

Cardiolipin (CL) and phosphatidylglycerol (PG) are two lipids synthesized in mitochondria and are described to be predominantly found in mitochondria[162]. Lipidomics analysis revealed that the CL showed the highest concentration in the MF, where it is significantly increased compared to the WCL (Fig. 33). Importantly, the lowest levels of total CL were found in the LDF, where it was only detected in 1 out of 6 donors, resulting in a significantly lower CL level in the LDF compared to the other three fractions. Similarly, the PG was strongly enriched in the MF compared to the WCL, the LDF and the ERF, reaching statistical significance when compared to the WCL and LDF (Fig. 33). These results suggest, that CL and PG are indeed accumulating in the MF in comparison to the LDF and ERF corresponding to previous results[162]. The observation that the LDF contains only little amounts of PG and CL, indicates that there is little contamination of the LDF by mitochondrial components.

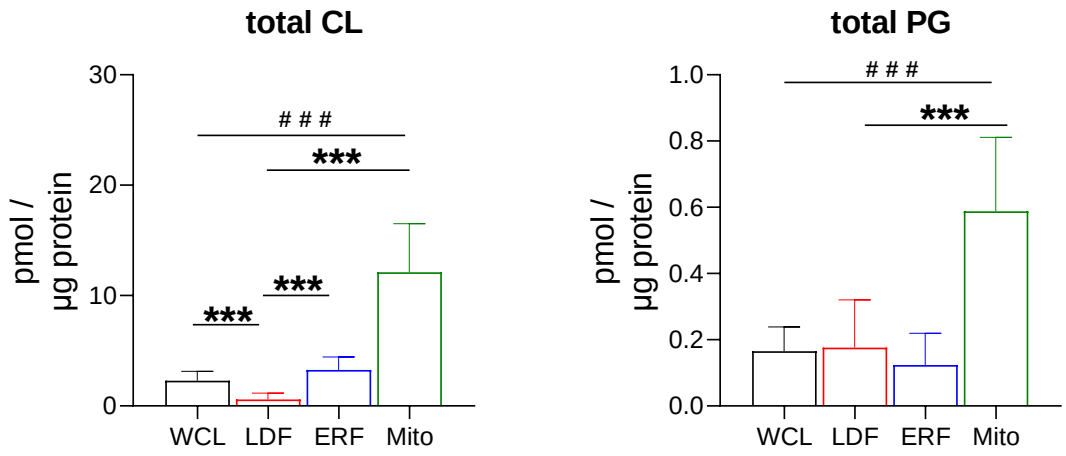

Figure 33: Total abundance of the mitochondrial lipids CL and PG in the WCL, LDF, ERF and MF isolated from primary human macrophages.

Human monocyte-derived macrophages were incubated for 7 days, lysed and subsequently, the MF, ERF and LDF were isolated from the WCL as described in section 3.2.8. The MF was pelleted from the WCL by centrifugation for 20 minutes at 10,200 x g. The supernatant was removed and centrifuged for 3 hours at 25,000 x g to separate the ERF (pellet) and LDF, which were floating on top. Methanol was added to the fractions and total lipids were extracted according to the MTBE-method. Subsequently, mass spectrometry was used to quantify the total abundance (pmol/µg protein) of CL and PG in the WCL, LDF, ERF and MF and normalized to the protein content as determined using a BCA-test. Statistical analysis was performed using one-way ANOVA followed by a Holm-Šídák's test for multiple comparison. For comparison to the LDF ***= $p \leq 0.001$; For comparison to the WCL ### = $p \leq 0.001$.

Lipids belonging to the class of PCs were the most abundant membrane lipids in all fractions (Fig. 34). However, significant differences in the total PC levels were observed between fractions, as demonstrated by significantly lower PC levels in the LDF compared to the WCL, ERF and MF. Furthermore, on average total PC levels were ~85% higher in the ERF compared to the WCL (Fig. 34), indicating that the ERF is a membrane-rich fraction. Lastly, also cholesterol levels were significantly reduced in the LDF in comparison to the ERF and MF amounting to a reduction of ~50% and ~22%, respectively. Similar to PCs, also cholesterol was most prominently found in the ERF. No substantial difference was detected in the cholesterol levels between WCL and LDF (Fig. 34). This analysis of selected membrane lipids indicates that the membrane lipid composition varies between the WCL, ERF, the MF and the LDF. It indicates high membrane content in the ERF compared to the LDF, where these lipids were detected at a lower level compared to the other fractions.

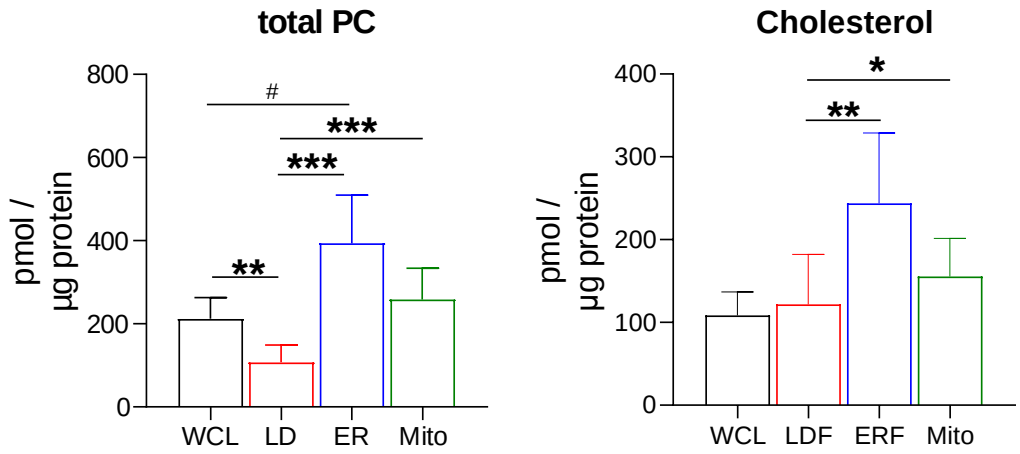

Figure 34: Total abundance of the neutral lipids TAG, DAG and CE in the WCL, LDF, ERF and MF isolated from primary human macrophages.

Human monocyte-derived macrophages were incubated for 7 days, lysed and subsequently, the MF, ERF and LDF were isolated from the WCL as described in section 3.2.8. The MF was pelleted from the WCL by centrifugation for 20 minutes at 10,200 x g. The supernatant was removed and centrifuged for 3 hours at 25,000 x g to separate the ERF (pellet) and LDF, which are floating on top. Methanol was added to the fractions and total lipids were extracted according to the MTBE-method. Subsequently, mass spectrometry was used to quantify the total abundance (pmol/µg protein) of TAG, DAG and CE in the WCL, LDF, ERF and MF and normalized to the protein content as determined using a BCA-test. Statistical analysis was performed using one-way ANOVA followed by a Holm-Šídák's test for multiple comparison. For comparison to the LDF * = $p \leq 0.05$; ** = $p \leq 0.01$; ***= $p \leq 0.001$; For comparison to the WCL # = $p \leq 0.05$.

In summary, the analyses of the lipidome of the LDF, ERF and MF suggest that the lipid composition differs significantly between each subcellular fraction with neutral lipids, mitochondrial lipids and membrane lipids being enriched in the LDF, the MF and the ERF, respectively. Furthermore, it might further support the enrichment of LDs in the LDF as high levels of neutral lipids and low levels of mitochondrial and membrane lipids were detected in the LDF.

4.3.2 Characterization of the lipid droplet-enriched fraction from uninfected and Mtb-infection primary human macrophages

4.3.2.1 Lipidomic analysis of neutral lipids in lipid droplets isolated from uninfected and Mtb-infected human macrophages

The above-described results suggest that the bulk of neutral lipids is stored in LDs (Fig. 33)[110]. Since Mtb infection had no effect on neutral lipid levels on a whole-cell level in hMDMs *in vitro*, it was hypothesized that changes in the neutral lipid levels might be specific to LDs. To investigate this, the neutral lipid composition of the LDF in uninfected hMDMs and hMDMs-infected with Mtb was analyzed.

4.3.2.1.1 Triacylglycerols levels are increased in lipid droplets isolated from Mtb-infected macrophages

As described above, TAGs are the major neutral lipid species detected in LDF isolated from hMDMs However, it is unclear how total TAG levels and individual TAG species in LDs are affected by Mtb infection.

As demonstrated in figure 35A, total TAG levels in LDFs isolated from hMDMs vary strongly between all donors tested (n=6), reaching from a minimum of ~2 pmol/µg protein to up to ~1460 pmol/µg protein in uninfected cells. Nevertheless, in 5 out of 6 donors, total TAG levels of LDFs isolated from Mtb-infected cells were increased by on average ~2.6-fold compared to uninfected control. Interestingly, the increase in TAG levels upon Mtb infection was strongest in donors 1 and 4, which showed the lowest total TAG levels in the uninfected LDF. However, in contrast to the other donors, donor 5 showed a decrease in total TAG levels upon Mtb infection compared to uninfected cells. When all six donors are taken together, total TAG levels in the LDF isolated hMDMs-infected with Mtb were induced by ~2.3-fold. However, this did not reach statistical significance yet (p=0.11).

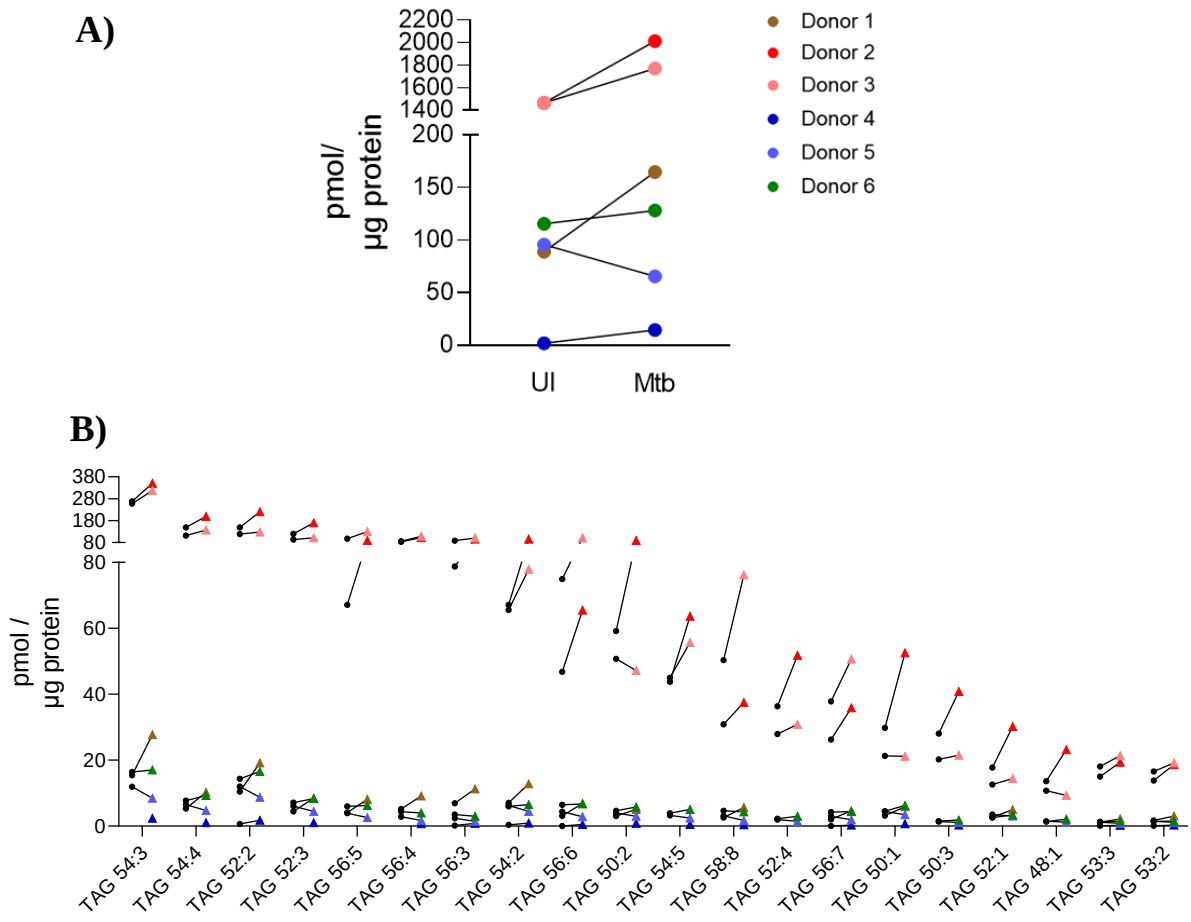

Figure 35: TAG levels are substantially increased in Mtb-infected human macrophages.

Human monocyte-derived macrophages infected with Mtb at an MOI of 0.1 or left untreated for 7 days, lysed and the LDF were isolated from the WCL as described in section 3.2.8. Methanol was added to the LDF and total lipids were extracted. Subsequently, mass spectrometry was used to quantify the total TAG levels (pmol/µg protein) **(A)** and the individual TAG species **(B)**. Uninfected (black circles) and Mtb infected samples (colored triangle) of one donor a connected with a line. Statistical analysis was performed using a paired t-test followed by a multiple testing correction using the false discovery rate.

Next, the effect of Mtb infection on individual TAG species in the LDF was analyzed. Similar to the total TAG levels, also the levels of individual TAG species vary strongly between donors. Mtb infection, on average, induced an increase in almost all TAG species compared to the uninfected control, however, this effect did not reach statistical significance due to donor variability. While donors 1-4 showed a consistent increase for almost all TAG species upon Mtb infection, several TAG species in donor 5 were substantially decreased upon Mtb infection compared to the uninfected control (Fig. 35B).

Collectively, these data indicate that Mtb infection resulted in an increase of TAG concentration in LDF isolated from human macrophages. However, this observation was not consistently observed in all 6 donors tested indicating that donors respond differently to Mtb infection. This variation in donors was further highlighted by a substantial difference in TAG levels in LDFs isolated from uninfected hMDMs, with donors having the lowest initial levels showing the strongest fold increase in total TAG levels upon infection.

4.3.2.1.2 Distinct diacylglycerol species are increased in lipid droplets isolated from Mtb-infected macrophages

DAGs are important neutral lipids, which are not only acting as storage lipids but are also key second messengers involved in activation, proliferation, migration and effector functions of innate immune cells[163].

In the LDF from Mtb-infected and uninfected hMDMs, no significant difference was observed in the total DAG levels (Fig. 36A). While 4 donors showed a moderate increase of 1.2 to 2-fold in total DAGs upon Mtb infection, no increase was observed in donors 2 and 6. Similar to what was observed for TAGs, also the levels of total DAGs showed a strong variation between the LDFs from all 6 donors tested.

Similarly, when analyzing the levels of individual DAG species, no significant differences in the were detected. However, for DAG 18:1_18:2, DAG 16:1_18:1 and DAG 16:0_18:2 a substantial increase was observed in the LDFs from Mtb-infected hMDMs compared to the uninfected control in all donors tested (p-value prior to multiple testing correction of ≤ 0.05) This might indicate, that only DAGs with specific acyl-CoA chain composition containing either a 16:1 or 18:2 fatty acid, are affected during Mtb infection. For the other DAG species detected in LDF, no uniform, Mtb-induced trend was observed in all donors tested (Fig. 36B).

In summary, these lipidomic data indicate that the LDF isolated from Mtb-infected hMDMs showed an increased enrichment of distinct DAG species. Interestingly, all DAG species containing a palmitoleic acid or linoleic acid side chain were substantially increased upon Mtb infection, which might imply that the incorporation of specific fatty acids into DAGs is promoted during Mtb infection.

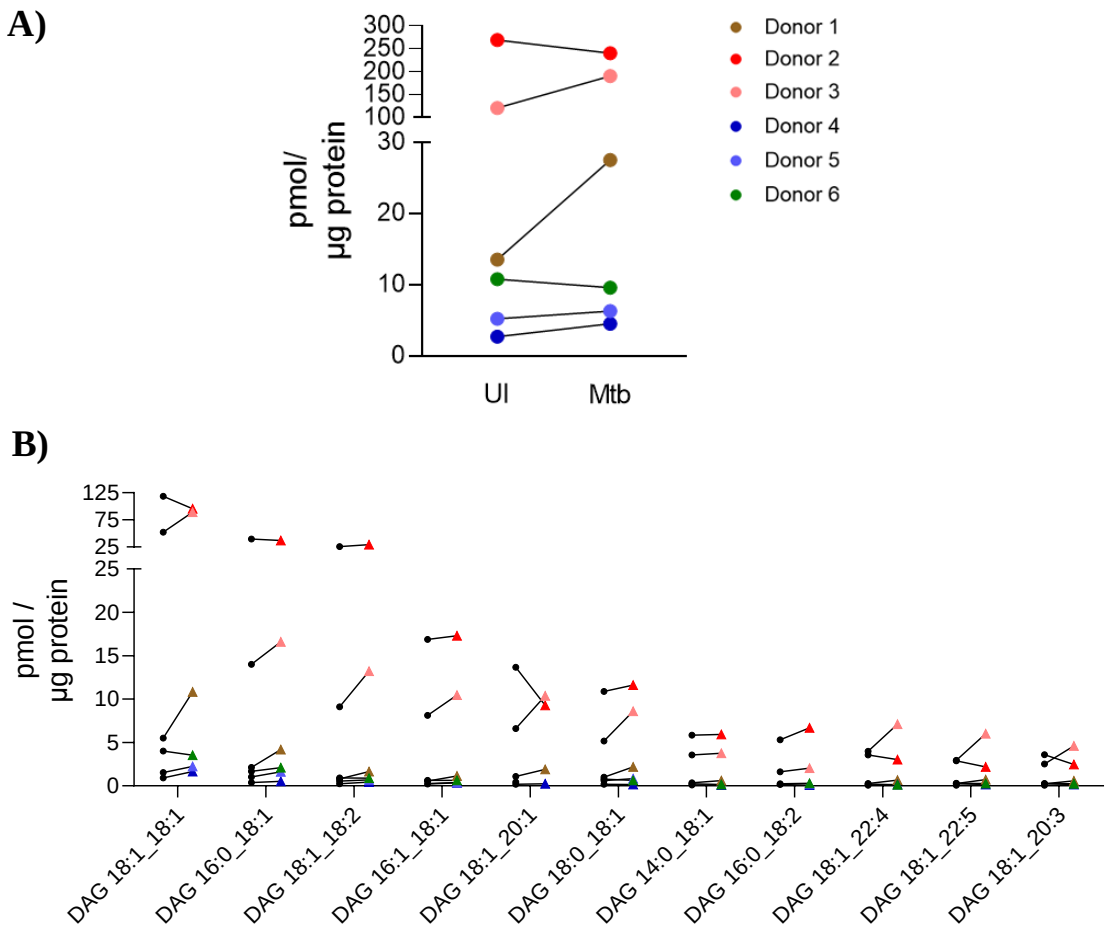

Figure 36: Several DAG species are significantly increased in Mtb-infected human macrophages.

Human monocyte-derived macrophages infected with Mtb at an MOI of 0.1 or left untreated for 7 days, lysed and the LDF were isolated from the WCL as described in the section 3.2.8. Methanol was added to the LDF and total lipids were extracted. Subsequently, mass spectrometry was used to quantify the total DAG levels (pmol/µg protein) **(A)** and the individual DAG species **(B)**. Uninfected (black circles) and Mtb infected samples (colored triangle) of one donor a connected with a line. Statistical analysis was performed using a paired t-test followed by a multiple testing correction using the false discovery rate.

4.3.2.1.3 Cholesterol esters are significantly increased upon Mtb infection in the lipid droplet-enriched fraction isolated from human macrophages

Aside from TAGs and DAGs, the effect of Mtb infection on total CEs as well as individual CEs was determined using mass spectrometry. Figure 37A shows the total CE levels in the LDF from uninfected and Mtb-infected human macrophages. Similar to the TAGs and DAGs, the CE levels vary strongly between all 6 donors ranging from approximately 0.1 and 20 pmol/µg protein in LDF from uninfected cells. However, upon Mtb infection, a substantial increase of ~3.6-fold was observed compared to the uninfected control. Similar to TAG levels, the Mtb-induced increase in total CE levels was strongest in donor 1, which showed the lowest basal CE levels under uninfected control conditions. Importantly, while LDFs of five donors showed an increase upon Mtb infection, no substantial changes in total CE levels were detected in donor 2.

Investigating the CE levels of individual CE species in LDFs from uninfected and Mtb-infected hMDMs revealed a substantial increase in all CEs detected. On average the increase was strongest for CE20:4, where it amounted to a ~2.8-fold increase, while for the other three CE species it reached between ~1.5 and ~2.2-fold increase in Mtb-infected LDFs compared to the uninfected control. Interestingly, only CE species attached to acyl-CoA chains with a high chain length, i.e. > 20 carbon atoms, and a high degree of desaturation, i.e. > 3 double bonds were uniformly detected in the LDFs of hMDMs, indicating these CE species are more prominently incorporated and stored in LDs compared to other CE species (Fig. 37B).

Collectively, these data indicate that Mtb infection results in a substantially increased accumulation of total CEs in the LDFs of human macrophages, affecting all CE species detected. This might imply that fatty acids are more strongly incorporated into CEs during Mtb infection, indicating that in human macrophages Mtb infection interferes with the metabolism of cholesterol, which has important structural and signaling functions in macrophages.

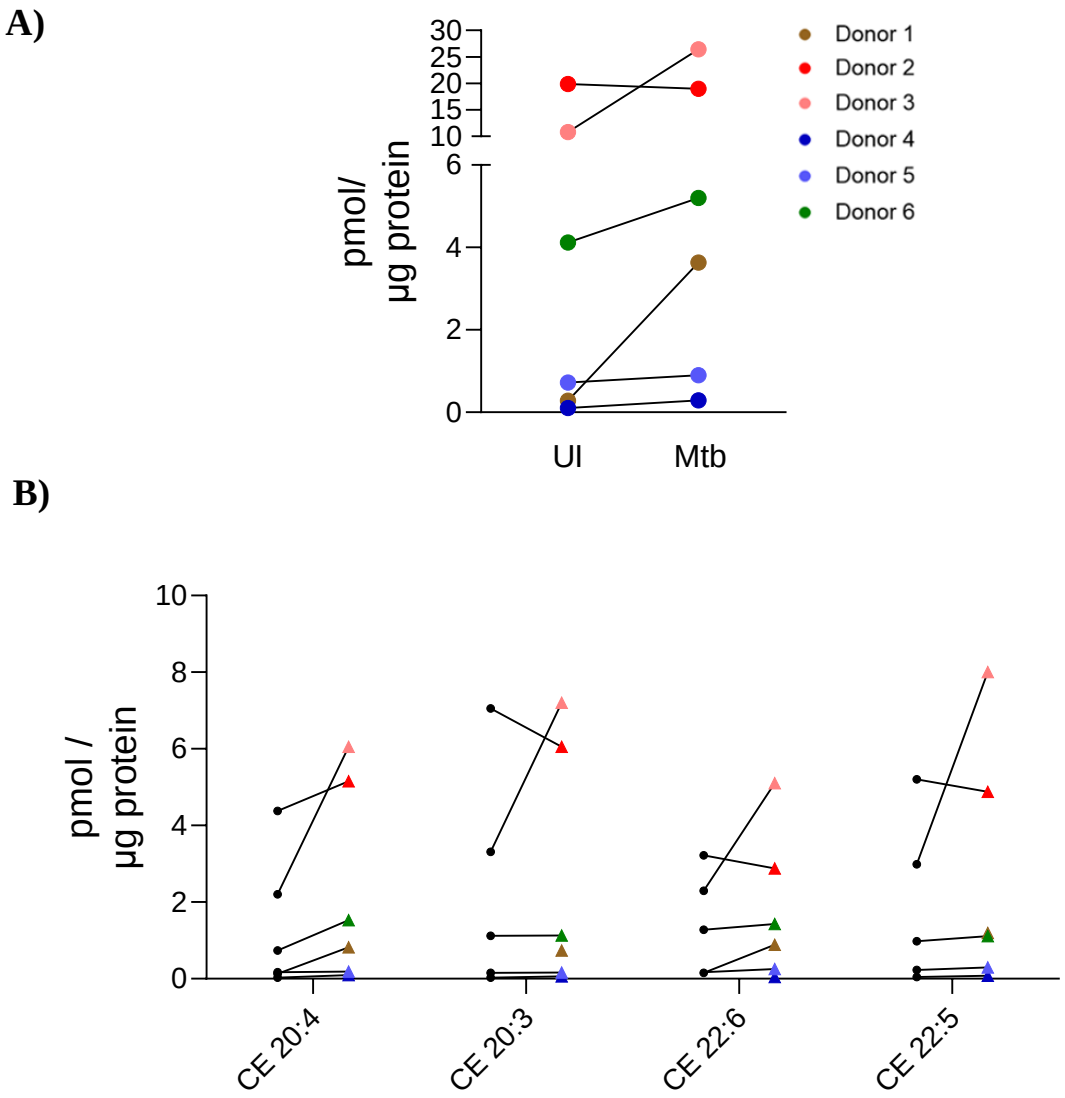

Figure 37: CE levels are significantly increased in Mtb-infected human macrophages.

Human monocyte-derived macrophages infected with Mtb at an MOI of 0.1 or left untreated for 7 days, lysed and the LDF were isolated from the WCL as described in section 3.2.8. Methanol was added to the LDF and total lipids were extracted. Subsequently, mass spectrometry was used to quantify the total CE levels (pmol/µg protein) **(A)** and the individual CE species **(B)**. Uninfected (black circles) and Mtb infected samples (colored triangle) of one donor a connected with a line. Statistical analysis was performed using a paired t-test followed by a multiple testing correction using the false discovery rate.

4.3.2.2 The size of isolated lipid droplets from human macrophages remains unchanged upon Mtb infection

As described in the previous section, Mtb infection leads to an overall increase in total neutral lipids, particularly CEs, in the LDF. This might suggest, that the size of isolated LDs might be changed when human macrophages are infected with Mtb. To this end, the ratio of neutral lipids (i.e. TAGs, DAGs and CEs) to the most abundant membrane lipids, PCs, was calculated to obtain information about the volume-to-surface ratio of LDs in the LDF of uninfected and Mtb-infected hMDMs.

A strong variation in the neutral lipid/PC ratio was observed in uninfected hMDMs, ranging from approximately 0.06 – 5.9, indicating strong differences in LDs size between donors (Fig. 38). Mtb infection has no uniform effect on the neutral lipid/PC in all donors tested, as shown by both increased and decreased neutral lipid/PC ratios in the LDF from Mtb-infected compared to uninfected hMDMs.

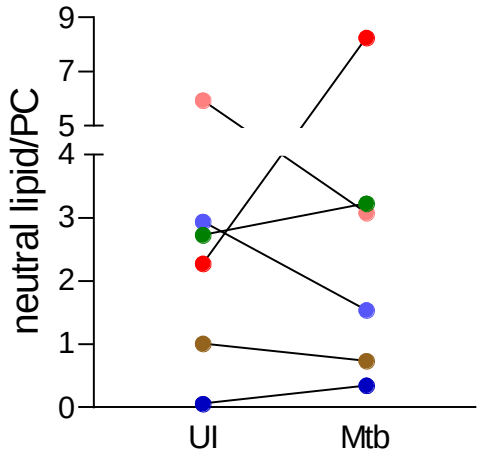

Figure 38: The neutral lipid/PC ratio is unchanged upon Mtb infection.

The LDF was isolated from human monocyte-derived macrophages left uninfected or infected with Mtb at an MOI of 0.1 for 7 days as described in section 3.2.8. Methanol containing 0.147% BHT was added to the LDF, total lipids were extracted, the neutral lipid and PC levels were quantified using mass spectrometry and the neutral lipid/PC ratio was calculated (n=6).

As the neutral lipid/PC ratio is not a clear indicator for LD size, the light scattering behavior of particles was analyzed to determine particle diameter (in nm) of LDs in LDF using ZetaSizer analysis. As depicted in figure 39A, a strong inter-and intradonor variability was observed in the size distribution of particles in the LDF isolated from uninfected hMDMs. For example, in one donor (brown dots) the particle sizes range from ~200 nm to ~1200nm, indicating that LDs appear in a broad range of different sizes within one donor. Also, between the donors, the size distribution is shifted either to the left (pink dots) or the right (red dots), indicating a shift towards smaller or bigger sized LDs, respectively. Similarly, when determining the mean particle size (Fig. 39B) in the LDF from uninfected hMDMs a strong variation was detected in

the six donors tested as evident by a mean diameter (d: nm) ranging from ~280 – 700 nm. However, upon Mtb infection, no consistent trend was observed in all donors tested. While three donors showed an increase (dark blue, brown and pink donor), the three other donors showed a decrease (light blue, red and green donor) in the mean particle size in Mtb-infected hMDMs compared to uninfected cells.

Collectively, these results indicate that LD size is highly variable between hMDMs from different donors. However, Mtb infection appears to have no consistent effect on the size of LDs isolated from hMDMs compared to the uninfected control.

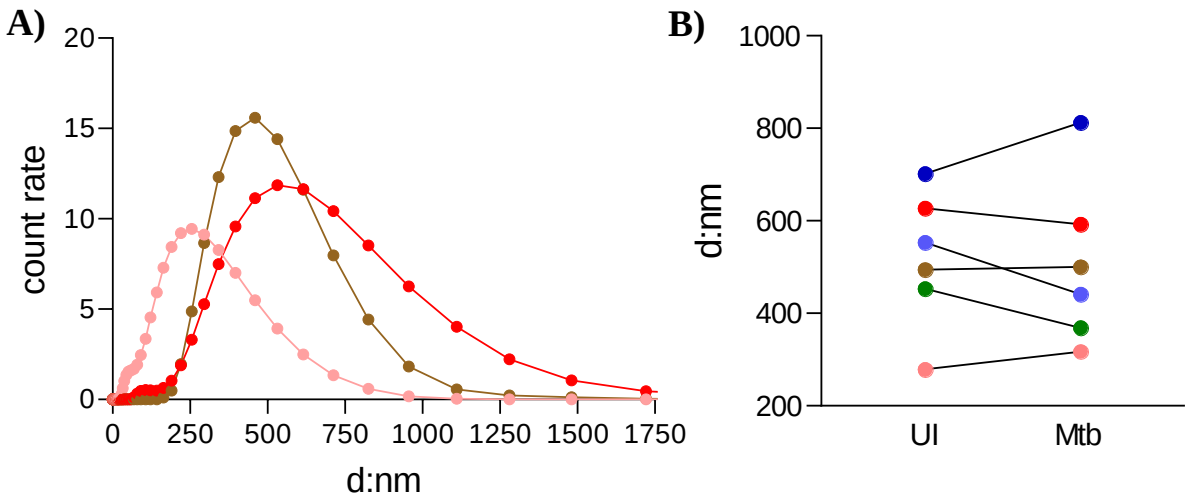

Figure 39: Size distribution and mean peak size of LDs isolated from human macrophages.

The LDF was isolated from human monocyte-derived macrophages left uninfected or infected with Mtb at an MOI of 0.1 for 7 days as described in section 3.2.8. LDs were diluted 1:10 in PBS, fixed with 4% PFA for 24h and the diameter in nanometer (d: nm) was determined on a ZetaSizer (Malvern Pananalytical). **A)** Depicted is the size distribution from LDs isolated from uninfected hMDMs from 3 donors. **B)** Depicted is the mean particle size from LDs isolated from uninfected and Mtb-infected hMDMs from 6 donors (n=6).

4.3.2.3 Mtb infection results in the enhanced presence of proteins involved in immune cells signaling in the lipid droplet-enriched fraction of primary human macrophages

Lipid droplets are highly dynamic organelles and their function is critically determined by their protein composition[110]. As significant alterations in the lipidome of the LDF upon Mtb infection may also be indicative of changes in the proteome. Therefore, a mass spectrometry-based approach was used to determine proteins with a significantly increased presence in the LDF from Mtb-infected cells.

Using proteomics, it was possible to quantify 2415 proteins in the LDF isolated from hMDMs. 2292 and 1960 proteins were detected in the LDF of either all 5 donors or ≥4, respectively, suggesting all donors express a similar repertoire of proteins on LDs (Suppl. Fig. 6A). Among the quantified proteins, 65 proteins were significantly enriched in the LDF isolated from Mtb-infected hMDMs compared to the uninfected control (Suppl. Fig. 6B and 7). Interestingly, it was observed that 35 of the enriched proteins belonged to the pathway "Immune System", indicating that LDs are involved in the Mtb infection-induced immune response of hMDMs. Furthermore, 14 and 9 of significantly enriched proteins are also represented in the pathways "Interferon signaling" and "Interferon gamma signaling", respectively. Among these proteins are for example STAT1 and the oligoadenylate synthetase 2 (OAS2), which have been described in the context of Mtb infection before[164,165]. Another pathway related to the immune response, which was significantly enriched in the LDF of Mtb-infected hMDMs was the pathway "Cytokine Signaling in Immune System", which in addition to the proteins involved in interferon signaling, comprised 6 more significantly upregulated proteins, such as the proteasome 20S subunit beta 9 and 10 (PSMB9 and 10) (fig 40). This might indicate that proteins involved in immune cell signaling are increasingly localized to LDs of Mtb infected hMDMs.

Also, a total of 7 proteins involved in "Antigen processing – cross-presentation" was found to be significantly enriched in the LDF of Mtb-infected hMDMs (Fig. 40). This suggests that upon Mtb infection, LDs might be involved in the processing and presentation of antigens thereby promoting the interaction between macrophages and T cells.

Collectively, these data indicate that Mtb infection enhances the presence of proteins involved in immune cell activation and signaling in the LDF of hMDMs as determined using reactome-based analysis. This might suggest that LDs act as hubs for immune cell signaling and thereby critically influence the immune response of human macrophages during Mtb infection.

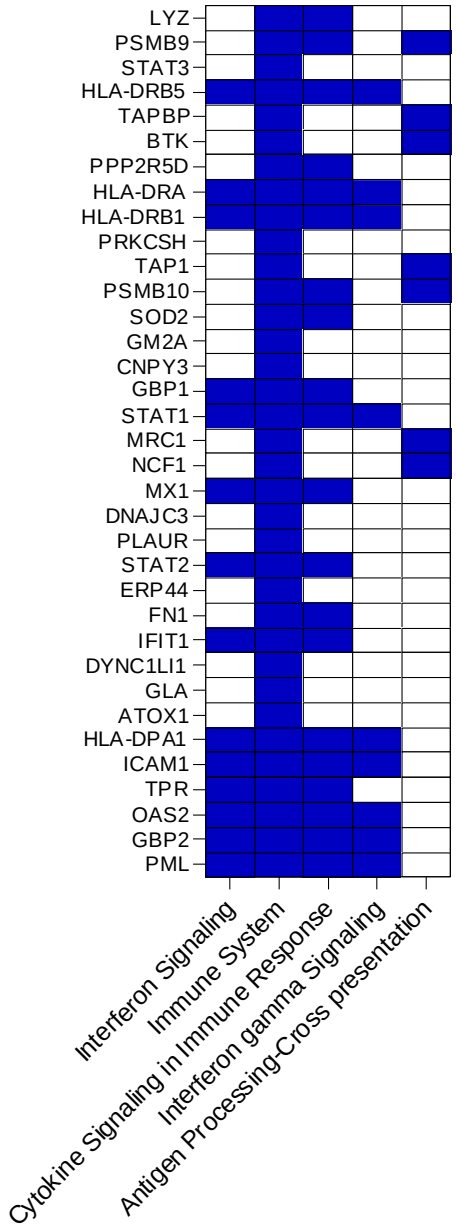

Figure 40: Top 5 pathways with significantly enriched proteins in the LDF of Mtb-infected human macrophages.

Human monocyte-derived macrophages infected with Mtb at an MOI of 0.1 or left untreated for 7 days, lysed and the LDF were isolated from the WCL as described in section 3.2.8. Samples were digested and a liquid chromatography-based approach was performed to determine relative protein levels sing label-free proteomics. Differentially enriched proteins ($p<0.05$) with an increased presence in Mtb-infected compared to uninfected hMDMs were determined and used for a reactome-based analysis using the online tool g: profiler. Depicted are the top 5 pathways comprising significantly enriched proteins in the LDF isolated from Mtb-infected hMDMs.

4.3.2.4 Mtb infection results in the decreased presence of proteins linked to RNA biology and cytoskeletal remodeling in the lipid droplet-enriched fraction of primary human macrophages

The results of this study indicate, that proteins belonging to pathways linked to immune cell function are significantly enriched in LDs during Mtb infection. To further investigate the function of LDs, significantly downregulated pathways were determined by comparing proteins with significantly reduced presence in the LDF of Mtb-infected hMDMs to the reactome-database as described before.

In total, 88 proteins were detected with decreased presence in the LDF isolated from Mtb-infected hMDMs compared to the uninfected control (Suppl. Fig. 6B and 7). Analyzing if there is an enrichment of these proteins in certain pathways revealed that "Infectious disease" is among the top 5 pathways, indicating that proteins involved in processes typical for bacterial and viral infections are less abundant in the LDF of Mtb-infected hMDMs (Fig. 41). Furthermore, in the LDF of Mtb-infected hMDMs, proteins related to the "Metabolism of RNA" were found to be significantly less present, indicating that Mtb infection interferes with the function of LDs in mRNA biology and processing. Among the proteins unique for the pathway "Metabolism of RNA" were for example the RNA helicase eucaryotic initiation factor 4a (EIF4A), members of the heterogeneous nuclear ribonucleoproteins (HNRNPs), such as HNRNPH1 and 2, or the decapping scavenger enzyme DCPS. This indicates that LDs might be involved in RNA processing in hMDMs and this process is interfered during Mtb infection.

In addition to these pathways, proteins related to the pathway "Recycling pathway of L1" were significantly less present, which included mostly subunits of the cytoskeletal tubulin beta chain (TUBB) or the dihydropyrimidinase-related protein 2 (DPYSL2), which is involved in cytoskeletal remodeling[166]. "Neutrophil Degranulation" and "Microtubule-dependent trafficking of connexons from Golgi to plasma membrane" were two more pathways, in which cytoskeletal proteins like TUBB proteins, the drebrin-like protein (DBNL) or rho GTPase-activating protein 45 (AHRGAP45) are represented, indicating that transport of LDs along the cytoskeleton might be altered during Mtb infection. However, also other proteins such as the glutathione S-transferase GSTP1, the vesicular trafficking molecules Ras-related protein Rab-4B and Rab-5B (RAB4B and RAB5B) or a catalytical subunit of the phosphatidylinositol 3-kinase, PIK3C3, were found to be significantly less abundant, further indicating additional functions of LDs beyond the storage of fatty acids during Mtb infection.

In summary, these data indicate that Mtb infection significantly reduced the abundance of several proteins in the LDF of hMDMs. Particularly proteins involved in the remodeling of the cytoskeleton or RNA metabolism were found less abundantly in the LDF upon Mtb infection. However, this further highlights that LDs are not only mere storage of lipids but are involved in several other processes in Mtb-infected hMDMs

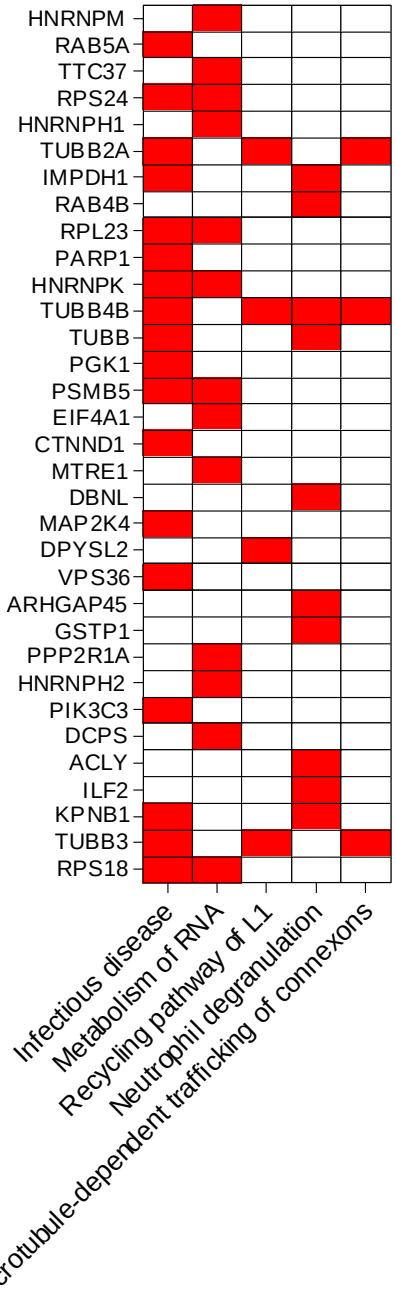

Figure 41: Top 5 pathways comprising proteins with decreased presence in the LDF of Mtb-infected human macrophages.

Human monocyte-derived macrophages infected with Mtb at an MOI of 0.1 or left untreated for 7 days, lysed and the LDF were isolated from the WCL as described in section 3.2.8. Samples were digested and a liquid chromatography-based approach was performed to determine relative protein levels using label-free proteomics. Differentially regulated proteins ($p<0.05$) with decreased presence in Mtb-infected compared to uninfected hMDMs were determined and used for a reactome-based analysis using the online tool g: profiler. Depicted are the top 5 pathways comprising proteins with significantly reduced abundance in the LDF isolated from Mtb-infected hMDMs. Microtubule-dependent trafficking of connexons = Microtubule-dependent trafficking of connexons from Golgi to the plasma membrane

5. Discussion

5.1.1 Studying Mtb-induced metabolic alterations in macrophages: choosing the right model

Energy metabolism of immune cells has become a major research interest due to new findings showing that metabolic reprogramming is a critical step in regulating the functions of immune cells. Particularly in macrophages, metabolic reprogramming appears to be critical for the activation of pro-inflammatory M1 macrophages or anti-inflammatory M2 macrophages, which are characterized by increased glycolysis or OXPHOS, respectively. As an intracellular bacterium, Mtb primarily survives and replicates in macrophages[32] and it is therefore not surprising that the energy metabolism of macrophages undergoes changes during Mtb infection.

Although metabolic alterations in macrophages are a critical step during Mtb infection, little is known about it, particularly in primary human macrophages. Several studies have already investigated metabolic alterations upon Mtb infection *in vivo* and *in vitro* in the murine system[113,114]. However, murine macrophages show significant differences in their metabolic response with regard to induction of OXPHOS and glycolysis compared to human macrophages, as has been recently demonstrated by Vijayan *et al.* [168]. The difference between the human and murine host is also reflected *in vivo,* as hallmark pathologies of human TB granulomas are not observed in the standard mouse models, such C57BL/6 and BALB/c mice[169]. While other mouse models, such as the C3HeB/FeJ mouse develop human-like TB pathologies *in vivo,* metabolic alterations are not studied well in these models[170].

To study Mtb infection in human macrophages *in vitro,* research often resorts to human monocyte/macrophage like cell lines, such as the THP-1 cell line[171,172] or the recently described BLaER1 cell line[117], which both show similarities to hMDMs in the context of an Mtb infection[173]. Nevertheless, differences in polarization and the inflammatory and metabolic phenotype compared to primary human macrophages represent some of the downsides of using these cells[174–176]. This was reflected by a reciprocal glycolytic response in THP-1 cells compared to hMDMs in response to Mtb or *Mycobacterium bovis* Bacillus Calmette-Guerin (BCG) infection[115]. Therefore, human primary macrophages, such as macrophages differentiated from peripheral blood monocytes used in this doctoral study, may be a better reflection of Mtb-induced metabolic alterations in the human system. Nevertheless, there are several pitfalls when working with hMDMs. The isolation technique and the purity of isolated monocytes have been found to significantly impact the phenotype of hMDMs [177]. In addition to that, variations in the macrophage polarization towards either an M1 or M2 phenotype can

significantly affect the metabolic state of hMDMs[114,178,179]. However, the major obstacle when working with primary human cells such as hMDMs is the high degree of donor heterogeneity, which in healthy donors can be caused by differences in sex, age, but also the diet and eating behavior of donors[180–183]. In this doctoral study, high variation between donors was observed particularly when analyzing the proteome and lipidome of hMDMs. For example, relative protein expression of ACSL1 (Fig. 23) in uninfected hMDMs ranged from a ~$1*10^6$ up to a $7.8*10^6$ LFQ intensity between the 5 donors tested. Similarly, absolute abundance of neutral lipids in uninfected hMDMs ranged from ~7 to 170 pmol/µg protein between the six donors tested (Suppl. fig. 4). This suggests, that hMDMs demonstrate a high degree of donor variation, which bears difficulties when determining statistically significant effects of an Mtb infection on macrophage metabolism. To increase the statistical significance of small datasets from primary cells, complex mathematical models have been used to fit datasets and reduce between-donor and within-donor data variations[184]. However, given that personalized medicine becomes increasingly important also for the treatment of TB, reducing donor variance might also result in loss of information about host determinants influencing Mtb infection[167,185]. Therefore, increasing the sample size might be an alternative option to increase statistical power. However, cost, time and feasibility are often determinants of choosing small samples sizes. Nonetheless, even a small sample size can have scientific merit without meeting the conventional definition of statistical significance, especially when using samples with high variations as has been done in this doctoral thesis [186,187].

In summary, this doctoral study uses primary human macrophages to study macrophage metabolism during infection with live, virulent Mtb *in vitro*. This bears the chance to deepen our understanding of the human TB pathogenesis and might aid to develop new, personalized treatment approaches against TB.

5.1.2 Mtb infection induces glycolytic metabolism in primary human macrophages at day 7 of infection

Previous studies analyzing the effect of Mtb infection on metabolism in hMDMs were exclusively performed at early time points of infection (~24h post infection)[115,184]. However, analysis of the Mtb growth kinetic in hMDMs revealed that at 24h post infection, Mtb bacterial loads are not increasing, but rather decreasing. This suggests, that metabolic programming at this time point might promote macrophage function and bacterial killing, as has been suggested before[42,43]. In contrast, at day 7 post infection, Mtb is actively replicating in hMDMs as reflected by high bacterial numbers compared to 24h post infection (Fig. 9). This may suggest that Mtb

induces a differential metabolic response in macrophages at day 7 post infection, which promotes Mtb replication. To get an idea about which pathways are regulated at day 7 post infection in hMDMs proteomics was performed in a set of 5 different donors. This showed that immune cell signaling processes undergo the strongest regulation upon Mtb infection in hMDMs (Fig. 10). However, it is important to consider that the magnitude of changes in the inflammatory response is substantially bigger compared to metabolic processes, which only undergo small changes in hMDMs upon infection[2,43]. Based on this observation, the high donor variations and the small sample size (n=5), the p-value threshold for differentially regulated proteins was raised to a $p \leq 0.1$ and the reactome-based analysis was repeated. This revealed that indeed more than 100 proteins related to metabolism are substantially differently regulated during an Mtb infection (Fig. 11), suggesting that Mtb infection alters the metabolism of hMDMs at day 7 post infection.

To validate this finding, extracellular flux analysis was performed to analyze macrophage metabolism during Mtb infection in real-time. This revealed a significant, dose-dependent increase in ECAR values, suggesting that Mtb infection induces glycolysis in hMDMs (Fig. 13). In agreement with that, the expression of several glycolytic proteins, such as the glucose transporters GLUT3 and GLUT6 was significantly increased in Mtb-infected macrophages (Fig. 14)[57]. Furthermore, two kinases catalyzing the phosphorylation of D-glucose, ADPGK and HK2, were also substantially upregulated, further corroborating that Mtb infection induces the uptake and metabolization of glucose through glycolysis. Increases in glycolytic capacity and reserve (Fig. 14) suggest that Mtb-infected hMDMs have a higher metabolic plasticity compared to uninfected cells. This has been reported to help maintain intracellular levels of ATP during conditions of high energy demands[188], which suggests that Mtb-infected human macrophages are faced with increasing energy demands. In agreement with that, the glycolytic ATP production rate was found to be significantly upregulated upon Mtb infection (Fig. 15). Collectively, these data strongly indicate that Mtb infection induces glycolysis and glycolytic ATP production in hMDMs at day 7 post infection. Interestingly, this is in stark contrast to the metabolism of hMDMs at 24h post Mtb infection, where a decrease in glycolytic metabolism was observed[115]. This might indicate, that indeed the metabolic response of hMDMs is different at day 7 compared to early time points of Mtb infection. However, further investigations are needed to understand the consequences of changes in glycolysis during Mtb infection. Previous studies *in vitro* and *in vivo* suggest that boosting glycolysis is critical for the macrophage host defence, promoting the production of pro-inflammatory cytokines and increasing Mtb killing[42,114]. Based on this, it can be speculated that induction of glycolysis at day 7 post infection might be a host-driven process to induce inflammation and limit bacterial growth[114].

5.1.3 Mtb infection alters mitochondrial and respiratory metabolism in primary human macrophages at late time points of infection

OXPHOS is another major metabolic pathway to produce energy[66]. Interestingly, similar to glycolytic metabolism, Mtb infection of hMDMs was found to also result in a significant induction of basal respiration rates (Fig. 17). In parallel, increased expression of several mitochondrial proteins was observed in Mtb-infected hMDMs (Fig. 19), suggesting that Mtb infection induces mitochondrial metabolism in human macrophages. Respiration has previously been shown to be regulated by STAT3, which is an important transcription factor of mitochondrial genes. Interestingly, STAT3 was also among the significantly upregulated proteins during Mtb infection of hMDMs (Fig. 19)[145]. This might suggest, that mitochondrial metabolism in Mtb-infected hMDMs is driven in a STAT3-dependent manner. It would therefore be interesting to analyze if mitochondrial metabolism is impaired upon inhibition of STAT3 and how this affects infection of macrophages with Mtb. Importantly, aside from STAT3, other important regulators of respiration, e.g. SURF1 and PLAUR, were also significantly upregulated in Mtb-infected hMDMs, which further substantiates that Mtb infection results in increased respiration in hMDMs[144,189,190].

Aside from basal respiration, significant Mtb-induced increases were also detected in the maximal respiration (Fig. 17), which could be due to increasing energy demands in hMDMs in response to an Mtb-infection[191]. In line with this, ATP-linked respiration was found to be upregulated in hMDMs upon Mtb infection, which indicates that increased respiration is coupled to increased ATP production. Supporting that notion, mitochondrial ATP production rates were significantly increased in hMDMs infected with Mtb (Fig. 15). Interestingly, hMDMs appear to produce the bulk of energy in mitochondria, as evident by substantially higher mitoATP production rates compared to glycoATP production rates. Upon Mtb infection, the shift towards mitochondrial ATP production was even further increased, underlining a strong dependency of Mtb-infected hMDMs on OXPHOS for energy production (Fig. 15). Energy production in mitochondria is dependent on the mitochondrial membrane potential $\Delta\boldsymbol{\Psi}$, which drives the translocation of protons through the ATP synthase[69]. Unsurprisingly, a significant increase in the signal intensity of Rho123 was observed in Mtb-infected, indicating an increase in the $\Delta\boldsymbol{\Psi}$ upon Mtb infection (Fig. 18)[192].

Collectively, results from this doctoral study demonstrate that Mtb infection induces respiratory metabolism and ATP production in hMDMs at day 7 post infection. Interestingly, the opposite was detected at 24h post Mtb infection of hMDMs[115]. Based on this, it can be speculated that

hMDMs indeed undergo differential metabolic reprogramming at day 7, when Mtb is replicating, compared to early time points of infection. However, further investigations are needed to link macrophage metabolism to Mtb replication in hMDMs.

Observing that Mtb infection induces mitochondrial respiration and energy production raises the question of the need for these metabolic changes. This can be explained by the upregulation of several, ATP consuming pathways during Mtb infection, such as the production of cytokines like type-1-IFNs, antigen processing, phagocytosis and phagosomal/endosomal trafficking (Fig. 11)[193–196]. Upregulation of OXPHOS could therefore provide the energy to execute these processes during Mtb infection. In line with this, proteomics revealed that several ATPases, e.g. ATP11A, ATP2A2 and ATP13A3, as well as the ATP-dependent (S)- NAD(P)H-hydrate dehydratase CARKD were found to be significantly upregulated in Mtb-infected cells (Suppl. fig. 1). Based on this finding, increased respiration and ATP production could be considered a host-driven process to battle Mtb infection. However, it is important to also consider the negative effects of increased mitochondrial metabolism. Maintaining a high $\Delta\boldsymbol{\Psi}$ also requires maintaining an energetically expensive electrical field across the inner mitochondrial membrane. As the ETC is a major producer of ROS, high respiratory rates and a high $\Delta\boldsymbol{\Psi}$ can also give rise to increased levels of oxidative stress[69,197]. In line with this, we observed a significant, dose-dependent increase in non-mitochondrial respiration (Fig. 17), which has been described as indicative of ROS generation[198]. Furthermore, a significant upregulation of the mitochondrial ROS detoxifier SOD2 upon Mtb infection (Fig. 19) suggests that the anti-oxidative response is induced in Mtb-infected cells. In macrophages, ROS act as a double-edged sword, as production is a fundamental antimicrobial defense mechanism, but excess production can lead to oxidative damage[199]. In Mtb-infected macrophages inhibition of ROS production by blocking the NADPH phagocyte oxidase (Phox) was associated with decreased bacterial killing and an increased bacterial burden[200,201]. In contrast, increased levels of ROS were also demonstrated to promote cell death in Mtb-infected macrophages resulting in an increased Mtb burden at later time points of infection *in vivo*[202]. This indicates that at early time points ROS might be required for bacterial killing [115,200], but as the infection persists, the continuous high levels of ROS might exceed antioxidant capacities of macrophages and cause cell death. Therefore, it would be interesting to see if reducing ROS levels at late time points of Mtb infection, without inhibiting the early antibacterial ROS response, would inhibit cell death and restrict Mtb growth in primary human macrophages.

It is noteworthy that the significant increase in non-mitochondrial respiration observed in this doctoral thesis could also be indicative an increased activity of other non-respiratory, inflammation-associated enzymes such oxidases and oxygenase[198], which has been described before in the context of TB infection[201,203–205]. In the present study, proteomics analysis revealed a significant upregulation of ACOX1 and 3 (Fig. 22) as well as L-amino acid oxidase IL4I1 (Suppl. fig. 1) in Mtb-infected hMDMs, which could be the cause of increased non-mitochondrial respiration in these cells. Therefore, a more direct measurement for ROS is needed to further investigate the Mtb-induced increase in ROS levels in hMDMs and its functional consequences.

Collectively, the results presented in this study show that Mtb infection induces energy metabolism in hMDMs at day 7 post infection. As targeting macrophage metabolism has previously been demonstrated a target for host-directed therapies against TB, the results from this study could have interesting therapeutic implications[2,117]. Moreover, in light of a previous study showing the opposite effect of Mtb infection during early infection, the results from the present study indicate that the late metabolic response of hMDMs to Mtb infection differs from the early metabolic response[115]. This should also be taken into account when testing pharmaceutical intervention strategies for TB therapy *in vitro*.

5.1.4 Mitochondria undergo structural changes in response to Mtb infection of human macrophages

Changes to mitochondrial respiration and bioenergetics have previously been linked to structural and morphological changes in mitochondria[73,206]. This suggests that in Mtb-infected hMDMs the increased mitochondrial activity may be accompanied by morphological changes in mitochondria. Indeed, it was observed that in Mtb-infected hMDMs proteins localized to or functioning in mitochondria show significantly upregulated expression rates, which may indicate that the mitochondria undergo substantial changes upon Mtb infection (Suppl. fig. 2 and Fig. 19). This was further substantiated by a significant, dose-dependent reduction in mtDNA levels in Mtb-infected hMDMs (Fig. 20). Importantly, alterations in mtDNA content have previously been shown to influence mitochondrial mass and morphology as well as mitochondrial biogenesis[146,207]. Moreover, mtDNA is also an endogenous trigger for the inflammatory response in macrophages[208]. In line with this, the release of mtDNA in murine macrophages was described to contribute to the production of type-1-IFNs in a ROS-dependent process[209]. Given the detrimental role of type-1-IFN production during Mtb infection,

mitochondrial damage leading to mtDNA release could also link metabolism to the inflammatory response during Mtb infection. Interestingly, although mitochondrial DNA content decreases in Mtb-infected cells, proteins involved in mitochondrial transcription and translation, such as mitochondrial transcription factor STAT3, PNPT1 and TYMP were found to be significantly increased in Mtb-infected hMDMs (Fig. 19). As these factors are involved in the translation of the OXPHOS complexes, upregulation of these proteins might explain why the mitochondrial activity is increased although mtDNA content decreases in Mtb-infected cells[143,145,210].

With regard to mitochondrial morphology, a significant upregulation of MTFP1, a protein involved in the fission of mitochondria, and SPG7, which is a protease involved in mitochondrial biogenesis, was observed in Mt-infected hMDMs compared to uninfected cells (Fig. 19). Increased expression of either MTFP1 or SPG7 has been associated with increased mitochondrial fragmentation and reduced mitochondrial mass, but also increased oxidative stress and ROS production in other cell types before[142,211,212]. Based on this, upregulation of MTFP1 and SPG7 in Mtb-infected hMDMs might indicate that infection results in increased mitochondrial fragmentation. Interestingly, in macrophages as well as other cell types, induction of mitochondrial fragmentation is an important step during necrotic cell death, which is a process long known to be induced by infection with virulent Mtb promoting bacterial replication and dissemination[213–215]. In line with that, for the neurodegenerative disease Parkinson, persistently high mitochondrial activity was postulated to cause mitochondrial dysfunction, which is followed by increased mitochondrial fragmentation and subsequent cell death[216,217]. Therefore, it is intriguing to speculate that persistently high mitochondrial activity results in mitochondrial damage, mitochondrial fragmentation and ultimately cell death of Mtb-infected hMDMs. Interestingly, two recent studies showed that mitochondrial fusion and fission occur in THP-1 and murine macrophages, respectively, in response to infection with virulent Mtb[218,219]. These contradicting observations highlight the need for detailed microscopic visualization of mitochondrial morphology and its role in Mtb-infected hMDMs.

In summary, changes in mitochondrial metabolism are accompanied by substantial structural alterations of mitochondria in Mtb-infected hMDMs. However, further studies are needed to visualize mitochondrial morphology in detail and to understand the role thereof during Mtb infection in primary human macrophages.

5.1.5 Mtb infection of primary human macrophages results in increased fatty acid degradation

It is well known from previous studies in cancer cells that mitochondrial structure and oxidative capacities are altered depending on which substrate, e.g. glucose, fatty acids or glutamine, is used for energy production[220]. Thus, the significant changes in mitochondrial and respiratory metabolism in Mtb-infected hMDMs might suggest that there is a change in substrate utilization upon Mtb infection. Indeed, the dependency of hMDMs on fatty acids was significantly increased upon Mtb infection, while the dependency on glucose decreased (Fig. 21). This indicates that upon Mtb infection, human macrophages preferentially use the oxidation of fatty acids to fuel mitochondrial respiration. In line with this observation, reactome-based analysis of the proteome of Mtb-infected hMDMs revealed "Fatty acid degradation" to be among the significantly enriched pathways (Suppl. fig. 3). With regard to that, ALDH2, which is involved in the oxidation of fatty acid-derived aldehydes, was found to be significantly upregulated (Fig. 22)[149]. Interestingly, in metabolic diseases such as hepatic steatosis or atherosclerosis, ALDH2 activity was described to ameliorate disease by counteracting the effects of lipid accumulation[221,222]. In parallel, activation of ALDH2 resulted in upregulation of FAO, suggesting that ALDH2 might also be involved in the degradation of fatty acids in Mtb-infected hMDMs[223]. Further supporting an increased upregulation of FAO upon Mtb infection, several other proteins such as CRAT, ACADSB and ETFA were substantially upregulated in Mtb-infected hMDMs (Fig. 22). These proteins were described to be associated with reduced accumulation of fatty acids, increased FAO and an increase in mitochondrial ATP production by coupling FAO to respiration[150–152,224,225].

Aside from mitochondria, peroxisomes are major organelles involved in the degradation of fatty acids. Interestingly, the expression of the enzymes ACOX1 and 3, which catalyze the first step in peroxisomal FAO, was significantly upregulated in Mtb-infected hMDMs (Fig. 22)[96]. This strongly suggests that peroxisomal metabolism and biogenesis are induced during Mtb infection. It is important to note that peroxisomes are mostly involved in the shortening of long-chain acyl-CoAs[96]. Therefore, it is intriguing to hypothesize that during Mtb infection, peroxisomes degrade long-chain acyl-CoA into shorter fragments, which are then transported to mitochondria. These short-chain fatty acids are then further degraded by ACADSB, which has a preference for short/branched fatty acids[151]. However, this speculation requires further substantiation using for example microscopic visualization of the trafficking of labeled fatty acids in Mtb-infected hMDMs. Importantly, fatty acid degradation in both, mitochondria and peroxisomes, requires the esterification of fatty acids to form acyl-CoAs prior to the transport

into these organelles. This esterification is mediated by ACSL proteins, which reversibly convert FFA to acyl-CoAs[226]. Given the importance of this step for FAO, it is unsurprising to see increased protein expression in ACSL1, 3, 4 and 5 in Mtb-infected hMDMs (Fig. 23). This suggests, that upon Mtb infection, the induced synthesis of acyl-CoAs from FFA mediated by ACSL leads to induction of fatty acid degradation. In line with this, previous studies could show that increased expression of ACSL1, 3 and 4 is associated with an induction in FAO in several cell types[227–229]. Furthermore, overexpression of ACSL5 in skeletal muscle cells was described to increase FAO, basal and maximal respiration as well as mitochondrial ROS production[230]. Based on these observations, increased formation of acyl-CoAs by upregulation of ACSLs could increase the availability of fatty acids for peroxisomal or mitochondrial FAO in Mtb-infected hMDMs.

Taken together, the data presented in this thesis support a model where Mtb infection induces ACSL expression resulting in increased acyl-CoA formation. These acyl-CoAs are transported to mitochondria or peroxisomes for degradation and subsequent respiration in Mtb-infected primary human macrophages. However, further analyses are required to understand the consequences of increased FAO on macrophage function and on Mtb survival in hMDMs. It is noteworthy, that FAO, aside from its role in energy production, is also involved in regulating inflammation. In line with that, type-1-IFN stimulation was described to induce FAO and OXPHOS. Then, in a feedback loop, this increase in FAO and OXPHOS results in the production of even more type-1-IFNs[231]. As type-1-IFN signaling is prominently induced in Mtb-infected hMDMs (Fig. 11), it can be hypothesized that increased FAO and type-1-IFNs are tightly linked during Mtb infection. In line with this, previous observations from Mtb-infected mice showed that alveolar macrophages, which are committed to FAO, promote bacterial growth *in vivo*. Furthermore, inhibition of FAO using the pharmacological inhibitor etomoxir results in Mtb growth restriction, as well as reduced type-1-IFN production *in vitro*[114,116].

In summary, this doctoral project revealed several critical proteins of peroxisomal and mitochondrial degradation of fatty are upregulated in Mtb-infected hMDMs at day 7 post infection. Furthermore, extracellular flux analyses demonstrated an increased dependency on fatty acid in Mtb-infected cells indicating that Mtb infection induces FAO in hMDMs. This Mtb-induced effect on FAO may indicate that hMDMs undergo substantial lipid metabolic reprogramming during Mtb infection. Therefore, pharmacological inhibition of FAO might represent a promising adjunctive therapeutic intervention for TB treatment.

5.1.6 Primary human macrophages infected with Mtb show decreased levels of free fatty acids

Mtb-induced reprogramming of macrophage lipid metabolism towards FAO might give rise to substantial changes in the fatty acid and lipid composition of hMDMs. Particularly, changes in intracellular FFA levels are expected, given the Mtb-induced upregulation of ACSL proteins, which catalyze the metabolization of FFA[226]. In agreement with this hypothesis, a substantial, dose-dependent decrease in total FFA was detected in Mtb-infected cells as determined (Fig. 24). This further supports the notion of increased ACSL activity in Mtb-infected hMDMs leading to increased conversion of FFA to acyl-CoAs. While several FFA species showed an overall decrease upon Mtb infection, the effect was most prominent for oleic acid (C18:1), palmitic acid (C16:0) and myristic acid (C14:0) (Fig. 25). This indicates that only certain fatty acid species are increasingly esterified in Mtb-infected hMDMs, which could be explained by the different substrate preferences described for the five ACSL isoforms[232,233]. Furthermore, a substantial decrease in palmitic, myristic and oleic acid and not the other FFA could also imply preferential oxidation of saturated C14-18 fatty acids over others species upon Mtb infection. This hypothesis is in line with previous findings, which showed that differential oxidation of distinct fatty acid species alters the composition of intracellular neutral lipids or FFA pools[234]. Based on this observation, it can be speculated that especially shorter chain, saturated or monounsaturated fatty acids are being esterified and oxidized in Mtb-infected hMDMs. However, further studies are required to link ACSL activity to alterations in FFA composition. Importantly, also the intracellular levels of acyl-CoAs should be analyzed to determine if there is a concomitant increase of acyl-CoAs when FFA levels are decreasing upon Mtb infection.

To date, only a few studies have investigated the implications of changes in intracellular FFA composition on cell function. Most of these studies analyzed the effect of exogenous supplementation of FFA on cell function. Regarding that, enrichment of palmitic or myristic acid was found to reduce phagocytic capacities of macrophages, but also increase production of pro-inflammatory cytokines such as TNF-α or IL-1β[235,236]. Therefore, reduction in free myristic and palmitic acid upon Mtb infection could also affect TNFα production or phagocytosis of Mtb-infected hMDMs. Interestingly, in the context of Hepatitis-C virus infection, accumulation of FFA was associated with a decrease in type-1-IFN response and viral clearance by blocking the activation of STAT1 and 2[237]. Based on this, a reduction in intracellular FFA levels in hMDMs could also be linked to the type-1-IFN response, which was significantly upregulated upon Mtb infection. However, further investigations are needed to understand the link between type-1-IFNs and FFA in hMDMs upon Mtb infection.

Nonetheless, when discussing the fatty acid levels in hMDMs upon Mtb infection, it is also important to consider that Mtb uses host-derived fatty acids as a carbon source. In line with this, several studies in murine and human models demonstrated the utilization of host lipids by intracellular Mtb, which expresses transporters mediating the import of host fatty acid[117,238–240]. Therefore, a reduction in palmitic, myristic and oleic acid upon Mtb infection could also be the result of increased uptake and utilization of these fatty acids by Mtb. In line with this, Brandenburg *et al* could show that host-derived oleic acid is indeed incorporated into intracellular Mtb[117]. This further suggests that a reduction of FFA could be caused by increased uptake of FFA by Mtb. However, further analysis, using for example microscopic visualization of the fatty acid uptake by macrophages and intracellular Mtb, is needed to characterize this. In addition, usage of mutant Mtb strains, which are deficient in fatty acid importers, could provide further insides into the uptake of host-derived FFA by Mtb.

Collectively, this doctoral study could show for the first time that Mtb infection affects intracellular FFA levels in macrophages. This Mtb-induced reduction of FFAs in hMDMs could be due to increased esterification by ACSL and result in increased FAO. However, the consequence of reduced FFA levels upon Mtb infection in hMDMs remains to be investigated.

5.1.7 Increased neutral lipid levels caused by supplementation with exogenous fatty acids affect Mtb growth in primary human macrophages

As described above, increased activity of ACSL could promote FAO in primary human macrophages infected with Mtb. However, it was described before that ACSL not only fuels FAO, but also neutral lipid synthesis (Fig. 4)[227–230]. Given the role of lipid accumulation and foam cell formation during Mtb infection, this prompted the analysis of neutral lipid accumulation in Mtb-infected hMDMs[22]. Surprisingly, no substantial change was observed, neither in TAG levels nor in total neutral lipid levels in hMDMs upon Mtb infection as determined using mass spectrometric and flow cytometric analyses (Fig. 26 and Suppl. Fig. 4). This suggests that total neutral lipid levels remain unchanged in primary human macrophages in response to Mtb infection. One explanation for this can be the parallel increase in both, synthesis and degradation of lipids, resulting in a net stabilization of neutral lipid levels, as has been proposed before[241]. This might indicate that primary human macrophages undergo an overall lipid metabolic reprogramming upon Mtb infection. However, further analyses tracing fluorochrome-labeled fatty acid probes in hMDMs could help to visualize fatty acid trafficking within hMDMs upon Mtb infection.

As Mtb infection alone did not induce accumulation of neutral lipids, Mtb-infected hMDMs were incubated with exogenous fatty acids to induce lipid accumulation, as has been described before[99]. Interestingly, in hMDMs infected with Mtb, only supplementation with oleic acid, but not palmitic acid, resulted in a significant enrichment of neutral lipids (Fig. 27). This suggests that in hMDMs oleic acid is more readily incorporated into TAGs compared to palmitic acid, as has been demonstrated before[99]. This could be due to structural differences in the saturation between oleic and palmitic acid. Indeed, it has been shown that the macrophage response is reciprocally modulated by saturated and unsaturated fatty acids, resulting also in alteration of the inflammatory response[235,242,243]. This suggests that the saturation state of fatty acids could also influence the lipid metabolic response of Mtb-infected macrophages. Moreover, palmitic or oleic acid treatment also results in differences regarding macrophage cell death. It is well appreciated that palmitic acid induces cell death in several cell types including macrophages, while unsaturated fatty acids protect against this palmitic acid-induced lipotoxicity[244,245]. In line with this, this doctoral study demonstrated that exogenously supplemented palmitic acid, but not oleic acid, induces cell death in uninfected hMDMs (Fig. 28) as determined by measuring DRAQ7 fluorescence. However, when hMDMs are additionally infected with Mtb, cell death was also significantly induced in oleic acid-treated cells. This suggests, that Mtb infection might increase the susceptibility of hMDMs to oleic acid-induced lipotoxicity and that an Mtb infection in a lipid-rich environment might promote TB pathogenesis by inducing cell death.

Since the accumulation of neutral lipids in foamy macrophages and macrophage cell death are both critical steps in the TB pathogenesis, the effect of exogenous fatty acid supplementation on Mtb growth was analyzed[22,117,246]. Interestingly, it was found that both, palmitic and oleic acid treatment, significantly induced Mtb growth in primary human macrophages (Fig. 29). As palmitic acid did not induce accumulation of neutral lipids, this might suggest lipotoxicity rather than the accumulation of neutral lipids is driving Mtb growth in a lipid-rich environment. In agreement with this, it has been described that TAG synthesis protects against lipotoxicity[99]. It can therefore be speculated that the initial accumulation of neutral lipids might be a protective mechanism during Mtb infection. However, when lipid levels exceed the fatty acid storage capacity of macrophages, toxic accumulation of fatty acids results in cell death in Mtb-infected macrophages. Cell death then leads to the release of more host lipids, which further contributes the lipid-rich environment promoting Mtb growth[247]. However, further analyses, using for example inhibition of TAG synthesis, are needed to investigate this in more detail. Nevertheless, supplementation of hMDMs with exogenous fatty acids *in vitro* might recapitulate the lipid-rich environment found in the granuloma and might therefore be an

interesting approach to further investigate the role of lipids during Mtb infection in macrophages.

5.2 Successful isolation of a high-purity lipid droplet fraction from primary human macrophages

Lipidomics revealed that in primary human macrophages, neutral lipids account for up to 15% of all lipids in the cell, suggesting that hMDMs provide a nutrient-rich environment for intracellular survival of Mtb (Fig. 31)[114,117]. Surprisingly, Mtb infection alone did not further increase neutral lipid levels in hMDMs on a whole-cell level (Fig. 26 and Suppl. fig. 4). However, as the synthesis and intracellular traffic of neutral lipids is a coordinated process involving several subcellular compartments, it was hypothesized that there is a subcellular change in neutral lipids upon Mtb infection[248,249]. As LDs are the main storage organelles for lipids, this doctoral study also focused on a detailed characterization of LDs in Mtb-infected hMDMs.

To this end, LDs were isolated from hMDMs and the purity of the LD-containing fraction was analyzed based on the protein and lipid content. The enhanced presence of the LD-coating protein PLIN3 in the LDF suggests that indeed there is an enrichment of LDs in this fraction (Fig. 30)[160]. Also, a high abundance of the cytoskeletal protein α-TUB was detected in the LDF, which was also observed in the WCL (Fig. 30). However, this is not surprising as LD motility is mediated by microtubules. Therefore, cytoskeletal elements have long been considered part of the LD proteome rather than being a contamination from the isolation process[250]. Enrichment of LDs in the LDF was further substantiated by lipidomic characterization demonstrating an increased abundance of TAGs, DAGs and CEs in the LDF compared to the WCL (Fig. 31 and 32). In contrast to the WCL, a significant decrease of membrane lipid PC was detected in LDF, suggesting a high neutral lipid to membrane lipid ratio in the LDF, as is expected upon enrichment of LDs (Fig 31, 32 and 34). Taken together, these data show that there is an increased enrichment of LDs in the LDF isolated from hMDMs. Concomitantly, low abundance of MnSOD and CAL, which are mitochondrial and ER proteins, respectively, as well as low abundance of mitochondrial lipids in the LDF compared to other fractions (Fig. 30, 31 and 33) suggest that there is little contamination from other organelles in the LDF.

Collectively, this suggests a strong enrichment of LDs with little contamination from other organelles in the LDF. Therefore, this doctoral describes a successful method to isolate LDs from primary human macrophages, which was then used to analyze the effect of Mtb infection on the lipid and protein composition of LDs.

5.2.1 Lipidomic analysis revealed substantial alterations in neutral lipid composition of LDs from human macrophages upon Mtb infection

5.2.1.1 Mtb infection induces an enrichment of total di- and triacylglycerols in LDs of human macrophages

Lipidomics revealed that TAGs are the most prominent neutral lipid in LDs from hMDMs accounting for more than 80% of total neutral lipids. In contrast, DAGs only account for 4.5% of neutral lipids, suggesting that in human macrophages fatty acids are primarily stored in TAGs. Interestingly, upon Mtb infection, total TAG levels were found to be substantially increased in LDs by 2.3-fold compared to the uninfected control (Fig 35). Similarly, also the levels of individual TAG species showed an overall enrichment in LDs upon Mtb infection. This suggests that the increase in total TAG levels is driven by an overall increase of all TAG species rather than in TAG species with distinct biochemical features. In contrast to TAGs, Mtb infection did not affect total DAG levels in LDs of hMDMs (Fig. 36). Interestingly, however, substantial changes were observed in the levels of individual DAG species upon Mtb-infected hMDMs. This was demonstrated by an increase in DAG 18:1_18:2, DAG 16:1_18:1 and DAG 16:0_18:2 upon Mtb infection in all donors tested (Fig. 36). This suggests that there is a preferential enrichment of DAGs containing either palmitoleic acid (C16:1) or linoleic acid (C18:2) in LDs of Mtb-infected hMDMs. However, due to donor variability and the small sample size, the Mtb-induced changes in TAG and DAG levels did not reach statistical significance.

Nevertheless, these results suggest that there is an enrichment of TAGs and DAGs in LDs upon Mtb infection. As neutral levels were unchanged in Mtb-infected hMDMs on a whole-cell level, these results indicate that there is a subcellular enrichment of TAGs and DAGs in LDs upon Mtb infection. This could be due to alterations in several lipid metabolic pathways, such as increased trafficking of neutral lipids to LDs. Moreover, reduced hydrolysis or increased on-site synthesis of TAGs and DAGs could give rise to the enrichment of neutral lipids in LDs upon Mtb infection. Interestingly, it was proposed before that enzymes involved in the synthesis of neutral lipids, such as DGAT and the acyl-coenzyme A:monoacylglycerol acyltransferase (MGAT) show substrate preferences for specific fatty acids[91,251,252]. Enrichment of distinct neutral lipid species could therefore be explained by the preferential incorporation of distinct fatty acids in Mtb-infected hMDMs. Other proteins linked to alterations in cellular lipid composition are FABPs, which are involved in the intracellular transport of fatty acids. Deficiency of FABP3, which was also significantly downregulated in Mtb-infected hMDMs compared to uninfected cells (Suppl. fig. 1), was found to result in a toxic accumulation of

neutral lipids. Importantly, FABP3 deficiency resulted in a particularly strong increase of C18:2 containing DAGs[253]. Based on these observations it can be speculated that downregulation of FABP3 in Mtb-infected hMDMs might promote the accumulation of neutral lipids in LDs. However, further analysis is required to understand which mechanism leads to the enrichment of TAGs and DAGs in LDs upon Mtb infection. To this end, ^{13}C-labelled or fluorescently fatty acids could be used to analyze the intracellular trafficking and synthesis of TAGs and DAGs in LDs of Mtb-infected hMDMs.

Independent of the mechanisms leading to enrichment of TAGs and DAGs, also the consequences of lipid enrichment in LDs need to be discussed. Peyron *et al* postulated that Mtb-containing phagosomes localized in close proximity to LDs and that Mtb subsequently translocate into LDs in order to gain access to host cell lipids[118]. This is further supported by observations that Mtb strains lacking the mycobacterial secreted hydrolase 1 (Msh1), which cleaves host cell lipids, show impaired growth in foamy macrophages[254]. Therefore, enrichment of TAGs and DAGs in LDs could further enhance the nutrient availability and promote the growth of Mtb, which localizes to LDs. Interestingly, lipidomics revealed that the Mtb-induced increase in TAGs was strongest in donors with low basal levels in TAGs in uninfected hMDMs. This suggests that depending on neutral lipid levels, the metabolic response of hMDMs differs upon Mtb infection. Indeed, it has been suggested before that certain donor characteristics may influence the metabolic response and growth of Mtb in hMDMs[255]. Moreover, this is in line with a study by Brandenburg *et al*, which indicated that Mtb growth and access to host lipids might be linked to a high threshold level of TAGs in hMDMs[117]. Therefore, it would be interesting to see if high TAG and DAG enrichment in LDs is also accompanied by higher replication rates of Mtb in hMDMs. Furthermore, a better understanding of metabolic host characteristics, which promote Mtb growth, might also have important implications for the development and clinical use of host directed-therapy approaches against TB.

5.2.1.2 Mtb infection induces an enrichment of CEs in LDs of human macrophages

Apart from TAGs and DAGs, CEs were the third class of neutral lipids detected in the LDs of primary human macrophages. As CEs represent only 1.2% of total neutral lipids in LDs, this indicates that CEs do not substantially contribute to the storage of fatty acids in neutral lipids in LDs (Fig. 31 and 37). Interestingly, particularly long-chain (20 carbons) polyunsaturated (3 to 6 double bonds) fatty acids were incorporated in CEs (Fig. 37) suggesting that CEs could act as stores for fatty acids such as arachidonic acid (20:4) or docosahexaenoic acid (C22:6). Analyzing the effect of Mtb infection on CEs composition in LDs, revealed a significant

enrichment of total CE levels and individual CEs species in LDs of Mtb-infected hMDMs (Fig. 37). In line with this, mycolic acid, which is a mycobacterial lipid virulence factor, was previously described to induce CEs accumulation in murine macrophages thereby promoting BCG growth[256]. This might suggest that the accumulation of CEs in LDs might also facilitate Mtb growth in primary human macrophages. In contrast to this hypothesis, cholesteryl arachidonate (CE20:4) was found to have antibacterial properties, suggesting that the accumulation of this lipid in LDs, as was observed in this doctoral study, could also be a host driven process to limit Mtb growth[257]. In line with this, the production of eicosanoids, which derive from arachidonic acid (20:4) and docosahexaenoic acid (C22:6)[258–260], was demonstrated to be a host-protective process during Mtb infection in macrophages[261]. Taken together, this might suggest that CEs may have a dual role during Mtb infection, on one side providing nutrients for Mtb growth and on the other side mediating a host protective immune response of hMDMs against Mtb[262,263]. Therefore, further analyses are needed to understand the consequences of CE enrichment in LDs during Mtb infection.

Taken together, the lipidomics results presented in this doctoral study, show a substantial change in neutral lipid composition of LDs during Mtb infection. This was reflected by an enrichment of total TAGs, CEs as well as distinct DAG species in LDs from Mtb-infected hMDMs. However, it is unclear if this subcellular increase of neutral lipids in LDs is due to alterations in synthesis and degradation on LDs or altered transport of these lipids to LDs. This could be answered by microscopy- or mass spectrometry-based tracing of labeled fatty acids in Mtb-infected hMDMs. In addition to that, the functional consequences of an increased enrichment of these neutral lipids in Mtb-infected hMDMs remain to be investigated.

5.2.1.3 LD size in human macrophages remains unchanged upon Mtb infection

As described above, lipidomics analysis revealed an increase in neutral lipid levels in LDs of Mtb-infected hMDMs. This might suggest that LDs also undergo structural changes and increase in size upon Mtb infection. To determine the diameter of LDs isolated from hMDMs, ZetaSizer analysis was performed. Interestingly, LDs of hMDMs show a very high degree of inter- and intra-donor variability in size and can range from less than 200nm to more 1500nm (Fig. 39). This is indicative of a high degree of diversity of LDs in hMDMs. As size is one determinant of LD functionality, this observation might also indicate that functionally different LD subsets are found in macrophages[264]. With regard to Mtb infection, no consistent alterations in LD size were detected upon infection in the six donors tested. In agreement with this, no uniform change in the neutral lipid/PC ratio was detected, suggesting that there are no

alterations in the volume to surface ratio of LDs upon Mtb infection. (Fig. 38). Collectively, this indicates that LDs do not change in size upon Mtb infection. However, considering the spherical structure of LDs, the ~2-fold increase in TAGs upon Mtb infection (Fig. 35) was not expected to induce a substantial increase in LD diameter. Given that the ZetaSizer also operates with a rather high standard deviation, analysis via the ZetaSizer might not be sensitive enough to detect small changes in LDs size.

Taken together, enrichment of neutral lipids was not accompanied by changes in LD size in hMDMs upon Mtb infection. However, further high-resolution microscopic approaches should be considered to investigate the size of LDs intracellularly. Furthermore, given the high diversity of LDs, microscopy could also elucidate potential changes in LD subpopulations in Mtb-infected hMDMs.

5.2.2 Mtb infection induces significant alterations in the proteome of LDs from human macrophages

An enrichment of neutral lipid species in LDs from Mtb-infected hMDMs might be indicative of functional and structural changes of LDs during infection. Thus, to better understand what those functional changes of LDs could be and how this might affect Mtb infection of primary human macrophages, analysis of the LD proteome was performed.

5.2.2.1 LDs of Mtb-infected human macrophages at as immune cell signaling hubs

Given the role of LDs in several cellular processes, substantial alterations in the protein composition of LDs during Mtb infection were expected[101,111]. Indeed, substantial alterations in the abundance of proteins involved in several cellular pathways were detected (Fig. 40 and 41, Suppl. fig. 6 and 7). Most strikingly, an increased enrichment of proteins involved in immune cell function and immune cell signaling was found in the LD proteome in response to an Mtb infection (Fig. 40 and Suppl. fig. 7). This suggests that LDs may be involved in regulating the inflammatory responses, particularly the type-1-IFN response, during Mtb infection. Given the significant enrichment of STAT1 and STAT2, it appears that already early type-1-IFN-related signal transduction is localized to LDs of Mtb-infected cells. Aside from STAT1 and STAT2, also significantly increased expression of type-1-IFN-inducible effectors such as the interferon-induced GTP-binding protein Mx1 (MX1), the interferon-induced protein with tetratricopeptide repeats 1 (IFIT1), OAS2 and guanylate binding protein (GBP) 1 and 2 was observed in LDs from Mtb-infected hMDMs (Fig. 40)[265]. Interestingly, significantly

increased expression of STAT2, MX1, IFIT1, OAS2 and GBP1 and 2 was only found in LDs, but not in whole cells during Mtb infection (Suppl. fig. 1 and 7). Based on this, it can be speculated that LDs are a major organelle regulating type-1-IFN response in Mtb-infected hMDMs, which has been postulated before[101]. To substantiate this finding, fluorescence microscopy could be used to validate the localization of the described factors at LDs in Mtb-infected hMDMs. Other immune cell modulatory roles of LDs upon Mtb infection were found in the function of macrophages as antigen-presenting cells. Enrichment of proteins such as Tapasin (TAPBP) or the PSMB9 in LDs upon Mtb infection, suggests a potential involvement of LDs in antigen processing and presentation through class 1 upon Mtb infection (Fig. 40)[266,267]. Interestingly, while in DCs a role of LDs in antigen cross-presentation has been suggested before, to date no study has analyzed the function of LDs in this process in macrophages yet[268].

In summary, the results demonstrate that mediators of type-1-IFN response and antigen presentation are significantly enriched in LDs upon Mtb infection. This suggests that LDs are involved in regulating the immune response of human macrophages during Mtb infection.

5.2.2.2 Proteomics revealed alterations in proteins involved in LD motility and RNA metabolism in LDs of Mtb-infected human macrophages

Surprisingly, further proteomic analysis also revealed that particularly proteins involved in the metabolism of RNA are significantly less abundant on LDs upon Mtb infection (Fig. 41). Although little is known about RNA metabolism with regard to LDs, an association of ribosomes and ribosomal proteins with LDs and the presence of RNAs within LDs was demonstrated before in LDs from mast cells and THP-1 cells[269,270] corroborating the role of LDs in RNA metabolism. Thus, the data presented in this doctoral study may indicate that LDs have a functional role in RNA metabolism in hMDMs and that this functional role is impaired during Mtb infection. Interestingly, trafficking of RNAs to subcellular organelles has been described before in order to maintain local homeostasis[271]. Therefore, it can be speculated that the reduced presence of ribosomal and RNA-processing proteins on LDs upon Mtb infection may affect the local protein synthesis on LDs. Furthermore, LDs have also been shown to closely associate with and even localize within the nucleus[272]. In line with this, a reduced presence of proteins from the nuclear ribonucleoprotein complex, for example, HNRNPH1 and 2, was found in LDs upon Mtb infection, which may suggest an altered LD-nucleus interaction

upon Mtb infection (Fig. 41). However, further analyses are required to understand the role and function of LDs in RNA metabolism in hMDMs, particularly during Mtb infection.

Aside from RNA metabolism, significant alterations were also detected in the abundance of cytoskeletal proteins in LDs upon Mtb infection. The abundance of tubulin beta subunits (TUBBs) was significantly decreased in LDs from Mtb-infected hMDMs (Fig. 41). Given the role of tubulins in LD transport and interaction with other organelles, a decrease in TUBB presence on LDs upon infection can have substantial effects on intracellular LD motility and dynamics[273]. Importantly, it is noteworthy that other cytoskeletal transport proteins belonging to the myosin and dynein complex (MYL6 and DYNC1LI1) were significantly more abundant on LDs upon Mtb infection (Suppl. fig. 7). This is another indicator that LD motility is altered upon Mtb infection. Interestingly, several mitochondrial proteins, for example, SOD2 or the cytochrome c oxidase subunit 4 isoform 1 (COX4I1), were found to be significantly enriched in LDs from Mtb-infected hMDMs. This suggests that upon Mtb infection, the altered motility of LDs could result in an increased interaction with mitochondria, which has been proposed to affect mitochondrial metabolism before[274,275]. Based on these findings it is intriguing to speculate that metabolic alterations in fatty acid metabolism are rather regulated through altered subcellular LD localization and interaction with other organelles rather than changes in protein expression levels. However, high-resolution microscopy-based analyses are required to further investigate a potential LD-mitochondria contact and changes to LD dynamics upon Mtb infection.

Collectively, proteomics analysis identified an altered abundance of proteins involved in RNA metabolism suggesting an alternative function of LDs in RNA processing during Mtb infection. Furthermore, alterations of proteins linked to transport and contact with other organelles suggest that upon Mtb infection LD motility and subcellular localization is significantly altered in hMDMs.

5.3 Concluding remarks

The findings in this study provide a detailed characterization of the effects of an Mtb infection on the metabolism of primary human macrophages using a broad spectrum of analytical approaches. The results demonstrate that Mtb infection of hMDMs results in the induction of respiration driven by an increased oxidation of free fatty acids, which may promote oxidative stress and inflammatory responses, such as the production of type-1-IFNs. This suggests that inhibition of fatty acid oxidation and respiration might be an interesting target for host-directed therapy against TB, as has been postulated before.

Moreover, this study describes a protocol for the successful isolation of LDs from primary human macrophages. Detailed lipidomic characterization of LDs demonstrated that there is a subcellular enrichment of neutral lipids in LDs of Mtb infected hMDMs, which could enhance the availability of host-derived nutrients for Mtb survival in macrophages. Furthermore, alterations in the protein composition of LDs indicate that LDs not only act as mere stores for neutral lipids but may also be involved in mediating the immune response of hMDMs during Mtb infection.

Taken together this doctoral study broadens our understanding of the role of LDs during Mtb infection in primary human macrophages. This study shows that hMDMs undergo significant global reprogramming of glycolytic, respiratory as well as lipid metabolism in response to an infection with Mtb. This might have important implications for the development of host-directed therapy approaches targeting macrophage metabolism and personalized treatment of TB.

Supplementary figures

#	Gene name	log2FC (Mtb/UI)	#	Gene name	log2FC (Mtb/UI)	#	Gene name	log2FC (Mtb/UI)
1	BTN3A3	3	**45**	RPL4	-0.78	**89**	SURF1	0.84
2	ALAS1	0.4	**46**	TMPO	0.4	**90**	MRPL14	0.82
3	MRPL13	0.88	**47**	GNPDA1	-0.47	**91**	NLRX1	-0.4
4	STAT1	2.15	**48**	NPEPPS	-0.27	**92**	GIMAP1	0.35
5	PPP1R9B	0.37	**49**	RPL31	-0.3	**93**	MYH2	-0.27
6	ACOX3	0.7	**50**	PPIA	-0.56	**94**	RBM25	0.32
7	HLA-DPB1	0.2	**51**	TAP1	0.98	**95**	FCN1	1.32
8	PSMB5	-0.45	**52**	BST2	0.5	**96**	TAP2	0.37
9	PLSCR1	0.63	**53**	EFTUD2	0.18	**97**	LAMTOR1	0.73
10	OAS1	0.45	**54**	Sep 07	-0.47	**98**	IL4I1	0.51
11	ICAM1	0.77	**55**	PARP14	1.01	**99**	ISCU	0.79
12	HLA-DPA1	1.31	**56**	RAB42	0.07	**100**	ACSL5	0.81
13	MATR3	0.2	**57**	PLGRKT	0.32	**101**	MTHFD2	0.87
14	PARP9	0.93	**58**	FARSB	-0.41	**102**	SDC2	0.82
15	NDRG2	-0.51	**59**	NCF1	1.1	**103**	RPS9	-0.49
16	CEBPB	0.94	**60**	TMEM33	-0.72	**104**	MECP2	0.42
17	NPTN	0.64	**61**	NDUFAF7	0.36	**105**	ATP13A3	0.81
18	SLC2A3	0.82	**62**	RAB24	0.5	**106**	TXNRD2	0.55
19	ITGB5	-0.43	**63**	MTFP1	0.61	**107**	HLA-DRB1	1.56
20	MARCKS	0.62	**64**	NRP1	0.34	**108**	SLC30A6	0.13
21	UNC13D	0.31	**65**	SPCS2	0.59	**109**	HINT2	0.3
22	CD163	-0.63	**66**	HTATSF1	0.95	**110**	SEC22B	0.36
23	ABI1	0.34	**67**	PAPSS2	0.28	**111**	LMNA	0.2
24	CPSF7	0.2	**68**	HLA-B	0.67	**112**	AGFG1	0.61
25	VPS4A	0.1	**69**	SOD2	1.5	**113**	VARS2	0.29
26	HLA-H	1.35	**70**	FAH	-0.46	**114**	ALG2	0.35
27	SNRNP200	0.28	**71**	ITGA3	-0.23	**115**	SCPEP1	0.59
28	ATP2A2	0.6	**72**	HLA-F	1.01	**116**	ZW10	0.35
29	ARPC4	-0.31	**73**	MRPS36	0.53	**117**	COPB2	0.56
30	LGALS3BP	1.88	**74**	CUL3	0	**118**	STAT3	0.6
31	PNPT1	0.48	**75**	CYFIP1	-0.48	**119**	CLPB	0.46
32	SLC2A6	1.09	**76**	CD274	1.59	**120**	ACOX1	0.7
33	ALDH2	0.83	**77**	THRAP3	0.39	**121**	SPG7	0.77
34	ARL6IP1	-0.95	**78**	PLBD1	0.25	**122**	MYO1C	0.5
35	LEPRE1	0.08	**79**	PRPF4B	0.39	**123**	FTH1	0.31
36	TMED10	0.52	**80**	CARKD	0.5	**124**	GAPDH	-0.38
37	ATP11A	0.55	**81**	SDF2L1	0.49	**125**	HSPD1	0.38
38	TXNIP	0.35	**82**	EMC3	0.33	**126**	EIF5A	-0.51
39	TMEM165	0.41	**83**	DNAJB11	0.33	**127**	HNRNPR	0.3
40	HLA-DRB5	0.74	**84**	ACSL4	0.37	**128**	PTPN1	0.89
41	UAP1L1	-0.66	**85**	FABP3	-0.66	**129**	TYMP	0.56
42	GPAA1	0.41	**86**	LAP3	0.9	**130**	NOMO3	0.4

43	PDCD6	-0.5	**87**	PRDX6	-0.37			
44	HLA-DRA	1.7	**88**	PLAUR	0.43			

Supplementary figure 1: List of significantly regulated proteins in Mtb-infected hMDMs compared to uninfected cells.

Human monocyte-derived macrophages were infected with Mtb at an MOI of 0.1 or left untreated for 7 days. Subsequently, cells were lysed, digested and liquid chromatography-based approach was performed to determine relative protein levels using label-free proteomics. A paired t-test followed by a Benjamini & Hochberg correction was used to determine significantly regulated proteins between Mtb-infected hMDMs compared to uninfected hMDMs ($p<0.05$). Depicted is the list of significantly regulated proteins including the log2FC of the mean LFQ intensities in Mtb-infected versus uninfected hMDMs (n=5). For the gene names please refer to the UniProt knowledgebase[276]. Proteins of particular interest were also described in the text.

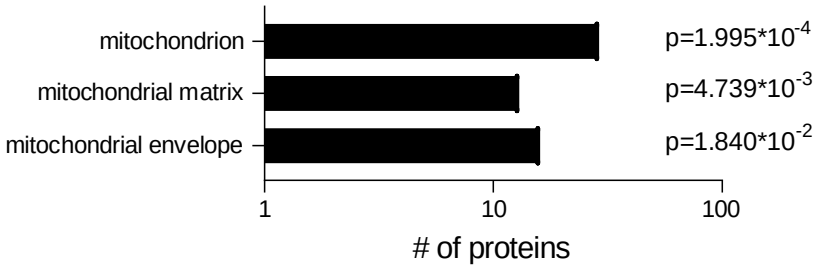

Supplementary Fig. 2: Differentially regulated proteins in Mtb-infected hMDMs are found in cellular components associated with mitochondria.

Human monocyte-derived macrophages were infected with Mtb at an MOI of 0.1 or left untreated for 7 days. Subsequently, cells were lysed, digested and liquid chromatography-based approach was performed to determine relative protein levels using label-free proteomics. A paired t-test was used to determine differentially regulated proteins between Mtb-infected hMDMs compared to uninfected hMDMs ($p<0.05$). Depicted is the fold-change of selected upregulated proteins ($p < 0.05$), which related to mitochondria, in Mtb-infected hMDMs compared uninfected cells (n=5).

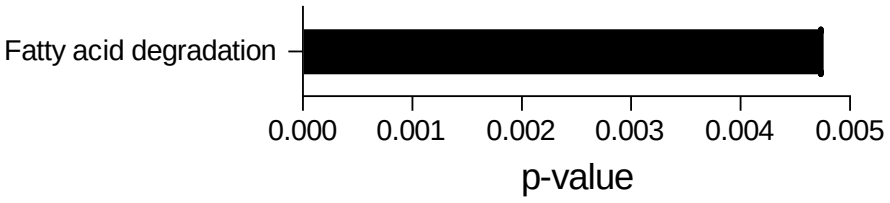

Supplementary figure 3: Fatty acid degradation is altered upon Mtb infection of human macrophages.

Human monocyte-derived macrophages were infected with Mtb at an MOI of 0.1 or left untreated for 7 days. Subsequently, cells were lysed, digested and liquid chromatography-based approach was performed to determine relative protein levels using label-free proteomics. A paired t-test was used to determine differentially regulated proteins between Mtb-infected hMDMs compared to uninfected hMDMs ($p<0.05$). Pathway enrichment analysis was performed and differentially regulated proteins were compared to the KEGG database using the online tool g:profiler. Depicted are the top 10 significantly enriched pathways ($p < 0.05$) in Mtb-infected hMDMs.

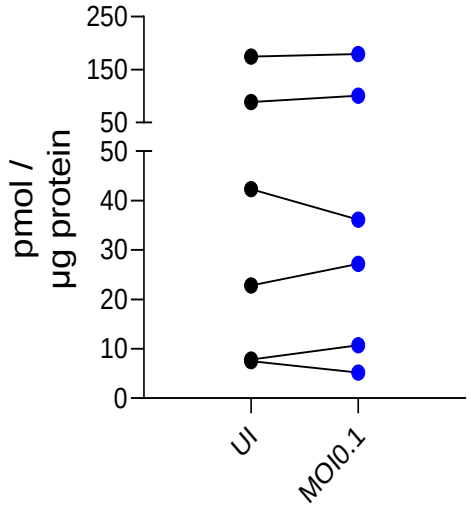

Supplementary figure 4: Total neutral lipid levels are unchanged upon Mtb infection of hMDMs.

Human monocyte-derived macrophages infected with Mtb at an MOI of 0.1 and 0.5 or left untreated for 7 days, subsequently lysed in methanol and total lipids were extracted according to the MTBE-method. Subsequently, mass spectrometry was used to quantify the total abundance (pmol/µg protein) of TAG, DAG and CE. Depicted are total neutral lipid levels, i.e. the sum of TAG, DAG and CE (n=6).

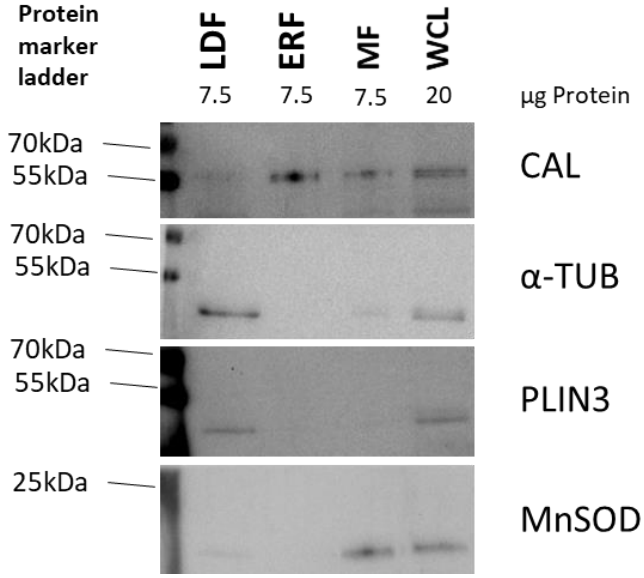

Supplementary figure 5: Western Blot analysis of the fractionation.

Human monocyte-derived macrophages were incubated for 7 days, lysed and subsequently, the MF, ERF and LDF were isolated from the WCL. SDS lysis buffer was added to each fraction and SDS-PAGE followed by a Western Blot analysis was performed. Antibodies against MnSOD, CAL, α-TUB and PLIN3 were used to measure the protein expression using a chemiluminescence detection approach on the Chemidoc Imaging System. Depicted is a representative image of the MnSOD, CAL, α-TUB and PLIN3 protein bands in the WCL, MF, ERF and LDF (n=1).

A)

name	# of proteins
Total quantifiable proteins	2415
≥4 uninfected donors	2292
5 uninfected donors	1960
log2FC <0 Mtb/UI	88
log2FC >0 Mtb/UI	65

B)

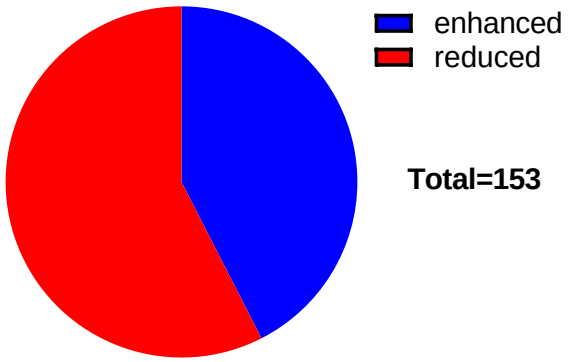

Supplementary figure 6: Number of quantifiable proteins in the LDF from primary human macrophages.
Human monocyte-derived macrophages were infected with Mtb at an MOI of 0.1 or left untreated (UI) for 7 days and cells were lysed and the LDF were isolated from the WCL as described in section 3.2.8. Subsequently, samples were digested and liquid chromatography-based approach was performed to determine relative protein levels using label-free proteomics. A paired t-test followed by a Benjamini-Hochberg correction was used to determine differentially regulated proteins in the LDF between Mtb-infected hMDMs compared to uninfected hMDMs ($p<0.05$). **A)** Depicted is the total number of quantifiable proteins in the number of proteins detected in all 5 or ≥4 donors in the LDF isolated from uninfected hMDMs. **B)** Furthermore, a paired t-test followed by a Benjamini-Hochberg correction was used to determine differentially regulated proteins in the LDF between Mtb-infected hMDMs compared to uninfected hMDMs ($p<0.05$). Depicted is the total number of significantly regulated proteins, with a log2FC <0 (reduced presence) or >0 (enhanced presence) in Mtb compared to UI (Mtb/UI) cells (n=5).

#	Gene name	log2FC (Mtb/UI)	#	Gene name	log2FC (Mtb/UI)	#	Gene name	log2FC (Mtb/UI)
1	LYZ	0.94	**52**	USP47	-0.21	**103**	LMNB2	0.78
2	PSMB9	0.48	**53**	PSMB10	0.73	**104**	PDS5A	0.22
3	STAT3	0.91	**54**	SOD2	1.74	**105**	ERP44	0.33
4	RPA1	0.53	**55**	GM2A	0.36	**106**	GSTP1	-0.28
5	LAP3	0.54	**56**	PDIA6	0.51	**107**	PPP5C	-0.54
6	RCN1	0.74	**57**	CNPY3	0.77	**108**	FN1	0.85
7	CLASP2	-0.36	**58**	SYNCRIP	-0.18	**109**	SCPEP1	0.53
8	MIA2	0.87	**59**	PARP1	-0.12	**110**	BTF3	-0.13
9	HLA-DRB5	1.43	**60**	GCHFR	-0.52	**111**	PPP2R1A	-0.38
10	CPNE2	-0.11	**61**	RAB5B	-0.27	**112**	HNRNPUL2	-0.31
11	AK4	0.46	**62**	HNRNPK	-0.40	**113**	ANP32B	-0.17
12	INPPL1	-0.37	**63**	TUBB4B	-0.44	**114**	VSIG4	-0.35
13	PRPSAP2	-0.50	**64**	HP1BP3	-1.14	**115**	PPM1G	-0.12
14	HNRNPM	-0.59	**65**	CCNY	-1.14	**116**	IFIT1	0.97
15	FCSK	-0.20	**66**	MYG1	-0.48	**117**	SUMO2	0.77
16	ARHGAP18	-0.26	**67**	GBP1	2.00	**118**	SLC35B2	0.41
17	GDAP2	-0.02	**68**	STAT1	2.12	**119**	CORO1C	-0.16
18	SEPTIN9	-0.41	**69**	PPP6R2	-0.08	**120**	HNRNPH2	-0.47
19	RAB5A	-0.44	**70**	S100A6	0.20	**121**	CAPG	-0.46
20	CALU	0.40	**71**	PCNA	0.75	**122**	TGOLN2	1.20
21	CALU	0.40	**72**	MRC1	0.59	**123**	CYTH1	0.50
22	TTC37	-0.79	**73**	TUBB	-0.45	**124**	THOC2	0.28
23	RPS24	-0.51	**74**	SH3GLB1	-0.22	**125**	m	0.26
24	TAPBP	0.95	**75**	PGK1	-0.58	**126**	OSBP	-0.01
25	NAPA	0.23	**76**	PSMB5	-0.30	**127**	CUL3	-0.47
26	BTK	0.22	**77**	EIF4A1	-0.38	**128**	PIK3C3	-0.44
27	BROX	-0.56	**78**	FKBP15	-0.30	**129**	DCPS	-0.56
28	GATD1	-0.14	**79**	NCF1	0.95	**130**	OSBPL11	-0.70
29	PPP1R2B	-0.42	**80**	MX1	2.96	**131**	UBXN6	-0.47
30	MAP7D1	-0.36	**81**	HSPE1	0.54	**132**	GLA	0.49
31	HNRNPH1	-0.26	**82**	DNAJC3	0.44	**133**	ACLY	-0.34
32	UQCRC2	0.97	**83**	PDCD10	0.24	**134**	ILF2	-0.25
33	PPP2R5D	0.12	**84**	CTNND1	-0.47	**135**	KPNB1	-0.27
34	CDIPT	-0.06	**85**	PIK3R1	-0.11	**136**	ARMT1	-0.26
35	TUBB2A	-0.17	**86**	MTREX	-0.08	**137**	ATOX1	0.65
36	ENOSF1	-0.65	**87**	C20orf27	-0.60	**138**	HLA-DPA1	1.01
37	NADK	0.53	**88**	RABGEF1	-0.09	**139**	RAPGEF1	-0.36
38	HLA-DRA	1.23	**89**	DBNL	-0.55	**140**	TUBB3	-0.46
39	HLA-DRB1	1.11	**90**	PLAUR	0.55	**141**	ICAM1	0.59
40	PRKCSH	0.83	**91**	MAP2K4	-0.36	**142**	TPR	0.53
41	TYMP	0.91	**92**	DPYSL2	-0.21	**143**	COX4I1	0.40
42	TAP1	0.77	**93**	VPS36	-0.02	**144**	OAS2	2.09
43	TOR1AIP2	0.47	**94**	ARHGAP45	-0.04	**145**	GBP2	0.51
44	TRNT1	0.16	**95**	SNX18	-0.09	**146**	ACOX1	0.46
45	MGST3	-0.12	**96**	SORT1	-0.05	**147**	ALDH1B1	-0.38

46	UMPS	-0.42	**97**	SLC12A9	-1.02	**148**	RPS18	-0.24
47	IMPDH1	-0.12	**98**	HDHD2	-0.55	**149**	FGD4	-0.31
48	AHCY	-0.23	**99**	USP24	-0.11	**150**	RTCA	-0.36
49	NPEPPS	-0.42	**100**	ACADVL	0.48	**151**	CCT6A	0.10
50	RAB4B	-0.62	**101**	STAT2	1.29	**152**	SNX17	-0.18
51	RPL23	-0.31	**102**	MYL6	0.42	**153**	PML	0.38

Supplementary figure 7: List of significantly regulated proteins in the LDF isolated from Mtb-infected hMDMs compared to uninfected cells.

Human monocyte-derived macrophages were infected with Mtb at an MOI of 0.1 or left untreated (UI) for 7 days and cells were lysed and the LDF were isolated from the WCL as described in the methods. Subsequently, samples were digested and liquid chromatography-based approach was performed to determine relative protein levels using label-free proteomics. A paired t-test followed by a Benjamini & Hochberg correction was used to determine differentially regulated proteins in the LDF between Mtb-infected hMDMs compared to uninfected hMDMs ($p<0.05$). Depicted is the list of significantly regulated proteins including the log2FC of the mean LFQ intensities in Mtb-infected versus uninfected hMDMs (n=5). For the gene names please refer to the UniProt knowledgebase[276]. Proteins of particular interest were also described in the text.

Summary

Mycobacterium tuberculosis (Mtb) is still a major cause of illness and death globally. Better understanding of the interaction of Mtb with its primary host cell, the macrophage, could help to understand human tuberculosis (TB) pathogenesis. Mtb infection is known to cause perturbations in macrophage metabolism, such as accumulation of fatty acids leading to foam cell formation. However, the exact metabolic changes during Mtb infection, particularly in human macrophages, are not well characterized. Thus, this doctoral study investigates the effects of Mtb infection on cellular metabolism in human monocyte-derived macrophages (hMDMs). When Mtb is actively replicating in hMDMs, glycolytic metabolism was substantially induced as demonstrated by extracellular flux analyses and protein expression analyses of glycolytic proteins. Similarly, an increased respiratory metabolism, upregulation of mitochondrial ATP production rate as well as an increase in mitochondrial membrane potential were observed in hMDMs during Mtb infection. In parallel, RT-PCR and proteomics revealed a significant reduction in mitochondrial DNA levels and an increased expression of mitochondrial proteins during Mtb infection indicating structural alterations in mitochondria. Moreover, Mtb infection increased the dependency of cells on fatty acids, which is in line with the increased expression of proteins involved in peroxisomal and mitochondrial fatty acid degradation. Mass spectrometry-based analysis revealed a substantial reduction in total free fatty acid levels in Mtb-infected hMDMs, suggesting that fatty acids levels are decreased due to enhanced fatty acid degradation. Interestingly, incubating cells with exogenous fatty acids induces neutral lipid levels and cell death, and promotes Mtb growth in hMDMs. Importantly, however, Mtb infection alone did alter lipid levels on a whole-cell level, which prompted the analysis of the subcellular levels of neutral lipids in lipid droplets (LDs). To do so, an LD-enriched fraction was isolated from hMDMs and its composition compared to other organelle fractions using lipidomic and Western Blot analysis. In LDs from Mtb-infected hMDMs, a substantial enrichment of triacylglycerols, but also distinct diacylglycerol and cholesterol esters, was detected. Analyzing the protein composition of LDs from Mtb-infected hMDMs revealed alterations in the enrichment of proteins involved in RNA metabolism and cytoskeletal arrangement, but also of proteins involved in the immune response, such as type-1 interferon signaling. Taken together, these data suggest that LDs not only act as lipid stores but also seem to be involved in the immune cell signaling during an Mtb infection. In conclusion, this doctoral study revealed that Mtb infection induces a significant metabolic reprogramming of glycolytic, respiratory and fatty acid metabolism, which might facilitate Mtb growth in primary human macrophages.

Zusammenfassung

Mycobacterium tuberculosis (Mtb) gehört nach wie vor zu den Hauptkrankheits- und Todesursachen weltweit. Ein besseres Verständnis der Interaktion von Mtb mit seiner primären Wirtszelle, dem Makrophagen, könnte dazu beitragen, die Pathogenese der Tuberkulose (TB) genauer zu verstehen. Es ist bekannt, dass eine Mtb-Infektion zu Störungen des Makrophagenstoffwechsels führt, was die Anhäufung von Fettsäuren und die Bildung von Schaumzellen fördert. Die genauen Veränderungen des Metabolismus während einer Mtb-Infektion, insbesondere in humanen Makrophagen, sind jedoch nicht gut charakterisiert. In dieser Doktorarbeit werden daher die Auswirkungen einer Mtb-Infektion auf den Zellstoffwechsel in primären humanen Makrophagen (hMs) untersucht. Wenn Mtb aktiv in hMs repliziert, wurde ein erheblich gesteigerter glykolytischer Stoffwechsel festgestellt, wie extrazelluläre Fluxanalysen und Proteinexpressionsanalysen von glykolytischen Proteinen zeigten. Gleichzeitig wurden in hMs während der Infektion auch eine erhöhte Respiration und eine Hochregulierung der mitochondrialen ATP-Produktionsrate, sowie des mitochondrialen Membranpotenzials beobachtet. Darüber hinaus erhöhte die Mtb-Infektion die Abhängigkeit der Makrophagen von Fettsäuren, sowie die Expression von Proteinen des peroxisomalen und mitochondrialen Fettsäureabbaus. Massenspektrometrische Analysen ergaben eine erhebliche Reduktion der freien Fettsäuren in Mtb-infizierten hMs, was auf einen verstärkten Fettsäureabbau hindeuten könnte. Interessanterweise führte die Inkubation von Mtb-infizierten Zellen mit exogenen Fettsäuren zu einer Anreicherung von Neutrallipiden und erhöhtem Zelltod, was das Mtb-Wachstum fördert. Eine Mtb-Infektion alleine, führte jedoch nicht zu einer Anreicherung von Neutrallipiden auf Gesamtzellebene. Deshalb wurden die subzelluläre Konzentration von Lipiden in den primären Lipidspeicherorganellen, den Lipidkörpern (LKs), analysiert. Zu diesem Zweck wurde eine mit LKs angereicherte Fraktion aus hMs isoliert und die Zusammensetzung mit anderen Organellfraktionen mittels Lipidom- und Western-Blot-Analysen verglichen. In den LKs führte eine Mtb-Infektion zu einer erheblichen Anreicherung sowohl von Di- und Triacylglyceriden, als auch von Cholesterolestern. Mittels Proteom-Analysen wurden nach der Mtb-Infektion eine veränderte Anreicherung von Proteinen, die unter anderem an Immunantworten und am RNA-Metabolismus beteiligt sind, in LKs festgestellt. Die Daten dieser Arbeit deuten darauf hin, dass LKs nicht nur als Lipidspeicher fungieren, sondern auch an der Regulation der Immunantwort während einer Mtb-Infektion beteiligt sind. Zusammenfassend zeigt diese Doktorarbeit, dass eine Mtb-Infektion zu einer Umprogrammierung des glykolytischen und respiratorischen Metabolismus führt. Insbesondere die Veränderungen des Fettsäurestoffwechsels können dabei einen positiven Einfluss auf das Mtb-Wachstum in primären humanen Makrophagen haben.

Bibliography

(1) World Health Organization. Global tuberculosis report 2021 https://www.who.int/publications/digital/global-tuberculosis-report-2021 (accessed 2022 -01 -12).

(2) Phelan, J. J.; McQuaid, K.; Kenny, C.; Gogan, K. M.; Cox, D. J.; Basdeo, S. A.; O'Leary, S.; Tazoll, S. C.; Ó Maoldomhnaigh, C.; O'Sullivan, M. P.; O'Neill, L. A.; O'Sullivan, M. J.; Keane, J. Desferrioxamine Supports Metabolic Function in Primary Human Macrophages Infected With Mycobacterium Tuberculosis. *Frontiers in Immunology* **2020**, *11*, 836. https://doi.org/10.3389/fimmu.2020.00836.

(3) Burrill, J.; Williams, C. J.; Bain, G.; Conder, G.; Hine, A. L.; Misra, R. R. Tuberculosis: A Radiologic Review. *RadioGraphics* **2007**, *27* (5), 1255–1273. https://doi.org/10.1148/rg.275065176.

(4) Loddenkemper, R.; Lipman, M.; Zumla, A. Clinical Aspects of Adult Tuberculosis. *Cold Spring Harb Perspect Med* **2016**, *6* (1), a017848. https://doi.org/10.1101/cshperspect.a017848.

(5) Behr, M. A.; Edelstein, P. H.; Ramakrishnan, L. Revisiting the Timetable of Tuberculosis. *BMJ* **2018**, *362*, k2738. https://doi.org/10.1136/bmj.k2738.

(6) Heemskerk, D.; Caws, M.; Marais, B.; Farrar, J. *Tuberculosis in Adults and Children*; Wellcome Trust–Funded Monographs and Book Chapters; Springer: London, 2015.

(7) Campbell, I. A.; Bah-Sow, O. Pulmonary Tuberculosis: Diagnosis and Treatment. *BMJ* **2006**, *332* (7551), 1194–1197. https://doi.org/10.1136/bmj.332.7551.1194.

(8) Hall, R. G.; Leff, R. D.; Gumbo, T. Treatment of Active Pulmonary Tuberculosis in Adults: Current Standards and Recent Advances. *Pharmacotherapy* **2009**, *29* (12), 1468–1481. https://doi.org/10.1592/phco.29.12.1468.

(9) Pontali, E.; Raviglione, M. C.; Migliori, G. B. Regimens to Treat Multidrug-Resistant Tuberculosis: Past, Present and Future Perspectives. *European Respiratory Review* **2019**, *28* (152). https://doi.org/10.1183/16000617.0035-2019.

(10) Patterson, B.; Wood, R. Is Cough Really Necessary for TB Transmission? *Tuberculosis (Edinb)* **2019**, *117*, 31–35. https://doi.org/10.1016/j.tube.2019.05.003.

(11) Ehlers, S.; Schaible, U. E. The Granuloma in Tuberculosis: Dynamics of a Host–Pathogen Collusion. *Front Immunol* **2013**, *3*, 411. https://doi.org/10.3389/fimmu.2012.00411.

(12) Lin, P. L.; Plessner, H. L.; Voitenok, N. N.; Flynn, J. L. Tumor Necrosis Factor and Tuberculosis. *J Investig Dermatol Symp Proc* **2007**, *12* (1), 22–25. https://doi.org/10.1038/sj.jidsymp.5650027.

(13) Flynn, J. L.; Chan, J.; Lin, P. L. Macrophages and Control of Granulomatous Inflammation in Tuberculosis. *Mucosal Immunol* **2011**, *4* (3), 271–278. https://doi.org/10.1038/mi.2011.14.

(14) Ndlovu, H.; Marakalala, M. J. Granulomas and Inflammation: Host-Directed Therapies for Tuberculosis. *Frontiers in Immunology* **2016**, *7*, 434. https://doi.org/10.3389/fimmu.2016.00434.

(15) Gideon, H. P.; Phuah, J.; Myers, A. J.; Bryson, B. D.; Rodgers, M. A.; Coleman, M. T.; Maiello, P.; Rutledge, T.; Marino, S.; Fortune, S. M.; Kirschner, D. E.; Lin, P. L.; Flynn, J. L. Variability in Tuberculosis Granuloma T Cell Responses Exists, but a Balance of Pro- and Anti-Inflammatory Cytokines Is Associated with Sterilization. *PLoS Pathog* **2015**, *11* (1), e1004603. https://doi.org/10.1371/journal.ppat.1004603.

(16) Herbst, S.; Schaible, U. E.; Schneider, B. E. Interferon Gamma Activated Macrophages Kill Mycobacteria by Nitric Oxide Induced Apoptosis. *PLOS ONE* **2011**, *6* (5), e19105. https://doi.org/10.1371/journal.pone.0019105.

(17) Khan, T. A.; Mazhar, H.; Saleha, S.; Tipu, H. N.; Muhammad, N.; Abbas, M. N. Interferon-Gamma Improves Macrophages Function against M. Tuberculosis in

Multidrug-Resistant Tuberculosis Patients. *Chemotherapy Research and Practice* **2016**, *2016*, e7295390. https://doi.org/10.1155/2016/7295390.

(18) Robinson, C. M.; O'Dee, D.; Hamilton, T.; Nau, G. J. Cytokines Involved in Interferon-γ Production by Human Macrophages. *JIN* **2010**, *2* (1), 56–65. https://doi.org/10.1159/000247156.

(19) Loxton, A. G. Bcells and Their Regulatory Functions during Tuberculosis: Latency and Active Disease. *Molecular Immunology* **2019**, *111*, 145–151. https://doi.org/10.1016/j.molimm.2019.04.012.

(20) Russell, D. G.; Barry, C. E.; Flynn, J. L. Tuberculosis: What We Don't Know Can, and Does, Hurt Us. *Science* **2010**, *328* (5980), 852–856. https://doi.org/10.1126/science.1184784.

(21) Alatas, F.; Alatas, Ö.; Metintas, M.; Özarslan, A.; Erginel, S.; Yildirim, H. Vascular Endothelial Growth Factor Levels in Active Pulmonary Tuberculosis. *CHEST* **2004**, *125* (6), 2156–2159. https://doi.org/10.1378/chest.125.6.2156.

(22) Russell, D. G.; Cardona, P.-J.; Kim, M.-J.; Allain, S.; Altare, F. Foamy Macrophages and the Progression of the Human Tuberculosis Granuloma. *Nat Immunol* **2009**, *10* (9), 943–948. https://doi.org/10.1038/ni.1781.

(23) Reiling, N.; Homolka, S.; Kohl, T. A.; Steinhäuser, C.; Kolbe, K.; Schütze, S.; Brandenburg, J. Shaping the Niche in Macrophages: Genetic Diversity of the M. Tuberculosis Complex and Its Consequences for the Infected Host. *Int J Med Microbiol* **2018**, *308* (1), 118–128. https://doi.org/10.1016/j.ijmm.2017.09.009.

(24) Ulrichs, T.; Kaufmann, S. H. New Insights into the Function of Granulomas in Human Tuberculosis. *The Journal of Pathology* **2006**, *208* (2), 261–269. https://doi.org/10.1002/path.1906.

(25) Eum, S.-Y.; Kong, J.-H.; Hong, M.-S.; Lee, Y.-J.; Kim, J.-H.; Hwang, S.-H.; Cho, S.-N.; Via, L. E.; Barry, C. E. Neutrophils Are the Predominant Infected Phagocytic Cells in the Airways of Patients With Active Pulmonary TB. *Chest* **2010**, *137* (1), 122–128. https://doi.org/10.1378/chest.09-0903.

(26) Corleis, B.; Korbel, D.; Wilson, R.; Bylund, J.; Chee, R.; Schaible, U. E. Escape of Mycobacterium Tuberculosis from Oxidative Killing by Neutrophils. *Cellular Microbiology* **2012**, *14* (7), 1109–1121. https://doi.org/10.1111/j.1462-5822.2012.01783.x.

(27) Pagán, A. J.; Ramakrishnan, L. Immunity and Immunopathology in the Tuberculous Granuloma. *Cold Spring Harb Perspect Med* **2015**, *5* (9), a018499. https://doi.org/10.1101/cshperspect.a018499.

(28) Keane, J.; Gershon, S.; Wise, R. P.; Mirabile-Levens, E.; Kasznica, J.; Schwieterman, W. D.; Siegel, J. N.; Braun, M. M. Tuberculosis Associated with Infliximab, a Tumor Necrosis Factor α–Neutralizing Agent. *N Engl J Med* **2001**, *345* (15), 1098–1104. https://doi.org/10.1056/NEJMoa011110.

(29) Lalvani, A.; Millington, K. A. T Cells and Tuberculosis: Beyond Interferon-γ. *The Journal of Infectious Diseases* **2008**, *197* (7), 941–943. https://doi.org/10.1086/529049.

(30) Pai, M.; Behr, M. A.; Dowdy, D.; Dheda, K.; Divangahi, M.; Boehme, C. C.; Ginsberg, A.; Swaminathan, S.; Spigelman, M.; Getahun, H.; Menzies, D.; Raviglione, M. Tuberculosis. *Nat Rev Dis Primers* **2016**, *2* (1), 1–23. https://doi.org/10.1038/nrdp.2016.76.

(31) Wu, M.; Aung, H.; Hirsch, C. S.; Toossi, Z. Inhibition of Mycobacterium Tuberculosis-Induced Signalling by Transforming Growth Factor-β in Human Mononuclear Phagocytes. *Scandinavian Journal of Immunology* **2011**, *75* (3), 301–304. https://doi.org/10.1111/j.1365-3083.2011.02668.x.

(32) Queval, C. J.; Brosch, R.; Simeone, R. The Macrophage: A Disputed Fortress in the Battle against Mycobacterium Tuberculosis. *Frontiers in Microbiology* **2017**, *8*, 2284. https://doi.org/10.3389/fmicb.2017.02284.
(33) de Martino, M.; Lodi, L.; Galli, L.; Chiappini, E. Immune Response to Mycobacterium Tuberculosis: A Narrative Review. *Frontiers in Pediatrics* **2019**, *7*, 350. https://doi.org/10.3389/fped.2019.00350.
(34) Meena, L. S.; Rajni. Survival Mechanisms of Pathogenic Mycobacterium Tuberculosis H37Rv. *The FEBS Journal* **2010**, *277* (11), 2416–2427. https://doi.org/10.1111/j.1742-4658.2010.07666.x.
(35) Glickman, M. S.; Jacobs, W. R. Microbial Pathogenesis of Mycobacterium Tuberculosis: Dawn of a Discipline. *Cell* **2001**, *104* (4), 477–485. https://doi.org/10.1016/S0092-8674(01)00236-7.
(36) Jee, B. Understanding the Early Host Immune Response against Mycobacterium Tuberculosis. *Cent Eur J Immunol* **2020**, *45* (1), 99–103. https://doi.org/10.5114/ceji.2020.94711.
(37) Moreira-Teixeira, L.; Mayer-Barber, K.; Sher, A.; O'Garra, A. Type I Interferons in Tuberculosis: Foe and Occasionally Friend. *Journal of Experimental Medicine* **2018**, *215* (5), 1273–1285. https://doi.org/10.1084/jem.20180325.
(38) Zhang, L.; Jiang, X.; Pfau, D.; Ling, Y.; Nathan, C. F. Type I Interferon Signaling Mediates Mycobacterium Tuberculosis–Induced Macrophage Death. *Journal of Experimental Medicine* **2020**, *218* (2), e20200887. https://doi.org/10.1084/jem.20200887.
(39) Liu, C. H.; Liu, H.; Ge, B. Innate Immunity in Tuberculosis: Host Defense vs Pathogen Evasion. *Cell Mol Immunol* **2017**, *14* (12), 963–975. https://doi.org/10.1038/cmi.2017.88.
(40) Teles, R. M. B.; Graeber, T. G.; Krutzik, S. R.; Montoya, D.; Schenk, M.; Lee, D. J.; Komisopoulou, E.; Kelly-Scumpia, K.; Chun, R.; Iyer, S. S.; Sarno, E. N.; Rea, T. H.; Hewison, M.; Adams, J. S.; Popper, S. J.; Relman, D. A.; Stenger, S.; Bloom, B. R.; Cheng, G.; Modlin, R. L. Type I Interferon Suppresses Type II Interferon–Triggered Human Anti-Mycobacterial Responses. *Science* **2013**, *339* (6126), 1448–1453. https://doi.org/10.1126/science.1233665.
(41) Chang, S. T.; Linderman, J. J.; Kirschner, D. E. Multiple Mechanisms Allow Mycobacterium Tuberculosis to Continuously Inhibit MHC Class II-Mediated Antigen Presentation by Macrophages. *PNAS* **2005**, *102* (12), 4530–4535. https://doi.org/10.1073/pnas.0500362102.
(42) Gleeson, L. E.; Sheedy, F. J.; Palsson-McDermott, E. M.; Triglia, D.; O'Leary, S. M.; O'Sullivan, M. P.; O'Neill, L. A. J.; Keane, J. Cutting Edge: Mycobacterium Tuberculosis Induces Aerobic Glycolysis in Human Alveolar Macrophages That Is Required for Control of Intracellular Bacillary Replication. *The Journal of Immunology* **2016**, *196* (6), 2444–2449. https://doi.org/10.4049/jimmunol.1501612.
(43) Hackett, E. E.; Charles-Messance, H.; O'Leary, S. M.; Gleeson, L. E.; Muñoz-Wolf, N.; Case, S.; Wedderburn, A.; Johnston, D. G. W.; Williams, M. A.; Smyth, A.; Ouimet, M.; Moore, K. J.; Lavelle, E. C.; Corr, S. C.; Gordon, S. V.; Keane, J.; Sheedy, F. J. Mycobacterium Tuberculosis Limits Host Glycolysis and IL-1β by Restriction of PFK-M via MicroRNA-21. *Cell Rep* **2020**, *30* (1), 124-136.e4. https://doi.org/10.1016/j.celrep.2019.12.015.
(44) Viola, A.; Munari, F.; Sánchez-Rodríguez, R.; Scolaro, T.; Castegna, A. The Metabolic Signature of Macrophage Responses. *Frontiers in Immunology* **2019**, *10*, 1462. https://doi.org/10.3389/fimmu.2019.01462.
(45) Genoula, M.; Franco, J. L. M.; Maio, M.; Dolotowicz, B.; Ferreyra, M.; Milillo, M. A.; Mascarau, R.; Moraña, E. J.; Palmero, D.; Matteo, M.; Fuentes, F.; López, B.; Barrionuevo, P.; Neyrolles, O.; Cougoule, C.; Lugo-Villarino, G.; Vérollet, C.; Sasiain, M. del C.; Balboa, L. Fatty Acid Oxidation of Alternatively Activated Macrophages

Prevents Foam Cell Formation, but Mycobacterium Tuberculosis Counteracts This Process via HIF-1α Activation. *PLOS Pathogens* **2020**, *16* (10), e1008929. https://doi.org/10.1371/journal.ppat.1008929.

(46) Shim, D.; Kim, H.; Shin, S. J. Mycobacterium Tuberculosis Infection-Driven Foamy Macrophages and Their Implications in Tuberculosis Control as Targets for Host-Directed Therapy. *Frontiers in Immunology* **2020**, *11*, 910. https://doi.org/10.3389/fimmu.2020.00910.

(47) Kaufmann, S. H. E.; Dorhoi, A.; Hotchkiss, R. S.; Bartenschlager, R. Host-Directed Therapies for Bacterial and Viral Infections. *Nat Rev Drug Discov* **2017**, *17* (1), 35–56. https://doi.org/10.1038/nrd.2017.162.

(48) Bonora, M.; Patergnani, S.; Rimessi, A.; De Marchi, E.; Suski, J. M.; Bononi, A.; Giorgi, C.; Marchi, S.; Missiroli, S.; Poletti, F.; Wieckowski, M. R.; Pinton, P. ATP Synthesis and Storage. *Purinergic Signalling* **2012**, *8* (3), 343–357. https://doi.org/10.1007/s11302-012-9305-8.

(49) Ritterhoff, J.; Tian, R. Metabolism in Cardiomyopathy: Every Substrate Matters. *Cardiovascular Research* **2017**, *113* (4), 411–421. https://doi.org/10.1093/cvr/cvx017.

(50) Tretter, L.; Patocs, A.; Chinopoulos, C. Succinate, an Intermediate in Metabolism, Signal Transduction, ROS, Hypoxia, and Tumorigenesis. *Biochimica et Biophysica Acta (BBA) - Bioenergetics* **2016**, *1857* (8), 1086–1101. https://doi.org/10.1016/j.bbabio.2016.03.012.

(51) Williams, N. C.; O'Neill, L. A. J. A Role for the Krebs Cycle Intermediate Citrate in Metabolic Reprogramming in Innate Immunity and Inflammation. *Frontiers in Immunology* **2018**, *9*, 141. https://doi.org/10.3389/fimmu.2018.00141.

(52) Liu, T. F.; Brown, C. M.; El Gazzar, M.; McPhail, L.; Millet, P.; Rao, A.; Vachharajani, V. T.; Yoza, B. K.; McCall, C. E. Fueling the Flame: Bioenergy Couples Metabolism and Inflammation. *Journal of Leukocyte Biology* **2012**, *92* (3), 499–507. https://doi.org/10.1189/jlb.0212078.

(53) Jones, W.; Bianchi, K. Aerobic Glycolysis: Beyond Proliferation. *Frontiers in Immunology* **2015**, *6*, 227. https://doi.org/10.3389/fimmu.2015.00227.

(54) Soto-Heredero, G.; Gómez de las Heras, M. M.; Gabandé-Rodríguez, E.; Oller, J.; Mittelbrunn, M. Glycolysis – a Key Player in the Inflammatory Response. *The FEBS Journal* **2020**, *287* (16), 3350–3369. https://doi.org/10.1111/febs.15327.

(55) Korga, A.; Ostrowska, M.; Iwan, M.; Herbet, M.; Dudka, J. Inhibition of Glycolysis Disrupts Cellular Antioxidant Defense and Sensitizes HepG2 Cells to Doxorubicin Treatment. *FEBS Open Bio* **2019**, *9* (5), 959–972. https://doi.org/10.1002/2211-5463.12628.

(56) Bouché, C.; Serdy, S.; Kahn, C. R.; Goldfine, A. B. The Cellular Fate of Glucose and Its Relevance in Type 2 Diabetes. *Endocrine Reviews* **2004**, *25* (5), 807–830. https://doi.org/10.1210/er.2003-0026.

(57) He, L.; Vasiliou, K.; Nebert, D. W. Analysis and Update of the Human Solute Carrier (SLC) Gene Superfamily. *Human Genomics* **2009**, *3* (2), 195. https://doi.org/10.1186/1479-7364-3-2-195.

(58) Li, X.; Gu, J.; Zhou, Q. Review of Aerobic Glycolysis and Its Key Enzymes – New Targets for Lung Cancer Therapy. *Thoracic Cancer* **2014**, *6* (1), 17–24. https://doi.org/10.1111/1759-7714.12148.

(59) Sun, F.; Dai, C.; Xie, J.; Hu, X. Biochemical Issues in Estimation of Cytosolic Free NAD/NADH Ratio. *PloS one* **2012**, *7*, e34525. https://doi.org/10.1371/journal.pone.0034525.

(60) Valvona, C. J.; Fillmore, H. L.; Nunn, P. B.; Pilkington, G. J. The Regulation and Function of Lactate Dehydrogenase A: Therapeutic Potential in Brain Tumor. *Brain Pathology* **2015**, *26* (1), 3–17. https://doi.org/10.1111/bpa.12299.

(61) Liberti, M. V.; Locasale, J. W. The Warburg Effect: How Does It Benefit Cancer Cells? *Trends in Biochemical Sciences* **2016**, *41* (3), 211–218. https://doi.org/10.1016/j.tibs.2015.12.001.
(62) Zheng, J. Energy Metabolism of Cancer: Glycolysis versus Oxidative Phosphorylation (Review). *Oncology Letters* **2012**, *4* (6), 1151–1157. https://doi.org/10.3892/ol.2012.928.
(63) Anderson, N. M.; Mucka, P.; Kern, J. G.; Feng, H. The Emerging Role and Targetability of the TCA Cycle in Cancer Metabolism. *Protein Cell* **2018**, *9* (2), 216–237. https://doi.org/10.1007/s13238-017-0451-1.
(64) Martínez-Reyes, I.; Chandel, N. S. Mitochondrial TCA Cycle Metabolites Control Physiology and Disease. *Nat Commun* **2020**, *11* (1), 102. https://doi.org/10.1038/s41467-019-13668-3.
(65) Wilson, D. F. Oxidative Phosphorylation: Regulation and Role in Cellular and Tissue Metabolism. *The Journal of Physiology* **2017**, *595* (23), 7023–7038. https://doi.org/10.1113/JP273839.
(66) Nolfi-Donegan, D.; Braganza, A.; Shiva, S. Mitochondrial Electron Transport Chain: Oxidative Phosphorylation, Oxidant Production, and Methods of Measurement. *Redox Biology* **2020**, *37*, 101674. https://doi.org/10.1016/j.redox.2020.101674.
(67) Zhao, R.-Z.; Jiang, S.; Zhang, L.; Yu, Z.-B. Mitochondrial Electron Transport Chain, ROS Generation and Uncoupling (Review). *Int J Mol Med* **2019**, *44* (1), 3–15. https://doi.org/10.3892/ijmm.2019.4188.
(68) Raimondi, V.; Ciccarese, F.; Ciminale, V. Oncogenic Pathways and the Electron Transport Chain: A DangeROS Liaison. *Br J Cancer* **2020**, *122* (2), 168–181. https://doi.org/10.1038/s41416-019-0651-y.
(69) Zorova, L. D.; Popkov, V. A.; Plotnikov, E. Y.; Silachev, D. N.; Pevzner, I. B.; Jankauskas, S. S.; Babenko, V. A.; Zorov, S. D.; Balakireva, A. V.; Juhaszova, M.; Sollott, S. J.; Zorov, D. B. Mitochondrial Membrane Potential. *Analytical Biochemistry* **2018**, *552*, 50–59. https://doi.org/10.1016/j.ab.2017.07.009.
(70) Jang, H.-S.; Noh, M. R.; Kim, J.; Padanilam, B. J. Defective Mitochondrial Fatty Acid Oxidation and Lipotoxicity in Kidney Diseases. *Frontiers in Medicine* **2020**, *7*, 65. https://doi.org/10.3389/fmed.2020.00065.
(71) Demine, S.; Renard, P.; Arnould, T. Mitochondrial Uncoupling: A Key Controller of Biological Processes in Physiology and Diseases. *Cells* **2019**, *8* (8), 795. https://doi.org/10.3390/cells8080795.
(72) Mookerjee, S. A.; Divakaruni, A. S.; Jastroch, M.; Brand, M. D. Mitochondrial Uncoupling and Lifespan. *Mechanisms of Ageing and Development* **2010**, *131* (7), 463–472. https://doi.org/10.1016/j.mad.2010.03.010.
(73) Galloway, C. A.; Lee, H.; Yoon, Y. Mitochondrial Morphology—Emerging Role in Bioenergetics. *Free Radical Biology and Medicine* **2012**, *53* (12), 2218–2228. https://doi.org/10.1016/j.freeradbiomed.2012.09.035.
(74) Guerrini, V.; Gennaro, M. L. Foam Cells: One Size Doesn't Fit All. *Trends in Immunology* **2019**, *40* (12), 1163–1179. https://doi.org/10.1016/j.it.2019.10.002.
(75) Tvrzicka, E.; Kremmyda, L.-S.; Stankova, B.; Zak, A. FATTY ACIDS AS BIOCOMPOUNDS: THEIR ROLE IN HUMAN METABOLISM, HEALTH AND DISEASE - A REVIEW. PART 1: CLASSIFICATION, DIETARY SOURCES AND BIOLOGICAL FUNCTIONS. *Biomed Pap Med Fac Univ Palacky Olomouc Czech Repub* **2011**, *155* (2), 117–130. https://doi.org/10.5507/bp.2011.038.
(76) Harayama, T.; Shimizu, T. Roles of Polyunsaturated Fatty Acids, from Mediators to Membranes. *Journal of Lipid Research* **2020**, *61* (8), 1150–1160. https://doi.org/10.1194/jlr.R120000800.

(77) Furuhashi, M.; Hotamisligil, G. S. Fatty Acid-Binding Proteins: Role in Metabolic Diseases and Potential as Drug Targets. *Nat Rev Drug Discov* **2008**, *7* (6), 489–503. https://doi.org/10.1038/nrd2589.
(78) Mashima, T.; Seimiya, H.; Tsuruo, T. De Novo Fatty-Acid Synthesis and Related Pathways as Molecular Targets for Cancer Therapy. *Br J Cancer* **2009**, *100* (9), 1369–1372. https://doi.org/10.1038/sj.bjc.6605007.
(79) Koundouros, N.; Poulogiannis, G. Reprogramming of Fatty Acid Metabolism in Cancer. *Br J Cancer* **2020**, *122* (1), 4–22. https://doi.org/10.1038/s41416-019-0650-z.
(80) Li, L.; Liu, B.; Håversen, L.; Lu, E.; Magnusson, L. U.; Ståhlman, M.; Borén, J.; Bergström, G.; Levin, M. C.; Hultén, L. M. The Importance of GLUT3 for De Novo Lipogenesis in Hypoxia-Induced Lipid Loading of Human Macrophages. *PLOS ONE* **2012**, *7* (8), e42360. https://doi.org/10.1371/journal.pone.0042360.
(81) Schneider, J. G.; Yang, Z.; Chakravarthy, M. V.; Lodhi, I. J.; Wei, X.; Turk, J.; Semenkovich, C. F. Macrophage Fatty-Acid Synthase Deficiency Decreases Diet-Induced Atherosclerosis *. *Journal of Biological Chemistry* **2010**, *285* (30), 23398–23409. https://doi.org/10.1074/jbc.M110.100321.
(82) Su, X.; Abumrad, N. A. Cellular Fatty Acid Uptake: A Pathway under Construction. *Trends in Endocrinology & Metabolism* **2009**, *20* (2), 72–77. https://doi.org/10.1016/j.tem.2008.11.001.
(83) Hamilton, J. A. Fast Flip-Flop of Cholesterol and Fatty Acids in Membranes: Implications for Membrane Transport Proteins. *Current Opinion in Lipidology* **2003**, *14* (3), 263–271. https://doi.org/doi: 10.1097/00041433-200306000-00006.
(84) Mashek, D. G.; Li, L. O.; Coleman, R. A. Long-Chain Acyl-CoA Synthetases and Fatty Acid Channeling. *Future Lipidol* **2007**, *2* (4), 465–476.
(85) Nie, L.; Pascoa, T. C.; Pike, A. C. W.; Bushell, S. R.; Quigley, A.; Ruda, G. F.; Chu, A.; Cole, V.; Speedman, D.; Moreira, T.; Shrestha, L.; Mukhopadhyay, S. M. M.; Burgess-Brown, N. A.; Love, J. D.; Brennan, P. E.; Carpenter, E. P. The Structural Basis of Fatty Acid Elongation by the ELOVL Elongases. *Nat Struct Mol Biol* **2021**, *28* (6), 512–520. https://doi.org/10.1038/s41594-021-00605-6.
(86) Deák, F.; Anderson, R. E.; Fessler, J. L.; Sherry, D. M. Novel Cellular Functions of Very Long Chain-Fatty Acids: Insight From ELOVL4 Mutations. *Frontiers in Cellular Neuroscience* **2019**, *13*, 428. https://doi.org/10.3389/fncel.2019.00428.
(87) Czumaj, A.; Śledziński, T. Biological Role of Unsaturated Fatty Acid Desaturases in Health and Disease. *Nutrients* **2020**, *12* (2), 356. https://doi.org/10.3390/nu12020356.
(88) Tatsuta, T.; Scharwey, M.; Langer, T. Mitochondrial Lipid Trafficking. *Trends in Cell Biology* **2014**, *24* (1), 44–52. https://doi.org/10.1016/j.tcb.2013.07.011.
(89) Jacquemyn, J.; Cascalho, A.; Goodchild, R. E. The Ins and Outs of Endoplasmic Reticulum-Controlled Lipid Biosynthesis. *EMBO reports* **2017**, *18* (11), 1905–1921. https://doi.org/10.15252/embr.201643426.
(90) Balla, T.; Sengupta, N.; Kim, Y. J. Lipid Synthesis and Transport Are Coupled to Regulate Membrane Lipid Dynamics in the Endoplasmic Reticulum. *Biochimica et Biophysica Acta (BBA) - Molecular and Cell Biology of Lipids* **2020**, *1865* (1), 158461. https://doi.org/10.1016/j.bbalip.2019.05.005.
(91) Eichmann, T. O.; Lass, A. DAG Tales: The Multiple Faces of Diacylglycerol—Stereochemistry, Metabolism, and Signaling. *Cell. Mol. Life Sci.* **2015**, *72* (20), 3931–3952. https://doi.org/10.1007/s00018-015-1982-3.
(92) Chang, C.; Dong, R.; Miyazaki, A.; Sakashita, N.; Zhang, Y.; Liu, J.; Guo, M.; Li, B.-L.; Chang, T.-Y.; Xu, M.-H. Human Acyl-CoA:Cholesterol Acyltransferase (ACAT) and Its Potential as a Target for Pharmaceutical Intervention against Atherosclerosis. *Acta Biochimica et Biophysica Sinica* **2006**, *38* (3), 151–156. https://doi.org/10.1111/j.1745-7270.2006.00154.x.

(93) Xu, S.; Zhang, X.; Liu, P. Lipid Droplet Proteins and Metabolic Diseases. *Biochimica et Biophysica Acta (BBA) - Molecular Basis of Disease* **2018**, *1864* (5, Part B), 1968–1983. https://doi.org/10.1016/j.bbadis.2017.07.019.

(94) Houten, S. M.; Violante, S.; Ventura, F. V.; Wanders, R. J. A. The Biochemistry and Physiology of Mitochondrial Fatty Acid β-Oxidation and Its Genetic Disorders. *Annual Review of Physiology* **2016**, *78* (1), 23–44. https://doi.org/10.1146/annurev-physiol-021115-105045.

(95) Brejchova, K.; Radner, F. P. W.; Balas, L.; Paluchova, V.; Cajka, T.; Chodounska, H.; Kudova, E.; Schratter, M.; Schreiber, R.; Durand, T.; Zechner, R.; Kuda, O. Distinct Roles of Adipose Triglyceride Lipase and Hormone-Sensitive Lipase in the Catabolism of Triacylglycerol Estolides. *PNAS* **2021**, *118* (2). https://doi.org/10.1073/pnas.2020999118.

(96) Wanders, R. J. A.; Waterham, H. R.; Ferdinandusse, S. Metabolic Interplay between Peroxisomes and Other Subcellular Organelles Including Mitochondria and the Endoplasmic Reticulum. *Frontiers in Cell and Developmental Biology* **2016**, *3*, 83. https://doi.org/10.3389/fcell.2015.00083.

(97) Schoors, S.; Bruning, U.; Missiaen, R.; Queiroz, K. C. S.; Borgers, G.; Elia, I.; Zecchin, A.; Cantelmo, A. R.; Christen, S.; Goveia, J.; Heggermont, W.; Goddé, L.; Vinckier, S.; Van Veldhoven, P. P.; Eelen, G.; Schoonjans, L.; Gerhardt, H.; Dewerchin, M.; Baes, M.; De Bock, K.; Ghesquière, B.; Lunt, S. Y.; Fendt, S.-M.; Carmeliet, P. Fatty Acid Carbon Is Essential for DNTP Synthesis in Endothelial Cells. *Nature* **2015**, *520* (7546), 192–197. https://doi.org/10.1038/nature14362.

(98) Pike, L. S.; Smift, A. L.; Croteau, N. J.; Ferrick, D. A.; Wu, M. Inhibition of Fatty Acid Oxidation by Etomoxir Impairs NADPH Production and Increases Reactive Oxygen Species Resulting in ATP Depletion and Cell Death in Human Glioblastoma Cells. *Biochimica et Biophysica Acta (BBA) - Bioenergetics* **2010**, *1807* (6), 726–734. https://doi.org/10.1016/j.bbabio.2010.10.022.

(99) Listenberger, L. L.; Han, X.; Lewis, S. E.; Cases, S.; Farese, R. V.; Ory, D. S.; Schaffer, J. E. Triglyceride Accumulation Protects against Fatty Acid-Induced Lipotoxicity. *PNAS* **2003**, *100* (6), 3077–3082. https://doi.org/10.1073/pnas.0630588100.

(100) Wajner, M.; Amaral, A. U. Mitochondrial Dysfunction in Fatty Acid Oxidation Disorders: Insights from Human and Animal Studies. *Biosci Rep* **2016**, *36* (1), e00281. https://doi.org/10.1042/BSR20150240.

(101) Bosch, M.; Sweet, M. J.; Parton, R. G.; Pol, A. Lipid Droplets and the Host–Pathogen Dynamic: FATal Attraction? *Journal of Cell Biology* **2021**, *220* (8). https://doi.org/10.1083/jcb.202104005.

(102) Jarc, E.; Petan, T. Lipid Droplets and the Management of Cellular Stress. *Yale J Biol Med* **2019**, *92* (3), 435–452.

(103) Zhang, C.; Liu, P. The Lipid Droplet: A Conserved Cellular Organelle. *Protein Cell* **2017**, *8* (11), 796–800. https://doi.org/10.1007/s13238-017-0467-6.

(104) Dvorak, A. M. Mast Cell Secretory Granules and Lipid Bodies Contain the Necessary Machinery Important for the in Situ Synthesis of Proteins. *Ultrastructure of Mast Cells and Basophils* **2005**, *85*, 252–315. https://doi.org/10.1159/000086520.

(105) Welte, M. A. Expanding Roles for Lipid Droplets. *Current Biology* **2015**, *25* (11), R470–R481. https://doi.org/10.1016/j.cub.2015.04.004.

(106) Meyers, A.; Weiskittel, T. M.; Dalhaimer, P. Lipid Droplets: Formation to Breakdown. *Lipids* **2017**, *52* (6), 465–475. https://doi.org/10.1007/s11745-017-4263-0.

(107) Gao, M.; Huang, X.; Song, B.-L.; Yang, H. The Biogenesis of Lipid Droplets: Lipids Take Center Stage. *Progress in Lipid Research* **2019**, *75*, 100989. https://doi.org/10.1016/j.plipres.2019.100989.

(108) Kounakis, K.; Chaniotakis, M.; Markaki, M.; Tavernarakis, N. Emerging Roles of Lipophagy in Health and Disease. *Frontiers in Cell and Developmental Biology* **2019**, *7*, 185. https://doi.org/10.3389/fcell.2019.00185.

(109) Fujimoto, T.; Parton, R. G. Not Just Fat: The Structure and Function of the Lipid Droplet. *Cold Spring Harb Perspect Biol* **2011**, *3* (3), a004838. https://doi.org/10.1101/cshperspect.a004838.

(110) Thiam, A. R.; Beller, M. The Why, When and How of Lipid Droplet Diversity. *Journal of Cell Science* **2017**, *130* (2), 315–324. https://doi.org/10.1242/jcs.192021.

(111) Onal, G.; Kutlu, O.; Gozuacik, D.; Dokmeci Emre, S. Lipid Droplets in Health and Disease. *Lipids in Health and Disease* **2017**, *16* (1), 128. https://doi.org/10.1186/s12944-017-0521-7.

(112) Itabe, H.; Yamaguchi, T.; Nimura, S.; Sasabe, N. Perilipins: A Diversity of Intracellular Lipid Droplet Proteins. *Lipids in Health and Disease* **2017**, *16* (1), 83. https://doi.org/10.1186/s12944-017-0473-y.

(113) Shi, L.; Salamon, H.; Eugenin, E. A.; Pine, R.; Cooper, A.; Gennaro, M. L. Infection with Mycobacterium Tuberculosis Induces the Warburg Effect in Mouse Lungs. *Sci Rep* **2015**, *5* (1), 18176. https://doi.org/10.1038/srep18176.

(114) Huang, L.; Nazarova, E. V.; Tan, S.; Liu, Y.; Russell, D. G. Growth of Mycobacterium Tuberculosis in Vivo Segregates with Host Macrophage Metabolism and Ontogeny. *Journal of Experimental Medicine* **2018**, *215* (4), 1135–1152. https://doi.org/10.1084/jem.20172020.

(115) Cumming, B. M.; Addicott, K. W.; Adamson, J. H.; Steyn, A. J. Mycobacterium Tuberculosis Induces Decelerated Bioenergetic Metabolism in Human Macrophages. *eLife* **2018**, *7*, e39169. https://doi.org/10.7554/eLife.39169.

(116) Chandra, P.; He, L.; Zimmerman, M.; Yang, G.; Köster, S.; Ouimet, M.; Wang, H.; Moore, K. J.; Dartois, V.; Schilling, J. D.; Philips, J. A. Inhibition of Fatty Acid Oxidation Promotes Macrophage Control of Mycobacterium Tuberculosis. *mBio* **2020**, *11* (4), e01139-20. https://doi.org/10.1128/mBio.01139-20.

(117) Brandenburg, J.; Marwitz, S.; Tazoll, S. C.; Waldow, F.; Kalsdorf, B.; Vierbuchen, T.; Scholzen, T.; Gross, A.; Goldenbaum, S.; Hölscher, A.; Hein, M.; Linnemann, L.; Reimann, M.; Kispert, A.; Leitges, M.; Rupp, J.; Lange, C.; Niemann, S.; Behrends, J.; Goldmann, T.; Heine, H.; Schaible, U. E.; Hölscher, C.; Schwudke, D.; Reiling, N. WNT6/ACC2-Induced Storage of Triacylglycerols in Macrophages Is Exploited by *Mycobacterium Tuberculosis*. *J Clin Invest* **2021**, *131* (16). https://doi.org/10.1172/JCI141833.

(118) Peyron, P.; Vaubourgeix, J.; Poquet, Y.; Levillain, F.; Botanch, C.; Bardou, F.; Daffé, M.; Emile, J.-F.; Marchou, B.; Cardona, P.-J.; de Chastellier, C.; Altare, F. Foamy Macrophages from Tuberculous Patients' Granulomas Constitute a Nutrient-Rich Reservoir for M. Tuberculosis Persistence. *PLoS Pathog* **2008**, *4* (11), e1000204. https://doi.org/10.1371/journal.ppat.1000204.

(119) Daniel, J.; Maamar, H.; Deb, C.; Sirakova, T. D.; Kolattukudy, P. E. Mycobacterium Tuberculosis Uses Host Triacylglycerol to Accumulate Lipid Droplets and Acquires a Dormancy-like Phenotype in Lipid-Loaded Macrophages. *PLoS Pathog* **2011**, *7* (6), e1002093. https://doi.org/10.1371/journal.ppat.1002093.

(120) Liu, Y.; Nan, B.; Niu, J.; Kapler, G. M.; Gao, S. An Optimized and Versatile Counter-Flow Centrifugal Elutriation Workflow to Obtain Synchronized Eukaryotic Cells. *Frontiers in Cell and Developmental Biology* **2021**, *9*, 905. https://doi.org/10.3389/fcell.2021.664418.

(121) Rooney, J.; Ryde, I.; Sanders, L.; Howlett, E.; Colton, M.; Germ, K.; Mayer, G.; Greenamyre, J.; Meyer, J. PCR Based Determination of Mitochondrial DNA Copy

Number in Multiple Species. *Methods Mol Biol* **2015**, *1241*, 23–38. https://doi.org/10.1007/978-1-4939-1875-1_3.

(122) Feoktistova, M.; Geserick, P.; Leverkus, M. Crystal Violet Assay for Determining Viability of Cultured Cells. *Cold Spring Harb Protoc* **2016**, *2016* (4), pdb.prot087379. https://doi.org/10.1101/pdb.prot087379.

(123) Brady, P. N.; Macnaughtan, M. A. Evaluation of Colorimetric Assays for Analyzing Reductively Methylated Proteins: Biases and Mechanistic Insights. *Anal Biochem* **2015**, *491*, 43–51. https://doi.org/10.1016/j.ab.2015.08.027.

(124) Nowakowski, A. B.; Wobig, W. J.; Petering, D. H. Native SDS-PAGE: High Resolution Electrophoretic Separation of Proteins With Retention of Native Properties Including Bound Metal Ions. *Metallomics* **2014**, *6* (5), 1068–1078. https://doi.org/10.1039/c4mt00033a.

(125) Gallagher, S.; Chakavarti, D. Immunoblot Analysis. *J Vis Exp* **2008**, No. 16, 759. https://doi.org/10.3791/759.

(126) Mahmood, T.; Yang, P.-C. Western Blot: Technique, Theory, and Trouble Shooting. *N Am J Med Sci* **2012**, *4* (9), 429–434. https://doi.org/10.4103/1947-2714.100998.

(127) Craske, J. D.; Bannon, C. D. Gas Liquid Chromatography Analysis of the Fatty Acid Composition of Fats and Oils: A Total System for High Accuracy. *J Am Oil Chem Soc* **1987**, *64* (10), 1413–1417. https://doi.org/10.1007/BF02636990.

(128) Herzog, R.; Schwudke, D.; Shevchenko, A. LipidXplorer: Software for Quantitative Shotgun Lipidomics Compatible with Multiple Mass Spectrometry Platforms. *Curr Protoc Bioinformatics* **2013**, *43*, 14.12.1-14.12.30. https://doi.org/10.1002/0471250953.bi1412s43.

(129) Sielaff, M.; Kuharev, J.; Bohn, T.; Hahlbrock, J.; Bopp, T.; Tenzer, S.; Distler, U. Evaluation of FASP, SP3, and IST Protocols for Proteomic Sample Preparation in the Low Microgram Range. *J Proteome Res* **2017**, *16* (11), 4060–4072. https://doi.org/10.1021/acs.jproteome.7b00433.

(130) Meier, F.; Brunner, A.-D.; Koch, S.; Koch, H.; Lubeck, M.; Krause, M.; Goedecke, N.; Decker, J.; Kosinski, T.; Park, M. A.; Bache, N.; Hoerning, O.; Cox, J.; Räther, O.; Mann, M. Online Parallel Accumulation–Serial Fragmentation (PASEF) with a Novel Trapped Ion Mobility Mass Spectrometer*. *Molecular & Cellular Proteomics* **2018**, *17* (12), 2534–2545. https://doi.org/10.1074/mcp.TIR118.000900.

(131) Prianichnikov, N.; Koch, H.; Koch, S.; Lubeck, M.; Heilig, R.; Brehmer, S.; Fischer, R.; Cox, J. MaxQuant Software for Ion Mobility Enhanced Shotgun Proteomics. *Mol Cell Proteomics* **2020**, *19* (6), 1058–1069. https://doi.org/10.1074/mcp.TIR119.001720.

(132) Cox, J.; Hein, M. Y.; Luber, C. A.; Paron, I.; Nagaraj, N.; Mann, M. Accurate Proteome-Wide Label-Free Quantification by Delayed Normalization and Maximal Peptide Ratio Extraction, Termed MaxLFQ. *Mol Cell Proteomics* **2014**, *13* (9), 2513–2526. https://doi.org/10.1074/mcp.M113.031591.

(133) Willems, E.; Leyns, L.; Vandesompele, J. Standardization of Real-Time PCR Gene Expression Data from Independent Biological Replicates. *Anal Biochem* **2008**, *379* (1), 127–129. https://doi.org/10.1016/j.ab.2008.04.036.

(134) Reimand, J.; Kull, M.; Peterson, H.; Hansen, J.; Vilo, J. G:Profiler—a Web-Based Toolset for Functional Profiling of Gene Lists from Large-Scale Experiments. *Nucleic Acids Research* **2007**, *35* (suppl_2), W193–W200. https://doi.org/10.1093/nar/gkm226.

(135) Yu, G.; He, Q.-Y. ReactomePA: An R/Bioconductor Package for Reactome Pathway Analysis and Visualization. *Mol Biosyst* **2016**, *12* (2), 477–479. https://doi.org/10.1039/c5mb00663e.

(136) Griss, J.; Viteri, G.; Sidiropoulos, K.; Nguyen, V.; Fabregat, A.; Hermjakob, H. ReactomeGSA - Efficient Multi-Omics Comparative Pathway Analysis. *Mol Cell Proteomics* **2020**, *19* (12), 2115–2125. https://doi.org/10.1074/mcp.TIR120.002155.

(137) Bommer, G. T.; Schaftingen, E. V.; Veiga-da-Cunha, M. Metabolite Repair Enzymes Control Metabolic Damage in Glycolysis. *Trends in Biochemical Sciences* **2020**, *45* (3), 228–243. https://doi.org/10.1016/j.tibs.2019.07.004.

(138) Kono, M.; Yoshida, N.; Maeda, K.; Skinner, N. E.; Pan, W.; Kyttaris, V. C.; Tsokos, M. G.; Tsokos, G. C. Pyruvate Dehydrogenase Phosphatase Catalytic Subunit 2 Limits Th17 Differentiation. *PNAS* **2018**, *115* (37), 9288–9293. https://doi.org/10.1073/pnas.1805717115.

(139) Wang, Y.; Branicky, R.; Noë, A.; Hekimi, S. Superoxide Dismutases: Dual Roles in Controlling ROS Damage and Regulating ROS Signaling. *J Cell Biol* **2018**, *217* (6), 1915–1928. https://doi.org/10.1083/jcb.201708007.

(140) Pecina, P.; Capková, M.; Chowdhury, S. K. R.; Drahota, Z.; Dubot, A.; Vojtísková, A.; Hansíková, H.; Houst'ková, H.; Zeman, J.; Godinot, C.; Houstek, J. Functional Alteration of Cytochrome c Oxidase by SURF1 Mutations in Leigh Syndrome. *Biochim Biophys Acta* **2003**, *1639* (1), 53–63. https://doi.org/10.1016/s0925-4439(03)00127-3.

(141) Sambri, I.; Massa, F.; Gullo, F.; Meneghini, S.; Cassina, L.; Carraro, M.; Dina, G.; Quattrini, A.; Patanella, L.; Carissimo, A.; Iuliano, A.; Santorelli, F.; Codazzi, F.; Grohovaz, F.; Bernardi, P.; Becchetti, A.; Casari, G. Impaired Flickering of the Permeability Transition Pore Causes SPG7 Spastic Paraplegia. *EBioMedicine* **2020**, *61*, 103050. https://doi.org/10.1016/j.ebiom.2020.103050.

(142) Morita, M.; Prudent, J.; Basu, K.; Goyon, V.; Katsumura, S.; Hulea, L.; Pearl, D.; Siddiqui, N.; Strack, S.; McGuirk, S.; St-Pierre, J.; Larsson, O.; Topisirovic, I.; Vali, H.; McBride, H. M.; Bergeron, J. J.; Sonenberg, N. MTOR Controls Mitochondrial Dynamics and Cell Survival via MTFP1. *Molecular Cell* **2017**, *67* (6), 922-935.e5. https://doi.org/10.1016/j.molcel.2017.08.013.

(143) Alodaib, A.; Sobreira, N.; Gold, W. A.; Riley, L. G.; Van Bergen, N. J.; Wilson, M. J.; Bennetts, B.; Thorburn, D. R.; Boehm, C.; Christodoulou, J. Whole-Exome Sequencing Identifies Novel Variants in PNPT1 Causing Oxidative Phosphorylation Defects and Severe Multisystem Disease. *Eur J Hum Genet* **2017**, *25* (1), 79–84. https://doi.org/10.1038/ejhg.2016.128.

(144) Gondi, C. S.; Kandhukuri, N.; Dinh, D. H.; Gujrati, M.; Rao, J. S. Downregulation of UPAR and UPA Activates Caspase Mediated Apoptosis, Inhibits the PI3k/AKT Pathway. *Int J Oncol* **2007**, *31* (1), 19–27.

(145) Carbognin, E.; Betto, R. M.; Soriano, M. E.; Smith, A. G.; Martello, G. Stat3 Promotes Mitochondrial Transcription and Oxidative Respiration during Maintenance and Induction of Naive Pluripotency. *The EMBO Journal* **2016**, *35* (6), 618–634. https://doi.org/10.15252/embj.201592629.

(146) Karbowski, M.; Youle, R. J. Dynamics of Mitochondrial Morphology in Healthy Cells and during Apoptosis. *Cell Death Differ* **2003**, *10* (8), 870–880. https://doi.org/10.1038/sj.cdd.4401260.

(147) Hu, T.; Foxworthy, P.; Siesky, A.; Ficorilli, J. V.; Gao, H.; Li, S.; Christe, M.; Ryan, T.; Cao, G.; Eacho, P.; Michael, M. D.; Michael, L. F. Hepatic Peroxisomal Fatty Acid β-Oxidation Is Regulated by Liver X Receptor α. *Endocrinology* **2005**, *146* (12), 5380–5387. https://doi.org/10.1210/en.2005-0591.

(148) Tillander, V.; Alexson, S. E. H.; Cohen, D. E. Deactivating Fatty Acids: Acyl-CoA Thioesterase-Mediated Control of Lipid Metabolism. *Trends Endocrinol Metab* **2017**, *28* (7), 473–484. https://doi.org/10.1016/j.tem.2017.03.001.

(149) Nene, A.; Chen, C.-H.; Disatnik, M.-H.; Cruz, L.; Mochly-Rosen, D. Aldehyde Dehydrogenase 2 Activation and Coevolution of Its EPKC-Mediated Phosphorylation Sites. *Journal of Biomedical Science* **2017**, *24* (1), 3. https://doi.org/10.1186/s12929-016-0312-x.

(150) Goldberg, E. L.; Dixit, V. D. Carnitine Acetyltransferase (CRAT) Expression in Macrophages Is Dispensable for Nutrient Stress Sensing and Inflammation. *Mol Metab* **2017**, *6* (2), 219–225. https://doi.org/10.1016/j.molmet.2016.12.008.

(151) Alfardan, J.; Mohsen, A.-W.; Copeland, S.; Ellison, J.; Keppen-Davis, L.; Rohrbach, M.; Powell, B. R.; Gillis, J.; Matern, D.; Kant, J.; Vockley, J. Characterization of New ACADSB Gene Sequence Mutations and Clinical Implications in Patients with 2-Methylbutyrylglycinuria Identified by Newborn Screening. *Mol Genet Metab* **2010**, *100* (4), 333–338. https://doi.org/10.1016/j.ymgme.2010.04.014.

(152) Zhang, J.; Frerman, F. E.; Kim, J.-J. P. Structure of Electron Transfer Flavoprotein-Ubiquinone Oxidoreductase and Electron Transfer to the Mitochondrial Ubiquinone Pool. *PNAS* **2006**, *103* (44), 16212–16217. https://doi.org/10.1073/pnas.0604567103.

(153) Blomme, A.; Ford, C. A.; Mui, E.; Patel, R.; Ntala, C.; Jamieson, L. E.; Planque, M.; McGregor, G. H.; Peixoto, P.; Hervouet, E.; Nixon, C.; Salji, M.; Gaughan, L.; Markert, E.; Repiscak, P.; Sumpton, D.; Blanco, G. R.; Lilla, S.; Kamphorst, J. J.; Graham, D.; Faulds, K.; MacKay, G. M.; Fendt, S.-M.; Zanivan, S.; Leung, H. Y. 2,4-Dienoyl-CoA Reductase Regulates Lipid Homeostasis in Treatment-Resistant Prostate Cancer. *Nat Commun* **2020**, *11*, 2508. https://doi.org/10.1038/s41467-020-16126-7.

(154) Brookheart, R. T.; Michel, C. I.; Schaffer, J. E. As A Matter of Fat. *Cell Metab* **2009**, *10* (1), 9–12. https://doi.org/10.1016/j.cmet.2009.03.011.

(155) Wlodkowic, D.; Akagi, J.; Dobrucki, J.; Errington, R.; Smith, P. J.; Takeda, K.; Darzynkiewicz, Z. Kinetic Viability Assays Using DRAQ7 Probe. *Curr Protoc Cytom* **2013**, *0* *9*, 10.1002/0471142956.cy0941s65. https://doi.org/10.1002/0471142956.cy0941s65.

(156) Lerner, T. R.; Borel, S.; Greenwood, D. J.; Repnik, U.; Russell, M. R. G.; Herbst, S.; Jones, M. L.; Collinson, L. M.; Griffiths, G.; Gutierrez, M. G. Mycobacterium Tuberculosis Replicates within Necrotic Human Macrophages. *J Cell Biol* **2017**, *216* (3), 583–594. https://doi.org/10.1083/jcb.201603040.

(157) Müller-Taubenberger, A.; Lupas, A. N.; Li, H.; Ecke, M.; Simmeth, E.; Gerisch, G. Calreticulin and Calnexin in the Endoplasmic Reticulum Are Important for Phagocytosis. *EMBO J* **2001**, *20* (23), 6772–6782. https://doi.org/10.1093/emboj/20.23.6772.

(158) Tischfield, M. A.; Engle, E. C. Distinct α and β–Tubulin Isotypes Are Required for the Positioning, Differentiation, and Survival of Neurons: New Support for the "Multi-Tubulin" Hypothesis. *Biosci Rep* **2010**, *30* (5), 319–330. https://doi.org/10.1042/BSR20100025.

(159) Rösch, K.; Kwiatkowski, M.; Schlüter, H.; Herker, E. Lipid Droplet Isolation for Quantitative Mass Spectrometry Analysis. *J Vis Exp* **2017**, No. 122, 55585. https://doi.org/10.3791/55585.

(160) Nose, F.; Yamaguchi, T.; Kato, R.; Aiuchi, T.; Obama, T.; Hara, S.; Yamamoto, M.; Itabe, H. Crucial Role of Perilipin-3 (TIP47) in Formation of Lipid Droplets and PGE2 Production in HL-60-Derived Neutrophils. *PLOS ONE* **2013**, *8* (8), e71542. https://doi.org/10.1371/journal.pone.0071542.

(161) Gu, Y.; Yang, Y.; Cao, X.; Zhao, Y.; Gao, X.; Sun, C.; Zhang, F.; Yuan, Y.; Xu, Y.; Zhang, J.; Xiao, L.; Ye, J. Plin3 Protects against Alcoholic Liver Injury by Facilitating Lipid Export from the Endoplasmic Reticulum. *Journal of Cellular Biochemistry* **2019**, *120* (9), 16075–16087. https://doi.org/10.1002/jcb.28889.

(162) Horvath, S. E.; Daum, G. Lipids of Mitochondria. *Progress in Lipid Research* **2013**, *52* (4), 590–614. https://doi.org/10.1016/j.plipres.2013.07.002.

(163) Manigat, L. C.; Granade, M. E.; Taori, S.; Miller, C. A.; Vass, L. R.; Zhong, X.-P.; Harris, T. E.; Purow, B. W. Loss of Diacylglycerol Kinase α Enhances Macrophage Responsiveness. *Frontiers in Immunology* **2021**, *12*, 4701. https://doi.org/10.3389/fimmu.2021.722469.

(164) Yi, X.; Zhang, B.; Fu, Y.; Yi, Z. STAT1 and Its Related Molecules as Potential Biomarkers in Mycobacterium Tuberculosis Infection. *J Cell Mol Med* **2020**, *24* (5), 2866–2878. https://doi.org/10.1111/jcmm.14856.

(165) Leisching, G.; Cole, V.; Ali, A. T.; Baker, B. OAS1, OAS2 and OAS3 Restrict Intracellular M. Tb Replication and Enhance Cytokine Secretion. *Int J Infect Dis* **2019**, *80S*, S77–S84. https://doi.org/10.1016/j.ijid.2019.02.029.

(166) Hensley, K.; Venkova, K.; Christov, A.; Gunning, W.; Park, J. Collapsin Response Mediator Protein-2: An Emerging Pathologic Feature and Therapeutic Target for Neurodisease Indications. *Mol Neurobiol* **2011**, *43* (3), 180–191. https://doi.org/10.1007/s12035-011-8166-4.

(167) Jolliffe, I. T.; Cadima, J. Principal Component Analysis: A Review and Recent Developments. *Philosophical Transactions of the Royal Society A: Mathematical, Physical and Engineering Sciences* **2016**, *374* (2065), 20150202. https://doi.org/10.1098/rsta.2015.0202.

(168) Vijayan, V.; Pradhan, P.; Braud, L.; Fuchs, H. R.; Gueler, F.; Motterlini, R.; Foresti, R.; Immenschuh, S. Human and Murine Macrophages Exhibit Differential Metabolic Responses to Lipopolysaccharide - A Divergent Role for Glycolysis. *Redox Biology* **2019**, *22*, 101147. https://doi.org/10.1016/j.redox.2019.101147.

(169) Singh, A. K.; Gupta, U. D. Animal Models of Tuberculosis: Lesson Learnt. *Indian J Med Res* **2018**, *147* (5), 456–463. https://doi.org/10.4103/ijmr.IJMR_554_18.

(170) Irwin, S. M.; Driver, E.; Lyon, E.; Schrupp, C.; Ryan, G.; Gonzalez-Juarrero, M.; Basaraba, R. J.; Nuermberger, E. L.; Lenaerts, A. J. Presence of Multiple Lesion Types with Vastly Different Microenvironments in C3HeB/FeJ Mice Following Aerosol Infection with Mycobacterium Tuberculosis. *Disease Models & Mechanisms* **2015**, *8* (6), 591–602. https://doi.org/10.1242/dmm.019570.

(171) Simeone, R.; Bobard, A.; Lippmann, J.; Bitter, W.; Majlessi, L.; Brosch, R.; Enninga, J. Phagosomal Rupture by Mycobacterium Tuberculosis Results in Toxicity and Host Cell Death. *PLOS Pathogens* **2012**, *8* (2), e1002507. https://doi.org/10.1371/journal.ppat.1002507.

(172) Jaisinghani, N.; Dawa, S.; Singh, K.; Nandy, A.; Menon, D.; Bhandari, P. D.; Khare, G.; Tyagi, A.; Gandotra, S. Necrosis Driven Triglyceride Synthesis Primes Macrophages for Inflammation During Mycobacterium Tuberculosis Infection. *Front Immunol* **2018**, *9*, 1490. https://doi.org/10.3389/fimmu.2018.01490.

(173) Madhvi, A.; Mishra, H.; Leisching, G.; Mahlobo, P.; Baker, B. Comparison of Human Monocyte Derived Macrophages and THP1-like Macrophages as in Vitro Models for M. Tuberculosis Infection. *Comparative Immunology, Microbiology and Infectious Diseases* **2019**, *67*, 101355. https://doi.org/10.1016/j.cimid.2019.101355.

(174) Shiratori, H.; Feinweber, C.; Luckhardt, S.; Linke, B.; Resch, E.; Geisslinger, G.; Weigert, A.; Parnham, M. J. THP-1 and Human Peripheral Blood Mononuclear Cell-Derived Macrophages Differ in Their Capacity to Polarize in Vitro. *Mol Immunol* **2017**, *88*, 58–68. https://doi.org/10.1016/j.molimm.2017.05.027.

(175) Huang, Z.; Luo, Q.; Guo, Y.; Chen, J.; Xiong, G.; Peng, Y.; Ye, J.; Li, J. Mycobacterium Tuberculosis-Induced Polarization of Human Macrophage Orchestrates the Formation and Development of Tuberculous Granulomas In Vitro. *PLoS One* **2015**, *10* (6), e0129744. https://doi.org/10.1371/journal.pone.0129744.

(176) Lund, M. E.; To, J.; O'Brien, B. A.; Donnelly, S. The Choice of Phorbol 12-Myristate 13-Acetate Differentiation Protocol Influences the Response of THP-1 Macrophages to a pro-Inflammatory Stimulus. *J Immunol Methods* **2016**, *430*, 64–70. https://doi.org/10.1016/j.jim.2016.01.012.

(177) Nielsen, M. C.; Andersen, M. N.; Møller, H. J. Monocyte Isolation Techniques Significantly Impact the Phenotype of Both Isolated Monocytes and Derived Macrophages in Vitro. *Immunology* **2020**, *159* (1), 63–74. https://doi.org/10.1111/imm.13125.

(178) Hamilton, T. A.; Zhao, C.; Pavicic, P. G.; Datta, S. Myeloid Colony-Stimulating Factors as Regulators of Macrophage Polarization. *Frontiers in Immunology* **2014**, *5*, 554. https://doi.org/10.3389/fimmu.2014.00554.

(179) Cumming, B. M.; Pacl, H. T.; Steyn, A. J. C. Relevance of the Warburg Effect in Tuberculosis for Host-Directed Therapy. *Frontiers in Cellular and Infection Microbiology* **2020**, *10*, 506. https://doi.org/10.3389/fcimb.2020.576596.

(180) Wieczorek, L.; Brown, B. K.; DelSarto Macedo, C.; Wesberry-Schmierer, M.; Ngauy, V.; Rosa Borges, A.; Michael, N. L.; Marovich, M. A.; Montefiori, D. C.; Polonis, V. R. Mitigation of Variation Observed in a Peripheral Blood Mononuclear Cell (PBMC) Based HIV-1 Neutralization Assay by Donor Cell Pooling. *Virology* **2013**, *447* (1), 240–248. https://doi.org/10.1016/j.virol.2013.09.014.

(181) Eady, J. J.; Wortley, G. M.; Wormstone, Y. M.; Hughes, J. C.; Astley, S. B.; Foxall, R. J.; Doleman, J. F.; Elliott, R. M. Variation in Gene Expression Profiles of Peripheral Blood Mononuclear Cells from Healthy Volunteers. *Physiological Genomics* **2005**, *22* (3), 402–411. https://doi.org/10.1152/physiolgenomics.00080.2005.

(182) Dixit, V. D.; Yang, H.; Sayeed, K. S.; Stote, K. S.; Rumpler, W. V.; Baer, D. J.; Longo, D. L.; Mattson, M. P.; Taub, D. D. Controlled Meal Frequency without Caloric Restriction Alters Peripheral Blood Mononuclear Cell Cytokine Production. *J Inflamm* **2011**, *8* (1), 6. https://doi.org/10.1186/1476-9255-8-6.

(183) Bouwens, M.; Afman, L. A.; Müller, M. Fasting Induces Changes in Peripheral Blood Mononuclear Cell Gene Expression Profiles Related to Increases in Fatty Acid β-Oxidation: Functional Role of Peroxisome Proliferator–Activated Receptor α in Human Peripheral Blood Mononuclear Cells. *The American Journal of Clinical Nutrition* **2007**, *86* (5), 1515–1523. https://doi.org/10.1093/ajcn/86.5.1515.

(184) Vrieling, F.; Kostidis, S.; Spaink, H. P.; Haks, M. C.; Mayboroda, O. A.; Ottenhoff, T. H. M.; Joosten, S. A. Analyzing the Impact of Mycobacterium Tuberculosis Infection on Primary Human Macrophages by Combined Exploratory and Targeted Metabolomics. *Sci Rep* **2020**, *10* (1), 7085. https://doi.org/10.1038/s41598-020-62911-1.

(185) Lange, C.; Aarnoutse, R.; Chesov, D.; van Crevel, R.; Gillespie, S. H.; Grobbel, H.-P.; Kalsdorf, B.; Kontsevaya, I.; van Laarhoven, A.; Nishiguchi, T.; Mandalakas, A.; Merker, M.; Niemann, S.; Köhler, N.; Heyckendorf, J.; Reimann, M.; Ruhwald, M.; Sanchez-Carballo, P.; Schwudke, D.; Waldow, F.; DiNardo, A. R. Perspective for Precision Medicine for Tuberculosis. *Frontiers in Immunology* **2020**, *11:566608*. https://doi.org/10.3389/fimmu.2020.566608.

(186) Bacchetti, P.; Deeks, S. G.; McCune, J. M. Breaking Free of Sample Size Dogma to Perform Innovative Translational Research. *Sci Transl Med* **2011**, *3* (87), 87ps24. https://doi.org/10.1126/scitranslmed.3001628.

(187) Amrhein, V.; Greenland, S.; McShane, B. Scientists Rise up against Statistical Significance. *Nature* **2019**, *567* (7748), 305–307. https://doi.org/10.1038/d41586-019-00857-9.

(188) Malinarich, F.; Duan, K.; Hamid, R. A.; Bijin, A.; Lin, W. X.; Poidinger, M.; Fairhurst, A.-M.; Connolly, J. E. High Mitochondrial Respiration and Glycolytic Capacity Represent a Metabolic Phenotype of Human Tolerogenic Dendritic Cells. *The Journal of Immunology* **2015**, *194* (11), 5174–5186. https://doi.org/10.4049/jimmunol.1303316.

(189) Pulliam, D. A.; Deepa, S. S.; Liu, Y.; Hill, S.; Lin, A.-L.; Bhattacharya, A.; Shi, Y.; Sloane, L.; Viscomi, C.; Zeviani, M.; Van Remmen, H. Complex IV Deficient Surf1−/− Mice Initiate Mitochondrial Stress Responses. *Biochem J* **2014**, *462* (2), 359–371. https://doi.org/10.1042/BJ20140291.

(190) Hayek, S. S.; Leaf, D. E.; Samman Tahhan, A.; Raad, M.; Sharma, S.; Waikar, S. S.; Sever, S.; Camacho, A.; Wang, X.; Dande, R. R.; Ibrahim, N. E.; Baron, R. M.; Altintas, M. M.; Wei, C.; Sheikh-Hamad, D.; Pan, J. S.-C.; Holliday, M. W.; Januzzi, J. L.; Weisbord, S. D.; Quyyumi, A. A.; Reiser, J. Soluble Urokinase Receptor and Acute Kidney Injury. *New England Journal of Medicine* **2020**, *382* (5), 416–426. https://doi.org/10.1056/NEJMoa1911481.

(191) Marchetti, P.; Fovez, Q.; Germain, N.; Khamari, R.; Kluza, J. Mitochondrial Spare Respiratory Capacity: Mechanisms, Regulation, and Significance in Non-Transformed and Cancer Cells. *The FASEB Journal* **2020**, *34* (10), 13106–13124. https://doi.org/10.1096/fj.202000767R.

(192) Follstad, B. D.; Wang, D. I.; Stephanopoulos, G. Mitochondrial Membrane Potential Differentiates Cells Resistant to Apoptosis in Hybridoma Cultures. *Eur J Biochem* **2000**, *267* (22), 6534–6540. https://doi.org/10.1046/j.1432-1327.2000.01743.x.

(193) Bonifaz, L. C.; Cervantes-Silva, M. P.; Ontiveros-Dotor, E.; López-Villegas, E. O.; Sánchez-García, F. J. A Role for Mitochondria in Antigen Processing and Presentation. *Immunology* **2015**, *144* (3), 461–471. https://doi.org/10.1111/imm.12392.

(194) Park, D.; Han, C.; Elliott, M. R.; Kinchen, J. M.; Trampont, P. C.; Das, S.; Collins, S.; Lysiak, J. J.; Hoehn, K. L.; Ravichandran, K. S. Continued Clearance of Apoptotic Cells Critically Depends on the Phagocyte Ucp2 Protein. *Nature* **2011**, *477* (7363), 220–224. https://doi.org/10.1038/nature10340.

(195) Chougnet, C. A.; Thacker, R. I.; Shehata, H. M.; Hennies, C. M.; Lehn, M. A.; Lages, C. S.; Janssen, E. M. Loss of Phagocytic and Antigen Cross-Presenting Capacity in Aging DCs Is Associated with Mitochondrial Dysfunction. *J Immunol* **2015**, *195* (6), 2624–2632. https://doi.org/10.4049/jimmunol.1501006.

(196) Tripmacher, R.; Gaber, T.; Burmester, G.; Radbruch, A.; Scheffold, A. Effects of Reduced ATP-Formation on Cytokine Production and Proliferation in Human Peripheral CD4+ T Cells. *Arthritis Res Ther* **2004**, *6* (1), 27. https://doi.org/10.1186/ar1069.

(197) Jastroch, M.; Divakaruni, A. S.; Mookerjee, S.; Treberg, J. R.; Brand, M. D. Mitochondrial Proton and Electron Leaks. *Essays Biochem* **2010**, *47*, 53–67. https://doi.org/10.1042/bse0470053.

(198) Chacko, B. K.; Kramer, P. A.; Ravi, S.; Benavides, G. A.; Mitchell, T.; Dranka, B. P.; Ferrick, D.; Singal, A. K.; Ballinger, S. W.; Bailey, S. M.; Hardy, R. W.; Zhang, J.; Zhi, D.; Darley-Usmar, V. M. The Bioenergetic Health Index: A New Concept in Mitochondrial Translational Research. *Clinical Science* **2014**, *127* (6), 367–373. https://doi.org/10.1042/CS20140101.

(199) Canton, M.; Sánchez-Rodríguez, R.; Spera, I.; Venegas, F. C.; Favia, M.; Viola, A.; Castegna, A. Reactive Oxygen Species in Macrophages: Sources and Targets. *Frontiers in Immunology* **2021**, *12*, 4077. https://doi.org/10.3389/fimmu.2021.734229.

(200) Yang, Q.; Liao, M.; Wang, W.; Zhang, M.; Chen, Q.; Guo, J.; Peng, B.; Huang, J.; Liu, H.; Yahagi, A.; Xu, X.; Ishihara, K.; Cooper, A.; Chen, X.; Cai, Y. CD157 Confers Host Resistance to Mycobacterium Tuberculosis via TLR2-CD157-PKCzeta-Induced Reactive Oxygen Species Production. *mBio* **2019**, *10* (4), e01949-19. https://doi.org/10.1128/mBio.01949-19.

(201) Olive, A. J.; Smith, C. M.; Kiritsy, M. C.; Sassetti, C. M. The Phagocyte Oxidase Controls Tolerance to Mycobacterium Tuberculosis Infection. *The Journal of Immunology* **2018**, *201* (6), 1705–1716. https://doi.org/10.4049/jimmunol.1800202.

(202) Smulan, L. J.; Martinez, N.; Kiritsy, M. C.; Kativhu, C.; Cavallo, K.; Sassetti, C. M.; Singhal, A.; Remold, H. G.; Kornfeld, H. Sirtuin 3 Downregulation in Mycobacterium Tuberculosis-Infected Macrophages Reprograms Mitochondrial Metabolism and Promotes Cell Death. *mBio* **2021**, *12* (1), e03140-20. https://doi.org/10.1128/mBio.03140-20.

(203) Costa, D. L.; Namasivayam, S.; Amaral, E. P.; Arora, K.; Chao, A.; Mittereder, L. R.; Maiga, M.; Boshoff, H. I.; Barry, C. E.; Goulding, C. W.; Andrade, B. B.; Sher, A. Pharmacological Inhibition of Host Heme Oxygenase-1 Suppresses Mycobacterium Tuberculosis Infection In Vivo by a Mechanism Dependent on T Lymphocytes. *mBio* **2016**, *7* (5), e01675-16. https://doi.org/10.1128/mBio.01675-16.

(204) Köster, S.; Upadhyay, S.; Chandra, P.; Papavinasasundaram, K.; Yang, G.; Hassan, A.; Grigsby, S. J.; Mittal, E.; Park, H. S.; Jones, V.; Hsu, F.-F.; Jackson, M.; Sassetti, C. M.; Philips, J. A. Mycobacterium Tuberculosis Is Protected from NADPH Oxidase and LC3-Associated Phagocytosis by the LCP Protein CpsA. *PNAS* **2017**, *114* (41), E8711–E8720. https://doi.org/10.1073/pnas.1707792114.

(205) Rockwood, N.; Costa, D. L.; Amaral, E. P.; Du Bruyn, E.; Kubler, A.; Gil-Santana, L.; Fukutani, K. F.; Scanga, C. A.; Flynn, J. L.; Jackson, S. H.; Wilkinson, K. A.; Bishai, W. R.; Sher, A.; Wilkinson, R. J.; Andrade, B. B. Mycobacterium Tuberculosis Induction of Heme Oxygenase-1 Expression Is Dependent on Oxidative Stress and Reflects Treatment Outcomes. *Front Immunol* **2017**, *8*, 542. https://doi.org/10.3389/fimmu.2017.00542.

(206) Silva Ramos, E.; Larsson, N.-G.; Mourier, A. Bioenergetic Roles of Mitochondrial Fusion. *Biochimica et Biophysica Acta (BBA) - Bioenergetics* **2016**, *1857* (8), 1277–1283. https://doi.org/10.1016/j.bbabio.2016.04.002.

(207) Jornayvaz, F. R.; Shulman, G. I. Regulation of Mitochondrial Biogenesis. *Essays Biochem* **2010**, *47*, 10.1042/bse0470069. https://doi.org/10.1042/bse0470069.

(208) Moya, G. E.; Rivera, P. D.; Dittenhafer-Reed, K. E. Evidence for the Role of Mitochondrial DNA Release in the Inflammatory Response in Neurological Disorders. *Int J Mol Sci* **2021**, *22* (13), 7030. https://doi.org/10.3390/ijms22137030.

(209) Wiens, K. E.; Ernst, J. D. The Mechanism for Type I Interferon Induction by Mycobacterium Tuberculosis Is Bacterial Strain-Dependent. *PLOS Pathogens* **2016**, *12* (8), e1005809. https://doi.org/10.1371/journal.ppat.1005809.

(210) Suh, B. C.; Jeong, H.-N.; Yoon, B. S.; Park, J. H.; Kim, H. J.; Park, S. W.; Hwang, J. H.; Choi, B.-O.; Chung, K. W. Compound Heterozygous Mutations of TYMP as Underlying Causes of Mitochondrial Neurogastrointestinal Encephalomyopathy (MNGIE). *Molecular Medicine Reports* **2013**, *8* (1), 17–22. https://doi.org/10.3892/mmr.2013.1479.

(211) Wali, G.; Kumar, K. R.; Liyanage, E.; Davis, R. L.; Mackay-Sim, A.; Sue, C. M. Mitochondrial Function in Hereditary Spastic Paraplegia: Deficits in SPG7 but Not SPAST Patient-Derived Stem Cells. *Front. Neurosci.* **2020**, *0*. https://doi.org/10.3389/fnins.2020.00820.

(212) Xiao, T.; Sun, J.; Xing, Z.; Xie, F.; Yang, L.; Ding, W. MTFP1 Overexpression Promotes the Growth of Oral Squamous Cell Carcinoma by Inducing ROS Production. *Cell Biol Int* **2020**, *44* (3), 821–829. https://doi.org/10.1002/cbin.11278.

(213) Robinson, N.; Ganesan, R.; Hegedűs, C.; Kovács, K.; Kufer, T. A.; Virág, L. Programmed Necrotic Cell Death of Macrophages: Focus on Pyroptosis, Necroptosis, and Parthanatos. *Redox Biology* **2019**, *26*, 101239. https://doi.org/10.1016/j.redox.2019.101239.

(214) Young, K. W.; Piñon, L. G. P.; Bampton, E. T. W.; Nicotera, P. Different Pathways Lead to Mitochondrial Fragmentation during Apoptotic and Excitotoxic Cell Death in Primary Neurons. *Journal of Biochemical and Molecular Toxicology* **2010**, *24* (5), 335–341. https://doi.org/10.1002/jbt.20343.

(215) Duan, L.; Gan, H.; Golan, D. E.; Remold, H. G. Critical Role of Mitochondrial Damage in Determining Outcome of Macrophage Infection with Mycobacterium Tuberculosis. *The Journal of Immunology* **2002**, *169* (9), 5181–5187. https://doi.org/10.4049/jimmunol.169.9.5181.

(216) Mor, D. E.; Murphy, C. T. Mitochondrial Hyperactivity as a Potential Therapeutic Target in Parkinson's Disease. *Transl Med Aging* **2020**, *4*, 117–120. https://doi.org/10.1016/j.tma.2020.07.007.

(217) Ganjam, G. K.; Bolte, K.; Matschke, L. A.; Neitemeier, S.; Dolga, A. M.; Höllerhage, M.; Höglinger, G. U.; Adamczyk, A.; Decher, N.; Oertel, W. H.; Culmsee, C. Mitochondrial Damage by α-Synuclein Causes Cell Death in Human Dopaminergic Neurons. *Cell Death Dis* **2019**, *10* (11), 1–16. https://doi.org/10.1038/s41419-019-2091-2.

(218) Ning, Y.; Cai, Y.; Dai, Y.; Li, F.; Mo, S.; Werz, O.; Chen, X. Mitochondrial Fusion Mediated by Mitofusin 1 Regulates Macrophage Mycobactericidal Activity by Enhancing Autophagy. *Infection and Immunity* **2021**. https://doi.org/10.1128/IAI.00306-21.

(219) Lee, J.; Choi, J.-A.; Cho, S.-N.; Son, S.-H.; Song, C.-H. Mitofusin 2-Deficiency Suppresses Mycobacterium Tuberculosis Survival in Macrophages. *Cells* **2019**, *8* (11), 1355. https://doi.org/10.3390/cells8111355.

(220) Rossignol, R.; Gilkerson, R.; Aggeler, R.; Yamagata, K.; Remington, S. J.; Capaldi, R. A. Energy Substrate Modulates Mitochondrial Structure and Oxidative Capacity in Cancer Cells. *Cancer Res* **2004**, *64* (3), 985–993. https://doi.org/10.1158/0008-5472.CAN-03-1101.

(221) Wang, S.; Wang, C.; Turdi, S.; Richmond, K. L.; Zhang, Y.; Ren, J. ALDH2 Protects against High Fat Diet-Induced Obesity Cardiomyopathy and Defective Autophagy: Role of CaM Kinase II, Histone H3K9 Methyltransferase SUV39H, Sirt1, and PGC-1α Deacetylation. *Int J Obes* **2018**, *42* (5), 1073–1087. https://doi.org/10.1038/s41366-018-0030-4.

(222) Guo, R.; Xu, X.; Babcock, S. A.; Zhang, Y.; Ren, J. Aldehyde Dehydrogenase-2 (ALDH2) Ameliorates Chronic Alcohol Ingestion-Induced Hepatic Steatosis and Inflammation: Role of Autophagy. *J Hepatol* **2015**, *62* (3), 647–656. https://doi.org/10.1016/j.jhep.2014.10.009.

(223) Zhong, W.; Zhang, W.; Li, Q.; Xie, G.; Sun, Q.; Sun, X.; Tan, X.; Sun, X.; Jia, W.; Zhou, Z. Pharmacological Activation of Aldehyde Dehydrogenase 2 Reverses Alcohol-Induced Hepatic Steatosis and Cell Death in Mice. *J Hepatol* **2015**, *62* (6), 1375–1381. https://doi.org/10.1016/j.jhep.2014.12.022.

(224) Seiler, S. E.; Martin, O. J.; Noland, R. C.; Slentz, D. H.; DeBalsi, K. L.; Ilkayeva, O. R.; An, J.; Newgard, C. B.; Koves, T. R.; Muoio, D. M. Obesity and Lipid Stress Inhibit Carnitine Acetyltransferase Activity. *J Lipid Res* **2014**, *55* (4), 635–644. https://doi.org/10.1194/jlr.M043448.

(225) Gupta, S. S.; Sharp, R.; Hofferek, C.; Kuai, L.; Dorn, G. W.; Wang, J.; Chen, M. NIX-Mediated Mitophagy Promotes Effector Memory Formation in Antigen-Specific CD8+ T Cells. *Cell Reports* **2019**, *29* (7), 1862-1877.e7. https://doi.org/10.1016/j.celrep.2019.10.032.

(226) El-Gharbawy, A.; Vockley, J. Inborn Errors of Metabolism with Myopathy: Defects of Fatty Acid Oxidation and the Carnitine Shuttle System. *Pediatric Clinics of North America* **2018**, *65* (2), 317–335. https://doi.org/10.1016/j.pcl.2017.11.006.

(227) Ellis, J. M.; Li, L. O.; Wu, P.-C.; Koves, T. R.; Ilkayeva, O.; Stevens, R. D.; Watkins, S. M.; Muoio, D. M.; Coleman, R. A. Adipose Acyl-CoA Synthetase-1 (ACSL1) Directs Fatty Acids towards β-Oxidation and Is Required for Cold Thermogenesis. *Cell Metab* **2010**, *12* (1), 53–64. https://doi.org/10.1016/j.cmet.2010.05.012.

(228) Li, L. O.; Ellis, J. M.; Paich, H. A.; Wang, S.; Gong, N.; Altshuller, G.; Thresher, R. J.; Koves, T. R.; Watkins, S. M.; Muoio, D. M.; Cline, G. W.; Shulman, G. I.; Coleman, R. A. Liver-Specific Loss of Long Chain Acyl-CoA Synthetase-1 Decreases Triacylglycerol Synthesis and β-Oxidation and Alters Phospholipid Fatty Acid Composition. *J Biol Chem* **2009**, *284* (41), 27816–27826. https://doi.org/10.1074/jbc.M109.022467.

(229) Padanad, M. S.; Konstantinidou, G.; Venkateswaran, N.; Melegari, M.; Rindhe, S.; Mitsche, M.; Yang, C.; Batten, K.; Huffman, K. E.; Liu, J.; Tang, X.; Rodriguez-Canales, J.; Kalhor, N.; Shay, J. W.; Minna, J. D.; McDonald, J.; Wistuba, I. I.; DeBerardinis, R. J.; Scaglioni, P. P. Fatty Acid Oxidation Mediated by Acyl-CoA Synthetase Long Chain 3 Is Required for Mutant KRAS Lung Tumorigenesis. *Cell Reports* **2016**, *16* (6), 1614–1628. https://doi.org/10.1016/j.celrep.2016.07.009.

(230) Kwak, H.-B.; Woodlief, T. L.; Green, T. D.; Cox, J. H.; Hickner, R. C.; Neufer, P. D.; Cortright, R. N. Overexpression of Long-Chain Acyl-CoA Synthetase 5 Increases Fatty Acid Oxidation and Free Radical Formation While Attenuating Insulin Signaling in Primary Human Skeletal Myotubes. *Int J Environ Res Public Health* **2019**, *16* (7), 1157. https://doi.org/10.3390/ijerph16071157.

(231) Wu, D.; Sanin, D. E.; Everts, B.; Chen, Q.; Qiu, J.; Buck, M. D.; Patterson, A.; Smith, A. M.; Chang, C.-H.; Liu, Z.; Artyomov, M. N.; Pearce, E. L.; Cella, M.; Pearce, E. J. Type 1 Interferons Induce Changes in Core Metabolism That Are Critical for Immune Function. *Immunity* **2016**, *44* (6), 1325–1336. https://doi.org/10.1016/j.immuni.2016.06.006.

(232) Yan, S.; Yang, X.-F.; Liu, H.-L.; Fu, N.; Ouyang, Y.; Qing, K. Long-Chain Acyl-CoA Synthetase in Fatty Acid Metabolism Involved in Liver and Other Diseases: An Update. *World J Gastroenterol* **2015**, *21* (12), 3492–3498. https://doi.org/10.3748/wjg.v21.i12.3492.

(233) Roelands, J.; Garand, M.; Hinchcliff, E.; Ma, Y.; Shah, P.; Toufiq, M.; Alfaki, M.; Hendrickx, W.; Boughorbel, S.; Rinchai, D.; Jazaeri, A.; Bedognetti, D.; Chaussabel, D. Long-Chain Acyl-CoA Synthetase 1 Role in Sepsis and Immunity: Perspectives From a Parallel Review of Public Transcriptome Datasets and of the Literature. *Frontiers in Immunology* **2019**, *10*, 2410. https://doi.org/10.3389/fimmu.2019.02410.

(234) Gaster, M.; Rustan, A. C.; Beck-Nielsen, H. Differential Utilization of Saturated Palmitate and Unsaturated Oleate: Evidence From Cultured Myotubes. *Diabetes* **2005**, *54* (3), 648–656. https://doi.org/10.2337/diabetes.54.3.648.

(235) Korbecki, J.; Bajdak-Rusinek, K. The Effect of Palmitic Acid on Inflammatory Response in Macrophages: An Overview of Molecular Mechanisms. *Inflamm. Res.* **2019**, *68* (11), 915–932. https://doi.org/10.1007/s00011-019-01273-5.

(236) Davanso, M. R.; Crisma, A. R.; Murata, G.; Newsholme, P.; Curi, R. Impact of Dietary Fatty Acids on Macrophage Lipid Metabolism, Signaling and Function. *Immunometabolism* **2020**, *2* (1). https://doi.org/10.20900/immunometab20200008.

(237) Gunduz, F.; Aboulnasr, F. M.; Chandra, P. K.; Hazari, S.; Poat, B.; Baker, D. P.; Balart, L. A.; Dash, S. Free Fatty Acids Induce ER Stress and Block Antiviral Activity of Interferon Alpha against Hepatitis C Virus in Cell Culture. *Virol J* **2012**, *9*, 143. https://doi.org/10.1186/1743-422X-9-143.

(238) Lee, W.; VanderVen, B. C.; Fahey, R. J.; Russell, D. G. Intracellular Mycobacterium Tuberculosis Exploits Host-Derived Fatty Acids to Limit Metabolic Stress. *J Biol Chem* **2013**, *288* (10), 6788–6800. https://doi.org/10.1074/jbc.M112.445056.

(239) Nazarova, E. V.; Montague, C. R.; Huang, L.; La, T.; Russell, D.; VanderVen, B. C. The Genetic Requirements of Fatty Acid Import by Mycobacterium Tuberculosis within Macrophages. *eLife* **2019**, *8*, e43621. https://doi.org/10.7554/eLife.43621.

(240) Pandey, A. K.; Sassetti, C. M. Mycobacterial Persistence Requires the Utilization of Host Cholesterol. *Proc Natl Acad Sci U S A* **2008**, *105* (11), 4376–4380. https://doi.org/10.1073/pnas.0711159105.

(241) Rambold, A. S.; Cohen, S.; Lippincott-Schwartz, J. Fatty Acid Trafficking in Starved Cells: Regulation by Lipid Droplet Lipolysis, Autophagy and Mitochondrial Fusion Dynamics. *Dev Cell* **2015**, *32* (6), 678–692. https://doi.org/10.1016/j.devcel.2015.01.029.

(242) Lee, J. Y.; Zhao, L.; Youn, H. S.; Weatherill, A. R.; Tapping, R.; Feng, L.; Lee, W. H.; Fitzgerald, K. A.; Hwang, D. H. Saturated Fatty Acid Activates but Polyunsaturated Fatty Acid Inhibits Toll-like Receptor 2 Dimerized with Toll-like Receptor 6 or 1*. *Journal of Biological Chemistry* **2004**, *279* (17), 16971–16979. https://doi.org/10.1074/jbc.M312990200.

(243) Lee, J. Y.; Plakidas, A.; Lee, W. H.; Heikkinen, A.; Chanmugam, P.; Bray, G.; Hwang, D. H. Differential Modulation of Toll-like Receptors by Fatty Acids: Preferential Inhibition by n-3 Polyunsaturated Fatty Acids. *Journal of Lipid Research* **2003**, *44* (3), 479–486. https://doi.org/10.1194/jlr.M200361-JLR200.

(244) Nemecz, M.; Constantin, A.; Dumitrescu, M.; Alexandru, N.; Filippi, A.; Tanko, G.; Georgescu, A. The Distinct Effects of Palmitic and Oleic Acid on Pancreatic Beta Cell Function: The Elucidation of Associated Mechanisms and Effector Molecules. *Frontiers in Pharmacology* **2019**, *9*, 1554. https://doi.org/10.3389/fphar.2018.01554.

(245) Urso, C. J.; Zhou, H. Palmitic Acid Lipotoxicity in Microglia Cells Is Ameliorated by Unsaturated Fatty Acids. *Int J Mol Sci* **2021**, *22* (16), 9093. https://doi.org/10.3390/ijms22169093.

(246) Mahamed, D.; Boulle, M.; Ganga, Y.; Mc Arthur, C.; Skroch, S.; Oom, L.; Catinas, O.; Pillay, K.; Naicker, M.; Rampersad, S.; Mathonsi, C.; Hunter, J.; Wong, E. B.; Suleman, M.; Sreejit, G.; Pym, A. S.; Lustig, G.; Sigal, A. Intracellular Growth of Mycobacterium Tuberculosis after Macrophage Cell Death Leads to Serial Killing of Host Cells. *eLife* **2017**, *6*, e22028. https://doi.org/10.7554/eLife.22028.

(247) Kim, M.-J.; Wainwright, H. C.; Locketz, M.; Bekker, L.-G.; Walther, G. B.; Dittrich, C.; Visser, A.; Wang, W.; Hsu, F.-F.; Wiehart, U.; Tsenova, L.; Kaplan, G.; Russell, D. G. Caseation of Human Tuberculosis Granulomas Correlates with Elevated Host Lipid Metabolism. *EMBO Mol Med* **2010**, *2* (7), 258–274. https://doi.org/10.1002/emmm.201000079.

(248) Chapman, K. D.; Ohlrogge, J. B. Compartmentation of Triacylglycerol Accumulation in Plants*. *Journal of Biological Chemistry* **2012**, *287* (4), 2288–2294. https://doi.org/10.1074/jbc.R111.290072.

(249) Mansbach, C. M.; Nevin, P. Intracellular Movement of Triacylglycerols in the Intestine. *J Lipid Res* **1998**, *39* (5), 963–968.

(250) Kilwein, M. D.; Welte, M. A. Lipid Droplet Motility and Organelle Contacts. *Contact (Thousand Oaks)* **2019**, *2*, 10.1177/2515256419895688. https://doi.org/10.1177/2515256419895688.

(251) Cao, J.; Cheng, L.; Shi, Y. Catalytic Properties of MGAT3, a Putative Triacylgycerol Synthase. *J Lipid Res* **2007**, *48* (3), 583–591. https://doi.org/10.1194/jlr.M600331-JLR200.

(252) Solé, E.; Ros-Freixedes, R.; Tor, M.; Pena, R. N.; Estany, J. A Sequence Variant in the Diacylglycerol O-Acyltransferase 2 Gene Influences Palmitoleic Acid Content in Pig Muscle. *Sci Rep* **2021**, *11* (1), 14797. https://doi.org/10.1038/s41598-021-94235-z.

(253) Zhuang, L.; Mao, Y.; Liu, Z.; Li, C.; Jin, Q.; Lu, L.; Tao, R.; Yan, X.; Chen, K. FABP3 Deficiency Exacerbates Metabolic Derangement in Cardiac Hypertrophy and Heart Failure via PPARα Pathway. *Frontiers in Cardiovascular Medicine* **2021**, *8*, 871. https://doi.org/10.3389/fcvm.2021.722908.

(254) Singh, K. H.; Jha, B.; Dwivedy, A.; Choudhary, E.; N, A. G.; Ashraf, A.; Arora, D.; Agarwal, N.; Biswal, B. K. Characterization of a Secretory Hydrolase from Mycobacterium Tuberculosis Sheds Critical Insight into Host Lipid Utilization by M. Tuberculosis. *J Biol Chem* **2017**, *292* (27), 11326–11335. https://doi.org/10.1074/jbc.M117.794297.

(255) Gleeson, L. E.; O'Leary, S. M.; Ryan, D.; McLaughlin, A. M.; Sheedy, F. J.; Keane, J. Cigarette Smoking Impairs the Bioenergetic Immune Response to Mycobacterium

Tuberculosis Infection. *Am J Respir Cell Mol Biol* **2018**, *59* (5), 572–579. https://doi.org/10.1165/rcmb.2018-0162OC.

(256) Vermeulen, I.; Baird, M.; Al-Dulayymi, J.; Smet, M.; Verschoor, J.; Grooten, J. Mycolates of Mycobacterium Tuberculosis Modulate the Flow of Cholesterol for Bacillary Proliferation in Murine Macrophages. *Journal of Lipid Research* **2017**, *58* (4), 709–718. https://doi.org/10.1194/jlr.M073171.

(257) Do, T. Q.; Moshkani, S.; Castillo, P.; Anunta, S.; Pogosyan, A.; Cheung, A.; Marbois, B.; Faull, K. F.; Ernst, W.; Chiang, S. M.; Fujii, G.; Clarke, C. F.; Foster, K.; Porter, E. Lipids Including Cholesteryl Linoleate and Cholesteryl Arachidonate Contribute to the Inherent Antibacterial Activity of Human Nasal Fluid. *The Journal of Immunology* **2008**, *181* (6), 4177–4187. https://doi.org/10.4049/jimmunol.181.6.4177.

(258) Yum, H.-W.; Na, H.-K.; Surh, Y.-J. Anti-Inflammatory Effects of Docosahexaenoic Acid: Implications for Its Cancer Chemopreventive Potential. *Seminars in Cancer Biology* **2016**, *40–41*, 141–159. https://doi.org/10.1016/j.semcancer.2016.08.004.

(259) Weldon, S. M.; Mullen, A. C.; Loscher, C. E.; Hurley, L. A.; Roche, H. M. Docosahexaenoic Acid Induces an Anti-Inflammatory Profile in Lipopolysaccharide-Stimulated Human THP-1 Macrophages More Effectively than Eicosapentaenoic Acid. *J Nutr Biochem* **2007**, *18* (4), 250–258. https://doi.org/10.1016/j.jnutbio.2006.04.003.

(260) Higgins, A. J.; Lees, P. The Acute Inflammatory Process, Arachidonic Acid Metabolism and the Mode of Action of Anti-Inflammatory Drugs. *Equine Vet J* **1984**, *16* (3), 163–175. https://doi.org/10.1111/j.2042-3306.1984.tb01893.x.

(261) Knight, M.; Braverman, J.; Asfaha, K.; Gronert, K.; Stanley, S. Lipid Droplet Formation in Mycobacterium Tuberculosis Infected Macrophages Requires IFN-γ/HIF-1α Signaling and Supports Host Defense. *PLoS Pathog* **2018**, *14* (1), e1006874. https://doi.org/10.1371/journal.ppat.1006874.

(262) Uda, S.; Spolitu, S.; Angius, F.; Collu, M.; Accossu, S.; Banni, S.; Murru, E.; Sanna, F.; Batetta, B. Role of HDL in Cholesteryl Ester Metabolism of Lipopolysaccharide-Activated P388D1 Macrophages. *J Lipid Res* **2013**, *54* (11), 3158–3169. https://doi.org/10.1194/jlr.M042663.

(263) Choi, S.-H.; Sviridov, D.; Miller, Y. I. Oxidized Cholesteryl Esters and Inflammation. *Biochim Biophys Acta* **2017**, *1862* (4), 393–397. https://doi.org/10.1016/j.bbalip.2016.06.020.

(264) Suzuki, M.; Shinohara, Y.; Ohsaki, Y.; Fujimoto, T. Lipid Droplets: Size Matters. *Journal of Electron Microscopy* **2011**, *60* (suppl_1), S101–S116. https://doi.org/10.1093/jmicro/dfr016.

(265) Sadler, A. J.; Williams, B. R. G. Interferon-Inducible Antiviral Effectors. *Nat Rev Immunol* **2008**, *8* (7), 559–568. https://doi.org/10.1038/nri2314.

(266) Boyle, L. H.; Hermann, C.; Boname, J. M.; Porter, K. M.; Patel, P. A.; Burr, M. L.; Duncan, L. M.; Harbour, M. E.; Rhodes, D. A.; Skjødt, K.; Lehner, P. J.; Trowsdale, J. Tapasin-Related Protein TAPBPR Is an Additional Component of the MHC Class I Presentation Pathway. *PNAS* **2013**, *110* (9), 3465–3470. https://doi.org/10.1073/pnas.1222342110.

(267) Rouette, A.; Trofimov, A.; Haberl, D.; Boucher, G.; Lavallée, V.-P.; D'Angelo, G.; Hébert, J.; Sauvageau, G.; Lemieux, S.; Perreault, C. Expression of Immunoproteasome Genes Is Regulated by Cell-Intrinsic and –Extrinsic Factors in Human Cancers. *Sci Rep* **2016**, *6* (1), 34019. https://doi.org/10.1038/srep34019.

(268) Bougneres, L.; Helft, J.; Tiwari, S.; Vargas, P.; Chang, B. H.-J.; Chan, L.; Campisi, L.; Lauvau, G.; Hugues, S.; Kumar, P.; Kamphorst, A. O.; Dumenil, A.-M. L.; Nussenzweig, M.; MacMicking, J. D.; Amigorena, S.; Guermonprez, P. A Role for Lipid Bodies in the Cross-Presentation of Phagocytozed Antigens by MHC Class I in Dendritic Cells. *Immunity* **2009**, *31* (2), 232–244. https://doi.org/10.1016/j.immuni.2009.06.022.

(269) Dvorak, A. M.; Morgan, E. S.; Weller, P. F. RNA Is Closely Associated with Human Mast Cell Lipid Bodies. *Histol Histopathol* **2003**, *18* (3), 943–968. https://doi.org/10.14670/HH-18.943.

(270) Menon, D.; Singh, K.; Pinto, S. M.; Nandy, A.; Jaisinghani, N.; Kutum, R.; Dash, D.; Prasad, T. S. K.; Gandotra, S. Quantitative Lipid Droplet Proteomics Reveals Mycobacterium Tuberculosis Induced Alterations in Macrophage Response to Infection. *ACS Infect Dis* **2019**, *5* (4), 559–569. https://doi.org/10.1021/acsinfecdis.8b00301.

(271) Thelen, M. P.; Kye, M. J. The Role of RNA Binding Proteins for Local MRNA Translation: Implications in Neurological Disorders. *Frontiers in Molecular Biosciences* **2020**, *6:161*. https://doi.org/10.3389/fmolb.2019.00161.

(272) Gao, Q.; Goodman, J. M. The Lipid Droplet—a Well-Connected Organelle. *Front Cell Dev Biol* **2015**, *3*, 49. https://doi.org/10.3389/fcell.2015.00049.

(273) Groebner, J. L.; Tuma, P. L. The Altered Hepatic Tubulin Code in Alcoholic Liver Disease. *Biomolecules* **2015**, *5* (3), 2140–2159. https://doi.org/10.3390/biom5032140.

(274) Benador, I. Y.; Veliova, M.; Mahdaviani, K.; Petcherski, A.; Wikstrom, J. D.; Assali, E.; Acín-Peréz, R.; Shum, M.; Oliveira, M. F.; Cinti, S.; Sztalryd, C.; Barshop, W. D.; Wohlschlegel, J. A.; Corkey, B. E.; Liesa, M.; Shirihai, O. S. Mitochondria Bound to Lipid Droplets Have Unique Bioenergetics, Composition, and Dynamics That Support Lipid Droplet Expansion. *Cell Metab* **2018**, *27* (4), 869-885.e6. https://doi.org/10.1016/j.cmet.2018.03.003.

(275) Shaw, C. S.; Jones, D. A.; Wagenmakers, A. J. M. Network Distribution of Mitochondria and Lipid Droplets in Human Muscle Fibres. *Histochem Cell Biol* **2008**, *129* (1), 65–72. https://doi.org/10.1007/s00418-007-0349-8.

(276) The UniProt Consortium. UniProt: The Universal Protein Knowledgebase in 2021. *Nucleic Acids Research* **2021**, *49* (D1), D480–D489. https://doi.org/10.1093/nar/gkaa1100.

List of abbreviations

Abbreviation	Name
2-DG	2-deoxyglucose
3-PG	3-phosphoglycerate
AB	Antibody
ACAD	Acyl-CoA dehydrogenase
ACAT	Acyl-CoA:cholesterol acyltransferase
ACC	Acetyl-CoA carboxylase
ACN	Acetonitrile
ACOT	Acyl-CoA thioesterase
ACOX	Acyl-CoA oxidases
ACSL	Long-chain acyl-CoA synthetase ligase
ADP	Adenosine 5′ diphosphate
ADPK	ADP-dependent glucokinase
AHRGAP45	Rho GTPase-activating protein 45
AKR1A1	Aldo-keto reductase family 1 member A1
ALDH2	Aldehyde dehydrogenase
AM	Alveolar macrophage
ANOVA	One-way analysis of variance
ATCC	American Type Culture Collection
ATGL	Adipose triglyceride lipase
ATP	Adenosine 5′ trisphosphate
ATPGK	ADP-dependent glucokinase
B2M	Beta-2 microglobulin
BCA	Bicinchoninic acid
BCG	Bacillus Calmette-Guerin
BHT	2,6-di-tert-butyl-4-methylphenol
BSA	Bovine serum albumin
C	Cytochrome C
CAL	Calreticulin
CAN	Acetonitrile
CCE	Counterflow centrifugal elutriation
CD	Cluster of differentiation
CE	Cholesterol ester
Cer	Ceramide
CFU	Colony forming units
CH_2N_2	Diazomethane
$CHCl_3$	Chloroform
CL	Cardiolipin
CoA	Coenzyme A
COVID-19	Coronavirus disease
CPT1	Carnitine-palmitoyl transferase
CRAT	Carnitine acetyltransferase
DAG	Diacylglycerol
DBNL	Drebrin-like protein
ddH_2O	double-distilled hydrogen dioxide
DECR1	2,4-dienoyl-CoA reductase 1
DGAT	Diacylglycerol-*O*-acyltransferase
DMSO	Dimethyl sulfoxide
DNA	Deoxyribonucleic acid
DPYSL2	Dihydropyrimidinase-related protein 2
DTT	Dithiothreitol
ECAR	Extracellular acidification
EIF4A	RNA helicase eucaryotic initiation factor 4a

ELOVL	Elongation of very long chain fatty acids protein
ER	Endoplasmic reticulum
ERF	Endoplasmic reticulum fraction
ETC	Electron transport chain
ETFA	Flavoprotein subunit alpha
F-1,6-BP	Fructose-1,6-biphosphate
FABP	Fatty acid binding proteins
$FADH_2$	Flavin adenine dinucleotide
FADS	Fatty acid desaturase
FAO	Fatty acid oxidation
FASN	Fatty acid synthase
FATP	Fatty acid transport protein
FCS	Forward scatter
FFA	Free fatty acids
Fig.	Figure
FITC	Fluorescein isothiocyanate
G-3-P	Glycerol-3-phosphate
GAP	Glyceraldehyde-3-phosphate
GAPDH	Glyceraldehyde-3-phosphate dehydrogenase
GBP	Guanylate binding protein
GLC	Gas-liquid chromatography
GLUT	Glucose transporters
glycoATP	Glycolytic ATP
GPAT	Glycero-3-phosphate acyl transferase
GSH	Glutathione
GTP	Guanosine triphosphate
h	Hours
HADH	Hydroxy acyl-CoA dehydrogenase
HBSS	Hank's buffered salt solution
HIF	Hypoxia-inducible factor
HK	Hexokinases
hMDM	Human monocyte-derived macrophage
HNRNP	Heterogeneous nuclear ribonucleoproteins
HRP	Horseradish peroxidase
HSL	Hormone-sensitive lipase
IAA	Iodoacetamide
IFIT	Interferon induced protein with tetratricopeptide repeats
IFN	Interferon
IFN	Interferon
IL	Interleukin
IMS	Inner membrane space
INH	Isoniazid
IRF	Interferon regulatory factor
LC	Liquid chromatography
LD	Lipid droplet
LDF	Lipid droplet-enriched fraction
LDH	Lactate dehydrogenase
LFQ	Label-free quantitation
LPC	Lysophosphatidylcholine
LPE	Lysophosphatidylethanolamine
LTBI	Latent tuberculosis infection
m/z	Mass–to–charge
M-CSF	Macrophage colony-stimulating factor
MDR	Multidrug-resistant
MeOH	Methanol

MF	Mitochondrial fraction
MFI	Mean fluorescence intensity
MHC	Major histocompatibility complex
min	Minutes
mitoATP	Mitochondrial ATP
MnSOD	Manganese-dependent superoxide dismutase
MOI	Multiplicity of infection
MS	Mass spectrometry
Mtb	*Mycobacterium tuberculosis*
MTBE	Methyl- tret- butyl ether
MTFP1	Mitochondrial fission process protein 1
MX1	Interferon-induced GTP-binding protein Mx1
NADH	Nicotinamide adenine dinucleotide
NADPH	Nicotinamide adenine dinucleotide phosphate
NaOH	Sodium hydroxide
O_2	Oxygen
OA	Oleic acid
OAS2	Oligoadenylate synthetase 2
OCR	Oxygen consumption rate
OD	Optical density
OXPHOS	Oxidative phosphorylation
P/S	Penicillin/Streptomycin
PA	Phosphatidic acid
PBMC	Peripheral blood mononuclear cell
PBS	Phosphate-buffered saline
PC	Phosphatidylcholine
PDH	Pyruvate dehydrogenase
PE	Phosphatidylethanolamine
PFA	Paraformaldehyde
PFK	Phosphofructokinase
PG	Phosphatidylglycerol
PGK	Phosphoglycerate kinase
Phox	NADPH phagocyte oxidase
PI	Phosphatidylinositol
PK	Pyruvate kinase
PL	Phospholipid
PLAUR	Urokinase plasminogen activator surface receptor
PLIN	Perilipin
PMN	Polymorphonuclear neutrophil
PNPT1	Polyribonucleotide nucleotidyltransferase 1
PPP	Pentose phosphate pathway
PS	Phosphatidylserine
PSMB	Proteasome 20S subunit beta 9 and 10
PVDF	Polyvinylidene fluoride
PWE	Pathway enrichment
RAB	Ras-related protein Rab
rcf	Relative centrifugal force
Rho123	Rhodamine 123
RIF	Rifampicin
RNP	Ribonucleoproteins
ROS	Reactive oxygen species
rpm	Rotations per minute
RR	Rifampicin-resistant

RT	Room temperature
RT-PCR	Real-time PCR
SARS-CoV-2	Severe acute respiratory syndrome – coronavirus 2
SDS-PAGE	Sodium dodecyl-sulfate polyacrylamide gel electrophoresis
SEM	Standard error of the mean
SLC	Solute carrier family
SM	Sphingomyelin
SOD2	Superoxide dismutase 2
SP3	Single-pot solid phase-enhanced sample preparation
SPG7	Paraplegin
SSC	Side scatter
STAT	Signal transducer and activator of transcription
SURF1	Surfeit locus protein 1
TAG	Triacylglycerol
TAPBP	Tapasin
TB	Tuberculosis
TBS	Tris-buffered saline
TCA	Tricarboxylic acid cycle
TGF	Transforming growth factor
Th	T helper
TNF	Tumor necrosis factor
TUBB	Tubulin beta chain
UI	Uninfected
WB	Western blot
WCL	Whole cell lysate
WNT	Wnt family member
XDR	Extensively drug-resistant
α-KG	α-ketoglutarate
α-TUB	Alpha-tubulin
ΔpH	Proton gradient
$\Delta\boldsymbol{\Psi}$	Mitochondrial membrane potential

List of figures

List of supplementary figures

List of tables

Acknowledgments

First and foremost, I would like to express my sincerest gratitude to my supervisor **PD Dr. Norbert Reiling**, who offered me the opportunity to work on this amazing doctoral project and who encouraged my fascination for metabolism and TB research with his never lessening enthusiasm for the field. Furthermore, I would like to thank my co-supervisor **Prof. Dr. Ulrich Schaible** for many thought-provoking and helpful discussions in our half-yearly meetings.

Moreover, I would also like to sincerely thank **PD Dr. Dominik Schwudke**, who performed the lipidome analysis, **Dr. Nicolas Gisch,** who analyzed the free fatty acid levels, and **Prof. Dr. Stefan Tenzer** and **Dr. David Gomez-Zepeda** for performing the proteomics analysis. Without your contribution, we would still be in the dark about metabolic alterations during Mtb infection.

Special thanks go to the great team of research technicians **Svenja Goldenbaum, Carolin Golin** and **Lisa Niwinski**. Countless times you have supported me with your technical and experimental assistance and created a cheerful and motivating working atmosphere.

Further thanks go to **Dr. Julius Brandenburg** for his indispensable expertise and guidance throughout my thesis, and to **Dr. Jost Enninga**, who welcomed me in his laboratory in Paris and provided me with important career guidance.

I would also like to thank our **Vidhisha Sonawane** and **Dr. Carine Sao-Emani** for their support and many interesting discussions.

Publications, conference presentations and awards

Publications:

- Brandenburg, J.; Marwitz, S.; **Tazoll, S. C.**, Waldow, F.; Kalsdorf, B.; Vierbuchen, T.; Scholzen, T.; Gross, A.; Goldenbaum, S.; Hölscher, A.; Hein, M.; Linnemann, L.; Reimann, M.; Kispert, A.; Leitges, M.; Rupp, J.; Lange, C.; Niemann, S.; Behrends, J.; Goldmann, T.; Heine, H.; Schaible, U. E.; Hölscher, C.; Schwudke, D.; Reiling, N. WNT6/ACC2-Induced Storage of Triacylglycerols in Macrophages Is Exploited by *Mycobacterium Tuberculosis*. *J Clin Invest* **2021**, *131* (16). https://doi.org/10.1172/JCI141833
- Sutton, J., Carnell, O. T., Lafage, L., Gray, J., Biboy, J., Gibson, J. F., Pollitt, E., **Tazoll, S. C.**, Turnbull, W., Hajdamowicz, N. H., Salamaga, B., Pidwill, G. R., Condliffe, A. M., Renshaw, S. A., Vollmer, W., & Foster, S. J. Staphylococcus aureus cell wall structure and dynamics during host-pathogen interaction. *PLoS pathogens* **2021**, 17(3), e1009468. https://doi.org/10.1371/journal.ppat.1009468
- Phelan, J. J.; McQuaid, K.; Kenny, C.; Gogan, K. M.; Cox, D. J.; Basdeo, S. A.; O'Leary, S.; **Tazoll, S. C.**; Ó Maoldomhnaigh, C.; O'Sullivan, M. P.; O'Neill, L. A.; O'Sullivan, M. J.; Keane, J. Desferrioxamine Supports Metabolic Function in Primary Human Macrophages Infected With Mycobacterium Tuberculosis. *Frontiers in Immunology* **2020**, *11*, 836. https://doi.org/10.3389/fimmu.2020.00836.
- Phelan, J. J., Basdeo, S. A., **Tazoll, S. C.**, McGivern, S., Saborido, J. R., Keane, J. Modulating Iron for Metabolic Support of TB Host Defense. *Frontiers in immunology* **2018**, *9*, 2296. doi:10.3389/fimmu.2018.02296

Conference presentations:

- 22nd Joint Meeting of the Signal Transduction Society; „Signal transduction – Receptors, Mediators and Genes"; Weimar; November 5th-7th 2018 **(Poster)**
- "NDI_3 – New developments in Immunology, Inflammation and Infection"; Borstel, November 16th 2018 **(Oral presentation)**
- Keystone Symposium "Tuberculosis: Mechanisms, Pathogenesis and Treatment"; Banff (CAN); January 17th – 21st 2019, **(Poster)**
- 23rd Symposium: "Infection and Immunity"; Burg Rothenfels; March 27th – 29th 2019 **(Oral presentation)**
- 23rd Joint Meeting of the Signal Transduction Society; „Trends in Cancer and Infection Weimar; November 4th-6th 2019 **(Poster)**
- "Lipidomics Forum 2019"; Borstel; November 10th – 12th 2019 **(Poster)**

Awards and grants:

- **Best oral presentation award:** "NDI_3 – New developments in Immunology, Inflammation and Infection"; Borstel, November 16th, 2018
- **DGfI Travel Grand** to the Keystone Meeting: "Tuberculosis: Mechanisms, Pathogenesis and Treatment" in Banff (CAN), January 17th – 21st 2019
- **STS Travel Grand** for the 23rd Joint Meeting of the Signal Transduction Society; Weimar; November 4th-6th 2019
- **Poster Price:** "Lipidomics Forum 2019"; Borstel, Herrenhaus; November 10th – 12th 2019
- **DAAD research stipend for doctoral candidates** for a three-month research stay at Institute Pasteur in the group of Dr. Jost Enninga, Paris, September – December 2021